FLOW-INFORMED STRATEGIES FOR TRAJECTORY DESIGN AND ANALYSIS

A Dissertation

Submitted to the Faculty

of

Purdue University

by

Cody R. Short

In Partial Fulfillment of the

Requirements for the Degree

of

Doctor of Philosophy

May 2016

Purdue University

West Lafayette, Indiana

"But why dwell upon these things as though human wit were satisfied with earthly regions and had not dared advance beyond?"

–Galileo Galilei, *Sidereus Nuncius*, 1610

For Branson, Grayson,

Jackson and Lori.

The Short Family on the Banks of the Wabash River Near West Lafayette, Indiana.

(Fall 2015; Jack, Lori, Bran, Cody and Gray)

ACKNOWLEDGMENTS

As a graduate student, I have sometimes been jealous of my colleagues who could work any time they wanted. Come in early—stay late—work from home. Each time this has occurred, I've only had to recall why it is that I can't do the same, and any feeling of jealousy has evaporated. I would never have had the motivation and stamina to accomplish this extended effort if it wasn't for my distractions waiting at home. Thank you Lori, Jack, Gray and Bran—you make all of my efforts away from home come second, and I couldn't be happier for it.

Of course, I would never have gotten to this point in life if it wasn't for my mother and my grandparents who gave me the support and encouragement to get started. Those first steps can absolutely be the hardest. Mindful of this fact, I'm also grateful for my teachers and friends in high school as well as early mentors Ray Stoker and Bettie Keetch. Reflecting upon my time as an undergraduate student, the impact of Profs. Michael Joner and Lawrence Rees at BYU continues to be felt.

I am grateful for my advisor, Professor Kathleen Howell—as one of her students I've enjoyed her support, encouragement and direction. She has always gone to great lengths to be here for her students, and I have seen myself grow under her guidance as a result. I still cannot fathom how she does as much as she does, but I am grateful to be a beneficiary of her efforts.

My committee members, Profs. James Longuski, Jeff Rhoads and Xavier Tricoche, have all shared of their time and insight over the years. I very much appreciate their service. I am also grateful for friends and colleagues from my years of working with Purdue's First Year Engineering program. Especially, I am grateful to Eric Holloway and Prof. Matthew Ohland, both for their mentoring and service. Additionally, I acknowledge and appreciate the collaboration and efforts of Dan Blazevski, Don Dichmann, George Haller and Daniel Pérez-Palau.

I have a great respect and fondness for all of my colleagues in the Multi-body Dynamics Research Group, both past and present. However, the greatest impact on me has come from some of my closest associates: Natasha Bosanac, Amanda Haapala Chalk, Diane Craig Davis, Chris Geisel, Chris Spreen and Geoff Wawrzyniak—their friendship and assistance throughout the years has been very meaningful. Regardless of the length of time we spent together at Purdue, each and every member of the research group has had a positive impact on my life, and I am grateful to know and count them all as friends.

Finally, I acknowledge the various forms of support that have made my graduate work possible. The School of Aeronautics and Astronautics as well as the School of Engineering Education have both supported me as a teaching assistant at times. The Rune and Barbara Eliasen Visualization Laboratory provided engaging technical work and associated support. The College of Engineering at Purdue and the Purdue Division of Financial Aid have also provided support through various fellowships, assistantships and scholarships. Some support associated with NASA grant number NNX13AM17G is also acknowledged. Most recently, the Purdue Forever Fellowship has provided additional support. For each of these groups and awards I express my sincerest appreciation.

TABLE OF CONTENTS

Page

LIST OF TABLES viii
LIST OF FIGURES ix
ABSTRACT xii
1 INTRODUCTION 1
1.1 Problem Scope and Definition 1
1.2 Previous Contributions 2
1.3 Overview of the Present Work 4
2 FLOW-BASED CONCEPTS 6
2.1 Recent Development of Flow-based Notions 6
2.2 The Cauchy–Green Strain Tensor 7
2.3 Cauchy–Green Eigendecomposition 9
2.4 Finite-time Lyapunov Exponents 10
2.5 Flow Control Segments 12
2.6 Lagrangian Coherent Structures 14
2.6.1 Ridges in FTLE Scalar Fields 15
2.6.2 Strainlines/Surfaces of CG Vector Fields 15
3 SYSTEM MODELS 17
3.1 The Two-body Problem 17
3.2 The Circular Restricted Three-body Problem 18
3.3 The Bicircular Four-body Problem 22
3.4 Ephemeris n-body Formulations 23
4 DYNAMICAL SYSTEMS THEORY: A CASE STUDY 25
4.1 History of the Three-body Problem 25
4.2 Equilibrium Points 28
4.3 Periodic Orbits, Fixed Points and Single Shooting 33
4.4 Invariant Manifolds 40
4.4.1 Stable and Unstable Manifolds of Equilibrium Points 43
4.4.2 Manifolds Associated with a Periodic Orbit (Maps) 46
4.5 Chaos 50

Page

5 APPROACHES 55
5.1 Mapping Strategies 55
5.1.1 State-space Maps 55
5.1.2 Stroboscopic FTLE Maps 56
5.1.3 FTLE Trace Maps 59
5.2 Flow-map Features 61
5.2.1 Candidate Point Identification 62
5.2.2 Vector Analysis and Strainlines 63
5.3 Material Curve Advection 66
5.4 Trajectory Sensitivity Analysis 66
6 COMPUTATIONAL CONSIDERATIONS 69
6.1 Challenges 69
6.2 Strategies 71
6.2.1 Integration 71
6.2.2 Linear and Cubic Interpolation 71
6.2.3 Adaptive Mesh Refinement 74
6.2.4 Point-wise Evaluation and Strainline Propagation 76
6.2.5 Complex-step Differentiation 76
6.2.6 Parallel Implementations 79
7 APPLICATIONS 82
7.1 Model Fidelity Independence 82
7.1.1 LEO to the Map: 2BP 83
7.1.2 From the Map to L_1: CRP 85
7.1.3 From the Map to L_1: 4BP 90
7.1.4 From the Map to L_1: MES 95
7.2 FCS Targeting 101
7.2.1 Comparing Control Segments Using Flow-based Context 101
7.2.2 A More General Case 107
7.3 Flow-guided System-to-system Transfers 110
7.3.1 Theoretical Establishment and Lower-fidelity Solutions 110
7.3.2 Higher-fidelity Validation 129
7.4 Map Region Characterization and Trajectory Selection 135
7.4.1 Isolating a Map Region 135
7.4.2 Numerical Analysis Within the Example Region 137
7.5 Maneuver Analysis and Insight 140

Page
7.6 Perturbation Analysis: Investigating Long-term Behavior 148
7.6.1 Perturbation Theory and the Kozai Parameter 151
7.6.2 Orbital Elements 154
7.6.3 Frequency Analysis 158
7.6.4 Additional Analysis of Solar and Lunar Contributions 163
7.6.5 Model Component Analysis 168
7.6.6 Nearby Solutions and FTLE Profiles 172
7.6.7 Conditions for Entering More Stable Modes 174
8 CONCLUDING REMARKS 182
LIST OF REFERENCES 184
VITA 192

LIST OF TABLES

Table		Page
2.1	The Lyapunov Spectrum and Steady-state Behavior	12
4.1	Earth–Moon Libration Points	32
4.2	Jacobi Constant Values for Earth–Moon Libration Points	32
4.3	Local Linear Stability of the Earth–Moon Libration Points	40
4.4	Example Stability Modes of a Periodic Orbit	41
7.1	Transfer Data: Maneuver Costs and Times of Flight	128
7.2	Corrected Ephemeris Solutions and Data	134
7.3	Maneuver and FTLE Alignment	146

LIST OF FIGURES

Figure		Page
2.1	Stretching Associated with Eigenvectors of the Cauchy–Green Tensor	9
2.2	Forward-Backward Method	13
3.1	The Circular Restricted Three-body Problem	19
3.2	Zero Velocity Curves in the P_2 Region	21
3.3	An Example System Modeled by the Bicircular Four-body Problem	22
4.1	Equilibrium Points in the CRP	31
4.2	Transition from a Linear Solution to Nonlinear Solutions	36
4.3	Families of Planar Orbits About Libration Points	38
4.4	Families of Planar Orbits About Each of the Libration Points	39
4.5	Poincaré Map of Manifold Crossings on an FTLE Field	42
4.6	Local Manifolds Associated with L_1 and L_2 in the Earth–Moon CRP	45
4.7	Position-space Projections of Eigenvectors Along an L_1 Orbit	47
4.8	Poincaré Map of Orbit Manifolds	48
4.9	Lyapunov Orbit Stable/Unstable Manifold Trajectories	49
4.10	Sensitive Dependence on Initial Conditions Illustrated	51
4.11	Example Poincaré Map Illustrating Chaotic Behavior	52
4.12	Mappings of Figure 4.11 Onto a Torus	54
5.1	FTLE Values Mapped as Height Ridges	57
5.2	FTLE Colored by Value	58
5.3	An FTLE Trace	59
5.4	A Map of FTLE Traces	60
5.5	Identifying and Refining LCS Candidate Points	64
5.6	Projection of Integrated Strainlines onto an FTLE Field	65
5.7	Three-dimensional Projections of a 4D Surface	67
5.8	A Forward FTLE Packet Identifying Stability Directions	68
6.1	An Illustration of Adaptive Mesh Refinement	75
6.2	Complex-step Derivative and Finite-difference Errors	78
6.3	Views of a GPU Isolated Flow Surface	80
7.1	Arcs from LEO to Region of Interest	84
7.2	P_1 Stable Manifold Branch for $C = C_{L_2}$	85
7.3	FTLE for $C = C_{L_2}$ in the CRP	86
7.4	Hohmann Projection & Selected Manifold	87

Figure Page
7.5 Two Trajectories from Map States 89
7.6 Manually Adjusted Trajectory 89
7.7 FTLE for Initial Sun Angle: 0.25π 91
7.8 FTLE for Initial Sun Angle: 0.50π 91
7.9 FTLE for Initial Sun Angle: 0.75π 92
7.10 Combined Sun Angles 92
7.11 CRP (green) vs. 0.25π 4BP (red) 93
7.12 CRP State Evolved in 4BP 94
7.13 4BP Manifold Arc 94
7.14 July 27 – August 5 Ephemeris FTLE 97
7.15 Composited FTLE Maps 98
7.16 Two Ephemeris Trajectories from the Map 98
7.17 Manually Adjusted Ephemeris Trajectory 99
7.18 Orbits and Control Segments 103
7.19 Connected Forward and Backward Segments 105
7.20 Corrected Ephemeris Solution 106
7.21 Generic Control Points and Advected Curves 107
7.22 Connection of Arbitrarily Selected Map Points 109
7.23 System-to-system Transfer Illustration 111
7.24 Surfaces of Section for FTLE Grids 114
7.25 Maps of FTLE Values Near Titania and Oberon 115
7.26 Strainlines for Figure 7.25 117
7.27 Selected Trajectories from a Strainline Enhanced FTLE Map 119
7.28 Transfer "Bookends" 120
7.29 Negative x-axis Trajectory Crossings 122
7.30 Initial FCS Images on Σ_3 Hyperplane (on the Negative x Axis) 123
7.31 Crossing Combinations 126
7.32 FCS Identified System-to-system Transfer 127
7.33 Ephemeris UTO Transfer Solution 130
7.34 Out-of-plane Excursions for Figure 7.33 130
7.35 Zoomed Views of Maneuver Locations 131
7.36 Temporary Capture at Titania 133
7.37 Longer Duration Capture at Titania 133
7.38 Strainline Enhanced Map for Further Analysis 136
7.39 Initial Filtering Within Isolated Region 136
7.40 FTLE Values and Discrete Constrained Optimum 138
7.41 Views of a Discrete Constrained Optimal Solution 139

Figure Page
7.42 Uncorrected ARTEMIS $P1$, L_2 Segment 141
7.43 Maneuver and Stability Directions (x–y) 142
7.44 Maneuver and Stability Directions (x–z) 143
7.45 Maneuver and Stability Directions (y–z) 143
7.46 Maneuver and Stability Directions (3D) 144
7.47 10 Periods of a TESS-like Science Orbit (Ephemeris Model) 150
7.48 Evolving Kozai Parameter for TESS-like Science Orbit 153
7.49 Osculating Orbital Elements and FTLE Profile 157
7.50 Rotating Frame Frequencies in Spacecraft a_y 158
7.51 Trace of the Principal a_y Spacecraft Period 160
7.52 Change in Amplitude for Three Tracked Peaks Over Time 162
7.53 Sun Directions for Early DRM Events 164
7.54 Sliding Ten-year Integrals of Gravity Perturbations on the Spacecraft 166
7.55 Overall Solar and Lunar Perturbative Contributions to the Motion 167
7.56 Specific Energy Imparted to the Spacecraft Over Time 168
7.57 FTLE Profiles for Baseline and Reduced-Fidelity Propagations 171
7.58 FTLE Profiles from the Baseline and $\pm\boldsymbol{\xi}_n$ Perturbations 173
7.59 FTLE Profiles, Baseline and Perturbations Just Prior to Transition 174
7.60 Unaveraged, Baseline and Perturbation FTLE Traces 176
7.61 Averaged State and Perturbation FTLE Traces 177
7.62 FTLE Trace and Radius Profile from Perturbation to Averaged State 178
7.63 100-year Ephemeris Orbit Evolution 180

ABSTRACT

Short, Cody R. Ph.D., Purdue University, May 2016. Flow-informed Strategies for Trajectory Design and Analysis. Major Professor: Kathleen C. Howell.

This research is focused on augmenting and extending classical dynamical methods by introducing flow-based methodologies into astrodynamical design and analysis. These flow-informed tools apply in extended phase spaces and through all levels of model fidelity. Thus, they apply where classical approaches begin to lose relevance and persist beyond this point. Such methodologies are common in various fields, and have recently begun to receive significant attention within the astrodynamical community for design and analysis efforts.

Trajectory design spaces are frequently vast and complex. In some cases, there are an infinite number of possibilities for particular solutions. Even after eliminating the infeasible choices, many options may still remain. Some strategies for selecting a candidate solution to incorporate into an astrodynamical design focus on simplification or reduction of the space. This approach has proven useful for many mission scenarios. However, such an approach, by its very nature, represents a potential loss of alternative solutions and may require reverting to the initial phases of the process when a new option is required. Approaches that reduce the distance from the initial design effort to its end result represent a potential improvement to the design process. Methods incorporating flow behaviors represent one such option where the understanding of the space is expanded and additional solutions are revealed.

1. INTRODUCTION

An intrinsic property of humanity is a collective desire and effort to understand its place and purpose. This understanding has been met with technological development, that is, critical thought and the resulting practical applications. The present document represents the efforts of one individual, working with others, to contribute to the collective endeavor. In this introduction, the broader analysis that comprises the document is situated and briefly outlined.

1.1 Problem Scope and Definition

Trajectory design spaces are frequently vast and complex. In some cases, there are an infinite number of possibilities for particular solutions. Even after eliminating the infeasible choices, many options may still remain. Some strategies for selecting a candidate solution to incorporate into an astrodynamical design focus on simplification or reduction of the space. This approach has proven useful for many mission scenarios. However, such an approach, by its very nature, represents a potential loss of alternative solutions and may require reverting to the initial phases of the process when a new option is required. Approaches that reduce the distance from the initial design effort to its end result represent a potential improvement to the design process. The goal of this work is to further establish, demonstrate, validate and extend flow-based tools and strategies that have seen only minimal application within astrodynamical contexts. In so doing, understanding of the space is expanded and additional solutions are revealed.

Classical approaches to obtaining a better understanding of astrodynamical contexts are reflected in conic and patched-conic analysis as well as in the application of dynamical systems theory. Such applications have yielded insight justifying previous

mission options based on the underlying natural dynamics and have been a means for developing entire mission trajectories. This insight is self-reinforcing as a better understanding of the dynamical characteristics of one system can be extended to inform the process for future efforts and results in additional, and potentially better, options. These methods, however, can limit the available solution options. The inherent simplifications may reduce the solution space and eliminate key environmental components that trigger characteristic behaviors. Therefore, alternative approaches are required to incorporate important behaviors, and these approaches necessitate the appropriate tools.

This analysis is focused on augmenting and extending classical dynamical methods by introducing flow-based methodologies into astrodynamical design and analysis. These flow-informed tools apply in extended phase spaces and through all levels of model fidelity. Thus, they apply where classical approaches begin to lose relevance and persist beyond this point. Such methodologies are common in various fields, but they have only recently received significant attention within the astrodynamical community. The flow-based ideas described here are related to the recent notions of Lagrangian coherent structures, a theory generally associated with the study of fluid dynamics. Not only does this work adopt and adapt such previously established tool sets, but contributes to the development and extension of these options.

1.2 Previous Contributions

Of fundamental importance in aerospace engineering, particularly within the field of astrodynamics, is a geometrical understanding of the possible motions a spacecraft or a satellite can assume under the influence of gravitational forces. In the presence of one body, the Keplerian motion of the massless body is integrable and yields explicit analytical solutions. In the case of the Circular Restricted three-body Problem (CRP, or "restricted problem"), the equations of motion are autonomous in a rotating frame, revealing periodic orbits, invariant manifolds, chaotic regions, and other clas-

sical phase-space structures. In more intricate gravitational fields, however, classical dynamical systems approaches do not apply. One goal of this work is to introduce new geometric techniques for such complex models.

Previous efforts to geometrically describe different trajectory behaviors employ the Finite-Time Lyapunov Exponent (FTLE) scalar field [2–5], which measures the locally largest stretching in the flow. Here, consideration of the direction of largest stretching is proposed as well. Throughout the flow, these directions are exploited to identify useful paths of motion from an initial point and to parametrize regions that separate distinct trajectory patterns using the related notions of *stretchlines* associated with the largest stretching direction as well as reduced *strainlines*, respectively. These extensions are motivated by the recent notions of hyperbolic Lagrangian Coherent Structures (LCS) developed in [6], [7], [8], and [9].

Both FTLE and the eigenvectors of the Cauchy–Green Strain Tensor (CGST) are associated with Lagrangian coherent structure theory, which features prominently in the field of fluid dynamics. These concepts appear in a number of examples in this document and supply a framework for targeting and transfer problem analysis in nonautonomous multi-body systems. In previous investigations, [10] discusses the application of FTLE over relatively short time spans, denoting the metric as the Local Lyapunov Exponent (LLE), to identify sensitive regions along a trajectory. Improved patch point placement for differential corrections strategies using FTLE values is investigated by [11], [12] and [13]. Various authors, including [14], [15], and [16], all apply fast Lyapunov chaoticity indicators, a metric similar in form to FTLE, for preliminary spacecraft trajectory design and stability analyses in multi-body environments. Some related Dynamical Systems Theory (DST) approaches that have direct relevance to system-to-system transfers are offered by [17], [18] and [19]. Such DST methods are enhanced by flow-based strategies as discussed in [20]. In another application closely associated with this investigation, [2] examines LCS in the mixed position-velocity phase space of the planar elliptic restricted three-body problem. Additional efforts to apply FTLE and LCS methods in the three-body

problem within the context of periapse mappings are offered by [3]. The detection of invariant manifolds from LCS in the circular restricted three-body problem is also examined in [21, 22]. An examination of the impact of increasing the fidelity of the multi-body model on FTLE analysis and LCS-guided design is investigated by [5]. Identification of linked orbits in the four-body problem using LCS is considered by [23]. Yet another application is presented by [24] where Jet Transport is considered in conjunction with CG theory.

1.3 Overview of the Present Work

The study of astrodynamics has benefited from centuries of innovation and insight. Yet, there still remain challenging and interesting problems to be solved, and many of these problems require new approaches. This work serves as one example of how ideas from one discipline may be used to inform new methods in another, and lead to new discovery. The document is organized as follows:

- Chapter 2: Flow-based Concepts

  While flow-based methodologies have been extensively applied to numerous problems, they have seen limited application in astrodynamical problems. This work serves to further adapt and establish such notions. This chapter outlines the mathematical concepts upon which the associated strategies are developed.

- Chapter 3: System Models

  As a basis for many of the examples and illustrations in the document, the underlying dynamical models must be established. Several different models are presented and their fundamental mathematics are summarized.

- Chapter 4: Dynamical Systems Theory: A Case Study

  The circular restricted three-body problem serves as a case study to discuss dynamical systems notions. A brief history of the three-body problem is given.

Then, the equilibrium points in the CRP are defined and computed for a particular system. Periodic orbits and fixed points are discussed. The topic of invariant manifolds is briefly explored, and the chapter concludes with a discussion of chaos.

- Chapter 5: Approaches

  The particular strategies utilized in this work are rooted in classical methods including conic tools and dynamical systems theory. However, these approaches are supplemented and superseded as necessary by adopting and developing flow-based strategies. Several such strategies are discussed.

- Chapter 6: Computational Considerations

  To some degree, the expansion of computational capabilities has revitalized research in dynamical systems and fluid mechanics. Poincaré maps and the eponymous computational fluid dynamics, for example, were largely infeasible only a few decades ago due to their numerically intensive nature. It is not surprising, then, that the methodology associated with the present discussion is largely computational. As such, an overview of the applicable computational challenges and strategies to meet these challenges is presented.

- Chapter 7: Selected Applications

  Results generated for several sample cases are presented. A comprehensive example of the ideas presented in previous chapters is discussed. Moreover, various ideas are demonstrated in unique ways and new strategies and theories are both established and expanded. Information resulting from such processes is validated by evolution and comparison through different levels of model fidelity.

- Chapter 8: Concluding Remarks

  A summary of the entire investigation is presented. Comments are included regarding potential future investigation associated with this analysis, and concluding remarks are given.

2. FLOW-BASED CONCEPTS

Ideas related to flows and their analysis are generally encountered in the context of fluid dynamics. However, the differential equations that simulate multi-body gravity environments are often studied by numerically integrating some initial state. This initial state may be considered as a particle subject to the natural flow of the system. The particle is said to be advected by the flow. In fact, a *flow map*, $\phi_{t_o}^{t}(\boldsymbol{x}_o)$, is defined as the mechanism that yields a state in a system that has evolved to a final time t from an initial state $\boldsymbol{x}_o$ at time t_o. Flow-based tools represent extensions of common methods utilized in dynamical systems approaches to astrodynamics and provide additional insight into alternative design possibilities.

2.1 Recent Development of Flow-based Notions

Lagrangian Coherent Structures (LCS) are a relatively recent development, introduced just over a decade ago, around which many of the recent flow-based approaches have evolved. Despite this recent development, the underlying concept of coherent structures within flows is timeless as a natural phenomenon. Peacock and Dabiri [25] indicate that da Vinci [26] was the first to capture structures in a moving fluid by sketching different patterns in water flowing over obstacles some 500 years ago. Much more recently, in 2000, Haller [27, 28] as well as Haller and Yuan [29] formalized the mathematics of LCS and gave the concept its name. While there are different metrics that can be employed within flow analysis, the Finite-Time Lyapunov Exponent (FTLE) is fairly common, where relatively high values of the FTLE indicate LCS. The FTLE measures the stretching between adjacent trajectories over a prescribed time interval. Criteria to distinguish between actual stretching and shear in flows have been established [30]. Shadden et al. [31] seek to establish the idea that LCS

act as transport barriers in the flow by showing that the flux across LCS is negligible. Mathur et al. [32] have improved on the criteria for extracting LCS, and Lekien et al. [33] help to establish the relevance of LCS methodology in n-dimensional motion and explore methods for identifying such structures. Ongoing mathematical development and formulation of the notions has persisted. Haller and Beron-Vera [34] explore various aspects of the Cauchy–Green Strain Tensor to supply a rigorous criteria for identifying flow patterns. The development is also supported by variational theory and higher-dimensional efforts ([6], [7], [8]).

Given a rapidly developing theoretical foundation, the popularity of coherent structures has blossomed recently such that active research is occurring in multiple disciplines. Simultaneous activities in computer science and visualization seek to effectively compute and extract LCS. Specifically, work by Garth et al. [35], featuring adaptive mesh refinement for the calculation of FTLE near structures, has provided one means for improving the time efficiency of methods for obtaining LCS. Additional applications of LCS have been presented regarding weather data, transport in the oceans, aeronautical computational fluid dynamics, and even human musculoskeletal biomechanics, circulation, and airway transport [25]. Many other applications have emerged in a multitude of disciplines, and the application of flow-based notions in astrodynamical contexts has received increasing attention as well. Several applicable references are noted in Section 1.2, and all of these efforts indicate the potential for the associated theory.

2.2 The Cauchy–Green Strain Tensor

The Cauchy–Green Strain Tensor (CGST) describes the relative stretching of nearby trajectories over a given time interval. As such, the Cauchy–Green tensor offers a means for identifying relatively larger or smaller directions of expansion. This relative information can be identified from the eigenvalues and eigenvectors of the tensor. The CGST is computed from the State Transition Matrix (STM, $\Phi_{t_o}^{t}(\boldsymbol{x}_o)$),

a matrix that describes the impact of initial state variations on the final state along a path or trajectory—essentially a sensitivity matrix. Mathematically, Φ evaluated along the arc for time t is expressed,

$$\Phi_{t_\mathrm{o}}^{t}(\boldsymbol{x}_\mathrm{o}) = \frac{d\phi_{t_\mathrm{o}}^{t}(\boldsymbol{x}_\mathrm{o})}{d\boldsymbol{x}_\mathrm{o}}. \tag{2.1}$$

This STM can be calculated by directly observing the effects of perturbed trajectories, or by integrating the first-order variational equations of the system equations of motion. For example, if several adjacent, initial state vectors are separated by small perturbations and subsequently evolved for a prescribed time, the STM is estimated (here, using only two dimensions for illustration) as described by [28] via finite differencing such as,

$$\left.\frac{d\phi_{t_\mathrm{o}}^{t}(\boldsymbol{x})}{d\boldsymbol{x}_\mathrm{o}}\right|_{(i,j)} = \begin{bmatrix} \frac{x_{i+1,j}(t)-x_{i-1,j}(t)}{x_{i+1,j}(t_\mathrm{o})-x_{i-1,j}(t_\mathrm{o})} & \frac{x_{i,j+1}(t)-x_{i,j-1}(t)}{y_{i,j+1}(t_\mathrm{o})-y_{i,j-1}(t_\mathrm{o})} \\ \frac{y_{i+1,j}(t)-y_{i-1,j}(t)}{x_{i+1,j}(t_\mathrm{o})-x_{i-1,j}(t_\mathrm{o})} & \frac{y_{i,j+1}(t)-y_{i,j-1}(t)}{y_{i,j+1}(t_\mathrm{o})-y_{i,j-1}(t_\mathrm{o})} \end{bmatrix}, \tag{2.2}$$

where the indices (i,j) indicate relative initial perturbations in (x,y), respectively.

Various schemes exist for calculating Φ, including numerical integration of the variational equations, direct calculation from a grid of points (as in Equation (2.2)) or through the use of an auxiliary grid as described by [7]. Direct computation from a grid of points that covers the domain of the simulation permits evaluation of the matrix in systems where variational equations are not available. Selecting an appropriate grid spacing is critical. An auxiliary grid that brackets each of the primary grid points increases the accuracy of the computation. Taking the matrix product of the transpose (indicated by $^\mathsf{T}$) of the STM with itself, $\Phi^\mathsf{T}\Phi$, gives the Cauchy–Green strain tensor [36],

$$\mathbf{C} = \Phi^\mathsf{T}\Phi. \tag{2.3}$$

Since the state transition matrix supplies the evolution of infinitesimal perturbations to an initial state of the system, the Cauchy–Green strain tensor represents a natural object that reveals the growth or decay of these perturbations. Further, the operation of "squaring" the STM results in a positive definite matrix that is generally better behaved than Φ itself, a consideration impacting the eigendecomposition of $\mathbf{C}$.

2.3 Cauchy–Green Eigendecomposition

Eigendecomposition of the Cauchy–Green tensor distills powerful metrics that enable study of the underlying flow behavior. As its name implies, the process yields the eigenvalues, λ_i, and eigenvectors, $\boldsymbol{\xi}_i$, of the tensor. These results may, in turn, be harnessed to illuminate the effects of the flow in particular regions of the phase space. Such an isolation of characteristic behavior associated with sets of initial states represents direct insight that can be exploited to inform the design process. Additionally, the eigenvalues and eigenvectors may be employed to supply context in the local phase space and analyze maneuvers.

The ubiquitous concept resulting from CG eigendecomposition relates the stretching of a portion of the phase space over time to λ_i and $\boldsymbol{\xi}_i$. Specifically, stretching occurs in the phase space along the eigenvector, $\boldsymbol{\xi}_i$, proportional to $\sqrt{\lambda_i}$,

$$\left|\mathrm{D}\phi_{t_\mathrm{o}}^{t}(\boldsymbol{x}_\mathrm{o})\boldsymbol{\xi}_i\right| = \sqrt{\lambda_i}\,|\boldsymbol{\xi}_i|\,. \tag{2.4}$$

Consequently, the greatest degree of stretching occurs along the eigenvector, $\boldsymbol{\xi}_n$, associated with the largest eigenvalue, λ_n. This notion is illustrated in Figure 2.1, where the double-headed red arrow represents $\boldsymbol{\xi}_n$ and the double-headed blue arrow

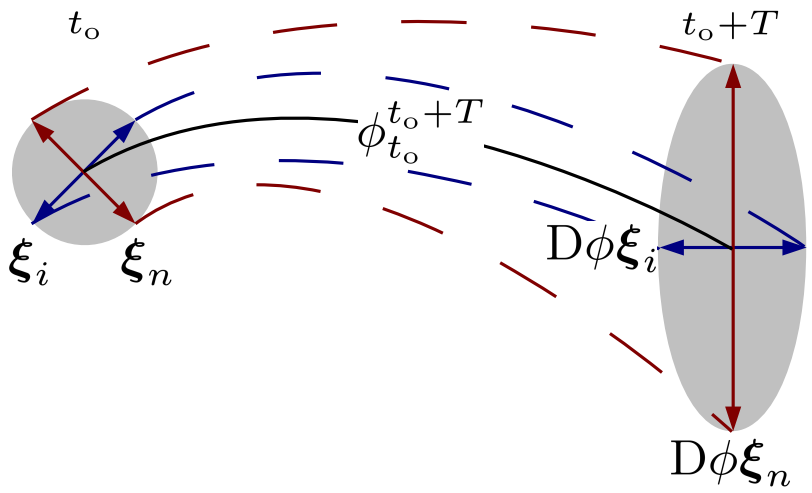

Figure 2.1.: Stretching Associated with Eigenvectors of the Cauchy–Green Tensor

conveys the remaining directions. The eigenvalues and eigenvectors of the CGST are embedded in the ideas of finite-time Lyapunov exponents, flow control segments, and Lagrangian coherent structures.

2.4 Finite-time Lyapunov Exponents

The Lyapunov exponents arise as the chief result of Lyapunov's study of stability in dynamical systems [37]. The most common approach for computation of the Lyapunov exponents traces back to Olseledec [38], where the necessary mathematical background of the Lyapunov exponents is detailed. A more contextual treatment is offered by Anderson [39]. Lyapunov exponents represent a metric that, in the limit, describes the relative balance of order and chaos in a system. In a given dynamical system, there are as many Lyapunov exponents as dimensions in the phase space, and collectively they comprise the Lyapunov spectrum. However, one exponent typically dominates and is often the value of interest, that is, the characteristic or maximal Lyapunov exponent. On a local scale, the Lyapunov exponents supply a measure of the contraction or expansion relative to a neighboring trajectory given an initial variation. The effect of such initial variations is typically approximated via the linear variational equations using the State Transition Matrix, $\Phi_{t_\mathrm{o}}^{t}(\boldsymbol{x}_\mathrm{o})$ or STM. Specifically, an initial variation, $\delta\boldsymbol{x}(t_\mathrm{o})$, results in a final variation $\delta\boldsymbol{x}(t)$ consistent with Equation (2.5), that is,

$$\delta\boldsymbol{x}(t) = \Phi_{t_\mathrm{o}}^{t}(\boldsymbol{x}_\mathrm{o})\delta\boldsymbol{x}(t_\mathrm{o}), \tag{2.5}$$

Assuming that the variations grow exponentially, the overall expansion or contraction indicated by the STM is dominated by the rate Λ_n (where n is the dimension of the phase space), and the norms of the initial and final variations can be compared, i.e.,

$$|\delta\boldsymbol{x}(t)| = |\delta\boldsymbol{x}(t_\mathrm{o})|\, e^{\Lambda_n t}, \tag{2.6}$$

where Λ_n represents the characteristic Lyapunov exponent. Solving for Λ_n, normalizing by time, and evolving the system such that time approaches infinity, yields the characteristic Lyapunov exponent, that is,

$$\Lambda_n = \lim_{t\to\infty} \frac{1}{t} \ln \frac{|\delta \boldsymbol{x}(t)|}{|\delta \boldsymbol{x}(t_\mathrm{o})|}. \tag{2.7}$$

The argument of the natural logarithm in Equation (2.7) is, effectively, "the norm of the STM". Thus, the spectral norm also produces the characteristic Lyapunov exponent,

$$\Lambda_n = \lim_{t\to\infty} \frac{1}{t} \ln \left|\left|\Phi_{t_\mathrm{o}}^{t}\right|\right|. \tag{2.8}$$

Parker and Chua [40] define the entire Lyapunov spectrum similarly, that is,

$$\Lambda_i = \lim_{t\to\infty} \frac{1}{t} \ln |\lambda_i(t)| \qquad i = 1, \ldots, n, \tag{2.9}$$

where $|\lambda_i(t)|$ are the n normalized eigenvalues of the STM, computed from the n eigenvalues of $\sqrt{\mathbf{C}} = \sqrt{\Phi^{\mathsf{T}}\Phi}$. In the limit, the Lyapunov exponents define the chaoticity of the local neighborhood in the vicinity of $\boldsymbol{x}_\mathrm{o}$. In Table 2.1, similar to the table appearing in Parker and Chua [40], the relative values of the Lyapunov exponents are summarized in terms of the corresponding steady state behavior in a local region.

The Lyapunov exponents characterize the future behavior in a particular region of the phase space in a system. This characterization is inherently associated with some initial position and time. However, the definition of the Lyapunov exponents implies knowledge of the system evolution as time approaches infinity. In some systems, such a limit is not readily available, and computing a metric such as a Lyapunov exponent requires modification of the definition for practical application.

Also available from the Cauchy–Green tensor, the Finite-Time Lyapunov Exponents (FTLE) supply a relative measure of growth or contraction of phase-space elements under the influence of the system flow over a given time period. Finite-time Lyapunov exponents are, effectively, finite-time truncations of the classical Lyapunov exponents. The largest FTLE value is frequently employed to help identify Lagrangian Coherent Structures (LCS), and is sometimes identified as *the FTLE* (this practice

Table 2.1: The Lyapunov Spectrum and Steady-state Behavior

Lyapunov Exponents	Associated Steady State
$0 > \Lambda_1 \geq \cdots \geq \Lambda_n$	Equilibrium Point
$\Lambda_1 = 0,$ $0 > \Lambda_2 \geq \cdots \geq \Lambda_n$	Periodic Orbit
$\Lambda_1 = \Lambda_2 = 0,$ $0 > \Lambda_3 \geq \cdots \geq \Lambda_n$	Two-periodic Torus
$\Lambda_1 = \cdots = \Lambda_K = 0,$ $0 > \Lambda_{K+1} \geq \cdots \geq \Lambda_n$	K-periodic Torus
$\Lambda_1 > 0, \quad \sum_{i=2}^{n} \Lambda_i < 0$	Chaotic

is adopted here unless otherwise noted). Relatively high values of the FTLE may, in some cases, indicate LCS. The FTLE essentially measures the stretching between adjacent trajectories over a prescribed time interval. Mathematically, the calculation of the FTLE is fairly straightforward—it is the largest normalized eigenvalue of $\mathbf{C}$, i.e., the matrix spectral norm of Φ. Thus, the expression for the FTLE is,

$$\Lambda_T = \frac{1}{|T|} \ln \lambda_{\max} \left(\sqrt{\mathbf{C}} \right), \tag{2.10}$$

where $\lambda_{\max}()$ is the operation that extracts the largest eigenvalue of the operand. The parameter $T = t - t_{\mathrm{o}}$ represents both the truncation time for the FTLE calculation as well as a means for normalizing the FTLE value.

2.5 Flow Control Segments

The eigenvectors of the Cauchy–Green tensor also yield relevant information. For example, examination of the eigenvector structure of the CGST within the context of coherent structures implies the relationship that $\boldsymbol{\xi}_n \widehat{=} \lambda_n$ is everywhere orthogonal

to repelling LCS in planar cases [6, 34], where $\boldsymbol{\xi}_n$ is the eigenvector associated with the largest eigenvalue, λ_n. Blazevski and Haller demonstrate the extension of this concept, with additional constraints, to three-dimensional flows [8]. More generally, $\boldsymbol{\xi}_n$ reveals the direction of greatest expansion along a particular trajectory arc.

The notion of control segments is introduced by Shinbrot et al. [41] with further extensions by Schroer and Ott [42]. In Schroer and Ott, the authors employ small arc segments or circles about specific points on a Poincaré map to join two periodic orbits from different regions in the chaotic CRP phase space. Working in the planar CRP, a map is defined in terms of position and velocity (Cartesian x and $\dot{x}$) components in the rotating frame. A strategy where a segment and circle are simultaneously iterated, forward from the vicinity of an initial orbit and backward from a target orbit region on the map, is utilized. As the segments are advected under the flow, their pre- or post-images grow until, after some (likely different) number of forward and backward iterations, an intersection occurs. This process is illustrated in Figure 2.2, reproduced from [42] with permission. Such an intersection is a connection in all components of the planar CRP state and represents an end-to-end trajectory joining the orbits with

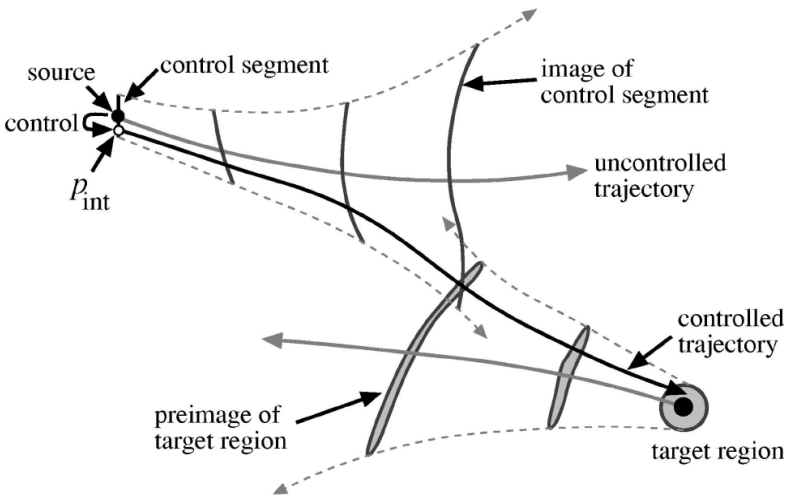

Figure 2.2.: Forward-Backward Method of [41] (Reprinted with permission from [42], ©1997, AIP Publishing LLC.)

small velocity discontinuities at departure and insertion. In Grebow [43], the example from Schroer and Ott is revisited. Grebow observes that the natural stretching of the target circle quickly collapses it to an arc. Thus, the process is equally well served by employing line segments for both forward- and backward-time evolutions.

A modest extension of the control segment concept takes into account the stretching of the phase space induced by the flow in the system. This extension is represented by Flow Control Segments (FCS), which are constructed along the eigenvector, $\boldsymbol{\xi}_n$, associated with the largest eigenvalue of the Cauchy–Green tensor. Recall from Equation (2.4), assuming an appropriate time scale for calculating the CGST, stretching occurs in the phase space along the eigenvector, $\boldsymbol{\xi}_i$, proportional to $\sqrt{\lambda_i}$. Thus, $\boldsymbol{\xi}_n$ supplies the most-stretching direction in the flow, and represents the optimal choice for divergent behavior. Consequently, the images resulting from evolving $\boldsymbol{\xi}_n$-aligned segments intersect after fewer iterations yielding a shorter time-duration transfer.

2.6 Lagrangian Coherent Structures

Lagrangian coherent structures are defined as influential material surfaces (sets of trajectories) that locally induce the largest deformation of nearby phase-space elements [6]. They exist in the form of hyperbolic and shear LCS where they display the largest attraction, repulsion or shear in a neighborhood. This notion of structures that characterize the flow in a region represents a powerful insight for describing useful options for trajectory design. The insight is particularly applicable in astrodynamical problems since LCS exist in complex settings where other, more restricted, options are not available. For example, the stable and unstable manifold tubes associated with unstable periodic orbits in the CRP, that are frequently exploited to guide trajectory design, are not available in higher-fidelity ephemeris models. In fact, in autonomous systems, there exists a correlation between LCS and invariant manifolds. However, classic stable and unstable manifolds are only guaranteed to act as governing elements of phase-space deformation over infinitely long times. Over finite times, LCS play this

role, evolving with the flow even in autonomous systems. As the finite-time interval of their extraction grows, LCS gradually converge to classic invariant manifolds, should the latter exist in the flow. Even in the restricted problem, options that employ manifold structures to guide the flow from some generic point may not be readily available. However, given any initial state in a system, a CG tensor can be evaluated and information can be deduced regarding the behavior of the flow resulting from the evolution of such a state. Structural information may be obtained in a general sense and LCS identified if they exist. A brief discussion of some common options for constructing Lagrangian coherent structures follows.

2.6.1 Ridges in FTLE Scalar Fields

In practice, an entire field of FTLE values is often computed and displayed on a map or section. Then, comparisons of FTLE values across a relatively large area are possible. Specifically, regions characteristic of similar FTLE values are identified. A single individual region may appear markedly different, in terms of FTLE value, than other regions within the field. Bounding these regions are height ridges corresponding to relatively large FTLE values. Such ridges are defined as curves where the FTLE values are maximal with respect to the largest principle curvature. These ridge values are largest with respect to the sides of the ridge but not necessarily along the top of the ridge where they may be greater or less than neighboring ridge values. Height ridges, their significance and computation, are discussed in [44]. These strongest FTLE ridges may represent Lagrangian coherent structures, and act as boundaries in the flow separating regions of different qualitative behavior.

2.6.2 Strainlines/Surfaces of CG Vector Fields

While the FTLE is a convenient and relatively well-behaved measure of the stretching between neighboring trajectories, it represents only part of the information available from the Cauchy–Green tensor. Other valuable insights are accessible directly

from the eigenvalues and eigenvectors of the tensor. In two-dimensional flows, Haller and Beron-Vera [34] establish various vector fields with the associated strainlines that correspond to transport barriers or LCS. Haller and Beron-Vera elaborate on exploiting all of the eigenvalues, eigenvectors and composite eigenvalue-eigenvector fields to identify different types of structures. For example, the particular strainlines that correlate with hyperbolic LCS are available from the eigenvector fields consistent with the smallest or largest eigenvalues. The vector fields associated with the eigenvalues are strain fields, hence, trajectories integrated through the fields are strainlines. The strainlines with the smallest point-wise geodesic deviation are identified as hyperbolic transport barriers. Moreover, a selected tolerance on the value of the geodesic deviation supplies a criterion to identify convergence of the LCS and to calibrate algorithms for detecting such structures. In higher-dimensional systems, the strainline concept extends to strainsurfaces and, similar to the planar case, LCS can be constructed by isolating the strainsurfaces that align with or are normal to certain eigenvectors of the Cauchy–Green tensor [8].

3. SYSTEM MODELS

Flow-based methodologies are not necessarily contingent on any assumptions in the derivation of a particular system of differential equations. Therefore, the associated tools can be applied to dynamical models regardless of their level of fidelity. Several such models are invoked in these efforts, including the Circular Restricted three-body Problem (CRP), a restricted Four-Body Problem (4BP) and point mass ephemeris formulations. Additionally, the Two-Body Problem (2BP) supplies some comparison information. The governing equations and some relevant considerations in each model are summarized.

3.1 The Two-body Problem

The equations of motion for a massless body (in this case, a spacecraft) under the influence of a central gravitational field are represented in a rotating frame. Directions are identified by unit vectors: $\hat{r}$ radially outward from the central body to the spacecraft, $\hat{\theta}$ oriented 90° with respect to $\hat{r}$ in the orbit plane and $\hat{h} = \hat{r} \times \hat{\theta}$ consistent with the orbital angular momentum. The equations are expressed as two second-order coupled nonlinear differential equations,

$$\ddot{r} = r\dot{\theta}^2 - \frac{\mu_{2b}}{r^2}, \tag{3.1}$$

$$\ddot{\theta} = -\frac{2\dot{r}\dot{\theta}}{r}, \tag{3.2}$$

where r is the distance of the spacecraft from the central body in the $\hat{r}$ direction, $\dot{\theta}$ is the angular velocity of the rotating frame with respect to an inertial frame, and μ_{2b} is the gravitational parameter.

Despite the nonlinear, coupled nature of the equations, closed-form analytical solutions exist in the form of well-known conic solutions. However, in this investigation,

Equations (3.1) and (3.2) are converted to a system of four first-order nonlinear differential equations suitable for numerical integration for convenience and consistency when comparing between models.

3.2 The Circular Restricted Three-body Problem

Some key space environments involve multiple gravity fields. Therefore, it is often necessary to incorporate as many of these gravity fields as possible into the governing models to ensure accurate simulation and to capture the essential features of the dynamical interactions. Models involving more than two bodies generally offer no analytical solutions, and introduce additional complexities, which may be small but significant. Formulating the problem in terms of three bodies produces a model sufficiently complex to reveal many important characteristics while remaining tractable. The general three-body problem possesses no closed-form analytical solution [45]. Thus, additional simplifications, such as those consistent with the CRP, offer significant insight. The circular restricted three-body problem incorporates the effects of two larger, massive *primaries* (for example, the Earth and the Moon evolving on circular orbits) on a third, much smaller primary of negligible mass (e.g., a spacecraft).

A mathematical definition for the CRP is necessary for numerical simulation. Figure 3.1 is included to illustrate the system definitions. The two primary bodies that appear in the model are designated as P_1 and P_2. Position variables, x, y, and z describe the position of the third body P_3, the spacecraft, with respect to the barycenter B of the primary system, which also serves as the origin of the rotating $(\hat{x}, \hat{y}, \hat{z})$ and inertial reference frames $(\hat{X}, \hat{Y}, \hat{Z})$. The system mass parameter is represented by $\mu = \frac{m_2}{m_1+m_2}$, a function of the masses of the primary bodies. Additionally, distances between the third body and each of the massive primaries are denoted r_{i3}. In a coordinate frame that rotates coincident with the circular motion of the primaries, a system

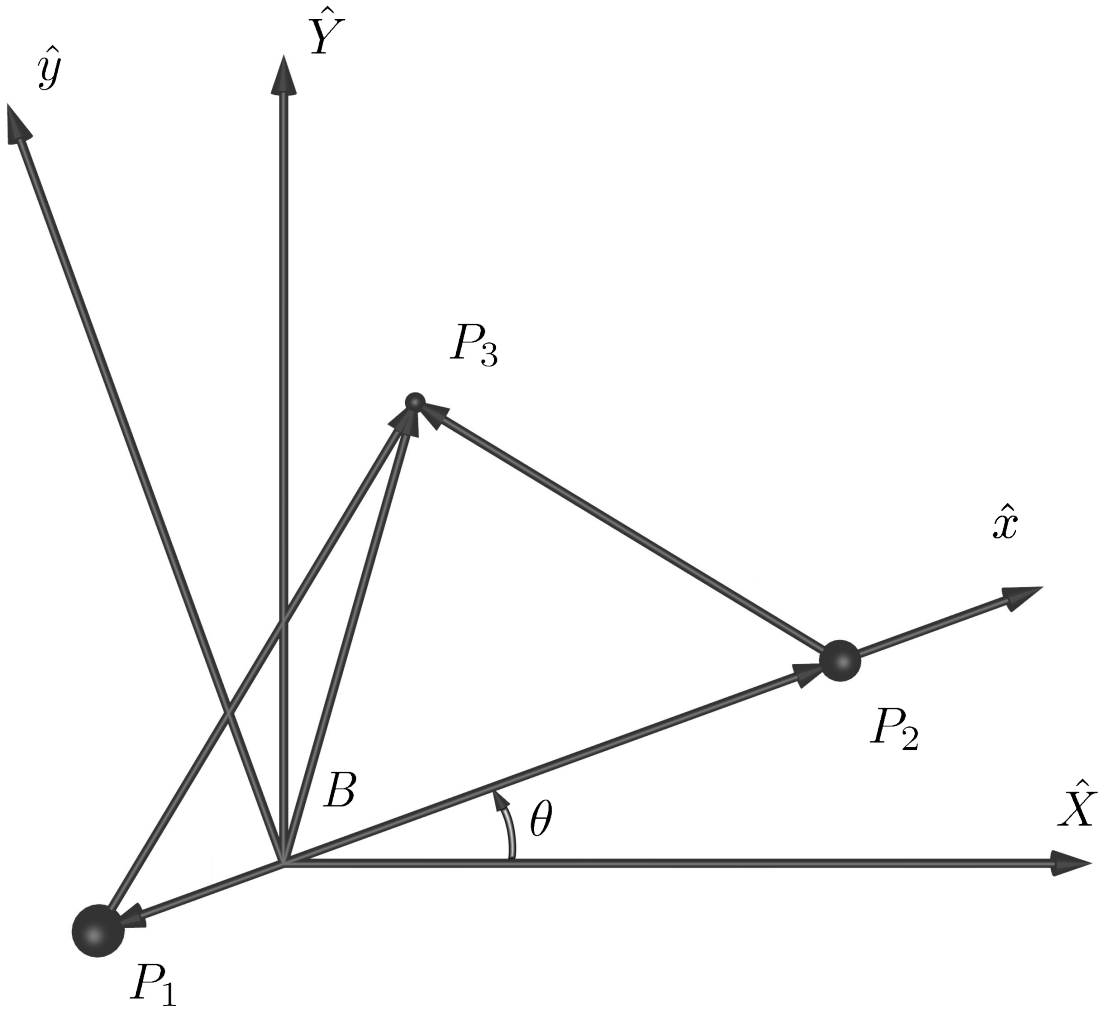

Figure 3.1.: The Circular Restricted Three-body Problem

of differential equations that describes the motion of the third body incorporates the potential function,

$$U^* = \frac{1-\mu}{r_{13}} + \frac{\mu}{r_{23}} + \frac{1}{2}(x^2 + y^2), \tag{3.3}$$

and is written,

$$\ddot{x} = \frac{\partial U^*}{\partial x} + 2\dot{y}, \quad \ddot{y} = \frac{\partial U^*}{\partial y} - 2\dot{x}, \quad \ddot{z} = \frac{\partial U^*}{\partial z}, \tag{3.4}$$

where the first derivatives in x and y appear as a result of the Coriolis acceleration.

The equations of motion in the restricted problem are consistent with [46] where they admit a single constant of the motion. This *Jacobi integral* is defined,

$$C = 2U^* - v^2, \tag{3.5}$$

where $v^2 = \dot{x}^2 + \dot{y}^2 + \dot{z}^2$, that is, the square of the magnitude of the relative velocity. The Jacobi integral, a scalar represented by C, should not be confused with the Cauchy–Green tensor, $\mathbf{C}$. The Jacobi constant allows for a reduction of order in the problem, and frequently plays an important role in the definition of maps. The integral also reveals boundaries on the motion of the third body in the restricted problem. These boundaries are defined when the velocity in Equation (3.5) is zero, separating regions of real and imaginary velocities. An example of the Jacobi limiting boundaries, or Zero Velocity Curves (ZVC) in the x-y plane, is depicted in Figure 3.2 along with the two libration points near the second primary (in this case, Saturn at 50× scale in the Sun–Saturn system). These types of boundaries on the motion are intimately associated with the definitions of the maps employed in this work.

The restricted problem represents a model of sufficient complexity to exhibit regions of both chaotic and relatively ordered behavior. Generally, the focus of an analysis in this model is understanding and exploiting behavior that is associated with the chaotic regions to identify useful trajectory arcs. The CRP model is frequently suitable to yield first-order mission design solutions, but its underlying assumptions narrow the overall design space. Analysis of the flow in the system, while increasing the model fidelity, yields additional insight.

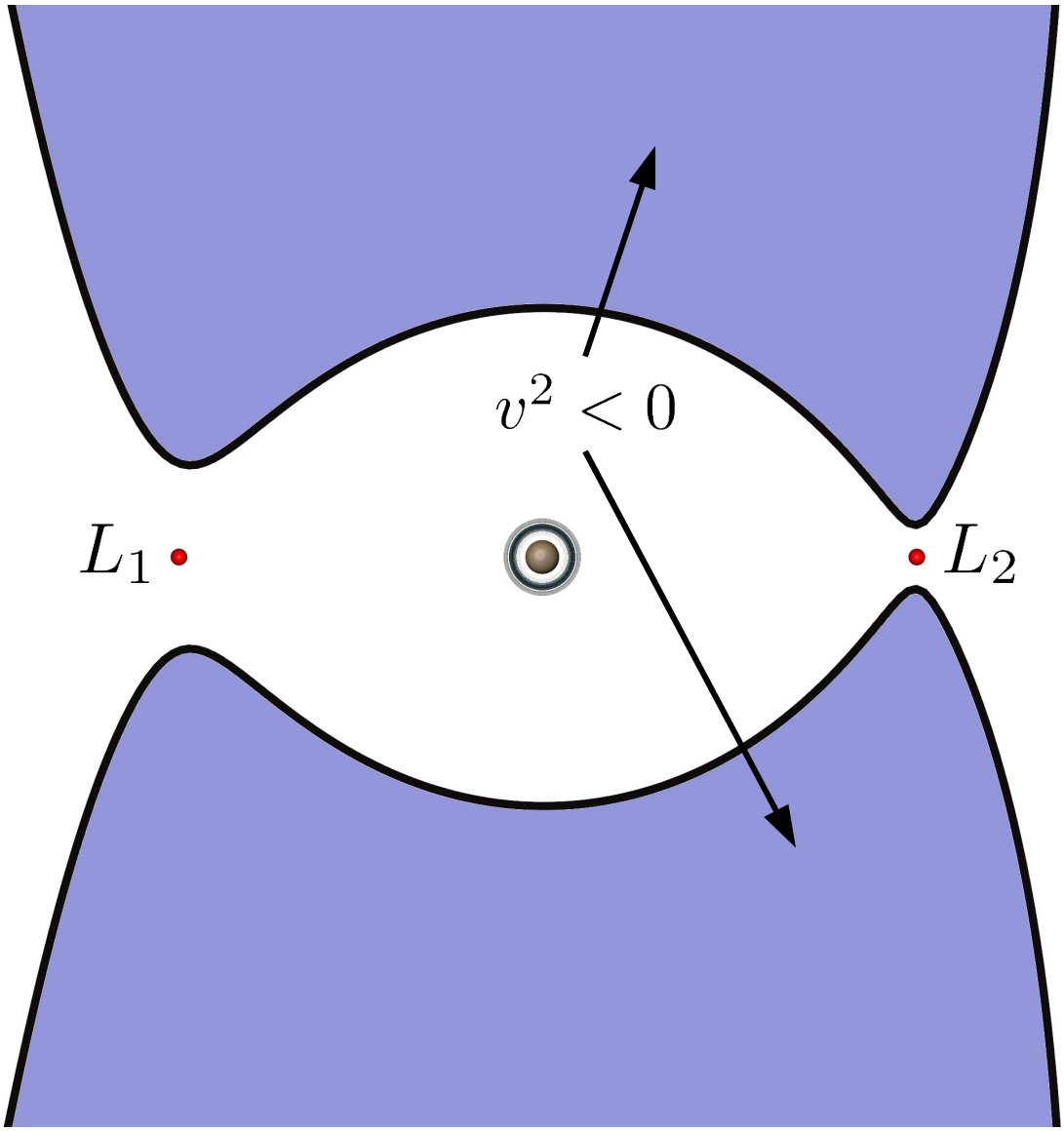

Figure 3.2.: Zero Velocity Curves in the P_2 Region

3.3 The Bicircular Four-body Problem

The bicircular four-body problem incorporates the influence of a fourth body as a perturbation to the restricted problem dynamics. The relative geometry of such a system is depicted in Figure 3.3, where an initial angle for the fourth body with respect to the CRP rotating x axis is denoted θ_0. Under this model, a fourth, distant

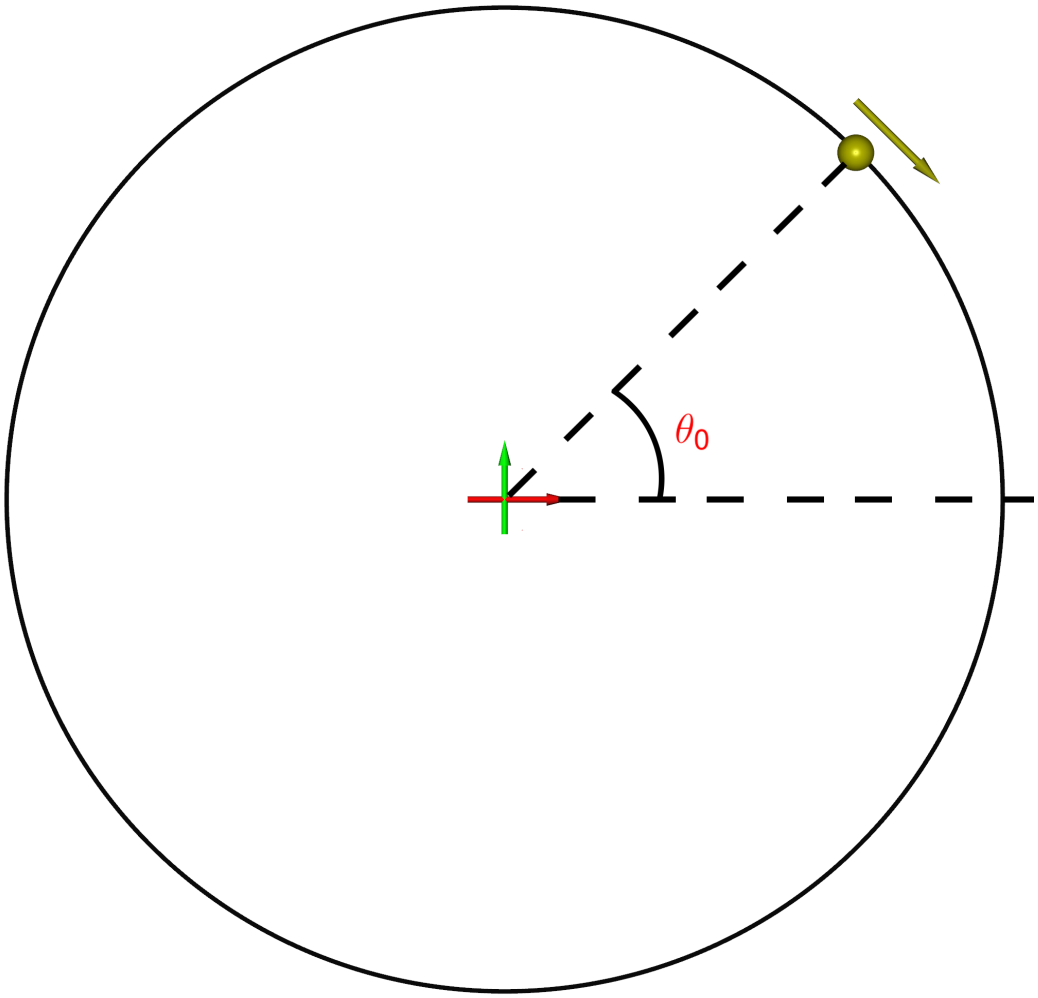

Figure 3.3.: An Example System Modeled by the Bicircular Four-body Problem

gravitating primary is placed on a circular orbit relative to the barycenter of the CRP. The Newtonian inverse-square gravity of the fourth body acts on the spacecraft in

addition to the gravitational effects of the two CRP primaries. However, the fourth body does not effect the circular Keplerian orbits of the two other primaries. In the figure, the Sun is added as the fourth body orbiting the Earth–Moon barycenter on a circular orbit at a distance of 1 AU. The equations of motion remain the same as Equations (3.4), but the potential function is now [47],

$$U^* = \frac{1-\mu}{r_{13}} + \frac{\mu}{r_{23}} + \frac{\mu_4}{r_{43}} + \frac{1}{2}(x^2+y^2), \tag{3.6}$$

with $\mu_4 = \frac{m_4}{m_1+m_2}$.

Such a four-body model, while still reflecting significant simplification, introduces an important transition. The presence of the perturbing fourth body results in a nonautonomous system. The transition in the nature of the system decreases or eliminates the applicability of many of the dynamical systems tools that are available in the CRP. A constant of the motion, and, consequently, a convenient expression for bounds on the motion, is no longer available. Due to the time-dependent nature of the underlying flow, careful consideration is now focused on the initial system geometry.

3.4 Ephemeris n-body Formulations

Various ephemeris formulations are constructed using point mass gravitational forces located with the position time-histories for the associated bodies from ephemeris data. For example, the ephemeris position time-histories of the Earth, Moon and Sun are invoked to form one model. This higher-fidelity, four-body ephemeris model is similar to that of Pavlak and Howell [48], a Moon–Earth–Sun (MES) point mass model with position histories supplied by JPL ephemerides. The present model, in contrast to Pavlak and Howell, does not include Solar radiation pressure. The governing equations are the n-body relative equations of motion,

$$\ddot{\boldsymbol{r}}_{qs} = -\frac{\mu_{2b,s}+\mu_{2b,q}}{r_{qs}^3}\boldsymbol{r}_{qs} + \sum_{\substack{j=1 \\ j\neq s,q}}^{n} \mu_{2b,j}\left(\frac{\boldsymbol{r}_{sj}}{r_{sj}^3} - \frac{\boldsymbol{r}_{qj}}{r_{qj}^3}\right). \tag{3.7}$$

Here, μ_{2b} is the familiar mass parameter from the two-body problem, nondimensionalized as appropriate. The position vector, $\boldsymbol{r}_{qj}$, indicates the position of the j^{th} body

with respect to the central body, q; the subscript s is associated with the spacecraft. In this model, states defined in the restricted problem are transitioned to body-centered J2000 states via an instantaneous rotating frame. Such ephemeris models naturally require six-dimensional states and trajectory propagation is performed in all spatial dimensions. Additionally, computation of the CGST employs *auxiliary grid* points about each state variable. In this model, one evaluation of $\mathbf{C}$ involves the propagation of several perturbations.

These models, as described and incorporating variations, are invoked to illustrate the wide applicability of flow-informed analysis to different types of systems. Ultimately, this extensibility indicates that flow-based tools can be employed in full-ephemeris design and analysis. Such capability is supported by previous literature in other fields that describes such methods as tools for directly analyzing empirical flow results when no underlying dynamical model is defined [25, 32].

4. DYNAMICAL SYSTEMS THEORY: A CASE STUDY

Many of the approaches employed for this analysis have direct ties to concepts from dynamical systems theory. In particular the notions of fixed points, periodic orbits, invariant manifolds and chaos all have relevance. A brief examination of these concepts as they manifest in the circular restricted three-body problem establishes context for more advanced approaches.

4.1 History of the Three-body Problem

The history of the three-body problem is expansive. Efforts to describe and explain the motion of celestial bodies are evident in the earliest recorded history. However, despite the combined efforts of generations of astronomers and philosophers, not until Kepler empirically established what became eponymous laws of planetary motion in 1609 [49], did a reasonably correct description of planetary motion emerge. Kepler postulated that the motion of a planet is elliptical, but he did not explain the cause. Galileo's investigations occurred concurrently and resulted in the methodological paradigm [50] that would explain the general basis of Kepler's kinematic description in terms of forces and motion. Employing the scientific process of Galileo, Newton deduced the law of gravitation [51], one of the chief results included in the *Principia* published in 1687. However, to fully establish the theoretical foundations of gravitation, the model should correctly solve for the combined motion of multiple bodies and, thus, examination of the n-body problem was initiated. Given the force model for gravity, Newton solved the two-body problem using geometry and calculus. Subsequently, in 1710, Bernoulli justified Kepler's empirical ellipses by proving that conics generally solve the two-body problem [52]. With the solution of the two-body problem, the next logical effort toward solving the n-body problem is to consider

three bodies. The addition of a single mass to the problem seemingly represents only a minor increase in detail but, in reality, the associated increase in dynamical complexity is dramatic. No closed-form analytical solution to the three-body problem is currently known [45].

Due to the inherent difficulties in the analysis of the three-body problem and the lack of a solution, alternative methods for approaching the problem are considered. Euler [53] reformulated the problem into the "restricted" problem (as later termed by Poincaré) in 1772. A significant component in this formulation was the introduction of a rotating reference frame [52]. Additionally, Euler identified three particular solutions of the problem, the collinear libration points; Lagrange, concurrently, identified both the collinear and the two triangular libration points for a total of five equilibrium solutions. Consequently, these equilibrium point solutions are frequently termed the Lagrange points.

In 1843, Jacobi reduced the order of the problem from eighteen (three positions and three velocities for three bodies) to six (positions and velocities for the body of interest). At the same time, he introduced an integral of the motion, later denoted the Jacobi integral [46]. With this constant, boundaries on the motion were formulated by Hill in 1878. These boundaries exist as curves or surfaces in two- or three-dimensional configuration space, respectively. An infinite number of periodic orbits in the restricted problem were predicted by Poincaré, who originally introduced surfaces of section (later, *Poincaré sections*) to gain insight into the behavior in the CRP. Poincaré also demonstrated the existence of deterministic chaos in the restricted problem. These significant contributions by Poincaré are given in *New Methods of Celestial Mechanics* (1893) [54]. The close of the 19^{th} century saw further development in periodic orbits with the efforts of Darwin, who built on ideas of Lagrange and Hill [52], beginning in 1897.

In 1912, Sundman [55] first offered a solution for the general three-body problem by means of a convergent power series. Several decades later, in 1991, Wang offered a similar solution for the general n-body problem with $n > 3$ [45, 56]. Unfortunately,

both series solutions are characterized by slow convergence and are generally of little practical use [45]. In 1920, Moulton published *Periodic Orbits* [57], surveying the status of work on periodic orbits in the CRP; the calculation of periodic orbits was included, thereby confirming their existence. Moulton, unable to predict future computational tools, indicated that the numerically intensive nature of identifying such orbits would prohibit periodic orbits from serious future study [58]. In 1966, Hénon employed Poincaré sections in his examination of the three-body problem, but it was a surprisingly rare application [59]. In 1967, Szebehely's *Theory of Orbits: The Restricted Problem of Three Bodies* [46] proved to be *the* comprehensive work on the three-body problem. Szebehely offers an extensive and cohesive overview of the aspects of the circular restricted problem, as well as numerous analytical and numerical results. *Theory of Orbits* remains an authoritative and widely cited text.

With one of the most famous speeches in recent history, President John F. Kennedy effectively transitioned the three-body problem from a curiosity to a very practical concern, when, on September 12, 1962, he stated, "We choose to go to the Moon." [60, 61] While the early investigators of the three-body problem, including Newton, had considered the Earth, Moon, and a third body as a suitable configuration for investigation, it wasn't until space exploration expanded into a multi-body regime, where a spacecraft would be under the continuous influence of two significant gravitational fields, that the three-body problem gained practical interest, typified by the Earth–Moon–Spacecraft configuration. In the early 1970's, toward the end of the Apollo program, and in support of options for the last few planned Apollo flights, Breakwell et al. [62] and Farquhar [63] explored trajectories that emerge within the context of the three-body problem. For a manned mission to the far side of the Moon, communications support may be supplied via a relay satellite in a "halo" orbit about the translunar collinear libration point. These analyses were largely theoretical in nature and, while the Apollo program ended before such a relay option was realized, such studies renewed interest in applications of the three-body problem in mission design. Halo orbits were extensively explored in a number of investigations, including

a numerical study accomplished by Howell and Breakwell (1984) [64, 65]. Since these early years of applied three-body analyses, many successful missions have incorporated libration point orbits beginning with ISEE-3 [66] and continuing through Genesis [67], ARTEMIS [68], TESS [69, 70] and many others. Currently, many missions in various stages of development and implementation exploit three-body dynamics for spacecraft motion.

4.2 Equilibrium Points

When observed in a rotating reference frame, the CRP is known to possess equilibrium points [46]. The equilibrium points are identified as solutions to the differential equations where the associated velocity and acceleration fields are zero. There are five such equilibrium point solutions of the CRP EOM, designated L_1 through L_5. Euler first identified the points designated as L_1 through L_3, while Lagrange identified all the equilibrium points, including L_4 and L_5 [52]. The five points associated with the equilibrium solutions are commonly termed the Lagrange points (after Lagrange) or libration points after the observed librating behavior of bodies existing naturally near these locations.

The libration points are determined as roots of equations that result when the gradient of the potential function (Equation (3.3)) is equal to zero; thus, the equilibrium equations become,

$$x = \frac{(1-\mu)(x+\mu)}{r_{13}^3} + \frac{\mu(x-1+\mu)}{r_{23}^3}, \tag{4.1a}$$

$$y = \frac{(1-\mu)y}{r_{13}^3} + \frac{\mu y}{r_{23}^3}, \tag{4.1b}$$

$$0 = \frac{(1-\mu)z}{r_{13}^3} + \frac{\mu z}{r_{23}^3}. \tag{4.1c}$$

Inspection of Equation (4.1c) implies that $z = 0$ for all equilibrium points, that is, all five equilibrium points exist in the plane of motion of the primaries. Further, substituting $z = 0$ into Equations (4.1a) and (4.1b) results in a coupled linear system of two equations in two unknowns. With $y \neq 0$, simplifying the system via substitution

leads to $r_{13} = r_{23} = 1$. Simple algebra reveals expressions for the x and y coordinates of the equilibrium points that appear off of the x axis with $y \neq 0$, that is,

$$x = \frac{1}{2} - \mu, \tag{4.2}$$

$$y = \pm\frac{\sqrt{3}}{2}. \tag{4.3}$$

These x and y values (with $y \neq 0$) correspond to points L_4 and L_5 and represent locations at the third vertex of equilateral triangles formed by P_1, P_2, and the respective point. The two equilateral points are denoted by convention such that L_4 corresponds to the equilibrium point with a positive y coordinate and L_5 corresponds to the equilibrium point with a negative y value. Three more equilibrium points exist when $y = 0$, thus these additional points lie along the rotating x axis and are termed the collinear points. When $y = z = 0$, the equilibrium equations simplify to,

$$x = \frac{(1-\mu)(x+\mu)}{|x+\mu|^3} + \frac{\mu(x-1+\mu)}{|x-1+\mu|^3}. \tag{4.4}$$

It is evident from Equation (4.4) that singularities exist for $x = -\mu$ and $x = 1 - \mu$. These singularities bound three regions that each contain a root of the equation. These three roots correspond to the remaining equilibrium points with the common convention designating L_1 as the point interior to both primaries, L_2 is the point exterior to P_2 in the positive $\hat{x}$ direction, and L_3 is the point exterior to P_1 in the negative $\hat{x}$ direction. To simplify a numerical root-finding scheme, it is common to substitute the distance between the primaries and the respective equilibrium points as the variable of interest into Equation (4.4). Specifically, the following substitutions are employed,

$$x_{L_1} = 1 - \mu - \gamma_1, \tag{4.5a}$$

$$x_{L_2} = 1 - \mu + \gamma_2, \tag{4.5b}$$

$$x_{L_3} = -\mu - \gamma_3. \tag{4.5c}$$

Equation (4.4) can be further simplified by considering the three distinct regions near each collinear point independently, that is,

$L_1 : -\mu < x < 1 - \mu :$

$$x - \frac{1-\mu}{(x+\mu)^2} + \frac{\mu}{(x-1+\mu)^2} = 0, \tag{4.6a}$$

$L_2 : x > 1 - \mu :$

$$x - \frac{1-\mu}{(x+\mu)^2} - \frac{\mu}{(x-1+\mu)^2} = 0, \tag{4.6b}$$

$L_3 : x < -\mu :$

$$x + \frac{1-\mu}{(x+\mu)^2} + \frac{\mu}{(x-1+\mu)^2} = 0. \tag{4.6c}$$

Substituting from Equation (4.5a) into Equation (4.6a) and multiplying to obtain a common denominator results in the following equation,

$$(1-\mu-\gamma_1)(1-\gamma_1)^2(-\gamma_1)^2 - (1-\mu)(-\gamma_1)^2 + \mu(1-\gamma_1)^2 = 0. \tag{4.7}$$

Expanding and collecting like terms yields a quintic polynomial that can be employed to obtain the x coordinate of L_1 to arbitrary precision. Similar steps produce relationships for the x coordinates of L_2 and L_3. In summary,

L_1 :

$$\gamma_1^5 - (3-\mu)\gamma_1^4 + (3-2\mu)\gamma_1^3 - \mu\gamma_1^2 + 2\mu\gamma_1 - \mu = 0, \tag{4.8a}$$

L_2 :

$$\gamma_2^5 + (3-\mu)\gamma_2^4 + (3-2\mu)\gamma_2^3 - \mu\gamma_2^2 - 2\mu\gamma_2 - \mu = 0, \tag{4.8b}$$

L_3 :

$$\gamma_3^5 + (2+\mu)\gamma_3^4 + (1+2\mu)\gamma_3^3 - (1-\mu)\gamma_3^2 - 2(1-\mu)\gamma_3 - (1-\mu) = 0. \tag{4.8c}$$

Solving these equations for γ_i and then back-substituting yields the physical x coordinate corresponding to the respective libration point. The exact location of each point depends upon the relative masses of the two primaries. A general representation of the locations appears in Figure 4.1, where the equilibrium points are depicted along with the two massive primaries (P_1 and P_2) in the rotating frame. Equilateral triangles associated with L_4 and L_5 are included to further illustrate the geometry.

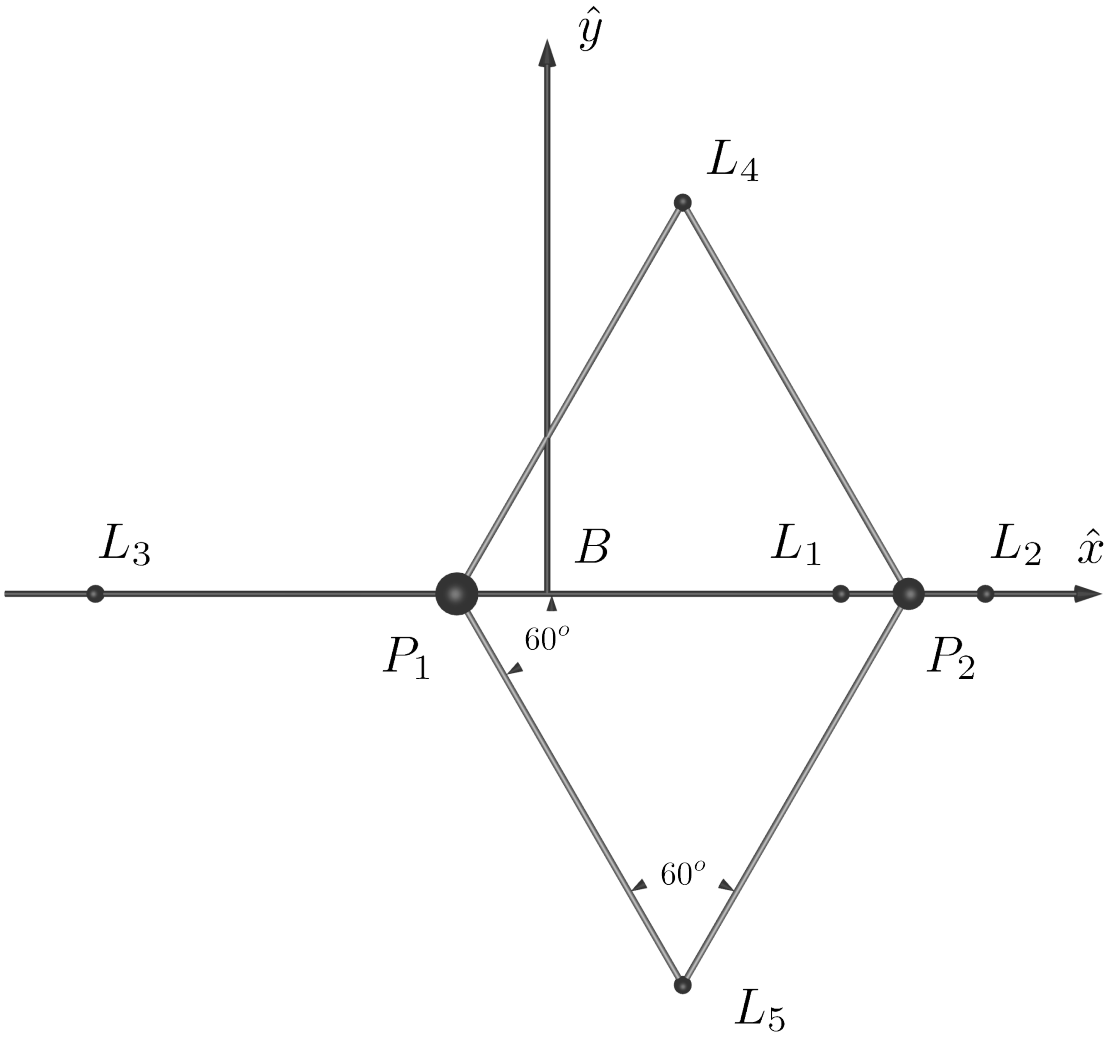

Figure 4.1.: Equilibrium Points in the CRP

Accurate knowledge of the locations of the equilibrium points in the CRP is critical to most numerical schemes in the study of this problem. These points become the foundation for both linear and topological analysis. This analysis, in turn, leads to a better understanding of the dynamical characteristics in the problem. The equilibrium point locations in the Earth–Moon CRP, ($\mu \approx 0.012151$, $l^* \approx 384{,}000$ km), are listed in Table 4.1 and the associated Jacobi constant values are tabulated in Table 4.2.

Table 4.1: Earth–Moon Libration Points

Libration Point	x_{L_i} (non-dim)	x_{L_i} (km)	y_{L_i} (non-dim)	y_{L_i} (km)
L_1	0.836915	321700	0.0	0.0
L_2	1.155682	444230	0.0	0.0
L_3	-1.005062	-386334	0.0	0.0
L_4	0.487849	187524	0.866025	332890
L_5	0.487849	187524	-0.866025	-332890

Table 4.2: Jacobi Constant Values for Earth–Moon Libration Points

Libration Point	C (dimensionless)
L_1	3.188341
L_2	3.172160
L_3	3.012147
L_4	2.987997
L_5	2.987997

4.3 Periodic Orbits, Fixed Points and Single Shooting

Dynamical systems often possess solutions in the form of periodic orbits. Such is the case for the CRP and, in fact, the complexity in the restricted problem generates conditions consistent with an infinite number of periodic orbits as well as families of such orbits. This infinity of orbits motivated an examination by Poincaré [54] and is further established by Moulton and others [57]. Poincaré invoked mappings of orbit crossings on a surface of section leading to the notion of the Poincaré map. When represented on such a map, a periodic orbit appears as one or more fixed points on the map. These fixed points represent an option for analyzing orbital characteristics.

One set of families of periodic orbits of particular interest, as a first step for analysis in the CRP, are the planar family of periodic Lyapunov orbits associated with the collinear libration points. These families of periodic orbits are named for Lyapunov and his associated work on stability analysis in dynamical systems [37]. Lyapunov families exist about each of the collinear points and, therefore, are categorized by their respective point. For example, the L_1 Lyapunov family is a family of planar periodic orbits that exist about L_1. Additional, related planar families of orbits exist in the vicinity of the equilateral libration points.

Given an initial orbit, for example, a linear approximation or nonlinear solution such as those plotted in Figure 4.2, additional solutions are generated by applying a targeting scheme. An entire family of solutions is produced through a continuation process. The targeting strategy is an example of a single shooting approach where an initial state is integrated for some prescribed duration $(t - t_\mathrm{o})$, and then the error between the final state and the targeted final state is employed to iteratively update the initial state until some convergence criteria is met. Ultimately, the goal is to identify the flow that departs a fixed point and returns exactly to the same fixed point on the map, that is, $\boldsymbol{x}_t = \phi_{t_\mathrm{o}}^t(\boldsymbol{x}_\mathrm{o}) = \boldsymbol{x}_\mathrm{o}$. To achieve this mapping a targeting scheme using STM relationships is invoked. In one example, components of the STM appear in an update equation to modify the initial state based on the difference

between an integrated final state on the x axis and a perpendicular crossing indicated by a state with $\dot{x} = \dot{z} = 0$. In this particular case, only certain parameters of the initial state are allowed to vary. Specifically, $\dot{y}_\mathrm{o}$ is fixed while x_o is allowed to shift based on the update information supplied by the STM. Variations in time are also incorporated as appropriate,

$$\delta \boldsymbol{x} = \left.\frac{\partial \boldsymbol{x}}{\partial \boldsymbol{x}_\mathrm{o}}\right|_{\boldsymbol{x}_\mathrm{o}(t)} \delta \boldsymbol{x}_\mathrm{o} + \left.\frac{\partial \boldsymbol{x}}{\partial t}\right|_{\boldsymbol{x}_\mathrm{o}(t)} \delta t, \tag{4.9}$$

or,

$$\delta \boldsymbol{x} = \Phi_{t_\mathrm{o}}^{t} \delta \boldsymbol{x}_\mathrm{o} + \dot{\boldsymbol{x}}|_t \, \delta t. \tag{4.10}$$

A matrix expression is often more convenient,

$$\delta \boldsymbol{x} = \begin{bmatrix} \Phi & \dot{\boldsymbol{x}}(t) \end{bmatrix} \begin{bmatrix} \delta \boldsymbol{x}_\mathrm{o} \\ \delta t \end{bmatrix}. \tag{4.11}$$

Many targeting schemes are available to correct a given parameter by varying one or several initial parameters, but only a subset of the relationships represented by Equation (4.11) apply to the current example. Specifically, the relationship that yields the correct $\dot{x}_f$ by varying x_o is required. Using $\delta \dot{x}_f$ from $\delta \boldsymbol{x}$ and the fourth row of the augmented matrix in Equation (4.11), produces the necessary expression,

$$\delta \dot{x}_f = \phi_{(4,1)} \delta x_\mathrm{o} + \phi_{(4,2)} \delta y_\mathrm{o} + \phi_{(4,3)} \delta z_\mathrm{o} + \phi_{(4,4)} \delta \dot{x}_\mathrm{o} + \phi_{(4,5)} \delta \dot{y}_\mathrm{o} + \phi_{(4,6)} \delta \dot{z}_\mathrm{o} + \ddot{x} \delta t. \tag{4.12}$$

For the planar Lyapunov families, the z and $\dot{z}$ terms are always zero. Choosing to constrain $\dot{y}_\mathrm{o}$ implies $\delta \dot{y}_\mathrm{o} = 0$, and the requirement, $\dot{x}_\mathrm{o} = 0$, for a perpendicular departure indicates that $\delta \dot{x}_\mathrm{o} = 0$. Finally, considering that the departure is always from the x axis, $\delta y_\mathrm{o} = 0$. Incorporating these considerations simplifies Equation (4.12), that is,

$$\delta \dot{x}_f = \phi_{(4,1)} \delta x_\mathrm{o} + \ddot{x} \delta t. \tag{4.13}$$

Next, enforcing $y_f = 0$ allows for the elimination of δt from Equation (4.13). Following steps similar to those above, with $\delta y_f = 0$, and solving for δt,

$$\delta y_f = \phi_{(2,1)} \delta x_\mathrm{o} + \dot{y} \delta t, \tag{4.14}$$

$$\delta t = -\phi_{(2,1)} \frac{\delta x_{\mathrm{o}}}{\dot{y}}. \tag{4.15}$$

Finally, substitution back into Equation (4.13) produces the targeting equation for this example, that is,

$$\delta \dot{x}_f = \left(\phi_{(4,1)} - \frac{\ddot{x}}{\dot{y}} \phi_{(2,1)} \right) \delta x_{\mathrm{o}}. \tag{4.16}$$

This targeting equation is employed in an iterative algorithm and, in general, such an algorithm is described by the following steps.

1. Obtain an initial guess, either from linear analysis or continuation.

2. Propagate the initial guess and the STM via numerical integration until reaching some state near the desired final condition (in the current example, propagate to the subsequent x-axis crossing).

3. Evaluate the difference between the actual final state and the desired final state. Use this difference to generate a correction via the update equation.

4. Update the initial guess and iterate until a desired criteria for accuracy is met (e.g., a final error on the order of 10^{-12} or similar).

In Figure 4.2, the process is illustrated. The sequence of frames in Figures 4.2(a–c) illustrates the computation of a periodic orbit near the L_1 libration point in the Earth–Moon ($\mu \approx 0.01215$) system. From a linear approximation, the corrections process produces a numerical solution. The nonlinear result is then employed as an initial guess to generate other nonlinear solutions. In Figure 4.2(a), an analytical linear ellipse about L_1 is plotted ($\xi_{\mathrm{o}} = 0.01$, $\eta_{\mathrm{o}} = 0$). In Figure 4.2(b), the linear initial conditions are propagated to the x axis in the nonlinear model and then numerically corrected. The linear ellipse is gray and subsequent iterations are colored in order from black to blue to red. In Figure 4.2(c), the corrected nonlinear Lyapunov orbit (red) is included along with the linear approximation (gray). Finally, in Figure 4.2(d), the first nonlinear solution is plotted in red with a second, related nonlinear orbit in blue. Other discretely spaced orbits in the family can be computed similarly.

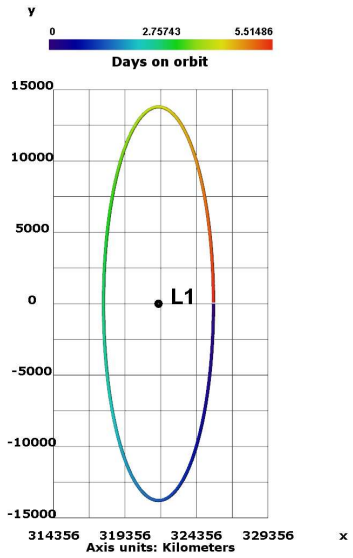

(a) A linear ellipse about L_1

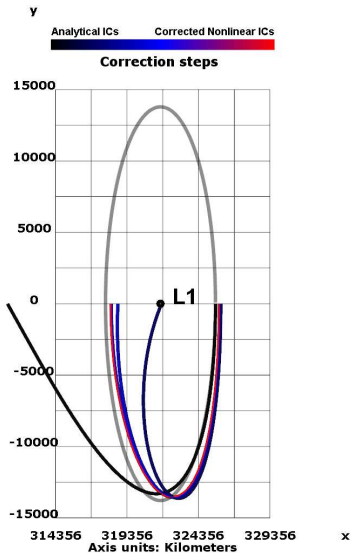

(b) Correcting the nonlinear solution

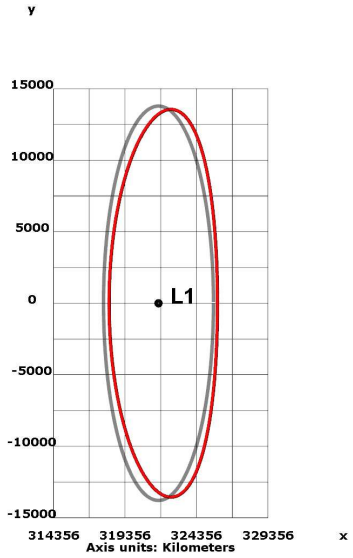

(c) Linear (gray) and nonlinear (red) solutions

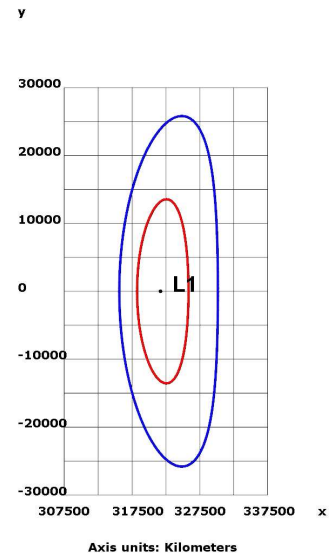

(d) Numerically determined periodic orbits

Figure 4.2.: Transition from a Linear Solution to Nonlinear Solutions

The success of the previously described algorithm, that is, generating periodic orbits that are symmetric across the x axis, depends on the "mirror theorem". The mirror theorem (Roy and Ovenden [71]) is based on the fact that the symmetric form of the equations of motion allow for mirroring across the x axis. After a single

"half-orbit" is generated in the nonlinear problem via single shooting, it is reflected across the x axis to form a full periodic orbit. The family of orbits is extended using continuation; a natural continuation parameter is selected as appropriate (for example, $\dot{y}_o$ or C are two of many available choices in the circular restricted problem). Families of planar orbits about each of the five libration points appear in Figures (4.3) and (4.4). The collinear Lyapunov families of planar periodic orbits are plotted near each collinear libration point. Planar families of periodic orbits in the vicinity of the equilateral points also appear in Figure 4.3(d). (Note that the corrections algorithm is modified to produce periodic orbits near L_4/L_5 since these orbits are asymmetric.) The direction of motion along all the orbits in Figure 4.3 is indicated by black arrows in each frame. These families are comprised of an infinite set of orbits but are represented by only a finite number of members. The orbits in the figures are colored consistent with the associated value of Jacobi constant. Other families of periodic orbits can be determined by locating bifurcating orbits in the planar families and then proceeding with continuation along intersecting directions. Many such families are known in the CRP and similar astrodynamical systems (see, for example, [72,73]). Finally, periodic orbits give way to related quasi-periodic structures in their vicinity—for an example of such motions, see Olikara [74].

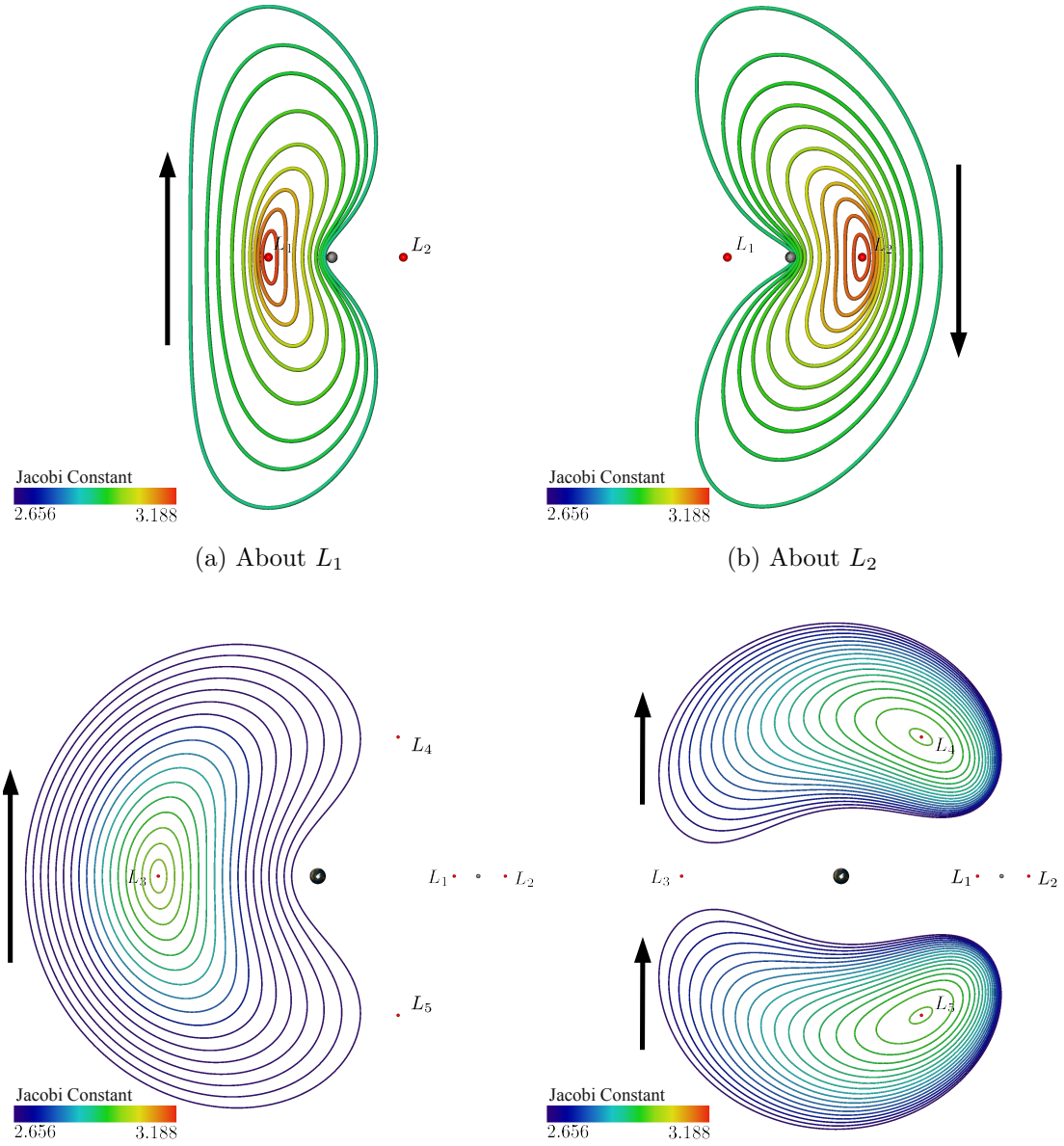

(a) About L_1

(b) About L_2

(c) About L_3

(d) About L_4 and L_5

Figure 4.3.: Families of Planar Orbits About Libration Points

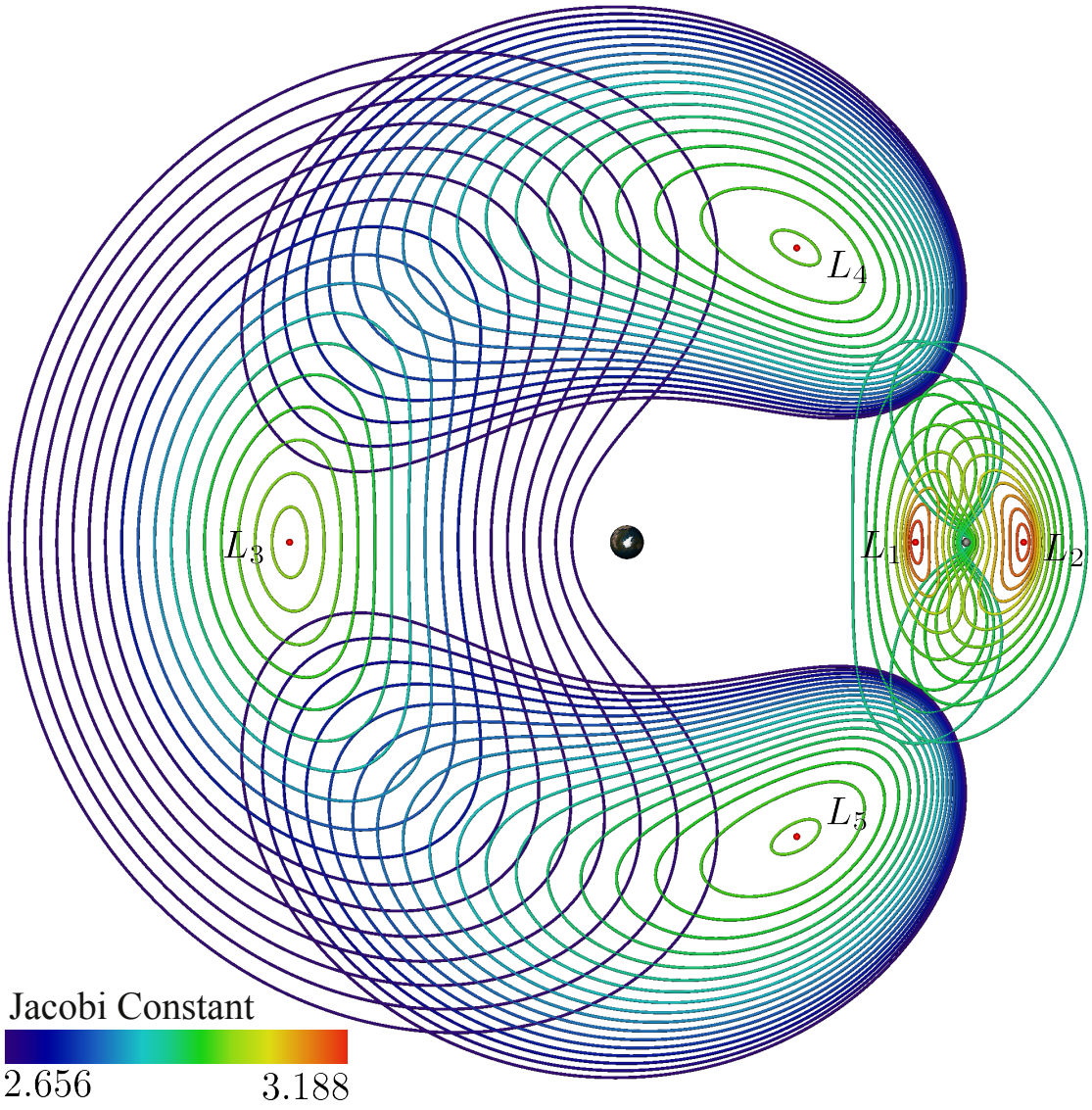

Figure 4.4.: Families of Planar Orbits About Each of the Libration Points

4.4 Invariant Manifolds

There are natural flows in a system that are associated with the structural stability of particular dynamical features. One manifestation of such flow behaviors is found in the notion of invariant and time-varying manifolds. A manifold is a structured subset of a space with a dimension less than the space itself that locally resembles the Euclidean space corresponding to its dimension [40]. As such, a particular manifold structure may exist as a common smooth geometrical object, for example, a curve or a surface. Of particular interest in the present context is how the flow behaves with respect to manifold structures, especially near equilibrium points and periodic orbits.

Depending on the stability characteristics of an equilibrium point or periodic orbit, the possibility exists for manifolds that asymptotically emanate from or approach the associated dynamical feature. In the case of the equilibrium points the Jacobian indicates the local linear stability of the points. Specifically, the eigenvalues of the Jacobian supply the stability information. As an example, in the Earth–Moon system, the local linear stability of the libration points is given in terms of flow behavior in Table 4.3 that follows from Olikara [74], where *center* indicates a conjugate pair of purely imaginary eigenvalues and *saddle* refers to a pair of eigenvalues with nonzero real parts (one positive and one negative). When the mass parameter in the CRP

Table 4.3: Local Linear Stability of the Earth–Moon Libration Points

Libration Point	Flow
L_1	center $\times$ center $\times$ saddle
L_2	center $\times$ center $\times$ saddle
L_3	center $\times$ center $\times$ saddle
L_4	center $\times$ center $\times$ center
L_5	center $\times$ center $\times$ center

is greater than a critical value, $\mu > 0.038521$, the stability of the equilateral points becomes consistent with that of the collinear points [46]. Given the stability characteristics indicated in Table 4.3, local linear stable and unstable eigendirections are computed and initial states along these directions produce the associated nonlinear manifolds when evolved in time under the nonlinear dynamics.

A process similar to the stability analysis leading to manifolds of equilibrium points may be performed for individual periodic orbits. In the case of periodic orbits, however, the analysis is performed with respect to $\Phi_{t_o}^{T}(\boldsymbol{x}_o) = D\phi_{t_o}^{T}(\boldsymbol{x}_o) = \mathbf{M}$, the monodromy matrix, where T is the associated orbital period and $\boldsymbol{x}_o$ is the initial state of the periodic orbit. For a particular orbit, the stability characteristics are also given by eigenvalue classifications, such as those indicated in Table 4.4. The

Table 4.4: Example Stability Modes of a Periodic Orbit

λ_i Nature $\overline{\lambda}_i$ Nature	Magnitude	Associated Mode
Real	< 1	Stable
Real	> 1	Unstable
Complex	1	Center
Complex	1	Center
Real	1	Center (orbit tangent)
Real	1	Center (family tangent)

possibility exists for various combinations of the pairs listed in the table. For example, some orbits exhibit a 6D center subspace (4 complex eigenvalues) while others exhibit 2×2 stable/unstable pairs (6 real eigenvalues). Other possibilities also exist [40, 75]. As is the case with equilibrium point manifolds, the equivalent periodic orbit structures are higher-dimensional, and are frequently represented by plotting their projection onto physical space. For orbits, these projections typically appear

as invariant surfaces taking the form of "tubes" that, in the planar CRP, act as separatrices of the flow. Again echoing the equilibrium point behavior, the nonlinear flow along the stable and unstable orbital manifolds asymptotically approaches and departs the orbit. The green contours depicted in Figure 4.5 are examples of manifold tubes, represented discretely by numerous trajectories crossing the hyperplane of a Poincaré map. The contours are plotted against a background colored by forward and backward FTLE values with brighter colors indicating a larger relative FTLE value. In general, manifolds offer significant insight into the behavior in the CRP. Moreover, the separatrix characteristics of the manifolds closely relate to the ideas of material boundaries associated with the FTLE [28, 31].

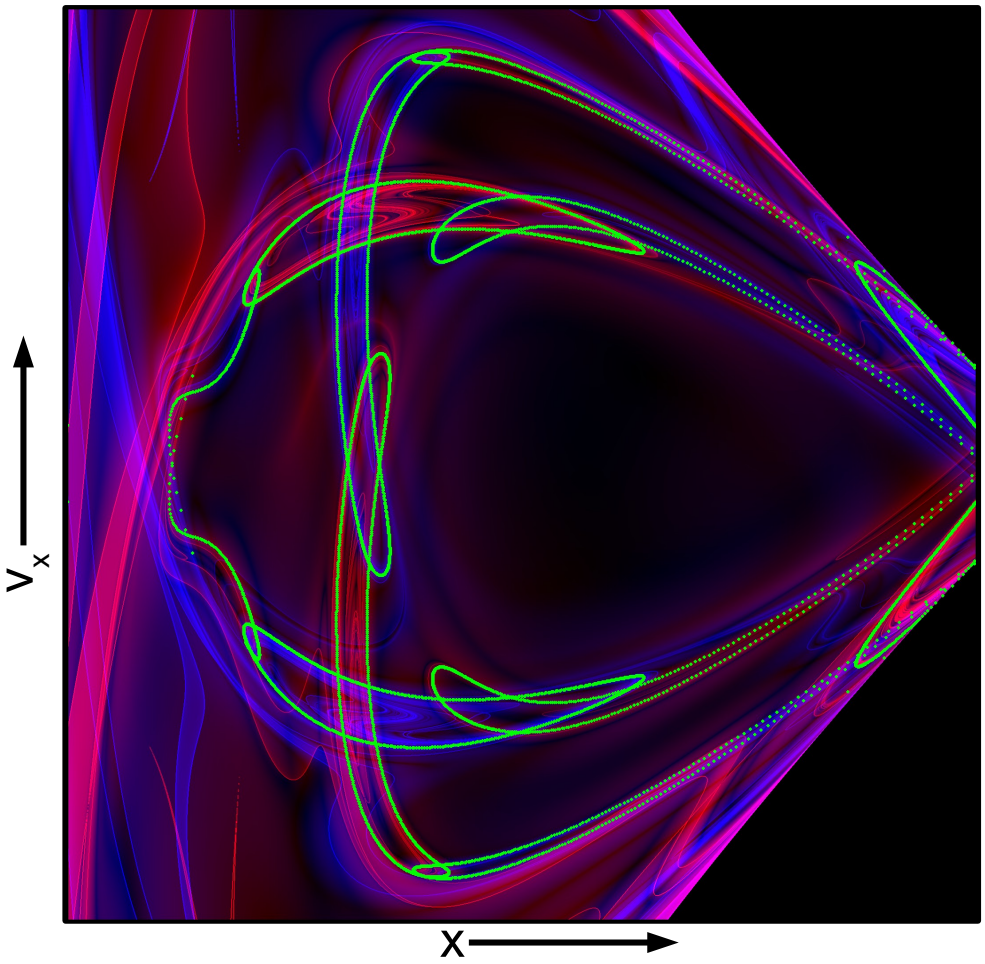

Figure 4.5.: Poincaré Map of Manifold Crossings on an FTLE Field

4.4.1 Stable and Unstable Manifolds of Equilibrium Points

Manifolds associated with a periodic orbit, and the process to generate these manifolds, are of specific interest. However, the approach to produce manifolds of periodic orbits results from a generalization of methods for computing the manifolds of critical points. Recall that the stability of the equilibrium points is characterized by the Jacobian matrix evaluated at the equilibrium points. Further, the collinear equilibrium points are characterized as hyperbolic, possessing both a stable and an unstable mode indicated by a Jacobian with one positive and one negative eigenvalue. The process for identifying the manifolds of the critical points originates with a perturbation of the 4D initial state along the position-normalized eigenvectors of the Jacobian. Propagating the state resulting from this perturbation along the normalized eigenvector corresponding to the positive eigenvalue results is an approximation to the unstable manifold. If, on the contrary, an initial state is perturbed along the normalized eigenvector associated with the negative eigenvalue and propagated *backward* in time, the result is an approximation of the stable manifold. In both cases, the state must be perturbed in two directions along the eigenvector, and subsequently evolved under the nonlinear dynamics in time, as appropriate, to obtain the global manifold.

Proper normalization of the eigenvectors corresponding to the Jacobian is critical to ensure an effective perturbation of the state. Thus, normalization is accomplished to retain the general velocity characteristics of the eigenvector but normalizing by the position components allowing for a displacement that is representative in physical space. Given such a position-normalized eigenvector, the required perturbation is accomplished by the addition of a relatively small scalar multiple of the normalized eigenvector to the initial state (in this case $\boldsymbol{x}_{L_i}$). Specifically, the normalized "stable" or "unstable" eigenvector, $\boldsymbol{v}^S$ or $\boldsymbol{v}^U$, respectively, is produced by dividing the original eigenvector, $\boldsymbol{Y}^{S/U}$, by the magnitude of the position, that is,

$$\boldsymbol{v}^{S/U} = \frac{\boldsymbol{Y}^{S/U}}{r}, \tag{4.17}$$

where $r = \sqrt{x^2 + y^2 + z^2}$. Some judicious displacement step, d, yields the perturbed initial state vector,

$$\boldsymbol{x}_0 = \boldsymbol{x}_{L_i} \pm d \cdot \boldsymbol{v}^{S/U}. \tag{4.18}$$

The perturbation displacement, d, is usually determined as some appropriate physical distance relative to the equilibrium point. In the Earth–Moon system, such a distance is typically a few dozen kilometers, while in the Sun–Earth system a more reasonable displacement might be a few hundred kilometers. The accuracy of the approximation to the manifold is inversely related to the magnitude of the displacement, d. However, since the manifolds arrive and depart from the point of interest asymptotically, a very small displacement requires extensive integration to move away from the point and increases the numerical error. The selection of the displacement is, therefore, somewhat subjective, but must be sufficiently small to produce a reasonably accurate approximation to the manifold and large enough to avoid excessive integration time. Given an appropriate initial perturbation, propagation of the new initial state generates an approximation to the actual nonlinear manifold.

In Figure 4.6, the stable and unstable manifolds associated with the equilibrium points in the neighborhood of the Earth–Moon L_1 and L_2 points are projected onto configuration space. The figure also includes other appropriate vectors and subspaces. Specifically, the position-space projections of the stable and unstable eigenvectors, $\boldsymbol{v}^S$ and $\boldsymbol{v}^U$, respectively, are depicted with arrow heads indicating the direction of the flow near these vectors. The stable and unstable eigenspaces, E^S and E^U, respectively, are indicated by the dashed lines extending from the points. The local stable and unstable manifolds are tangent to their respective eigenspaces and are indicated in red (W^S_{loc}) and blue (W^U_{loc}), respectively. Further, the + and − designations serve to identify the manifold branches consistent with a particular direction of the flow, initially indicated by directions $+\boldsymbol{v}^{S/U}$ or $-\boldsymbol{v}^{S/U}$ along the position-normalized eigenvector in which the perturbations are made. The localized manifolds in Figure 4.6 are propagated for an arbitrary duration to globalize the manifolds with associated symbols W^U and W^S. All of the quantities and symbols in the figure are distinct for each libration

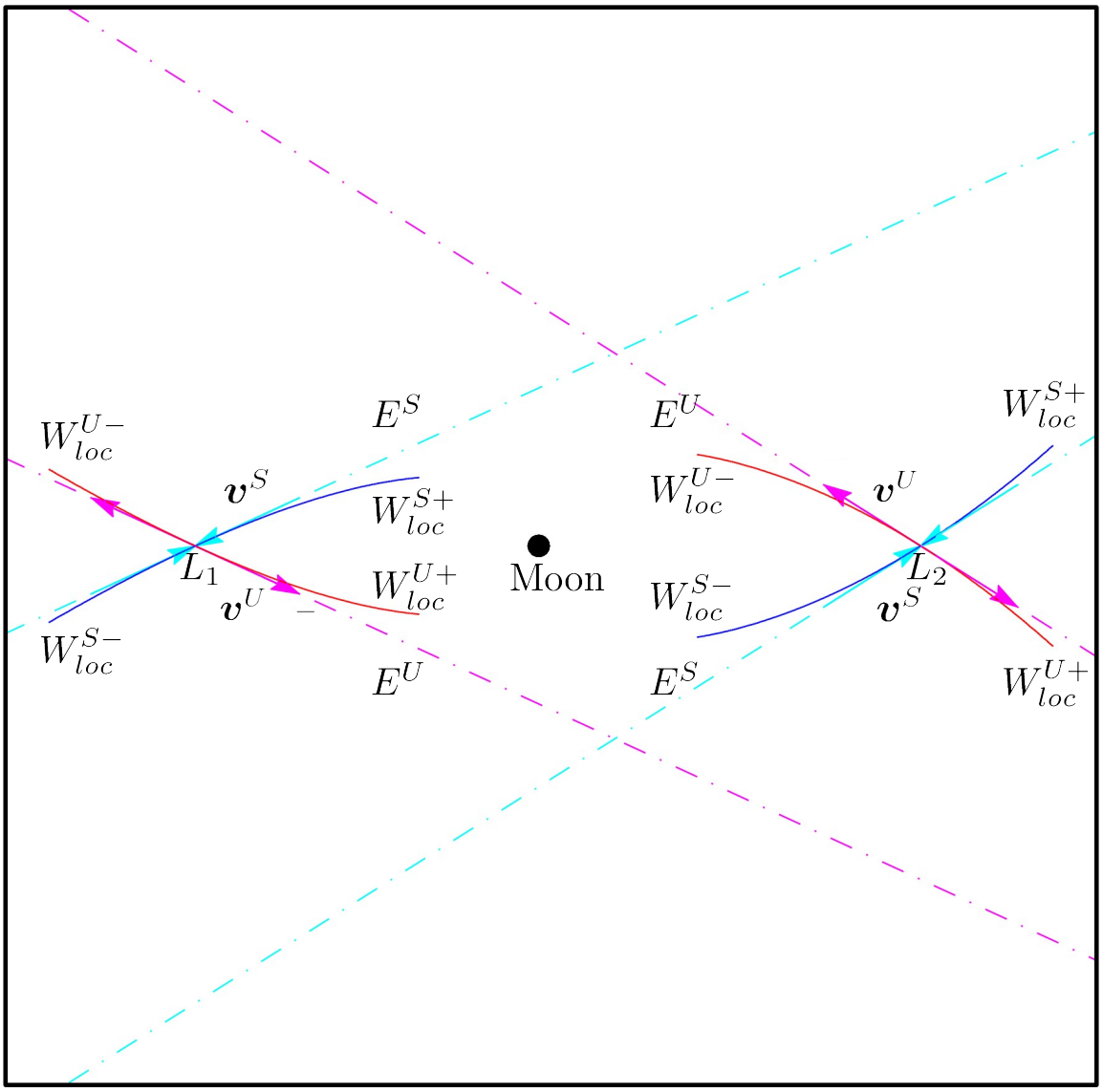

Figure 4.6.: Local Manifolds Associated with L_1 and L_2 in the Earth–Moon CRP

point. Moreover, the approximations to the manifolds associated with each libration point L_1 and L_2, possess Jacobi constant values that are close, but not precisely equal, to C_{L_1}/C_{L_2} given the initial offset relative to the points that is required for computation. The theoretical manifolds possess Jacobi constant values equal to their respective point and act as separatrices for motion, consistent with C_{L_1} and C_{L_2}.

4.4.2 Manifolds Associated with a Periodic Orbit (Maps)

The process for identifying manifolds that correspond to equilibrium points is extended to periodic libration point orbits by introducing maps. Stability information for a periodic orbit is available through **M**, the monodromy matrix that is, in fact, the STM of a fixed point after its first return to a Poincaré map [37]. This matrix is the analog of the Jacobian matrix for an equilibrium point. The eigenvalues of the monodromy matrix reveal stable and unstable modes, if they exist, and the associated eigenvectors supply the necessary perturbation directions to generate individual manifold trajectories associated with an orbit. The eigenvalues of the monodromy matrix are independent of the starting point along the orbit, which may be considered as a fixed point of the first-return map. If a given orbit is discretized into a number of representative fixed points along the orbit, and the eigenvalues and eigenvectors of the monodromy matrix are calculated at each, then the resulting manifold trajectories produce a "wireframe" for the manifold surface. Properties of the STM, as described by Katsiaris and Goudas [76] as well as Parker and Chua [40], are used to transform the eigenvectors of the monodromy matrix for the first fixed point to each successive fixed point as described by Marchand [77]. Given the eigenvectors for the first fixed point, the eigenvectors for the remaining $N-1$ points are computed from,

$$\boldsymbol{v}^S(n\Delta t) = \Phi(n\Delta t, 0)\boldsymbol{v}^S(0), \tag{4.19}$$

$$\boldsymbol{v}^U(n\Delta t) = \Phi(n\Delta t, 0)\boldsymbol{v}^U(0), \tag{4.20}$$

with $n = 1 \cdots N-1$. The position-space projections of the eigenvectors for 20 fixed points along an L_1 Lyapunov orbit are illustrated in Figure 4.7, with stable vectors colored blue and unstable vectors colored red. The Lyapunov orbit is sized in terms of its amplitudes. The amplitude in x is $A_x \approx 7000$ km and the corresponding amplitude in y is $A_y \approx 26,000$ km. As in the case of the equilibrium points a perturbation, d, is made to initiate the manifolds. One perspective for the perturbation in the context of periodic orbits, is that various values of d generate manifolds associated with orbits characteristic of different C values—a consideration that doesn't necessarily

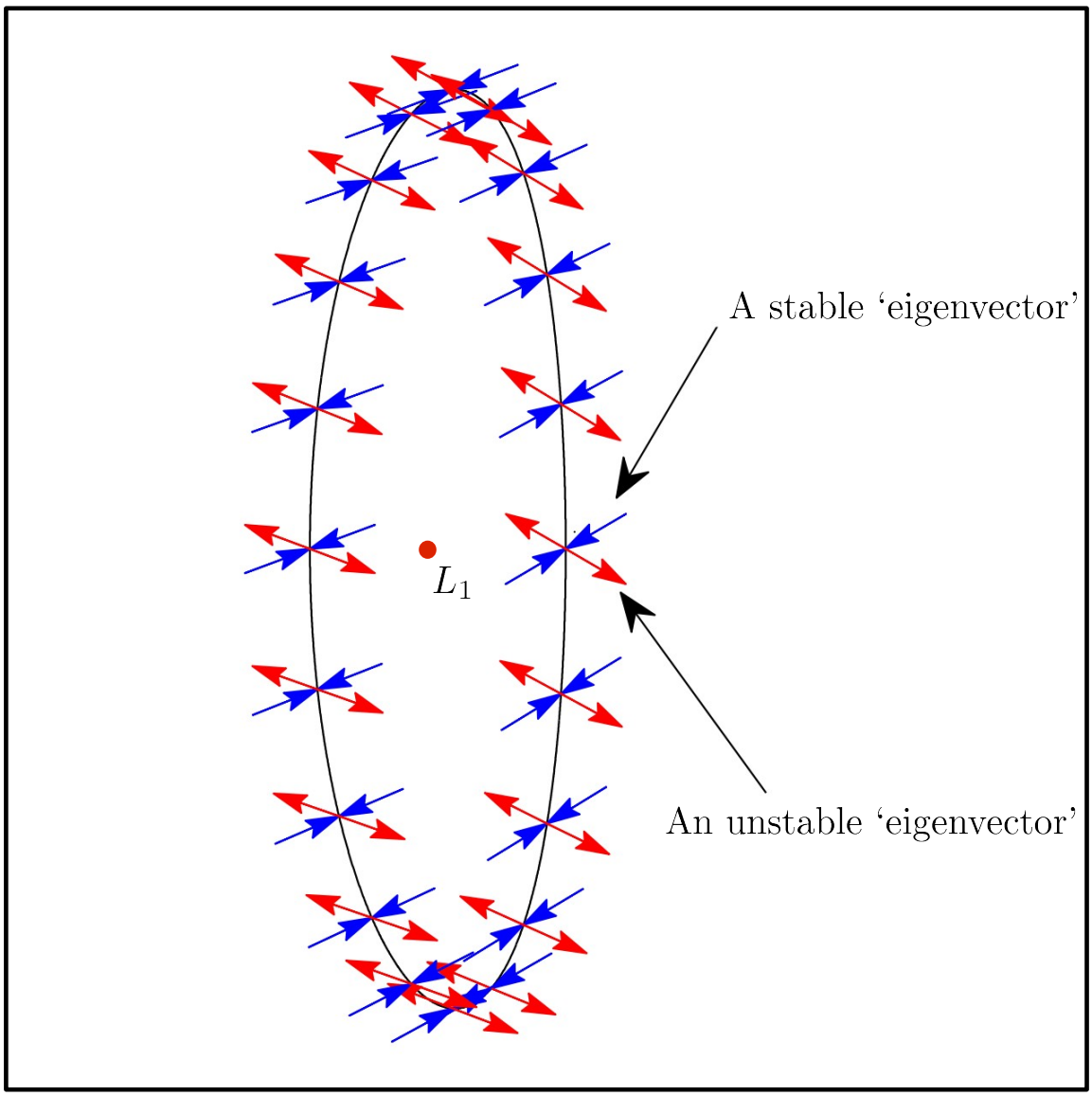

Figure 4.7.: Position-space Projections of Eigenvectors Along an L_1 Orbit

apply in the case of equilibrium point manifolds. After perturbing the state at each fixed point by $d = 50$ km in the appropriate directions and integrating forward and backward in time, several crossings of the manifolds associated with the periodic orbit are plotted on a Poincaré map in Figure 4.8. In this case, the discrete map fully represents the manifolds, because each point on the map is a projection of a full 4D state constrained by an energy level C and a hyperplane crossing Σ. Additionally,

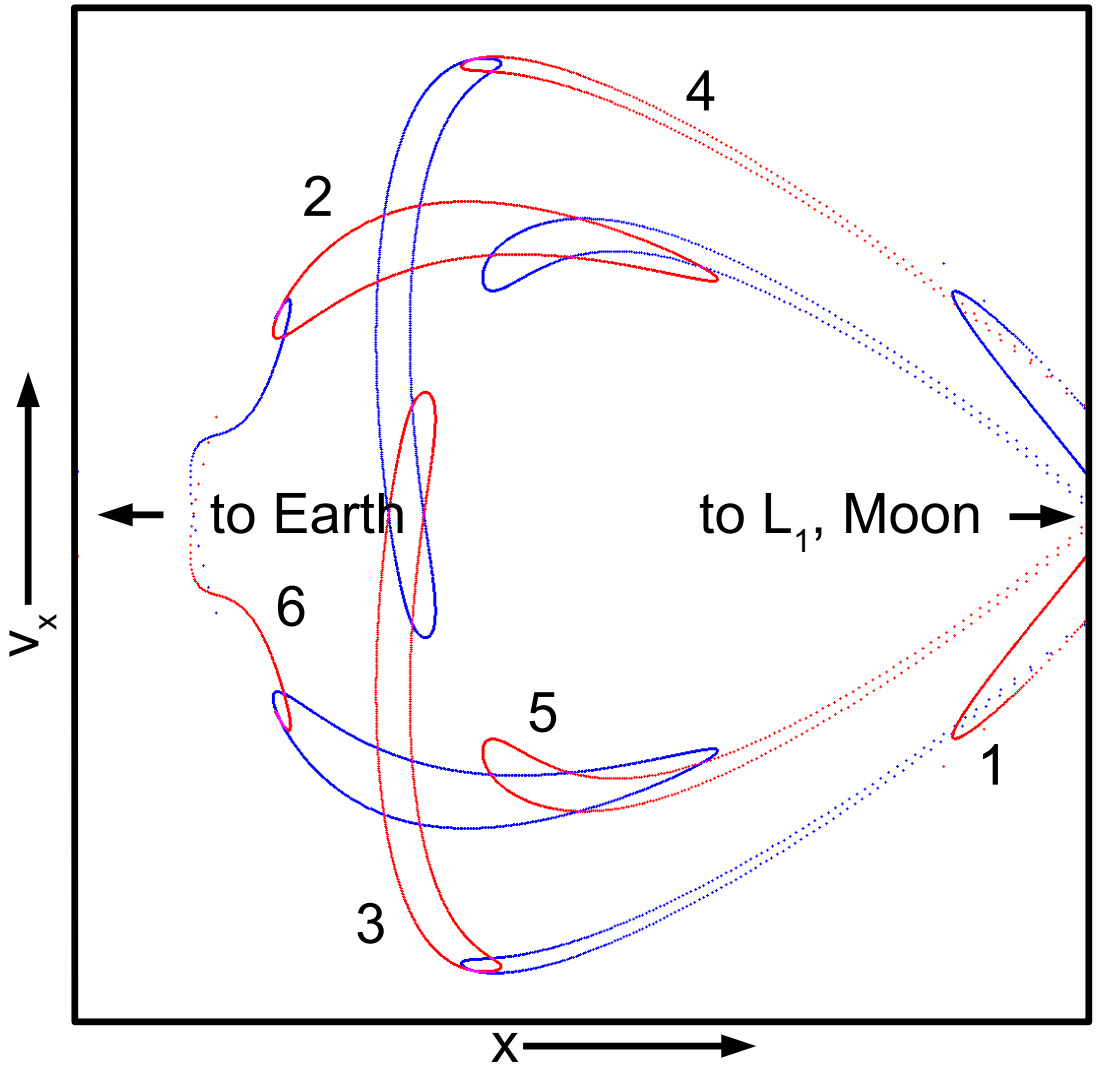

Figure 4.8.: Poincaré Map of Manifolds Associated with Periodic Orbit Fixed Points

the trajectories representing the P_1 manifold branches are plotted in configuration space in Figure 4.9. Again, red is used in both Figures 4.8 and 4.9 to indicate the unstable manifold and blue is used to indicate the stable manifold. Arrows reflecting the general direction of the flow are included in Figure 4.9 along with representations of the Earth, Moon and zero velocity curves. The manifolds are terminated at a particular crossing of the x axis for purposes of illustration (such a condition does not represent a physical termination of the manifold trajectories). Ultimately, manifold

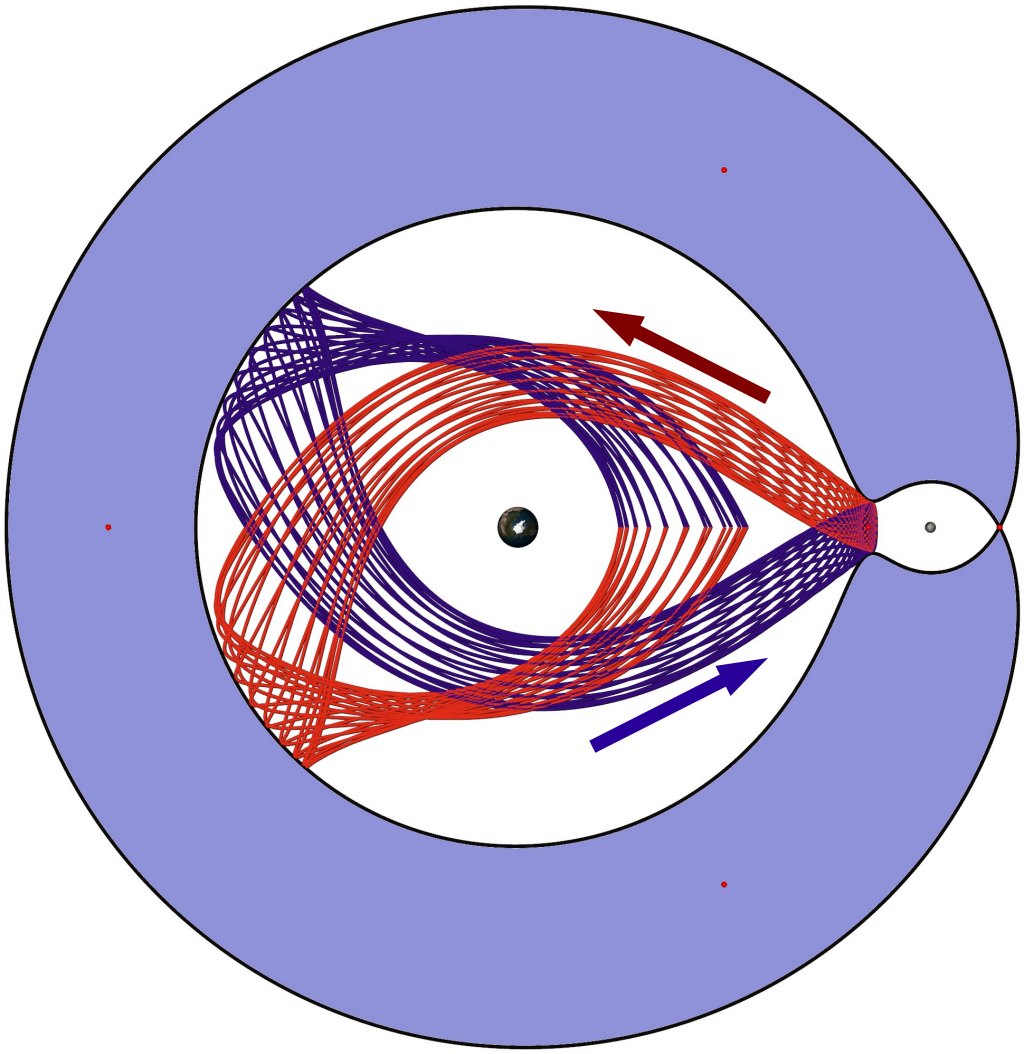

Figure 4.9.: Lyapunov Orbit Stable/Unstable Manifolds Represented by Trajectories

concepts reflect characteristics of the natural dynamics that may be exploited for effective mission design. The usefulness of manifolds, particularly stable and unstable manifolds, supplies an impetus for identifying such structures. The methods described in this section represent only one way of identifying manifolds, require a prescribed process and a priori knowledge of their existence. Invariant manifolds and their time-dependent analogs may also be identified through flow-based analysis.

4.5 Chaos

As energy in a system increases, regular motion begins to give way to more complex and unpredictable behaviors. At some point the associated motions are deemed *chaotic*, motions that may not be categorized as equilibrium states, periodic orbits or quasi-periodic behavior. Yet, in many cases, such chaotic motion may remain bounded [40]. There exists a breadth and depth of chaotic theory that is beyond the scope of the present analysis. However, as some results of this work reflect chaotic tendencies, some discussion of the notion of sensitive dependence on initial conditions, as well as of the chaotic features of a Poincaré map, is pertinent.

Sensitive dependence on initial conditions is a hallmark characteristic of chaotic systems. From Parker and Chua[1], "given two distinct initial conditions *arbitrarily* close to one another, the trajectories emanating from these initial conditions diverge, at a rate characteristic of the system, until for all practical purposes, they become uncorrelated." In both numerical simulations and physical experiments there is always some error. This error arises from inaccuracies in the numerical representation, operation or from actual measurements. Given sensitive dependence on initial conditions, the overall system response will ultimately and unpredictably diverge for two neighboring initial states separated by even arbitrarily small errors (or intended perturbation). This difference in macro-behavior is illustrated in Figure 4.10, where the results of two numerical evolutions under CRP dynamics are presented. In each case, the initial states (green dots) are identical in all state components. All numerical processes are likewise identical, including the duration of integration. The only difference is introduced in the system mass parameter. Both parameters are equal to each other to 16 digits of precision. However, in (a) the value is calculated and input by hand, while, in the case of (b), the calculated result is used directly. Thus, a difference in representation of less than the machine epsilon (actual difference $\approx 3 \times 10^{-18}$, epsilon $\approx 2 \times 10^{-16}$) results in dramatically different behavior. Also included in the figure

[1]From [40], page 22, emphasis added.

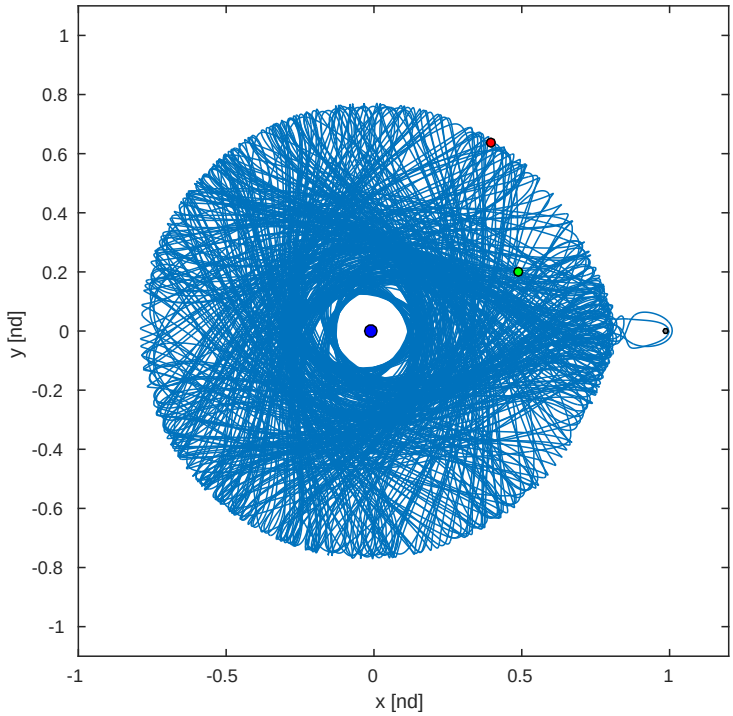

(a) Manually Entered System Mass Parameter

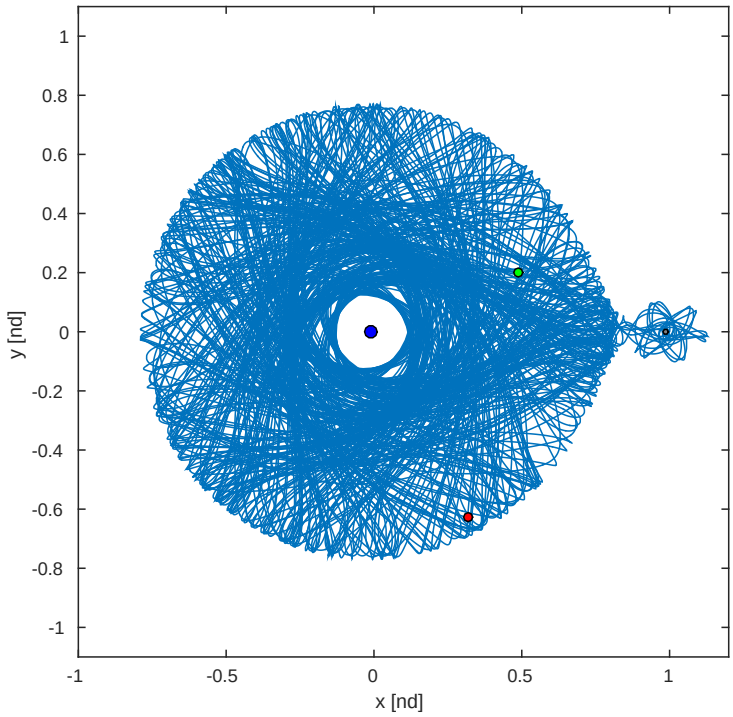

(b) Directly Calculated Mass Parameter

Figure 4.10.: Sensitive Dependence on Initial Conditions Illustrated

are the trajectory end points (red dots) as well as representations of the larger (blue) and smaller (gray) primaries.

Chaotic behavior is frequently observed in Poincaré maps. For example, consider Figure 4.11, a representation of the *Chirikov–Taylor Map* (or, so-called *Standard*

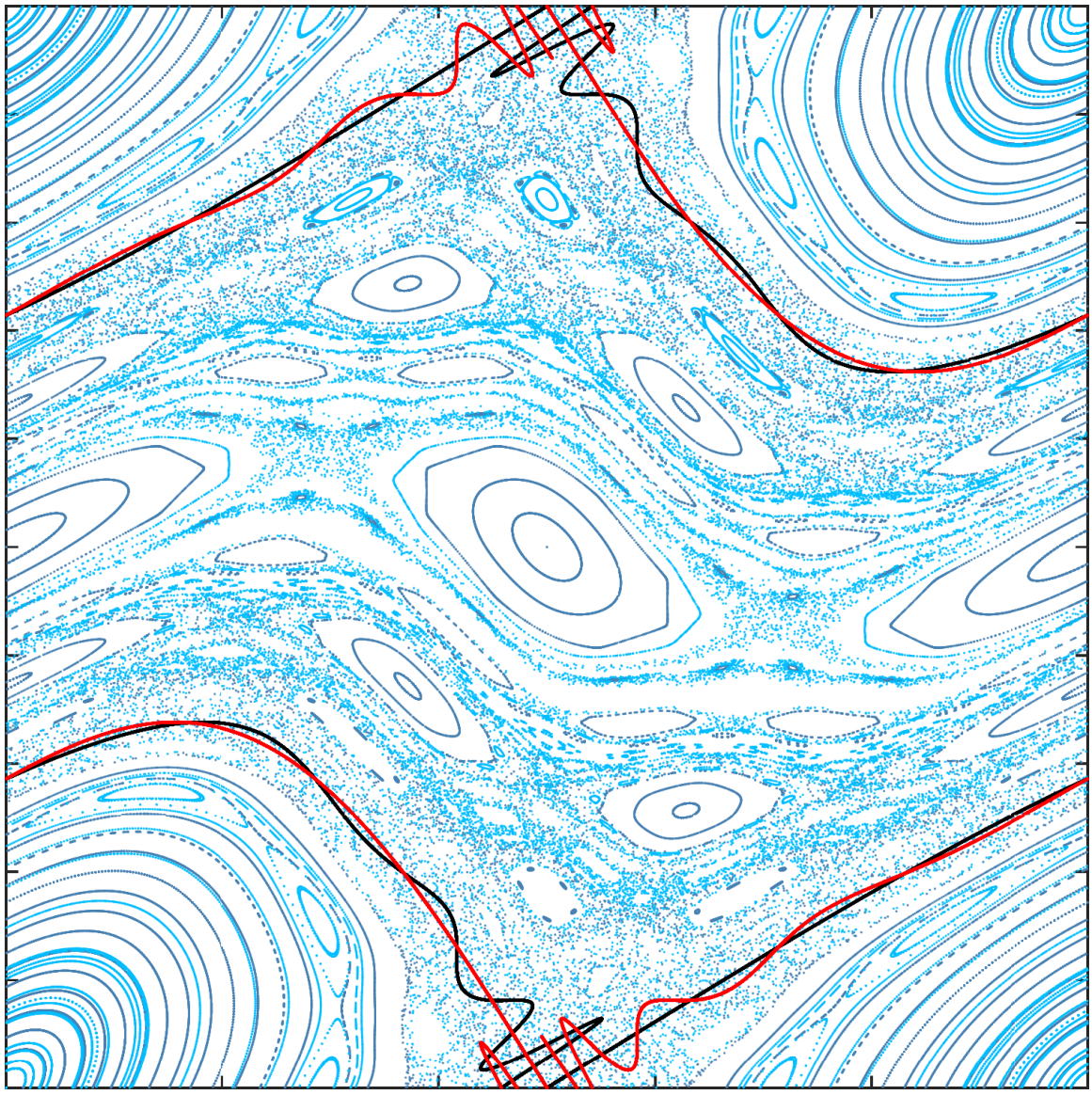

Figure 4.11.: Example Poincaré Map Illustrating Chaotic Behavior

Map). In this particular plot, the associated chaos factor of the system, essentially a scaling constant, is set at a value of 1.0, indicative of pronounced chaotic behav-

ior. Many interesting behaviors are apparent in the associated visual, but only a few are pertinent to the present discussion. The visual is flat, but the map wraps at each edge—thus, opposing edges join and the map surface is, in fact, toroidal (see Figure 4.12 for examples of the map on a toroidal surface). One structure spanning all corners is a set of concentric curves. At the center of these curves is a periodic solution—the same is true for the center of the image itself. The concentric curves, in general, are indicative of KAM tori and are consistent with quasi-periodic solutions. Some groupings of curves are part of larger sets indicating higher order periodicities (i.e., periodic solutions that return to the map several times before repeating). "Dusty" regions of apparent visual disorder are typical of chaotic states. Finally, one known set of stable and unstable manifolds, identifiable by inspection, is included as thick black and red lines. These manifolds serve to separate regions of different behavior. However, the presence of tangled intersections is indicative of leakiness past the manifold barriers. Other manifolds exist in such a system, but are not included in the visual. Such leakiness increases with the chaoticity of the map. All of these map features help to capture the chaotic nature of an example system. Such features are likewise observed in astrodynamical systems of higher dimensions, and the associated chaotic behavior is frequently exploited to identify flow patterns and select useful trajectory options.

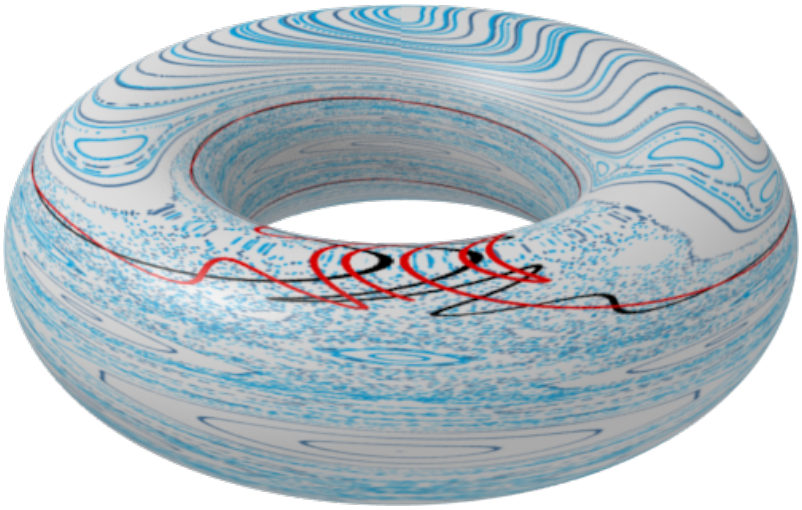

(a)

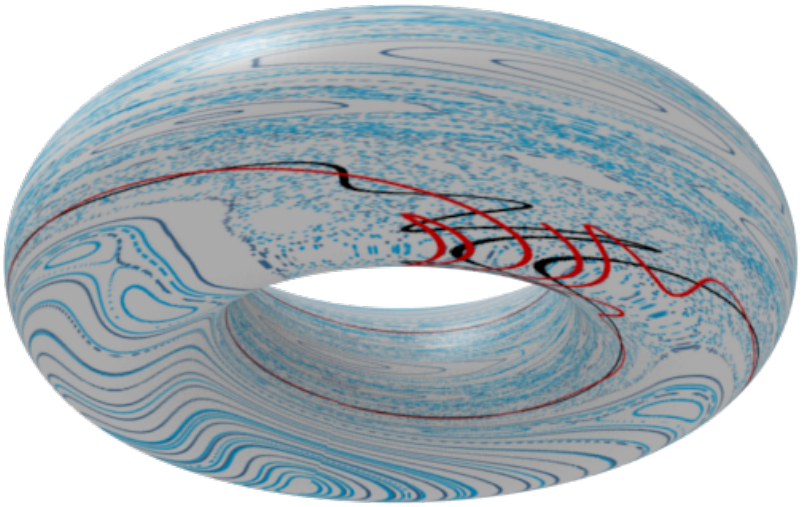

(b)

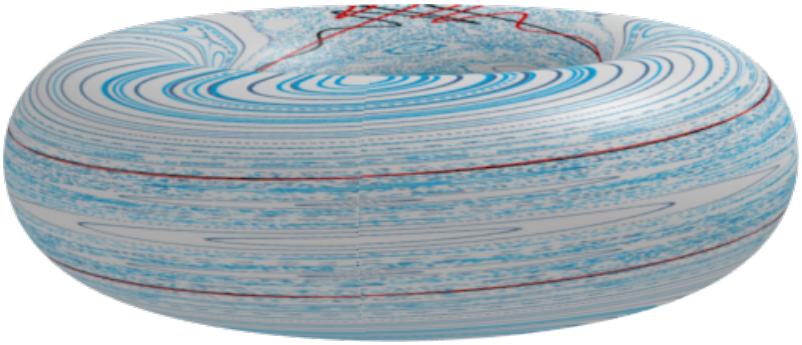

(c)

Figure 4.12.: Mappings of Figure 4.11 Onto a Torus

5. APPROACHES

Specific steps for the application of theory are not always obvious, and bridging the associated gap may result in meaningful solutions to problems. While strategies focused on observation and analysis of flow evolution exist in various disciplines, less has been accomplished with these tool sets in astrodynamics. Whether a reflection of previously inadequate computational resources or as a byproduct of existing, comfortable frameworks, these less frequently applied theoretical options signal a potential for added insight and increased understanding. Some details of methods incorporating familiar approaches along with flow-based strategies are discussed.

5.1 Mapping Strategies

Mapping analysis within the context of multi-body regimes has proven to effectively reveal design options that are otherwise difficult to identify (see, for example, [75, 78–80]). Maps are also used to analyze trajectory behavior in various ways (e.g., [5, 9, 12, 13]). Some advantages of a map-based approach include a broader view of the design space as well as a cleaner visual that offers easier categorization of the behavior in a specific region. The maps employed in this analysis generally employ relatively well-known mapping strategies as well as some novel approaches. In particular, Poincaré maps (or *puncture plots*) in state-space, stroboscopic flow maps and plots that compare trajectory metric traces are all utilized.

5.1.1 State-space Maps

Analysis in many systems involves a traditional Poincaré mapping to create a puncture plot that facilitates the investigation. The map discussed in Section 4.5 and

illustrated by Figure 4.11 is an example of a puncture plot. The construction of such a map depends on the dimension of the phase space, and the result reveals salient information by reducing the dimension of the system. For example, in a 4D phase space, a hyperplane corresponding to some value of a single state variable is defined. A grid supplies the relationship between two other state variables, and the fourth state is constrained by a system integral.

While there are many possible map representations available for observing the behavior in a system, strategies frequently involve the investigation of position-velocity phase spaces. For example, a map can be plotted in terms of a position variable and its associated velocity component. Additionally, maps can also be constructed in terms of only position or velocity coordinates or in terms of other functions of the states. Plotting only trajectory apses is one possible option for such a mapping—in this case, the apse condition serves as the hyperplane.

5.1.2 Stroboscopic FTLE Maps

Traditional stroboscopic maps are constructed as Poincaré maps with a hyperplane condition selected as a particular time, for example, the characteristic period of a system. Mappings that overlay relative FTLE values, computed for a common time condition, on coordinates corresponding to initial states are of particular interest in this analysis. The time may be arbitrarily defined, however, if the desire is to iterate the map a particular timing condition is required. Consider the map $F = \phi_{t_o}^{t_o+T}$ then $F \circ F$, two iterations of F, has no physical meaning, unless the gravity field is periodic in the frame of integration. Composing $F_1 = \phi_{t_o}^{t_o+T}$ and $F_2 = \phi_{t_o+T}^{t_o+2T}$ makes physical sense, since $F_1 \circ F_2$ is $\phi_{t_o}^{t_o+2T}$. In this case, though, fixed points of F_1 generally have no meaning or interest beyond $t_o + T$. Stroboscopic mapping strategies yield a snapshot of a grid of trajectories in terms of a particular time, thus the timing condition used to define the map is a critical consideration.

Aspects from various mapping strategies can be combined to effectively illustrate the flow in an astrodynamical model. Instead of searching for periodic orbits and manifolds in systems with complicated time dependence, an alternate method invokes maps of FTLE values. Maps of FTLE values in dynamical models with time-varying gravitational fields are typically constructed after a specified time and represent a single iteration of a stroboscopic map. A particular propensity of the finite-time Lyapunov exponent for predicting behavior is captured by examining large groupings of FTLE values in a region. Creating maps of initial states characterized by their associated FTLE values consistent with a particular time reveals patterns in the subsequent flow and guides strategies that exploit such patterns. An example of such a plot where FTLE scalar values have been rendered as a height mapping over initial state coordinates with larger values exhibiting greater height is displayed in Figure 5.1. Typically, however, such a map is displayed simply by coloring the relative

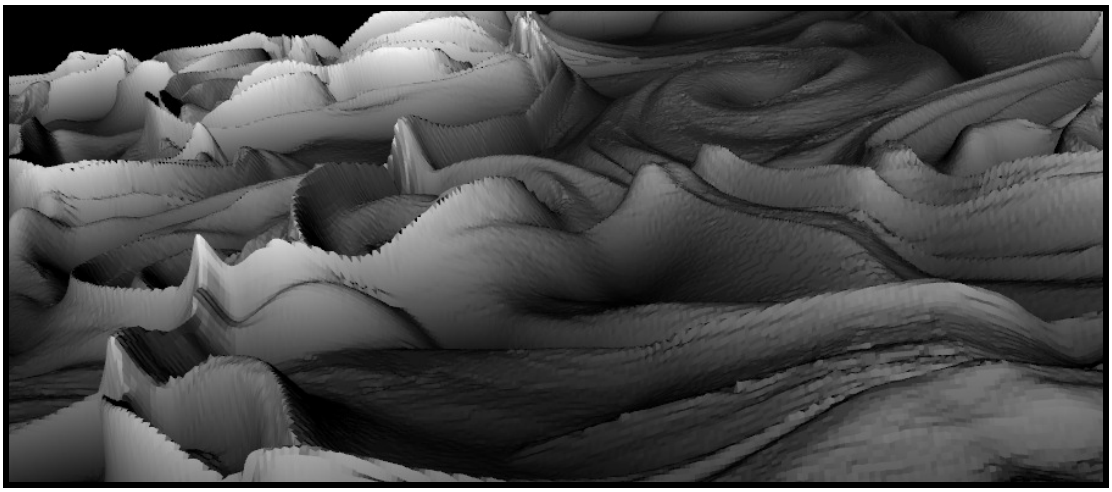

Figure 5.1.: FTLE Values Mapped as Height Ridges

values of FTLE on a 2D plot as in Figure 5.2 where lighter colors correspond to higher FTLE values. The information that emerges from FTLE maps guides additional flow analysis and aids in informing different phases of mission design and analysis.

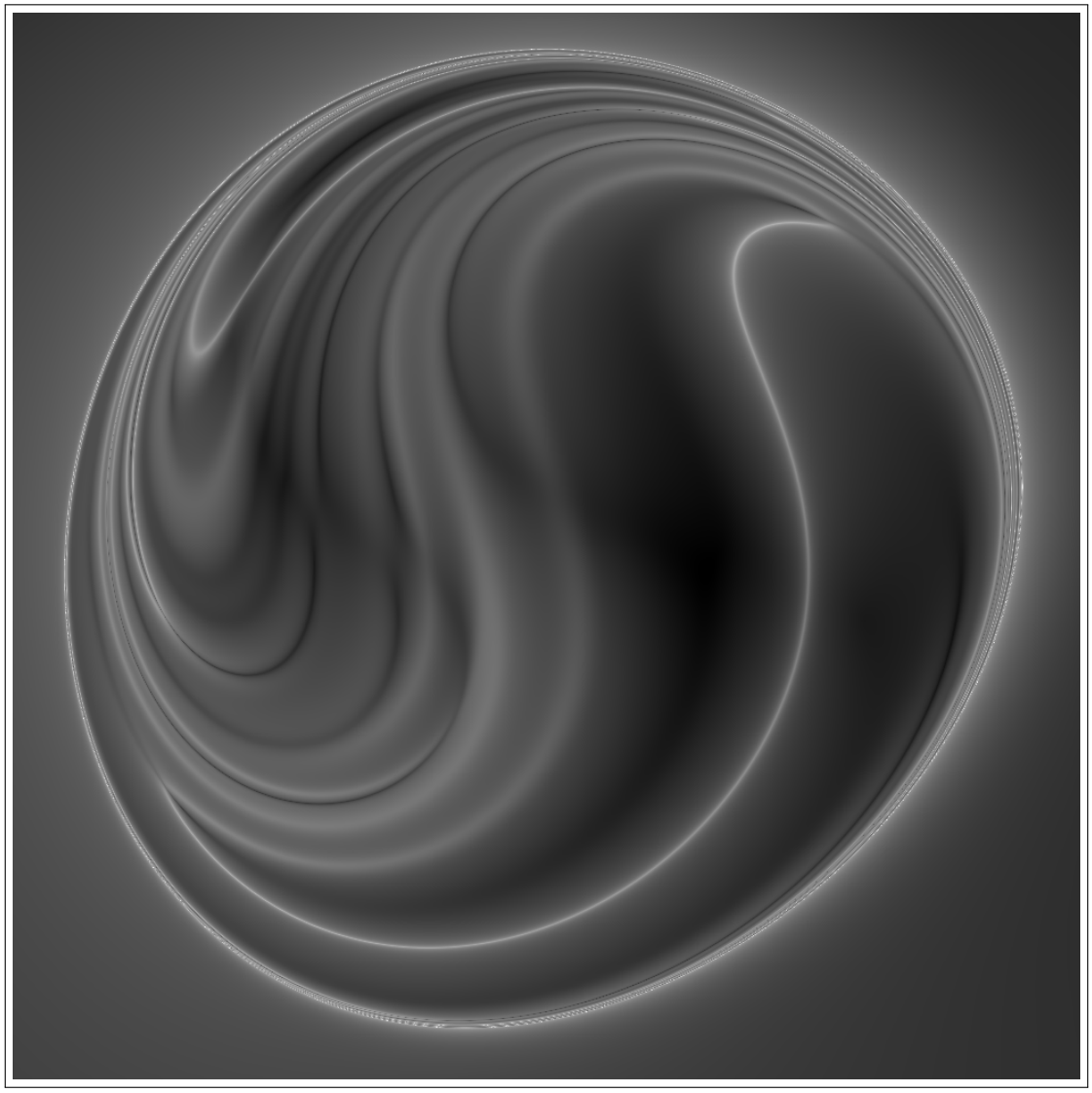

Figure 5.2.: FTLE Colored by Value

5.1.3 FTLE Trace Maps

While summary information is captured and explored through stroboscopic mappings, such processes are designed to eliminate intermediate detail. Often it is necessary to examine trajectory behavior in context. Plotting a particular metric for a trajectory and its neighbors as they evolve over time supplies such contextual information. Consider the FTLE values, associated with some trajectory over nearly 100 years, included as Figure 5.3. A stroboscopic FTLE map taken after 90 years

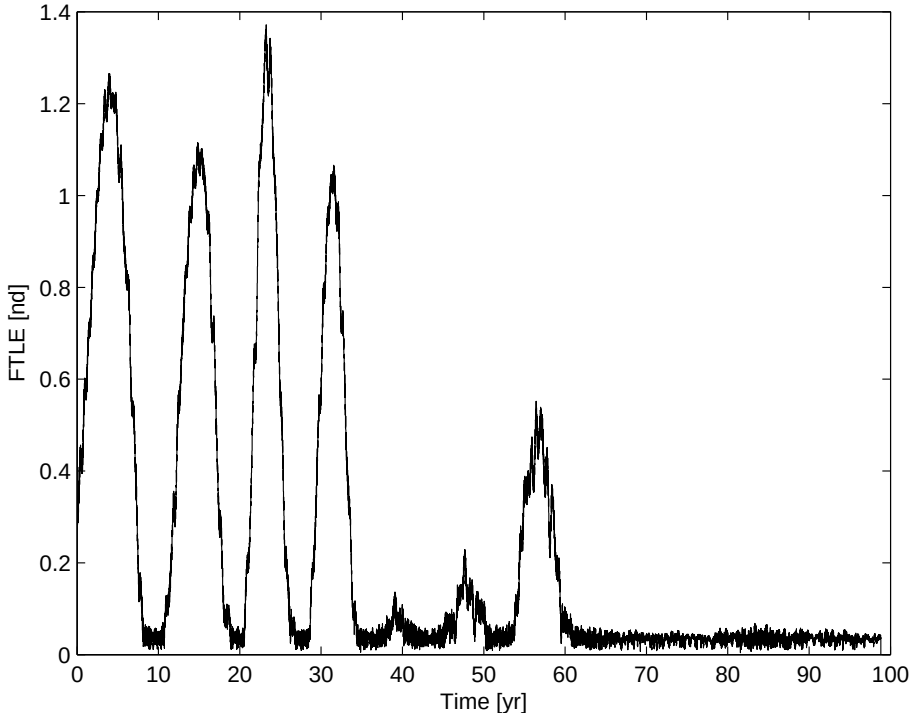

Figure 5.3.: An FTLE Trace

in this particular trajectory's evolution would give some idea of the state of local phase space, but it wouldn't capture the range of behavior observed throughout the preceding time. Thus, if the objective is to capture the intermediate behavior in neighboring trajectories, the trace in Figure 5.3 may be collapsed and plotted as a flat, one-dimensional line colored by relative FTLE values. This trace may then be accompanied by traces associated with neighboring trajectories. Such is the case

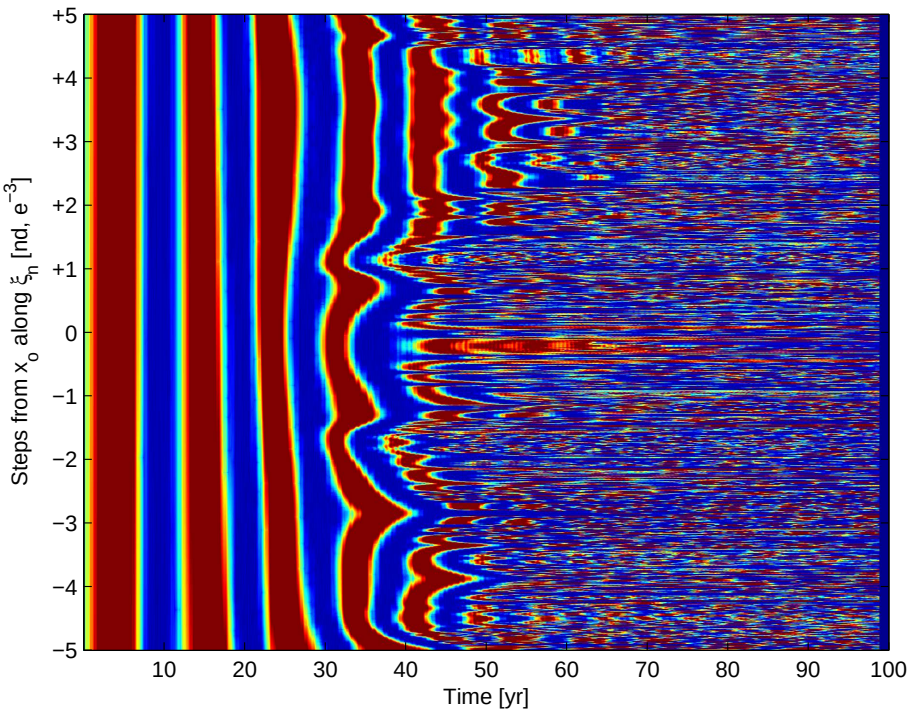

Figure 5.4.: A Map of FTLE Traces

in Figure 5.4 where the FTLE trace of Figure 5.3 appears at ordinate 0 and runs across the plot. FTLE values are represented in the figure by color using a traditional rainbow color scheme. Large values are indicated in red and small values are blue. Neighboring trajectories are selected by perturbing the original initial state in specific directions, namely by taking small steps along the eigenvector, $\boldsymbol{\xi}_n$, associated with the largest eigenvalue of $\mathbf{C}$. Recall that such a direction is aligned with the largest stretching direction of the phase space (Section 2.5). Consequently, these perturbations will lead to the largest possible dispersion in the shortest amount of time and the associated directions are optimal for exploring the phase space. A map of FTLE traces like the one given in Figure 5.4 yields temporal context and captures significant information. This particular map is featured in a later example where additional analysis is discussed (Sections 7.6.6–7.6.7). Alternate FTLE trace strategies are offered by Anderson [10, 39], Harden et al. [12] and Spreen et al. [13].

5.2 Flow-map Features

The features visible in an FTLE map are reflections of the evolution of the trajectory flow that emerge directly from inspection of the largest eigenvalue of the Cauchy–Green tensor. However, harnessing these features in an automated manner can be challenging given a discrete map resolution. Exploitation of the additional eigencomponents of $\mathbf{C}$ supplies directional information and a means for parametrizing map features. Specifically, lines that follow the curvatures of the FTLE field, denoted *strainlines* or *reduced strainlines*, are computed. These strainlines help to characterize the flow originating from initial conditions and highlight various regions in the map. In fact, the reduced strainlines are cross sections of the strongest repelling hypersurfaces in the flow, and, as such, they are expected to separate regions of different behavior. The calculation of reduced strainlines results in 4D parametrizations of Lagrangian coherent structure cross sections. Not only do the strainlines offer an immediate visual indication of different flow regions, useful in searching for potential trajectory options, but they can also be directly harnessed in algorithms with precise calculated states. Given the sensitive, chaotic nature of models for simulating astrodynamical systems, very small inaccuracies (even on the order of double precision numerical truncation errors) can be significant. Extracting an accurate solution for LCS states through reduced strainlines enables additional numerical analysis within a region. The process for producing these strainlines is enumerated:

1. Identify LCS candidate points based on high FTLE values, and refine these points to arbitrary precision by seeking nearby maxima.

2. Calculate the Cauchy–Green tensor and eigenvectors for the points from (1).

3. Using the eigenvector directions and normals $\boldsymbol{n}_i$ to the state space, calculate the unique direction orthogonal to $\boldsymbol{n}_i$ and the eigenvector associated with the largest eigenvalue, $\boldsymbol{\xi}_n$, which is the tangent direction for repelling strainlines.

In general, if the state space is defined by scalar functions $F_i = c_i$ then ∇F_i are vectors orthogonal to the state space. In the CRP, the state space may be reduced by fixing an initial Jacobi constant $C = C_{\mathrm{o}}$ and a state variable $c_i = c_{i_{\mathrm{o}}}$. Then, the vector $\boldsymbol{n}_1 = \nabla C$ as well as the remaining $\boldsymbol{n}_i$ are used as normals to the state space to calculate the reduced strainlines. The strainlines, then, follow the vectors orthogonal to both $\boldsymbol{n}_i$ and $\boldsymbol{\xi}_n$ under numerical propagation and outline distinct regions characteristic of specific flow behavior. Moreover, the strainlines support the visual insight supplied by the underlying FTLE and represent parametrized curves that can be exploited as needed for additional feature evolution. Details of the specific steps in this process are elaborated.

5.2.1 Candidate Point Identification

The initial effort of seeding points for strainlines requires some care. Manually placing initial points for strainlines guided by the features in an FTLE map may be a useful strategy. However, a more automated possibility is available. Begin with a simple line search across the FTLE field identifying all local maxima along this line. In fact, multiple lines may be used, for example, four such line searches: a horizontal line centered vertically and running across the field, a vertical line centered horizontally and running from the top to the bottom of the field, and two diagonal lines joining opposing corners. This search strategy is depicted in Figure 5.5(a) where the coloring has been inverted for illustration; darker colors represent higher FTLE values, black lines represent the search space, and white dots illustrate potential maxima of the underlying FTLE field. The FTLE profile along a particular line is frequently noisy leading to multiple local maxima in a small neighborhood and may benefit from subsampling or culling. It is desirable to identify local FTLE maxima along a line to sufficient numerical precision that the resulting CG eigenvectors are consistent and usable. Given the several maximal points identified along a field-wide line, a refinement to isolate a constrained maximum in their local neighborhoods is

performed. This refinement is illustrated in Figure 5.5(b) centered on a single white point from one of the initial lines. Additional searches along much smaller lines (in this case about 300× smaller than the larger lines) in the local neighborhood supply the maximum line-wise FTLE values (gray points in the figure), from among which the overall maximum is obtained (black marker) as the refined point for further analysis. To accomplish arbitrary resolution (and overcome truncation errors from finite-differencing) along any of the line searches, complex-step differentiation as described by [81] is invoked to evaluate the CGST. The refined points are not necessarily the global maxima within their associated neighborhoods, but they are assumed to be crossings of a curve of interest (also depicted in Figure 5.5(b)).

5.2.2 Vector Analysis and Strainlines

The Cauchy–Green tensor is evaluated for the points identified in the preceding step. The flow parameters are consistent with the parameters defining the FTLE maps. The integration time associated with the map is employed to calculate the CGST at each step. The CG eigenvectors from the associated points are retained for the subsequent step. Beginning with a seed point identified through refinement, a vector is calculated that is simultaneously orthogonal to the CG eigenvector $\boldsymbol{\xi}_4$, the hyperplane and the variation of Jacobi constant (i.e., the gradient of the Jacobi constant expression), as described previously. This *reduced* vector is tangent to the desired strainline and a single numerical integration step along the four-dimensional vector evolves the strainline forward to a new point. Repelling strainlines are computed by propagating through the reduced field $\hat{\boldsymbol{\xi}}_n$, and care is required since the field is defined only up to a sign. As for two- and three-dimensional phase space flows [7,8], the differential equation is solved for parametrizations $\mathbf{r}$ of repelling strainlines,

$$\frac{d}{ds}\mathbf{r}\left(s\right) = \text{sign}\left(\left\langle \hat{\boldsymbol{\xi}}_n\left(\mathbf{r}\left(s-\Delta\right)\right), \hat{\boldsymbol{\xi}}_n\left(\mathbf{r}\left(s\right)\right)\right\rangle\right)\hat{\boldsymbol{\xi}}_n\left(\mathbf{r}\left(s\right)\right) \tag{5.1}$$

Thus, to compute curves tangent to $\hat{\boldsymbol{\xi}}_n$, the previous orientation of $\hat{\boldsymbol{\xi}}_n$ is considered to account for the likelihood of a sign change in $\hat{\boldsymbol{\xi}}_n$ at the next time step. The calculation

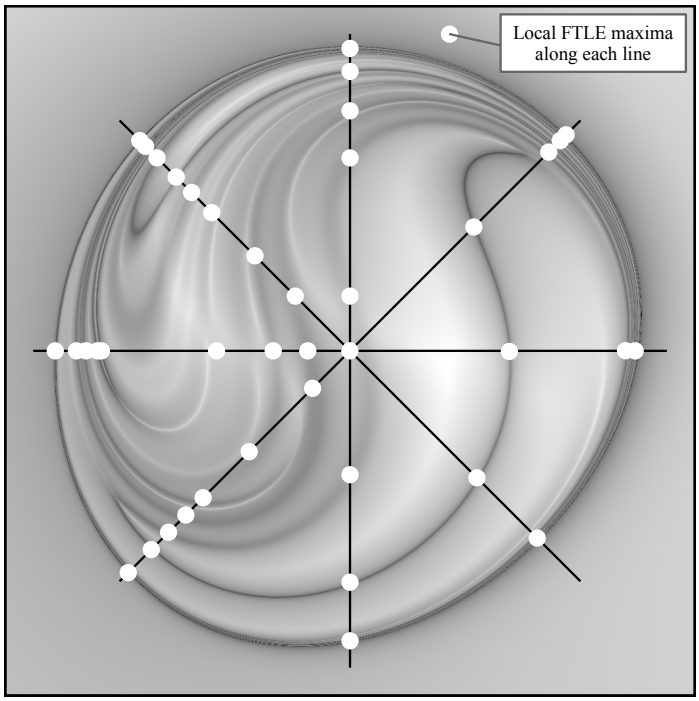

(a) Search Strategy for High FTLE Points

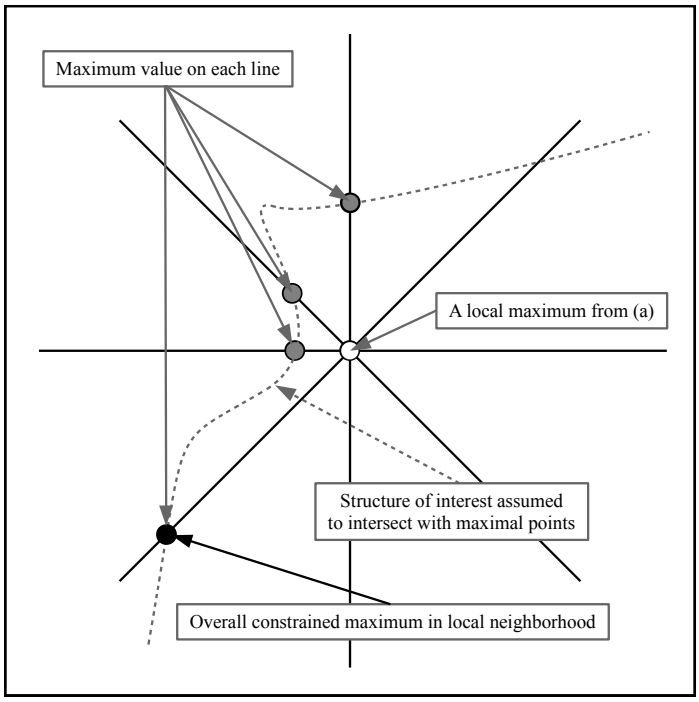

(b) LCS Candidate Point Refinement

Figure 5.5.: Identifying and Refining LCS Candidate Points from FTLE Maxima

of a new reduced vector is accomplished by evaluating the CGST at the new point and performing the requisite vector operations again. This process continues for each integration step until some prescribed final integration time (i.e., an nD arc length) is met. The result is a set of curves such as those depicted in Figure 5.6.

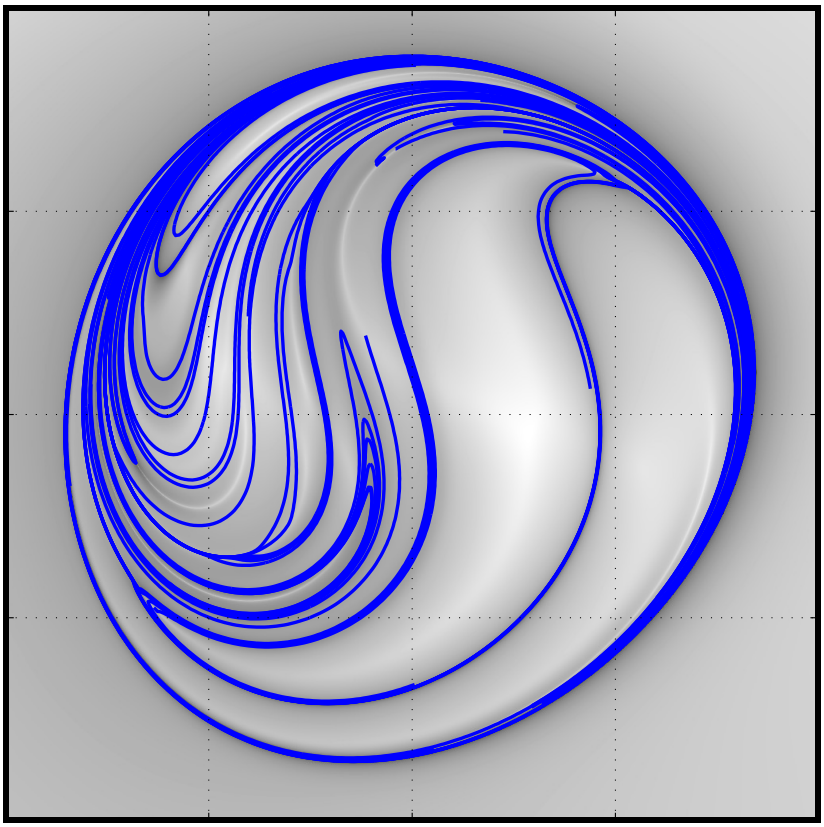

Figure 5.6.: Projection of Integrated Strainlines onto an FTLE Field

The process for identifying reduced strainlines may be extended to higher dimensions. This extension is useful when working in astrodynamical systems with six-dimensional phase spaces. Such applications require additional constraints to appropriately construct the requisite vector fields. Ultimately, the computation of strainlines in higher dimensions under additional constraints becomes application specific, reducing to the same lower-dimensional process described. The resulting, well-defined maps continue to inform the design process and supply actionable insight into flow behaviors.

5.3 Material Curve Advection

Numerical propagation of an initial state under the influence of a governing model is a useful process for observing and analyzing the evolution of a particular solution. However, it is frequently desirable to establish the context for such a solution. While the variational behavior and phase-space stretching are available from the state transition matrix and the Cauchy–Green tensor, it is sometimes useful to examine the evolution of multiple trajectories simultaneously. For example, a curve of initial conditions, a *material curve*, may be advected under the flow as it cuts a swath through the phase space. Similarly, a higher dimensional patch or packet of initial states, a *material surface*, may be observed as it evolves. This strategy is useful for observing separations and confluences in the flow as well as for seeking intersecting regions in the phase space as they evolve forward or backward in time. An example of the advection of a material curve selected as the four-dimensional strainline outlining the structures in Figure 5.6 is depicted in Figure 5.7. In Figure 5.7(a), the strainline is seen to evolve in time to form a tube that retreats into the page, while the same structure is viewed from the side in Figure 5.7(b). This particular structure represents the evolution of a boundary that separates flow behavior. Specifically, flow inside the tube is characteristic of different behavior than flow exterior to the tube. This structure is isolated in a nonautonomous problem, and it is analogous to an invariant manifold structure in the autonomous CRP. Traditional methods for identifying manifolds are not available in the nonautonomous problem and the structure is identified directly from flow-based techniques.

5.4 Trajectory Sensitivity Analysis

The description of the flow isolated from the Cauchy–Green tensor may also be utilized to characterize the sensitivity along a trajectory. Such a sensitivity analysis helps to identify useful places for maneuvers and lends context for optimal maneuver planning. This type of analysis includes FTLE traces for a single trajectory

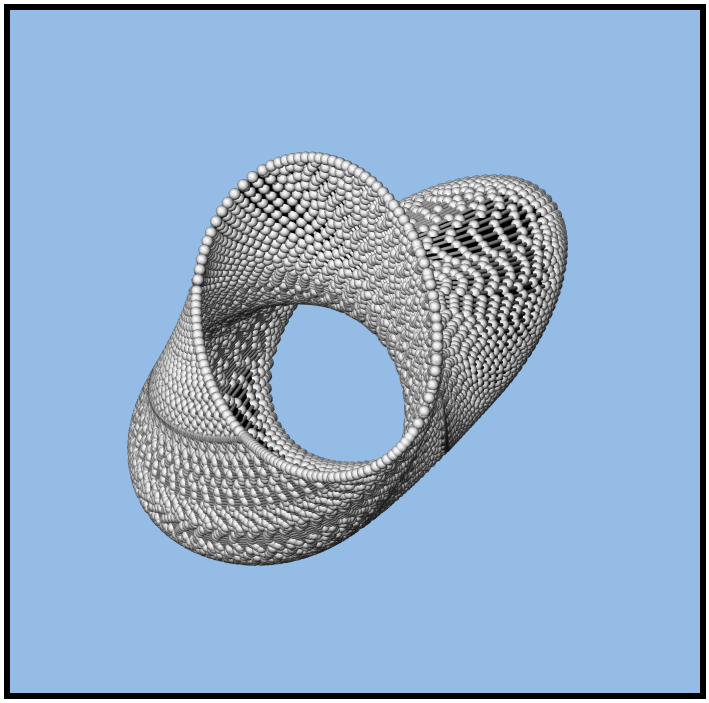

(a) Edge-on View of Material Curve Evolution

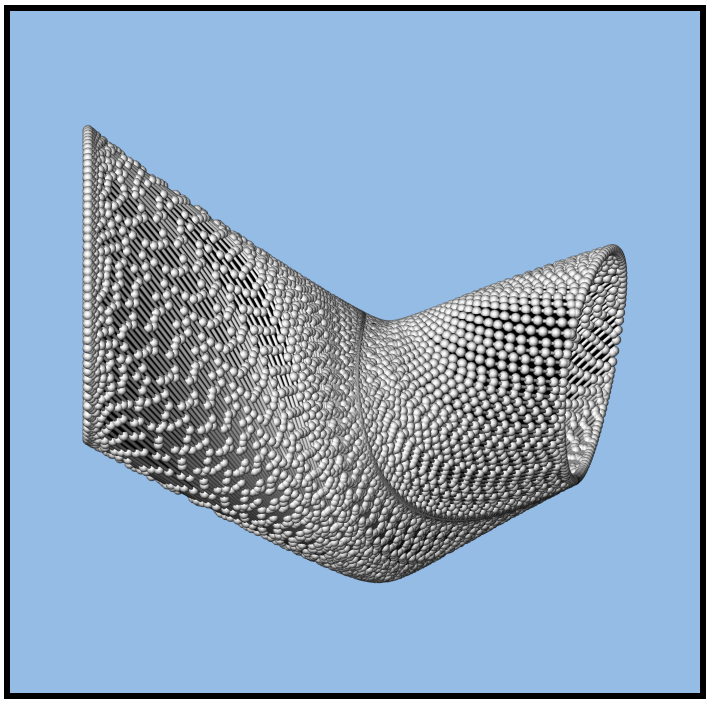

(b) Side View as Material Curve Evolves to the Right

Figure 5.7.: Three-dimensional Projections of a 4D Material Curve Advection

parametrized by horizon time ([12, 13]), as well as sensitivity characterization along an arbitrary path ([10, 39]). Yet another example is given by analysis of maneuver directions for the ARTEMIS mission. This maneuver analysis is detailed in Section 7.5 and employs phase-space FTLE packets like the one depicted in Figure 5.8 where a "cube" of FTLE values are used to support maneuver alignment findings of Folta et al. [82, 83] and Pavlak and Howell [84]. In the figure, a performed maneuver (cyan) aligns with the stable eigendirection (blue) from the monodromy matrix, $\mathbf{M}$, associated with an approximate orbit. The maneuver also points in the direction of smallest FTLE values. Such a result illustrates how the flow context can help to isolate maneuver directions with particular qualities.

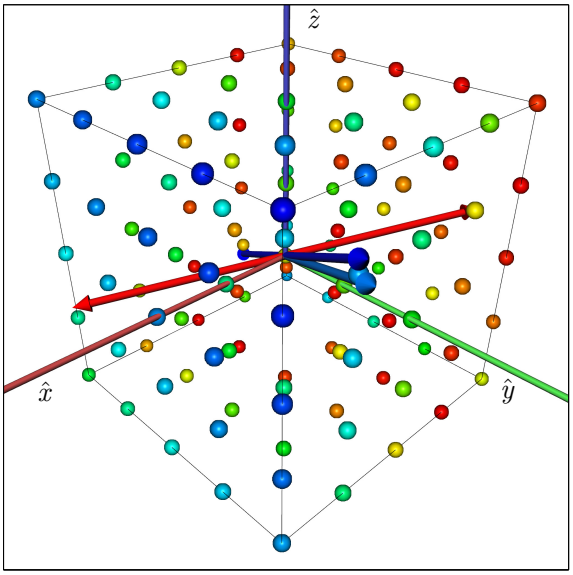

Figure 5.8.: A Forward FTLE Packet Identifying Stability Directions

Flow-based methods represent a perspective to astrodynamical systems that has rarely been examined. As such, some advantages are immediately offered. For example, observation of the evolution of the flow reveals patterns that may not be otherwise available. Additionally, the methods are not restricted to any particular system characteristics. The system need not be autonomous or even exhibit repeating behavior. These advantages are reflected in the examples of Chapter 7.

6. COMPUTATIONAL CONSIDERATIONS

Numerical methods supply an effective means for solving problems that are otherwise analytically intractable or recalcitrant. However, such methods often introduce their own complexities associated with the computational framework. For example, a number of challenges are encountered when computing the flow field in a given system. The problem of sufficient grid resolution is ubiquitous, and a finite grid requires careful treatment. Strategies that look good on paper are often problematic to implement computationally for systems characterized by high dimensionality. Astrodynamical systems introduce issues of scale and associated numerical sensitivity. Finally, flow-based strategies require a flow model, which is equivalent to bulk evolution through gravitational fields—extensive numerical integration. Each of these challenges are elaborated and some computational strategies for their resolution are discussed.

6.1 Challenges

An advantage of an analytical expression for a problem is a continuous solution space. For system models that don't possess such solutions, computational methods must be applied in a finite, discrete way. Flow computation is often performed by using a finite mesh or grid of points. Unfortunately, a mesh that is too coarse may not capture important flow behaviors. In general, the discrete nature of any mesh also leads to situations where values are required "between the nodes". Such a situation in the context of numerical integration means that an integration step may take a function to an undefined state. Finally, a strategy of arbitrary mesh refinement may lead to excessive computation.

Many simple dynamical systems are formulated with only a single dependent variable, and this variable, coupled with its derivative, gives rise to a two-dimensional

phase space. Frequently, however, to completely represent a particular behavior like the translation of a spacecraft, the associated phase space is higher-dimensional. Two or three dependent variables are more common leading to four- or six-dimensional phase spaces. Such a higher-dimensional system not only inherently reflects theoretical complexities but it also displays unique numerical and computational hurdles. While many notions that hold for lower-dimensional systems may, in some cases, theoretically extend to more dimensions, the computational realization of such principles may no longer be tractable. In a practical sense, higher dimensionality translates directly to additional memory requirements.

In a model that displays chaotic behavior, a sensitive dependence on initial conditions is acknowledged. From an implementation perspective, this indicates that, for some problems, small variations lead to computational issues. In fact, a difference in a particular initial state variable may lead to dramatically different behavior over longer times. This sensitivity is particularly apparent in astrodynamical contexts where many gravity models display such behaviors. An associated consequence is revealed again by an issue of resolution—sometimes very small initial changes are required to obtain viable results, but small separations lead to numerical precision and truncation issues.

Yet another challenge encountered when working in these computational regimes is simply a problem of implementation scale. Specifically, flow analysis requires extensive numerical integration, and such integration translates directly to computational time. More processing time is required based on the dimensionality of the analysis and the resolution of the underlying mesh. Appropriate measures, then, must be taken to acquire meaningful information within a reasonable computational duration.

Each of these computational challenges can be met with a variety of strategies. However, numerical approaches perform with varying levels of efficacy, and a judicious application of several options may be required. Several methods are considered in the context of how they address each of the outlined challenges.

6.2 Strategies

While numerical challenges are frequent in a largely computational research effort, there are many strategies for addressing such challenges. Several such strategies are discussed in this section. Some of these approaches may apply in various contexts or be relevant for only a specific application. In some cases, several options are required to accomplish a particular research goal.

6.2.1 Integration

Several numerical integration schemes are employed in this analysis. Some simple, lower-accuracy integrators are used for exploratory efforts. A trapezoid method is employed for implementation in settings that require simple function integrations. Lower-order Runge–Kutta integration algorithms are also employed. After regions of interest are identified and designated for a more careful inspection, an adaptive step size Runge–Kutta–Fehlberg (RKF) $4^{\text{th}}/5^{\text{th}}$-order integrator, one included in the GNU Scientific Library (GSL) [85], is sometimes applied. Most often, a Runge–Kutta Prince–Dormand $8^{\text{th}}/9^{\text{th}}$-order scheme, also from the GSL, is employed for operations. Additionally, a Runge–Kutta $4^{\text{th}}/5^{\text{th}}$-order option from the Boost [86] library, that supports complex data types, is exploited for cases where complex-step derivatives of the flow map are needed. Despite the various numerical integrators employed for particular steps in this analysis, care is taken to use consistent tolerances and parameters. The accuracy required of the integrator is generally on the order of 10^{-12} or smaller.

6.2.2 Linear and Cubic Interpolation

A disadvantage of a grid-based numerical method is that no data is defined between grid points. While an effective mesh may alleviate such a concern, some numerical processes will necessarily require function evaluations that fall between grid

points. Such is the case for numerical integration. One approach when data is required in an undefined location is interpolation. Interpolation may be sufficient to accomplish some goals, and two particular options are common.

Linear interpolation uses a linear fit between adjacent grid nodes. In the case of a multi-dimensional grids, a linear interpolation is required in each coordinate. If two dimensions define the grid, a bilinear interpolation is invoked and such a process may be recursively adapted to any dimension. To define the bilinear interpolation scheme, consider the notation associated with a linear interpolation [87],

$$f(x) = x(f_1 - f_0) + f_0, \tag{6.1}$$

where the value of the function, f, at some point, x, interior to the interval $[x_0, x_1]$ is a function of the value of $f(x_0) = f_0$ and $f(x_1) = f_1$. Bilinear interpolation arises as a natural extension of linear interpolation, and essentially represents linear interpolation repeated twice over two parameters. The key formula for bilinear interpolation produces the value of a 2D function, $f(u, v)$, where u and v are the coordinates of a point interior to the four points on the corners of a grid,

$$f(u, v) = (1 - v)\left((1 - u)f_{00} + uf_{10}\right) + v\left((1 - u)f_{01} + uf_{11}\right). \tag{6.2}$$

Consistent with linear interpolation, the values at the points on the corners of the grid are represented by $f(u_0, v_0) = f_{00}$, $f(u_0, v_1) = f_{01}$, $f(u_1, v_0) = f_{10}$ and $f(u_1, v_1) = f_{11}$.

Sometimes, linear interpolation is insufficient, and cubic interpolation is another option. Again the interpolation scheme relies on a single cubic interpolation applied recursively to the required dimensionality. In the case of cubic interpolation four grid nodes are required to form a cubic fit as the coordinates and derivatives of the grid are required. To find the cubic interpolant, begin with a cubic function and its derivative (this derivation follows [88] and [89]).

$$\begin{aligned} f(x) &= ax^3 + bx^2 + cx + d \\ f'(x) &= 3ax^2 + 2bx + c \end{aligned} \tag{6.3}$$

As in the linear case, the cubic interpolation is defined over local coordinates, and function values are required both at the end points of $x = [0, 1]$ and on the nodes

"to the left and right" of this interval at $x = -1, 2$. Evaluating Equation 6.3 on the endpoints gives,

$$\begin{aligned} f(0) &= d \\ f'(0) &= c \\ f(1) &= a + b + c + d \\ f'(1) &= 3a + 2b + c, \end{aligned} \tag{6.4}$$

which can be solved for the constants,

$$\begin{aligned} a &= 2f(0) - 2f(1) + f'(0) + f'(1) \\ b &= -3f(0) + 3f(1) - 2f'(0) - f'(1) \\ c &= f'(0) \\ d &= f(0). \end{aligned} \tag{6.5}$$

It is assumed that values are given on the nodes such that $f(-1) = f_{-1}$, $f(0) = f_0$, $f(1) = f_1$ and $f(2) = f_2$, and the derivatives at 0 and 1 may be written $f'(0) = \frac{f_1 - f_{-1}}{2}$ and $f'(1) = \frac{f_2 - f_0}{2}$. Substituting these values into Equation 6.5 gives,

$$\begin{aligned} a &= -\frac{1}{2}f_{-1} + \frac{3}{2}f_0 - \frac{3}{2}f_1 + \frac{1}{2}f_2 \\ b &= f_{-1} - \frac{5}{2}f_0 + 2f_1 - \frac{1}{2}f_2 \\ c &= -\frac{1}{2}f_{-1} + \frac{1}{2}f_1 \\ d &= f_0, \end{aligned} \tag{6.6}$$

and the interpolant is,

$$\begin{aligned} f(f_{-1}, f_0, f_1, f_2, x) = &\left(-\frac{1}{2}f_{-1} + \frac{3}{2}f_0 - \frac{3}{2}f_1 + \frac{1}{2}f_2\right)x^3 \\ &+ \left(f_{-1} - \frac{5}{2}f_0 + 2f_1 - \frac{1}{2}f_2\right)x^2 \\ &+ \left(-\frac{1}{2}f_{-1} + \frac{1}{2}f_1\right)x + f_0. \end{aligned} \tag{6.7}$$

To perform bicubic interpolation, four cubic interpolations are performed. Likewise, for tricubic and n-cubic interpolations, recursive calls of the cubic interpolant are

made. Either the grid boundaries must be truncated at the edges to deal with interpolations that require values beyond the domain, or extrapolations are required at the edges to interpolate up to the boundaries.

Interpolation methods allow for approximations of continuous data where only discrete values are known. Such an approach is often sufficient for many applications, and may be performed with varying degrees of accuracy depending on the requirements. However, in some cases, even the most accurate interpolation scheme may not provide sufficient accuracy. In such cases, either the mesh must be refined or values must be calculated on demand.

6.2.3 Adaptive Mesh Refinement

Often computation of a flow field may be mitigated by focusing directly on areas of interest. However, which areas may be of interest may not be known prior to the simulation. One option to accommodate a focused approach without previous knowledge of the flow behavior is available through Adaptive Mesh Refinement (AMR) ([35], [90]). The strategy works such that a coarse mesh initiates the process. Then, the mesh is evaluated at its nodes to determine if the interior cells should be subdivided. Such subdivision continues to some prescribed depth for refinement. An example of such a process is offered in Figure 6.1 where an FTLE field is computed at a resolution of 2048×2048 and, then, also adaptively computed. In the adaptively refined case, the grid is initiated with a resolution of 128×128 and the finer detail exhibits a resolution as in the fully computed case. The interior structure is noticeably preserved in the refined case, but the computation is reduced by 97%. Such a dramatic reduction in computational cost is a tremendous advantage if the particular case is amenable to such refinement. Frequently, however, flow fields display complexity throughout, and all features may be of interest. In such a case, AMR may not be as advantageous.

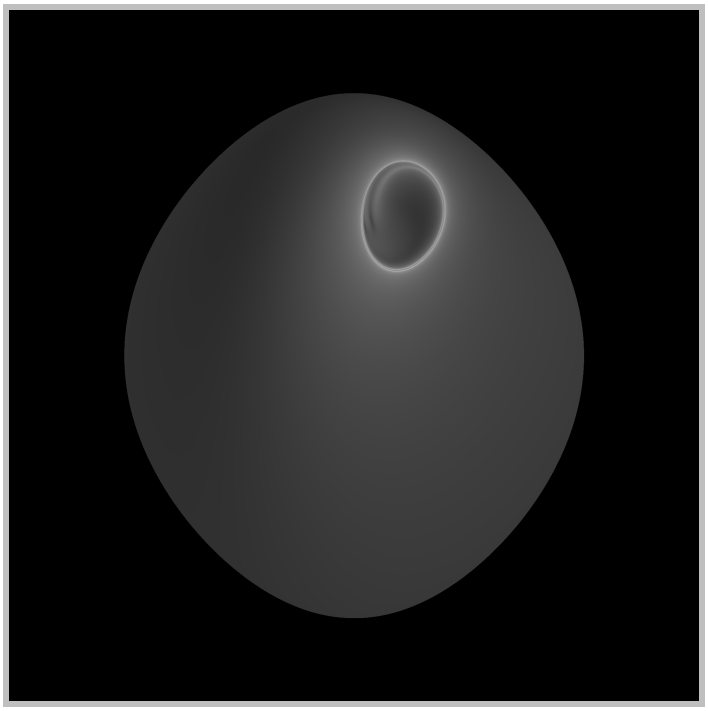

(a) Entire FTLE Field Computed (2048×2048)

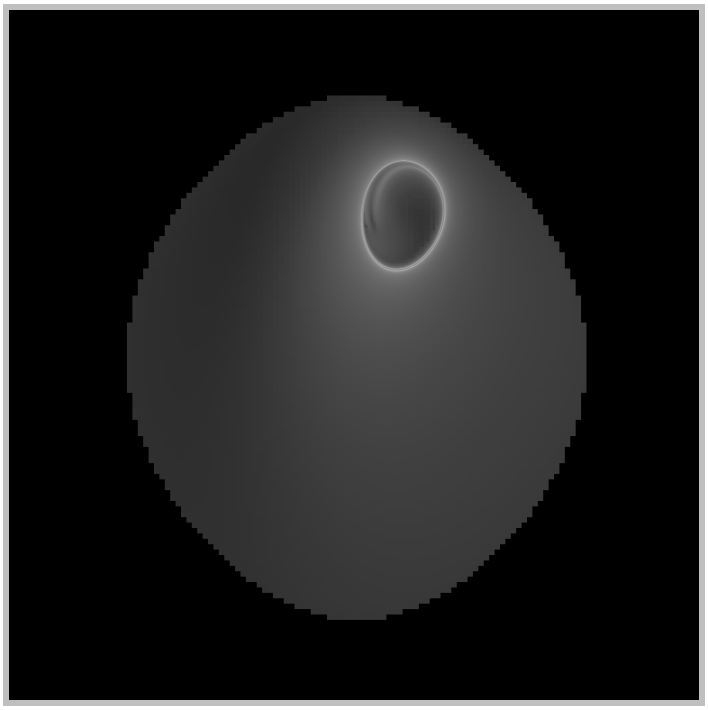

(b) Adaptively Computed FTLE Grid

Figure 6.1.: An Illustration of Adaptive Mesh Refinement

6.2.4 Point-wise Evaluation and Strainline Propagation

In the case where interpolation methods and advanced mesh strategies are insufficient to accurately identify flow features, another option may be available. Given a simulated nature of the underlying flow map, a point-wise evaluation of the flow may be possible. Consider a numerical integration "on the map", where Cauchy–Green metrics are available on a finite mesh. Strainlines will follow a vector field defined by particular operations on the metrics, all of which are available on the nodes or at refined map points. However, the strainlines will immediately depart from the nodes regardless of resolution upon numerical integration. It is observed that accurately refined points on the map can seed strainlines, and at each integration step across the map the new, required flow map information should be computed. Recall, from Section 5.2.2, that repelling strainlines are computed from the reduced $\hat{\boldsymbol{\xi}}_n$ field, which is defined only up to a sign. Further, the numerical propagation is accomplished by solving the differential equation parametrized by $\mathbf{r}$ for repelling strainlines [7, 8],

$$\frac{d}{ds}\mathbf{r}\left(s\right) = \text{sign}\left(\left\langle \hat{\boldsymbol{\xi}}_n\left(\mathbf{r}\left(s-\Delta\right)\right), \hat{\boldsymbol{\xi}}_n\left(\mathbf{r}\left(s\right)\right)\right\rangle\right)\hat{\boldsymbol{\xi}}_n\left(\mathbf{r}\left(s\right)\right) \tag{6.8}$$

Thus, the previous orientation of $\hat{\boldsymbol{\xi}}_n$ resolves any sign change in $\hat{\boldsymbol{\xi}}_n$ at the next time step. For each integration step, a new CG tensor should be evaluated as required. The process continues for each integration step until some prescribed final integration time (i.e., an nD arc length) is met. Such an approach often proves to be less computationally intensive than isolating structures through indeterminate ridge extractions.

6.2.5 Complex-step Differentiation

To obtain more precise results in a numerical process, often very small discrete steps are required. Such fine resolution considerations are somewhat related to the interpolation and mesh discussions above, but they also come into play in the context of finite-difference derivative approximations. In particular, some flow strategies require derivative calculations for points along a line that are separated by only a

very small perturbation (e.g., a difference on the order 10^{-12}). However, such a small separation raises issues associated with finite-differencing, where perturbations may be larger than the separation between neighbors. This may or may not cause numerical issues depending on the particular situation. Regardless, it is well known that the accuracy of finite-difference derivatives increases as the step size decreases until the step size becomes too small and truncation error overwhelms the numerical process. In these cases, an alternative option is available in the form of complex-step differentiation ([81], [91]). Complex-step derivatives work much like a finite-difference derivative such as the central difference derivative approximation,

$$f'(x) \approx \frac{f(x+h) - f(x-h)}{2h}, \tag{6.9}$$

where h is the step size. The approximation of the derivative, in the central difference case, reflects error on the order of h^2. In the complex-step derivative approximation an imaginary step is taken from a real-valued argument into complex space to approximate the derivative of the argument's function, and the approximation is given,

$$f'x \approx \frac{\mathrm{Im}\left(f(x+ih)\right)}{h} \tag{6.10}$$

where the error is again order h^2. However, the complex-step derivative calculation is not subject to truncation or cancellation error since the step is not taken with respect to the real argument. The limitation on accuracy due to the the step size h is now determined by the representation accuracy for the particular floating point type (not the machine epsilon). Consequently, the error associated with Equation 6.10 may be driven below machine precision by choosing a step, h, sufficiently small (for example, $h = 10^{-30}$). This comparison in accuracy is illustrated in Figure 6.2 reproduced from [91] with the publisher's permission. After a point, as the step size decreases, both central-difference and forward-difference errors begin to grow rather than shrink. Ultimately, the error dominates the numerical process. Rather, a sufficiently small step size drives the complex-step approximation error below machine precision. The complex-step differentiation option is a frequently convenient, and often required, tool for many numerical applications.

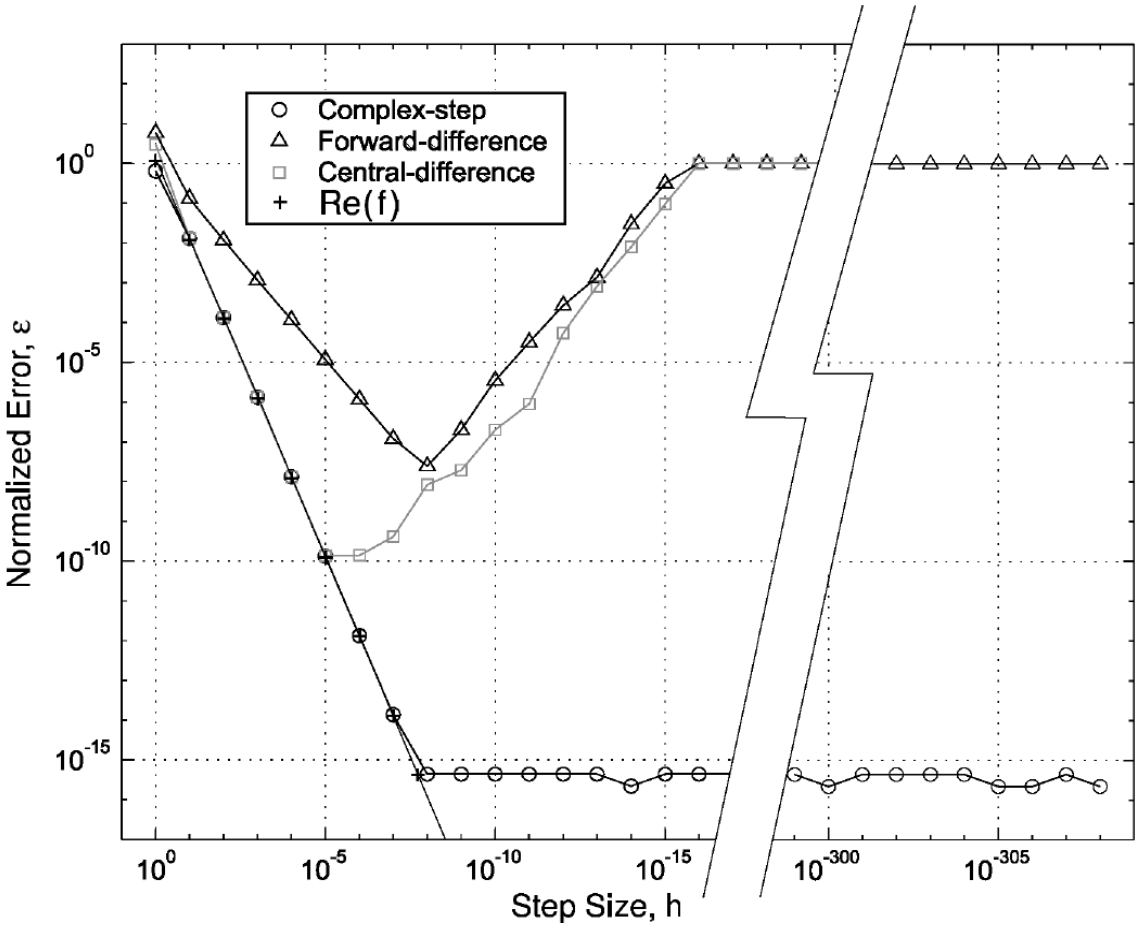

Figure 6.2.: Complex-Step Derivative and Finite-Difference Error Comparison, Reproduced from "Fig. 1 Relative error in the sensitivity estimates given by the finite-difference and the complex-step methods using the analytic result as the reference; $\epsilon = \left|f' - f'_{ref}\right| / \left|f'_{ref}\right|$" of [91] `http://doi.acm.org/10.1145/838250.838251`

6.2.6 Parallel Implementations

The isolation of flow behaviors in a complex system requires some knowledge of particle evolution through the system. This knowledge may be gained by empirical observation or through computational modeling. The computational simulation approach is particularly applicable within an astrodynamical context where the flow induced by interacting gravitational fields or other perturbing forces may be difficult to simulate physically. Thus, significant numerical integration is frequently required to capture flow behaviors. Fortunately, such a process is inherently independent where one trajectory may be simulated apart from its neighbors. This independence gives rise to a propensity for parallel computation.

Many strategies exist for parallel computing. Shared memory and distributed computing options are two possibilities that have seen extensive application for trajectory simulation. For example, shared memory, single node parallelization on multiprocessing core systems may be accomplished using a computing library such as the OpenMP (Open Multi-Processing) Application Programming Interface (API) [92] while multi-node distributed computing can be accomplished using Open MPI (Message Passing Interface) [93]. Both of these options are suitable in different situations depending on the scale or nature of the parallelization. Yet another option, potentially more suitable for single-user interactive investigations, is parallelization on the Graphics Processing Unit (GPU). Each of these options is viable for everyday use in scientific investigations and has been exploited to address the extensive numerical requirements of flow-based analysis in astrodynamics.

A particular example that illustrates parallel computation is represented by Figure 6.3. Illustrated is a surface computed as an isosurface extraction from a 3D volume of FTLE data associated with the four-body dynamics near a moon in a particular system. Following the initial criteria for identifying flow-structures, a threshold is selected for high relative FTLE values, and points on the grid with values larger than the threshold are used to construct the isosurface. For the underlying com-

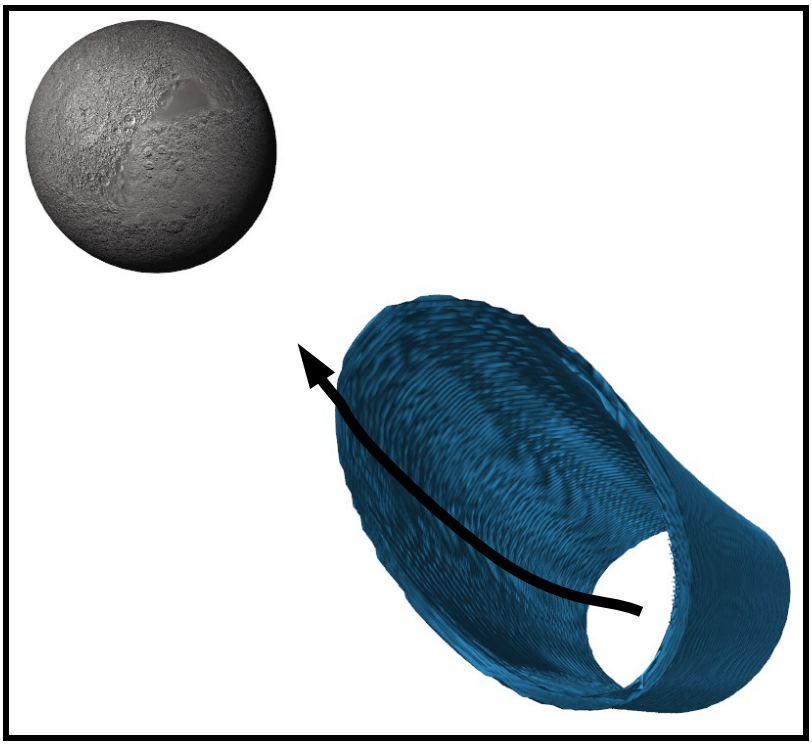

(a) Flow Toward a Moon: Isosurfaces of FTLE Data

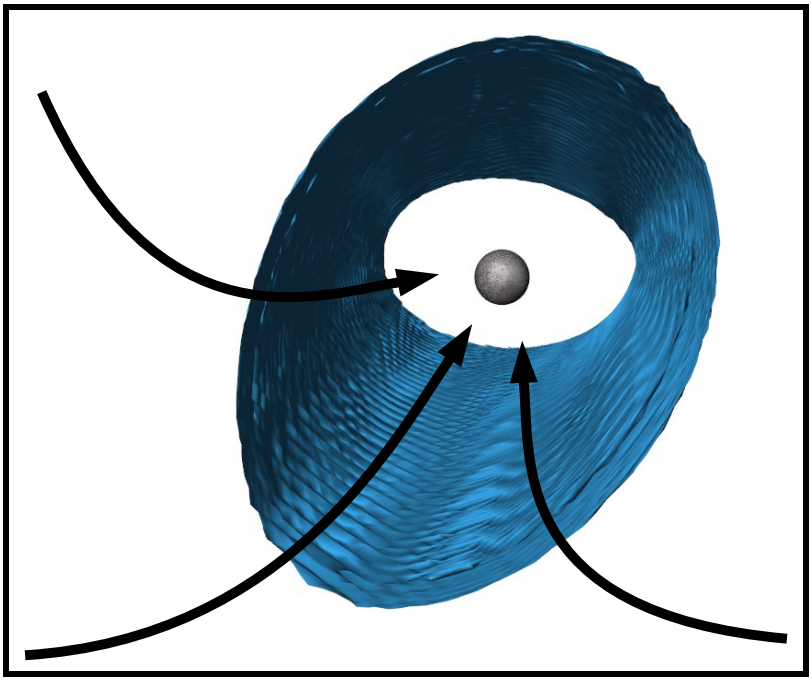

(b) Alternate View of (a)

Figure 6.3.: Views of a GPU Isolated Flow Surface

putations to produce the blue structure in the figure, a hybrid parallel approach is implemented as a test of concept. Initially, a coarse grid is employed to identify an effective step size in time. Then, a less complex numerical integrator, a Runge–Kutta 4^{th} order propagator with a fixed step size, is used to evaluate the dense grid on the GPU. Such an approach is employed to ensure accuracy for the calculations from the GPU and to take advantage of the GPU's strength in performing less complex mathematical operations with little branching logic. For this example, where minimal optimization of the numerical algorithm is made, a speed up of $\sim$100$\times$ over a serial CPU implementation is observed.

Each of the computational strategies discussed in this section apply to the various outlined challenges. Some, as indicated, supply options that address multiple issues while others only apply for isolated considerations. While each of the approaches corresponds to a varied breadth of application and efficacy, the combined repertoire represents a powerful tool set poised to face compelling problems.

7. APPLICATIONS

Flow-based strategies are emerging as effective tools in support of trajectory design and analysis activities. In more complex gravitational regimes, dynamical systems tools no longer apply directly. Under the dynamics of such systems, time-evolving barriers do exist and inspection of the flow can reveal these structure. For a given reference time, these flow-separating structures can be exploited in much the same way as the invariant manifolds in the CRP. The additional context and insight imparted from the flow can also help to establish optimal directions for desired behavior and illustrate system behavior. The following examples highlight some of the uses of flow-based methodologies in astrodynamics.

7.1 Model Fidelity Independence

A strategy of initiating an analysis from a well-defined CRP map, and successively increasing the fidelity of the model, illustrates the applicability of flow-based tools regardless of the model fidelity. Incorporating additional model components, one at a time, to form more complex models highlights the effects of the individual contributions to the behavior in a system. The example in this section centers on FTLE maps from the Earth–Moon circular restricted three-body problem. These maps are then transitioned into a four-body model that incorporates the gravitational attraction of the Sun on the spacecraft. They are also independently transitioned into an Earth–Moon–Sun ephemeris model that reflects the interactions of each of the gravitating bodies on the spacecraft as well as on each other. The ephemeris model also reflects all other external forces on the primary masses as it incorporates their motions from ephemeris solutions. The qualitative changes observed in the maps reveal the impact of individual masses on the flow.

7.1.1 LEO to the Map: 2BP

Transfers from LEO to the neighborhood of the cislunar (L_1) libration point involving manifold and "pseudo-manifold" arcs in the Earth–Moon system serve as specific examples of LCS applications. Many recent missions have involved revolutions in the vicinity of the libration points for phasing or other considerations. The objective of this example is to identify transfers from FTLE/LCS maps that result in a successful revolution about L_1 (indicating a potential for insertion into an orbit about L_1). A Hohmann-type transfer arc from LEO to the vicinity of the stable branch of a L_1 Lyapunov orbit manifold-crossing with the y axis in the CRP rotating frame is employed to establish this particular scenario. The CRP energy level is selected to be consistent with an L_1 gateway that is slightly open (as defined by the zero velocity curves), and an L_2 gateway that is closed.

The Hohmann transfer in this example is selected simply to result in a final state to compare with initial conditions in a scenario that illuminates the insight available from an FTLE mapping. The transfer arc is a two-body arc that departs a 300 km altitude low Earth orbit at perigee for a maneuver cost of slightly less than $3\frac{\text{km}}{\text{s}}$. The arc is constructed to specifically reach apogee at the y axis crossing in a rotating frame consistent with the CRP (i.e., $x = 0$). The LEO parking orbit (yellow) and the Hohmann arc are illustrated in Figure 7.1. In Figure 7.1, the magenta and blue arcs represent inertial and rotating views of the Hohmann arc, respectively. Green and red arrows indicate the y and x rotating axes (inertial axes are omitted). The rotating frame and the inertial frame are aligned such that the two frames coincide when the Hohmann arc reaches $x = 0$ as viewed by a rotating observer. The Hohmann arc is computed using two-body conic analysis, and this segment could be corrected in the restricted problem. However, such correction is not necessary for this example. The arc allows for a simple estimate of maneuver cost to depart LEO, and based on the resulting state at the manifold insertion point (i.e., at the $x = 0$ crossing) an estimate for a maneuver cost to insert onto a manifold structure.

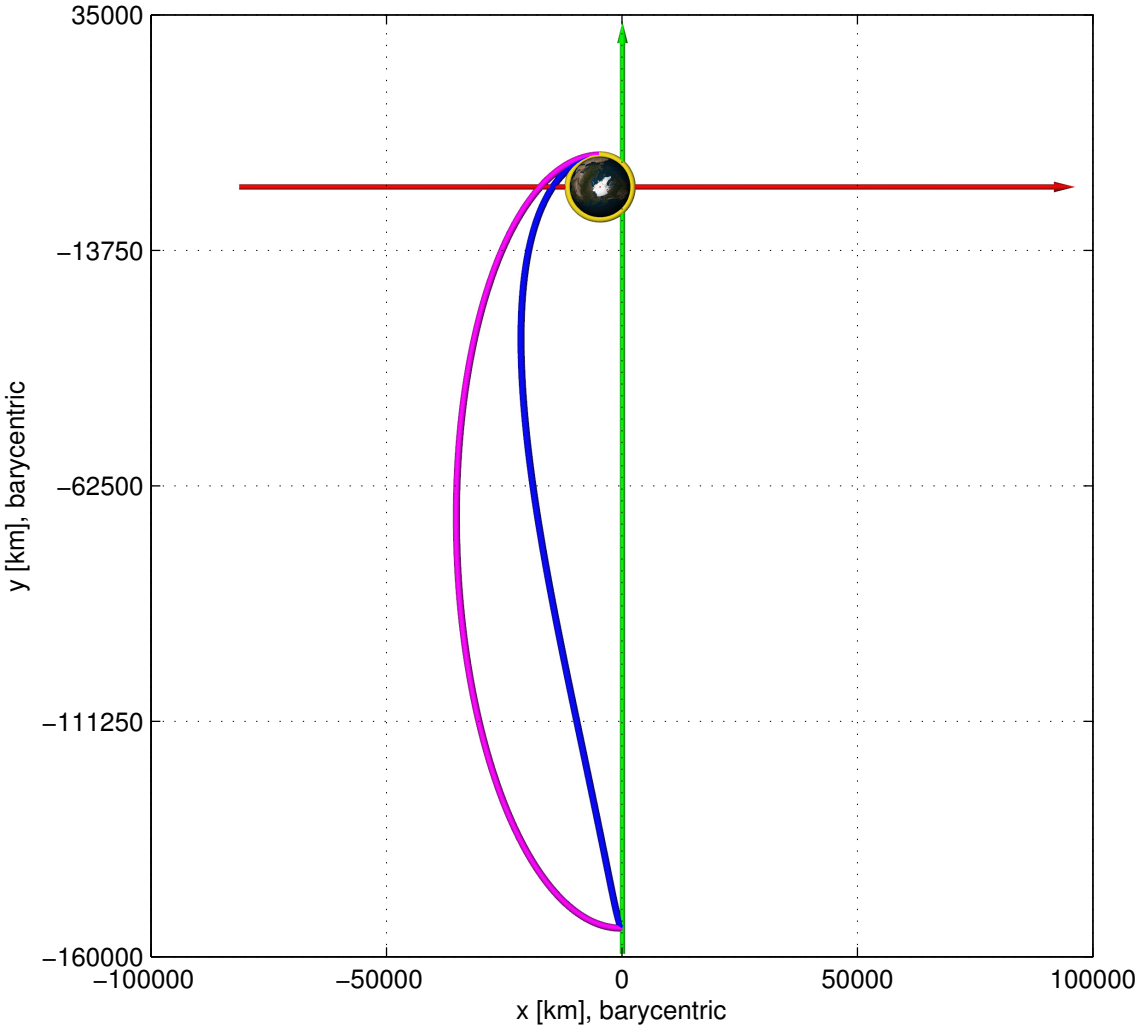

Figure 7.1.: Arcs from LEO to $\Sigma : x = 0$ (Magenta: Inertial, Blue: Rotating)

7.1.2 From the Map to L_1: CRP

Selection of an energy level in the CRP, consistent with an open L_1 gateway and an L_2 gateway that is closed, enables the computation of a periodic Lyapunov orbit about L_1 and the associated invariant manifolds. For the purposes of illustrating the map employed in this example, the P_1 branch of the stable manifold is depicted in configuration space in Figure 7.2. The surface of section in this example ranges from

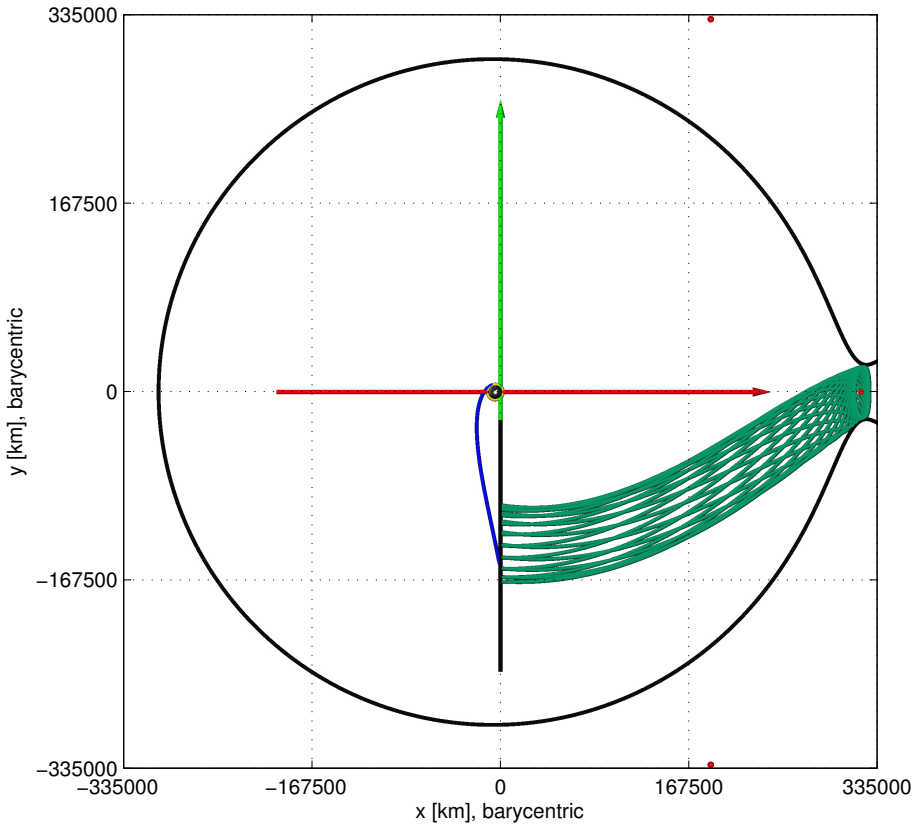

Figure 7.2.: P_1 Stable Manifold Branch for $C = C_{L_2}$

approximately $-250{,}000$ km to $-20{,}000$ km along the rotating y-axis and is colored black in Figure 7.2. Also included in the figure, for perspective, are the interior ZVC for this energy level (black contour) as well as the L_1, L_4 and L_5 libration points represented as the middle, upper and lower red spheres, respectively, near the edges of the frame. The transfer arc also appears in the rotating frame. The section for analysis

is selected as $x = 0$, $(-250112 < y < -19239)$ km, $(-0.9733 < \dot{y} < 0.5635)$ $\frac{\text{km}}{\text{s}}$ and $\dot{x}$ is recovered from $C = C_{L_2}$. However, many of the visuals are zoomed to $(-192,394 < y < -76,957.2)$ km, $(-0.5891 < \dot{y} < 0.1793)$ $\frac{\text{km}}{\text{s}}$, to focus on the structures of interest. Introducing the appropriate initial conditions, and allowing them to evolve forward in time for 3.5 nondimensional (nd) time steps (∼15.198 days) yields FTLE values consistent with Figure 7.3. The time parameter for FTLE calculations (3.5 nd) was selected consistent with the amount of time required for the emerging LCS to stabilize as identified by observation. This same time parameter is utilized for results from other models in this example as a basis for comparison. In Figure 7.3, as well as others, the FTLE value is indicated by the color bar near the top of the image. Central to Figure 7.3 is a curve with relatively higher FTLE

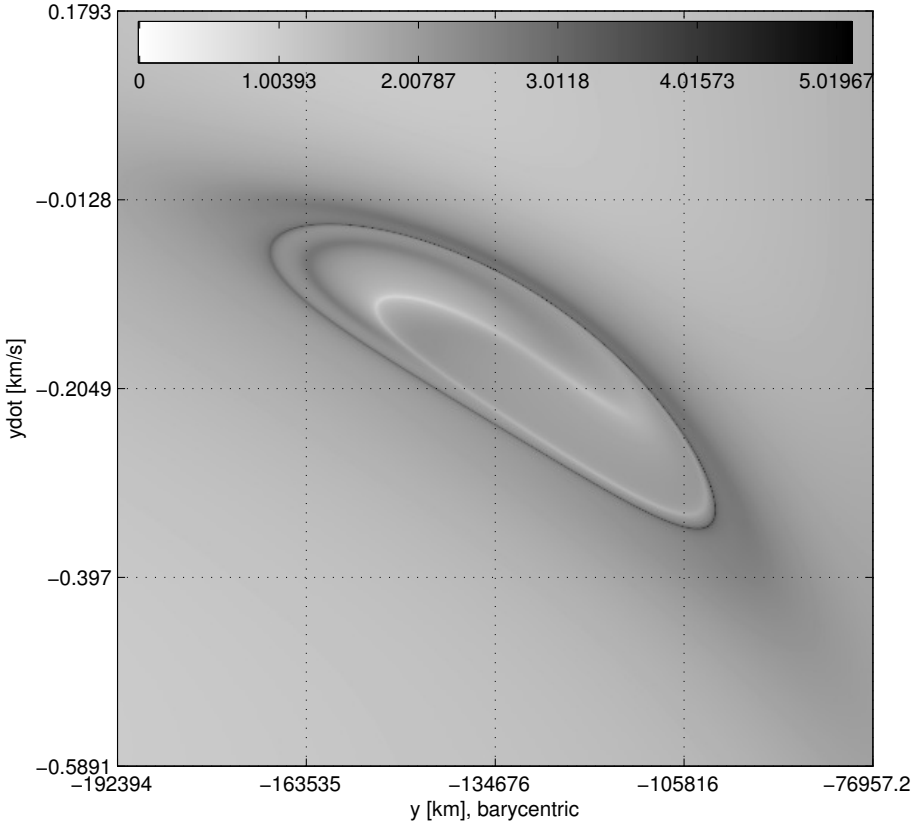

Figure 7.3.: FTLE for $C = C_{L_2}$ in the CRP

values along its edge. This contour corresponds to a Lagrangian coherent structure consistent with the interior, or P_1, branch of the stable manifold that flows into the Lyapunov orbit near L_1.

The state along the Hohmann arc as it terminates at $x = 0$ is projected onto the map from Figure 7.3. While the x, y and $\dot{y}$ components lie on the map, the $\dot{x}$ component from the arc is not constrained. From the position of the projected state on the map, it is observed that velocity adjustments in both components allow for insertion into two possible manifold trajectories. These two potential insertion points lie on the map where a transfer arc possesses the same y value as the manifold contour. These various options appear in Figure 7.4. The state marked in blue represents the

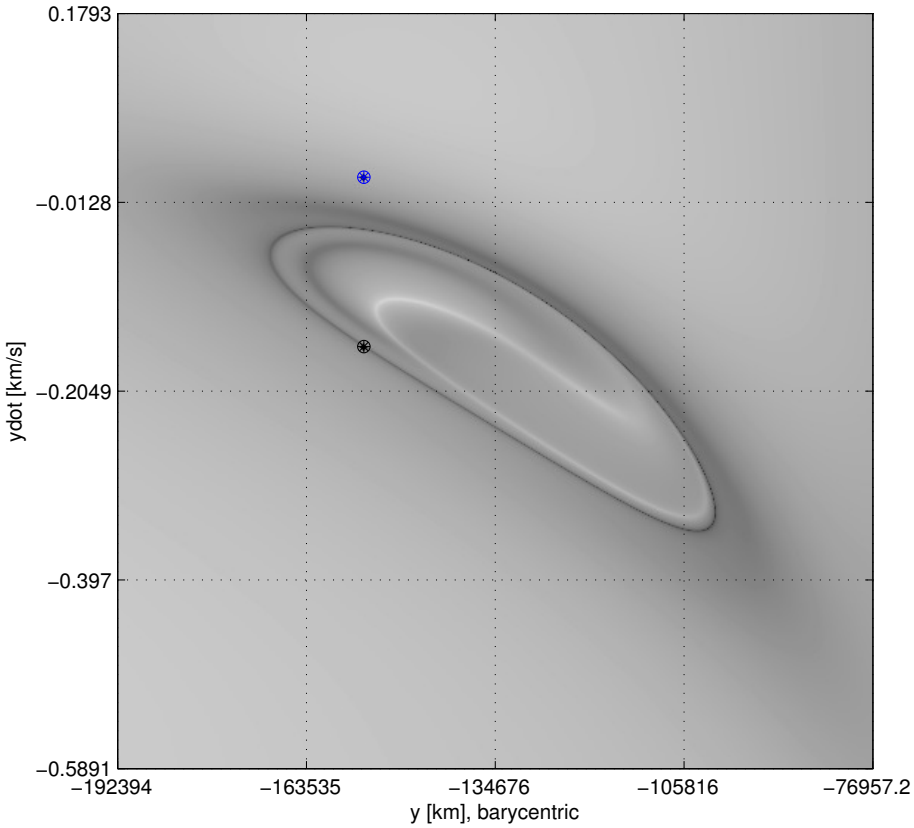

Figure 7.4.: Hohmann Projection & Selected Manifold

projection of the Hohmann arc state onto the map. Of the two insertion possibilities on the contour with the same y value, the lower $\dot{y}$ option is selected, marked black in

the figure. The two-body Hohmann arc allows for a rough estimate of the maneuver cost to insert onto the manifold arc in the CRP. In this scenario, the cost is computed,

$$|\Delta v| \approx \sqrt{\left(v_{x,m} - v_{x,h}\right)^2 + \left(v_{y,m} - v_{y,h}\right)^2} \tag{7.1}$$

or,

$$\begin{aligned} |\Delta v| &\approx \sqrt{\left(1.823 - 0.451\right)^2 + \left(-0.147 - 0.014\right)^2} \\ &= 1.373 \frac{\text{km}}{\text{s}} \end{aligned}$$

where subscripts $_{,m}$ and $_{,h}$ correspond to the manifold and Hohmann arc components, respectively. This maneuver cost, coupled with the LEO departure maneuver cost, together $\approx (1.4 + 3.0)\,\frac{\text{km}}{\text{s}}$, is reasonable given the assumptions made, and the consideration that no optimal solution is sought for this example.

The state selected from the map serves only as an approximation for the associated manifold trajectory since the resolution of the map is significantly larger than the precision required for actual manifold trajectories. Nevertheless, a very slight adjustment to the map state yields manifold-like results. In Figures 7.5 and 7.6, two trajectories selected from the map are plotted along with a state reflecting minimal, manual adjustment of the velocity. The two grid points that bound the adjusted state correspond to $\dot{y} \approx -0.1546$ nd (trajectory enters P_2 region) and $\dot{y} \approx -0.1561$ nd (trajectory does not enter P_2 region). Selecting $\dot{y} = -0.155$ produces the black trajectory with the desired behavior, that is, a revolution about L_1 resembling a Lyapunov orbit as is apparent in Figure 7.6.

Since the map resolution is relatively large (as compared to the level of accuracy required for manifold states), some correction is necessary to generate a better value for an insertion velocity state. However, in general, the map supplies a very good initial guess for the manifold. This insight is less critical in the CRP since alternate schemes/approaches are available to directly produce the manifolds. In contrast, for more complex models, the manifold-like structures are more obscure and information from the map helps to isolate them.

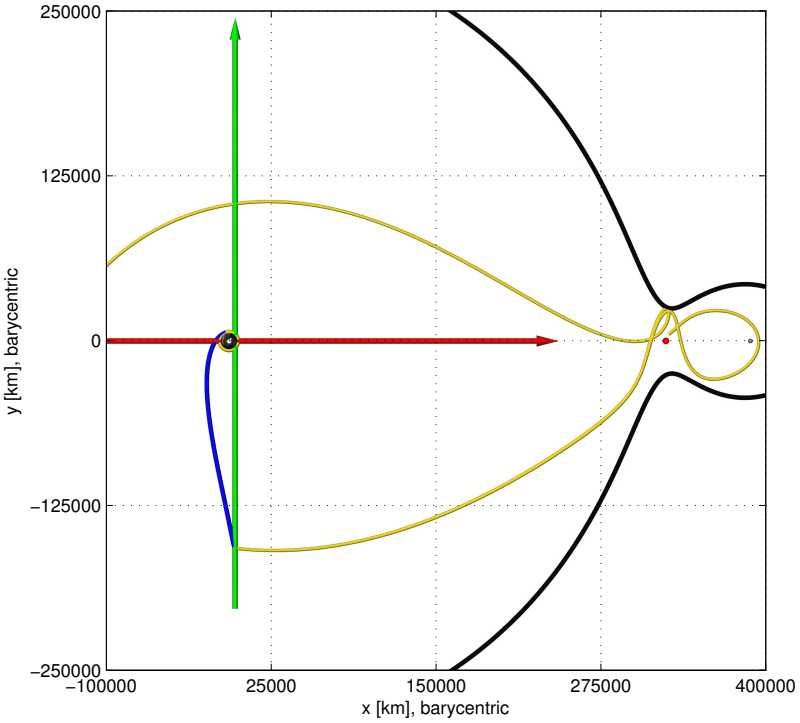

Figure 7.5.: Two Trajectories from Map States

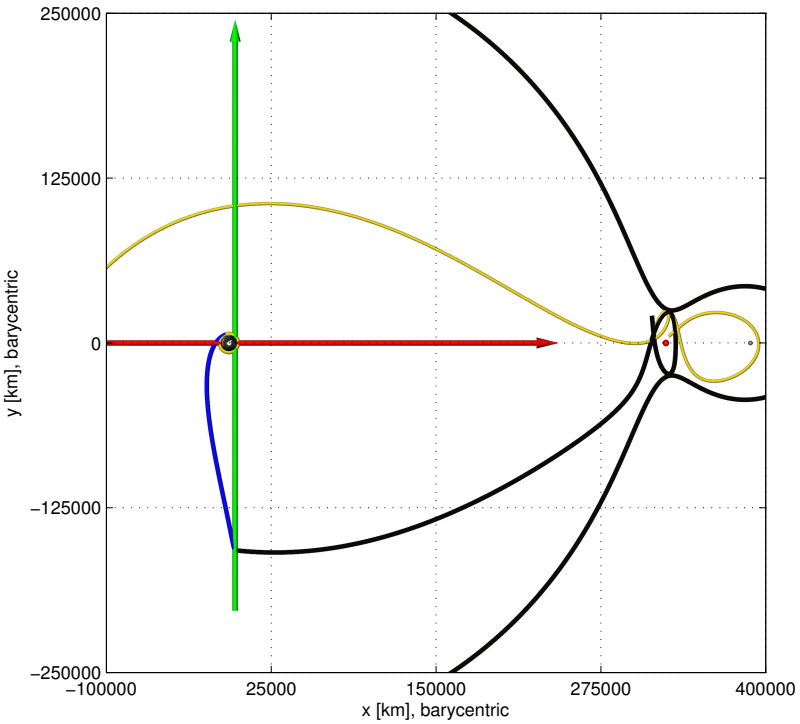

Figure 7.6.: Manually Adjusted Trajectory

7.1.3 From the Map to L_1: 4BP

The power of FTLE analysis lies in the ability to describe the flow in complex models. Transitioning the initial states associated with the map in the CRP into the bicircular four-body problem represents a first step towards using FTLE in a higher-fidelity astrodynamical context. Introducing the perturbing effect of the Sun's gravity on the CRP dynamics renders the resulting system nonautonomous. To demonstrate the applicability of the same FTLE tools, several maps are generated with varying initial Sun angles with respect to the Earth–Moon rotating frame. From the rotating frame perspective, the Sun revolves entirely about the Earth–Moon system in one synodic period of the Moon. Thus, the perturbation resulting from the addition of the Sun's gravity periodically repeats. Moreover, the Solar gravity effects on the trajectory arc for some initial angular offset essentially reflect across the origin. For example, an initial offset of 0.25π radians for the Sun's position with respect to the rotating x-axis will induce results that are similar to those that emerge if the initial offset is 1.25π radians. Thus, selecting initial offsets between 0 and π radians is sufficient for preliminary analysis. Considering the time frame in this example, $\sim$15.198 days, or roughly half of the synodic Earth–Moon period, a number of initial Sun angles should reveal different structures. For extended time frames in this model, despite the periodic nature of the perturbation, the effect of the *initial* Solar angle persists in the cumulative result. In Figures 7.7–7.9, different initial Sun angles morph the LCS in an FTLE map. For ease of comparison, differences are highlighted in Figure 7.10.

In an assessment of the bicircular four-body problem, over time scales of about 15 days, the Solar gravity does little to alter the structure qualitatively. However, to a small degree, the structures do shrink, grow, or translate along the "long axis" of the lobe described by the LCS. While these modifications are slight, they are significant since an initial state close to the manifold in the CRP would move further away from the corresponding structure in the 4BP. More precisely, the structures are shifted

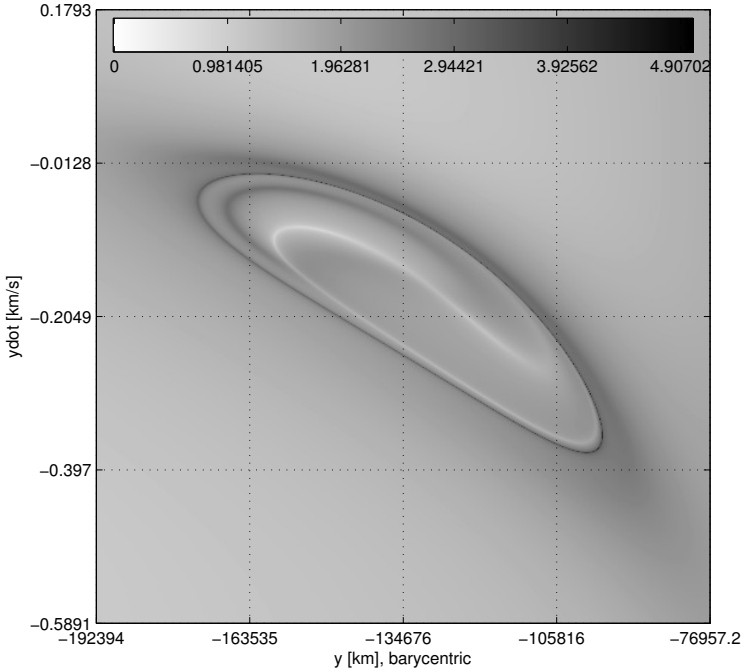

Figure 7.7.: FTLE for Initial Sun Angle: 0.25π

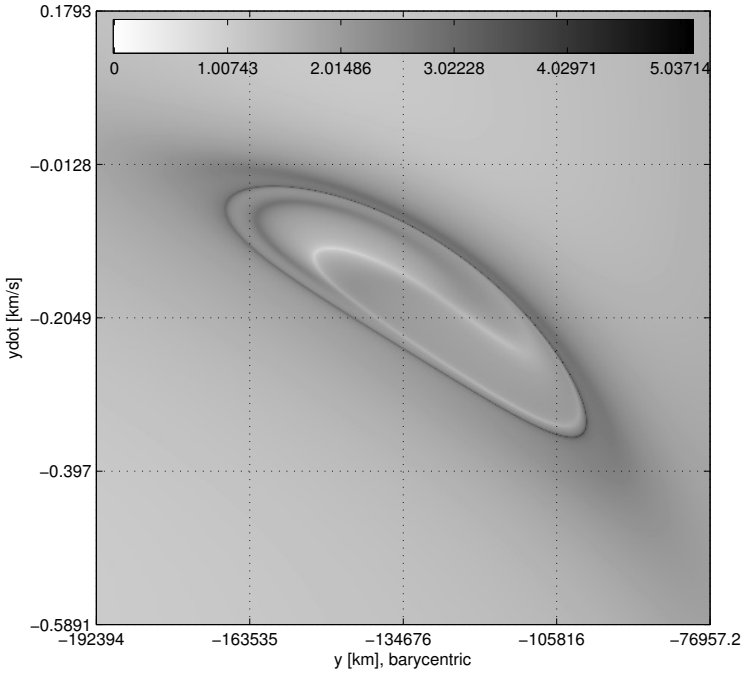

Figure 7.8.: FTLE for Initial Sun Angle: 0.50π

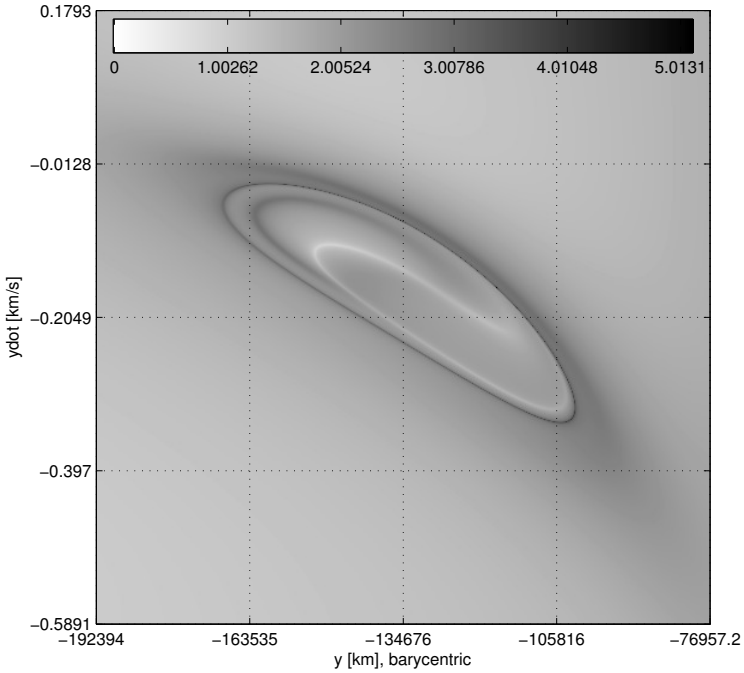

Figure 7.9.: FTLE for Initial Sun Angle: 0.75π

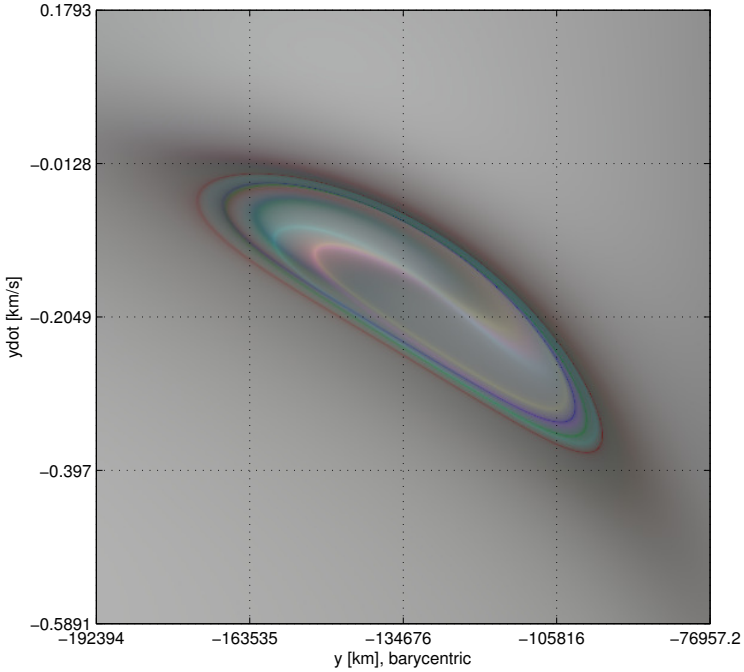

Figure 7.10.: Combined Sun Angles: 0.25π (red), 0.50π (green), 0.75π (blue)

between the two models. This displacement depends on the initial location of the Sun, and changes as the LCS evolve in time.

Comparison between the structures that appear under the CRP versus the 4BP, suggests an idea of the type of adjustment required, based on the initial Sun angle, to place the state on the four-body "manifold". Depicted in Figure 7.11, the difference between the CRP map in Figure 7.3 and the 0.25π 4BP map is apparent. The red contour is the LCS from the 4BP while the green contour is the structure from the CRP map. Propagating the initial conditions associated with the state marked in black in Figure 7.11 (i.e., the black trajectory from Figure 7.6) in the 4BP results in a trajectory that enters the P_2 region as illustrated by the red colored trajectory in Figure 7.12. The CRP arc is included, again in black, for comparison. Finally, selecting an alternative state directly from the map that lies near the 4BP contour (red marker in Figure 7.11) produces the red trajectory in Figure 7.13 (associated CRP evolution in black).

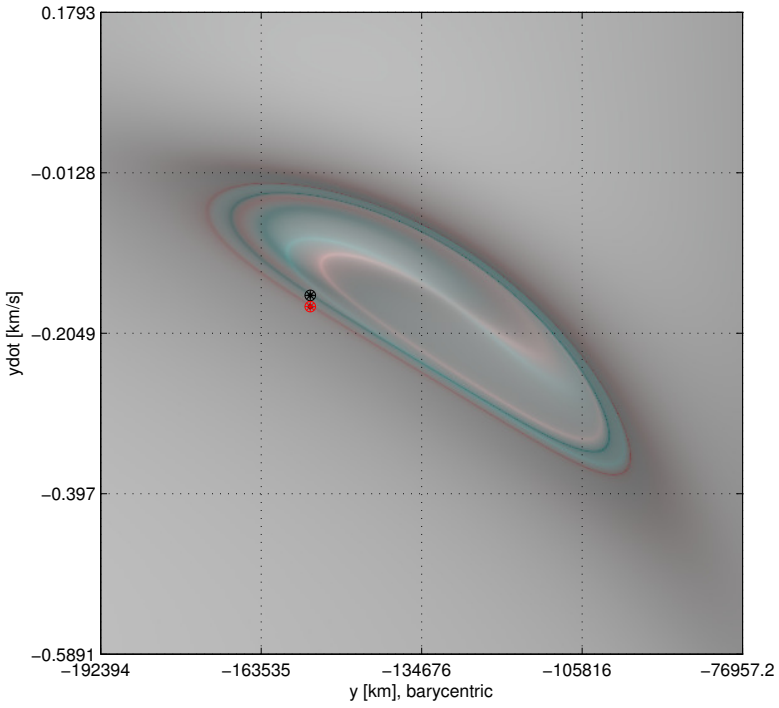

Figure 7.11.: CRP (green) vs. 0.25π 4BP (red)

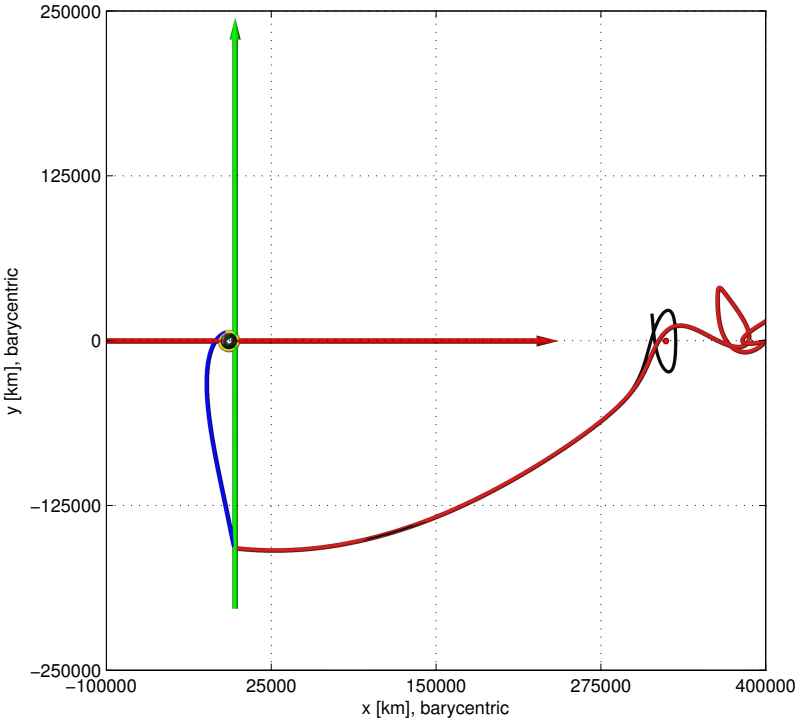

Figure 7.12.: CRP State Evolved in 4BP

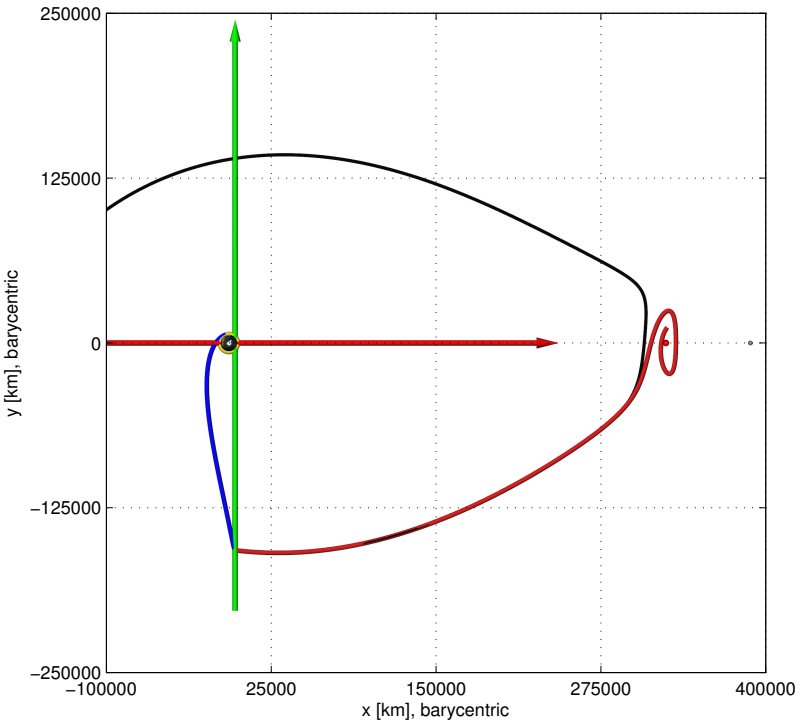

Figure 7.13.: 4BP Manifold Arc

The comparison between structures in the restricted problem and the bicircular problem demonstrates the use of a procedure for applying FTLE/LCS concepts in different models. The ability to visually identify features in the 4BP is encouraging since the structures themselves are not as readily calculable from the traditional methods applied to generate manifolds in the autonomous CRP. Additionally, in both cases, the flow behavior is characterized through the relatively simple computation of FTLE values. Investigation of FTLE maps and the underlying structures in the bicircular model provides an incremental step toward applying these tools in even more complex models and assists in establishing and verifying the conceptual progression between models. Further analysis in a higher-fidelity model solidifies the applicability of these methods in practical scenarios.

7.1.4 From the Map to L_1: MES

Transition to an ephemeris model, such as a Moon–Earth–Sun model using the n-body formulation described in Section 3.4, immediately introduces several new considerations. The previous models in this example involve a planar, four-dimensional state space. Since Solar System bodies move in all three spatial dimensions, the trajectories integrated to evaluate the FTLE now must also be evolved spatially (i.e., in all 6 dimensions of the state space). Fortunately, the formulation of the FTLE still applies directly since the value of interest, the eigenvalue associated with the direction of largest expansion, can still be calculated. Thus, transitioning from CRP to J2000 states for a particular epoch supplies initial conditions that are directly integrated using the relative equations of motion defined in Equation (3.7). Moreover, neighboring states integrated forward or backward in time still expand and contract with the flow as dictated by the dynamics. Thus, representing the FTLE on the same map space continues to apply. The process begins by transitioning a CRP state, and ends with the resulting FTLE value indicated by a colored pixel on the initial state coordinates of the map. The structures in the map are expected to shift for each different initial

epoch. In Figure 7.14, maps of FTLE values are again represented on the section previously defined, but zoomed out to its full extent. The epochs associated with the maps in the sequence progress down the first column and then down the second column. Initial dates for integrating the field were selected about August 1, 2012 at 00:00:00 UTC. Thus, referencing from the upper left corner of the figure, the initial epochs range from July 27 through August 5 in the bottom right corner (all starting at 00:00:00 UTC). The lower left corner in each frame of the figure reflects a region beyond the CRP zero velocity curves in y–$\dot{y}$ space. Thus, this region is empty of FTLE values.

As is apparent from the ephemeris sequence in Figure 7.14, there are some dates for which the structures of interest do not appear and others for which the structures no longer form closed contours on the map. Comparing the map for a selected ephemeris epoch with the maps constructed in the CRP and the 4BP illustrates the similarities to the maps developed in the previous models. The view in Figure 7.15 is consistent with the map in the restricted problem for $C = C_{L_2}$, and with the map in the bicircular problem for an initial Solar offset of 0.25π, as well as the resulting ephemeris map for the epoch August 1, 2012 at 00:00:00 UTC. The CRP structures appear in green and the 4BP structures are colored red. The new ephemeris map information appears in blue where blue levels have been slightly enhanced for clarity. The position/velocity states of interest are again marked with different colors. As before, the state corresponding to the trajectory from the model for the restricted problem is marked in black and the state associated with the 4BP trajectory is marked red. The state employed in the subsequent ephemeris propagation appears as well, with a blue marking. Taking state vectors directly from the grid near the ephemeris structure and evolving them forward in time produces the tan arcs depicted in Figure 7.16. The arc that continues towards P_2 results from an initial state with $\dot{y} \approx -0.1868$ nd, while the arc that revolves about L_1 and presumably returns to the P_1 region originates from a state with $\dot{y} \approx -0.1883$ nd. Next, in Figure 7.17, a manually adjusted trajectory with initial $\dot{y} = -0.18809$ appears colored in blue. As was observed when transitioning

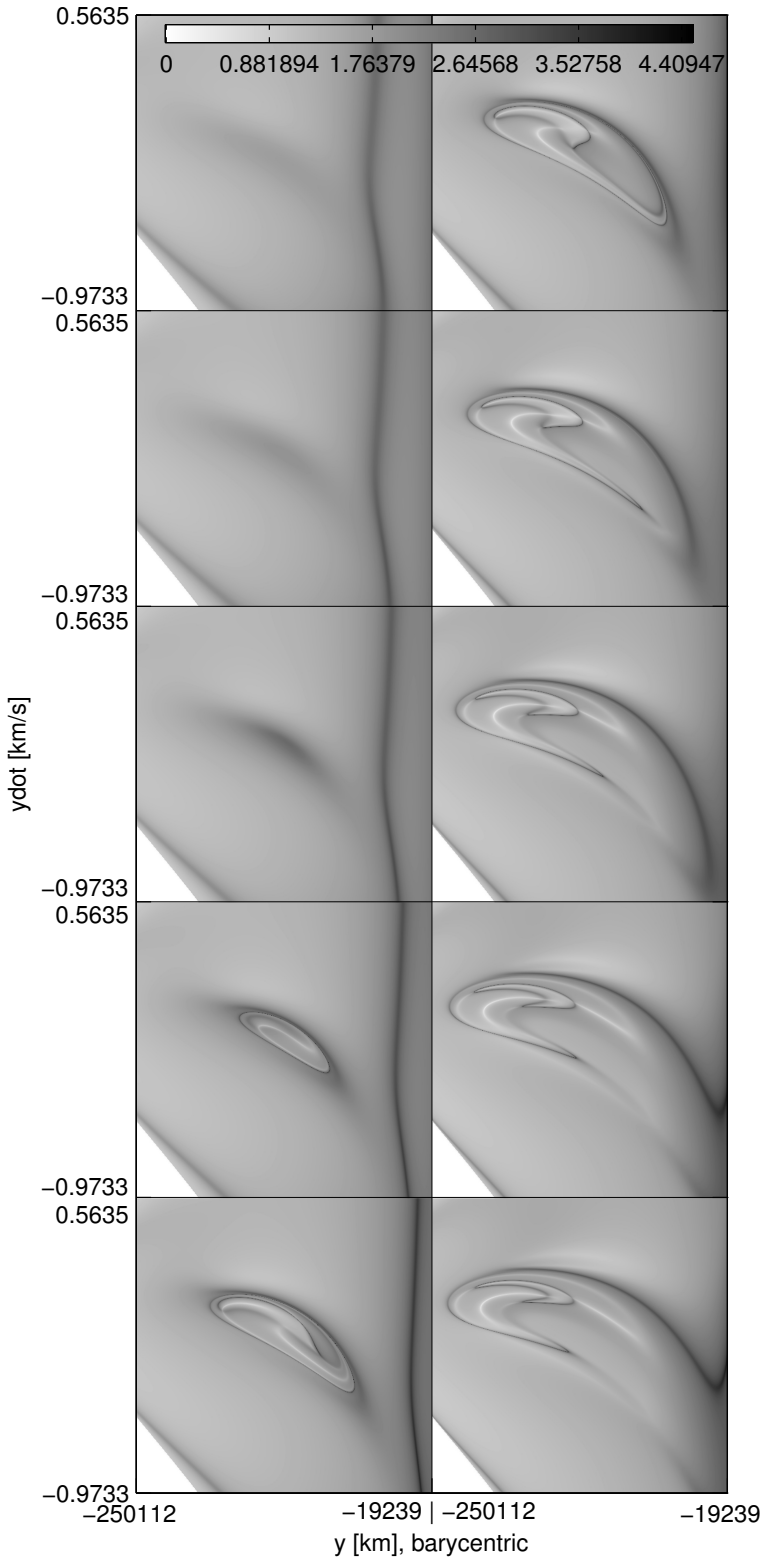

Figure 7.14.: July 27 – August 5 Ephemeris FTLE

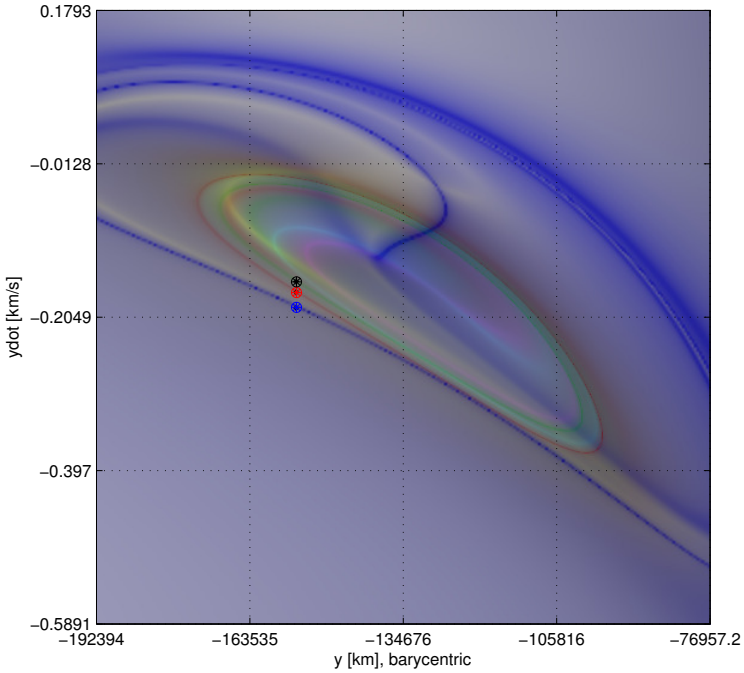

Figure 7.15.: CRP C_{L_2} (green), 4BP $\theta_0 = 0.25\pi$ (red), MES Aug. 1, 2012 (blue)

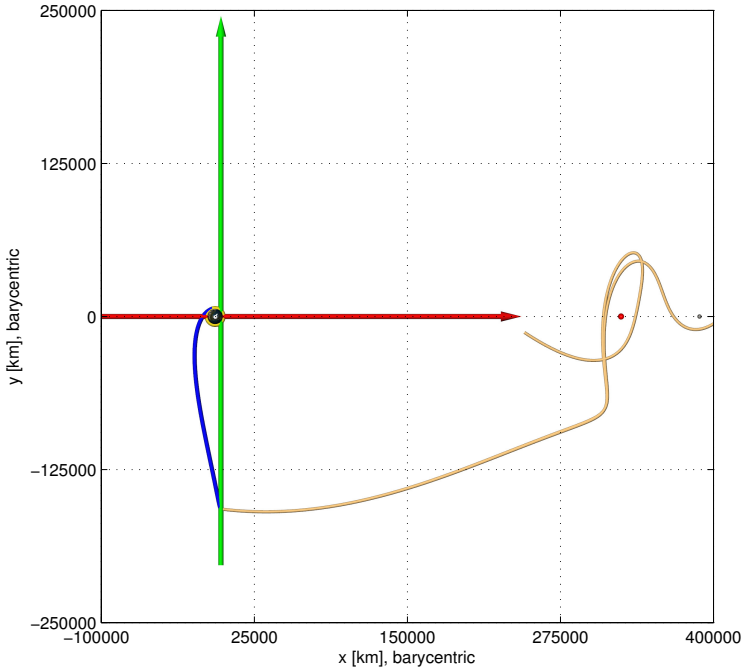

Figure 7.16.: Two Ephemeris Trajectories from the Map

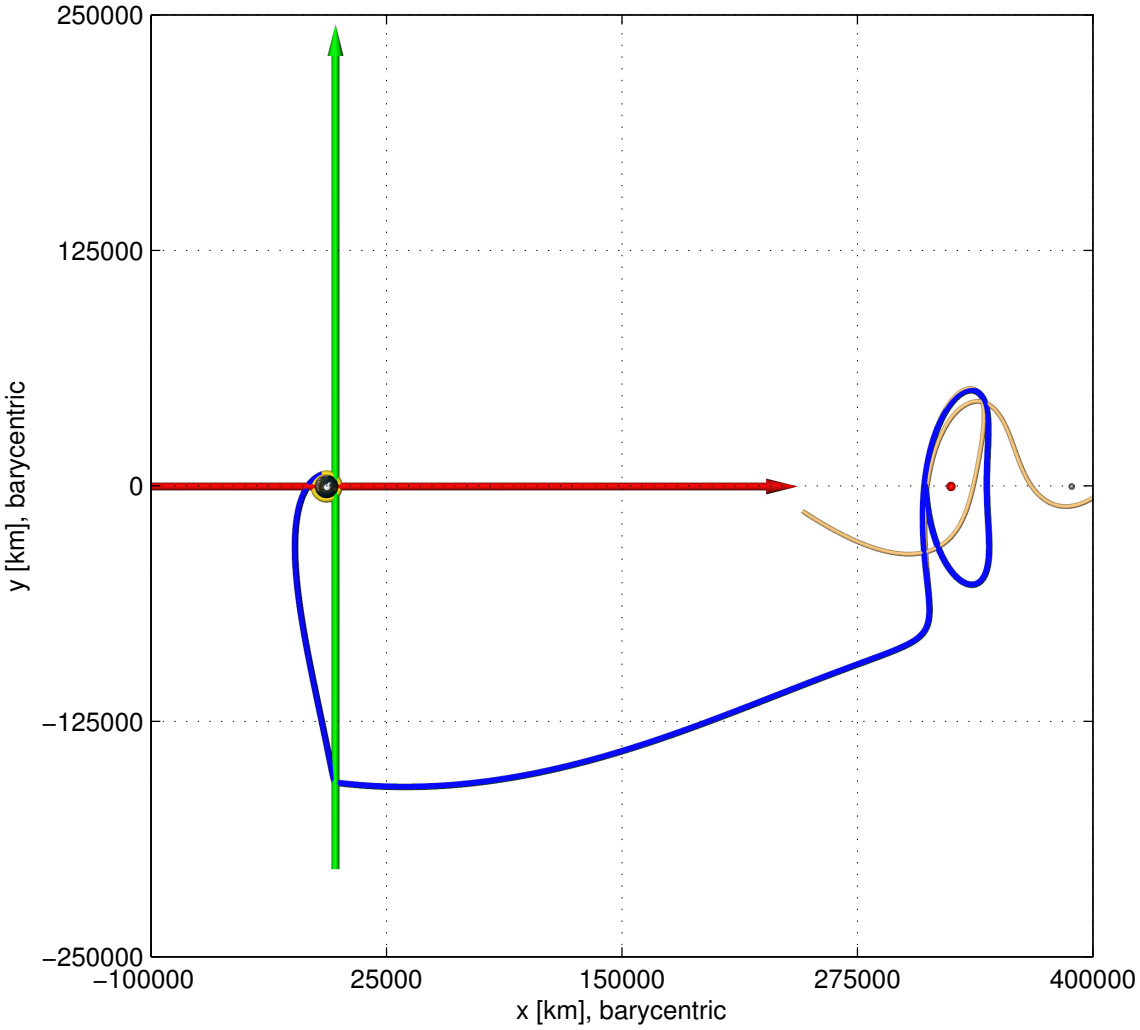

Figure 7.17.: Manually Adjusted Ephemeris Trajectory

from the restricted problem to the bicircular problem, the maps from the ephemeris propagations and the associated LCS offer good estimates for (1) the locations for the likely existence of potentially useful, or (2) the existence of any, manifold-like arcs for particular conditions. Moreover, the ephemeris maps supply predictive information that is valuable in a design scenario. The fact that, for a given CRP energy level, ephemeris "manifolds" may not exist for a particular epoch, or that these structures may possess a significantly different qualitative nature is useful. Such observations illustrate how maps of FTLE values yield significant insight in complex models.

Comparing maps of FTLE across different models supplies significant insight into the flow similarities and differences under the models. Additionally, such a comparison highlights the magnitude of various effects. In the bicircular problem, it is apparent that the gravitational perturbation from the Sun over time scales consistent with this analysis, while significant, does little to alter the qualitative nature of the structures appearing in FTLE maps. In scenarios where non-Keplerian gravitational sources are present, it is apparent that the initial epoch can impact the dynamical structure significantly. These types of comparisons can offer dynamical context for design and yield more understanding of the nature of the flow.

7.2 FCS Targeting

The forward and backward time-advection of small segments bracketing a control point, denoted control segments, is investigated by Shinbrot et al. [41], further expanded by Schroer and Ott [42] and revisited by Grebow [43]. These control segments are created as small segments along a particular velocity component without consideration of the underlying flow behavior. This initialization approach is a consequence of the desire to vary velocity only in a "feasible" direction while restricting any variation in initial or final position to zero. However, small adjustments in the direction of the phase space that naturally leads toward greater flow divergence augment the approach of joining forward and backward segments. This produces a trajectory that can subsequently be corrected with a differential corrections scheme. Thus, control segments constructed exploiting the flow context may yield a better result depending on the desired characteristics.

7.2.1 Comparing Control Segments Using Flow-based Context

Schroer and Ott produce an example to illustrate forward-time control segment advection and backward-time target region advection to join two periodic orbits in the Earth–Moon circular restricted three-body problem. In the following example, the mass-parameter and energy levels are consistent with Schroer and Ott ($\mu = 0.0123$, and $C = 3.17948$). The initial and final periodic orbits are generated numerically after observation of the trajectory characteristics as elaborated by Grebow. The following orbits and the associated map representations compare closely with Grebow. The initial orbit, in this case, is a period-3 orbit and is depicted in green in Figure 7.18(a), along with the final orbit about the Moon (red). The initial points on both orbits are marked with black arrows near the x axis; the forward time evolution from both points is in the positive y direction. Moreover, the trajectories are subsequently represented as fixed points (both numbered as iteration "0" for their propagations) on the x–$\dot{x}$ phase-space Poincaré map in Figure 7.18(b). From the control points on the map,

small segments (magnitude 1×10^{-4}) are created along the map-space components of the eigenvector associated with the largest eigenvalue of the Cauchy–Green tensor, that is, along $\boldsymbol{\xi}_2$, in this case. These segments are, in fact, stretchlines that are used as control segments, and are termed *Flow Control Segments* (FCS) given their incorporation of the flow behavior. The CGST is computed only with respect to the map via finite-difference derivatives in x and $\dot{x}$ for this case. The integration time for the Cauchy–Green tensor is generally selected as appropriate for the time scale of the application. For this example, it is observed that the time to reach the first crossing of the map is sufficient to yield predictive CG eigenvectors. The control segments are evolved under the flow of the system backward and forward in time from the lunar-proximal control point and triply-periodic control point, respectively. For comparison with the previous investigations of this specific example, segments along only $\dot{x}$ as well as a segment defined as a circle about the control point near the Moon are also integrated. The images of each of these curve evolutions corresponding to iterations of the map also appear in Figure 7.18(b). The curves are colored based on their initial nature: green curves result from advection of purely $\dot{x}$ segments, red and blue curves from the $\boldsymbol{\xi}_2$-aligned FCS and, in the case of the circular target region, black points mark the associated curves. Observation of the initial backward iterations of the circular target region reveals that it quickly deforms to align with the flow control segment, a fact that is exploited to verify the CG integration time in this case—if the circular region deforms to conform with images of $\boldsymbol{\xi}_2$, the time scale is appropriate. Later iterations in both time directions reflect longer curves associated with the flow-aligned control segments; the green points resulting from the initial $\dot{x}$ segments require additional iterations before an intersection is observed. Also marked on Figure 7.18(b) are the map crossings associated with trajectory arcs that intersect after 14 forward iterations from a perturbation off the triply-periodic orbit and 8 backward iterations from the lunar orbit step-off.

The trajectory arcs necessarily include discontinuities at the departure and arrival points. Since perturbations are introduced along the eigendirection, these discontinu-

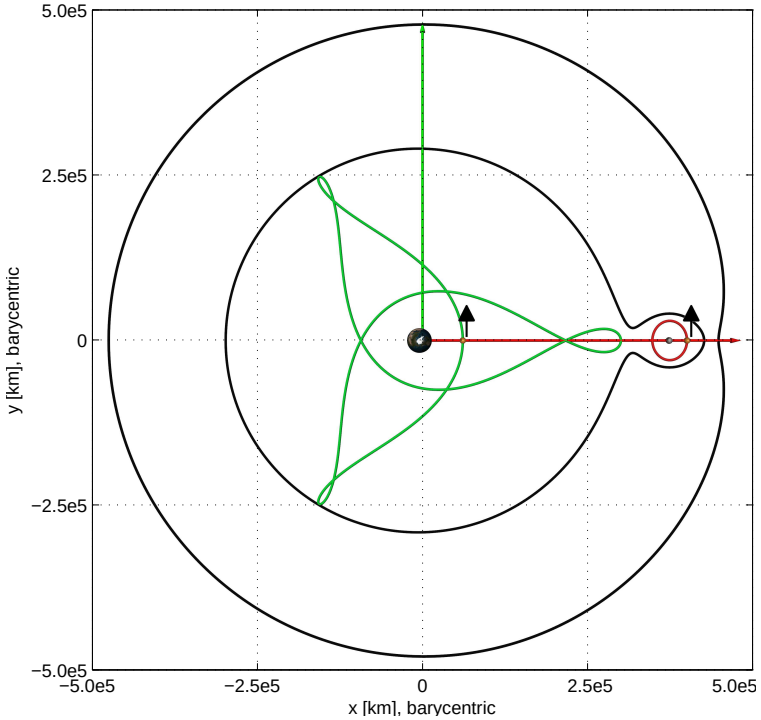

(a) Candidate Orbits for Connection

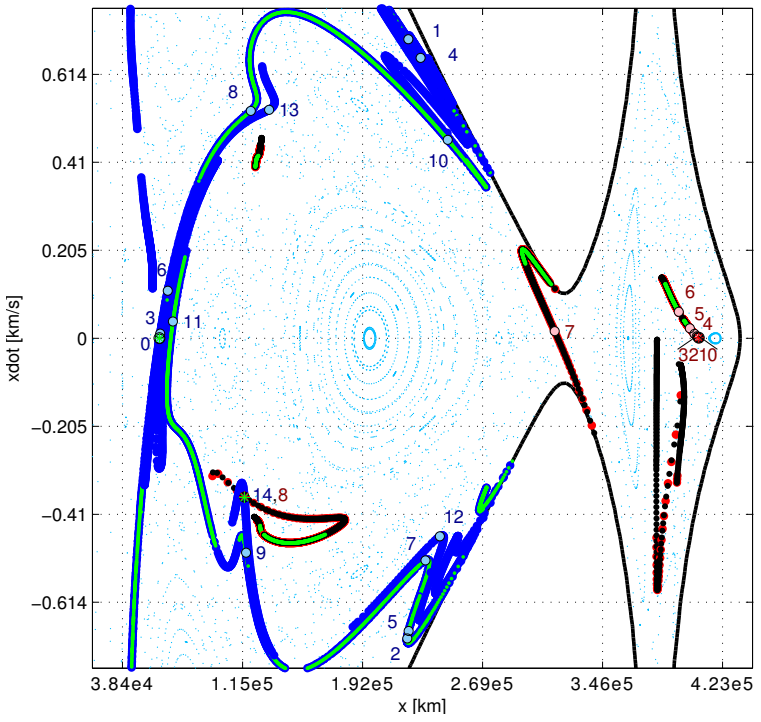

(b) Control Segment Images on x–$\dot{x}$ Section

Figure 7.18.: Orbits and Control Segments

ities are in position as well as velocity. Rather than employ an iterative scheme such as bisection to refine the intersection between the forward and backward arcs, a discontinuity is allowed at this point. These discontinuities are resolved by implementing a parallel shooting differential corrections scheme as described in [94]. Upon convergence of the corrections process, the only remaining discontinuities are the requisite velocity changes to render the transfer. Figure 7.19 includes views of the backward arc and the differentially corrected CRP solution. The connection point is visible where the backward propagation meets the x axis ($x \approx 100{,}000$ km). The trajectory evolution in time is reflected in color by a gradual transition from green to red. The maneuver requirement at departure is 1.99 $\frac{\text{m}}{\text{s}}$, while the Δv upon arrival is 1.04 $\frac{\text{m}}{\text{s}}$ (total: 3.03 $\frac{\text{m}}{\text{s}}$). These maneuver costs compare with an example from Schroer and Ott at 0.62 $\frac{\text{m}}{\text{s}}$ and 2.61 $\frac{\text{m}}{\text{s}}$, respectively, for a total of 3.23 $\frac{\text{m}}{\text{s}}$. They likewise compare with figures reported by Grebow for a somewhat qualitatively different solution—0.39 $\frac{\text{m}}{\text{s}}$ and 1.46 $\frac{\text{m}}{\text{s}}$ (total: 1.85 $\frac{\text{m}}{\text{s}}$). A significant difference, and potential advantage of the FCS approach, is a shorter time-of-flight. Each example reported in previous references requires more than 290 days; the sample transfer here is completed in 265 days. This shorter duration is a direct consequence of a path that reaches an intersection in fewer iterations given maximal stretching from $\boldsymbol{\xi}_2$-aligned FCS.

The solution is validated in a more complete model. For a carefully selected initial epoch, the CRP solution is transitioned into the higher-fidelity ephemeris n-body model. Views of the transitioned solution appear in Figure 7.20; the states are numerically corrected for velocity and position continuity to within $3{\times}10^{-6}$ $\frac{\text{m}}{\text{s}}$ and 0.8 m, respectively. The ephemeris solution necessarily experiences fully three-dimensional motion with maximum out-of-plane excursions greater than 2000 km. The convergence of the solution in the higher-fidelity model lends support to the process of seeking solutions by perturbing in position space as well as velocity space. Not only can the relatively complex solution be corrected in the simplified three-body model, but it can also be replicated in a system that mimics the actual three-dimensional behavior of the primary bodies.

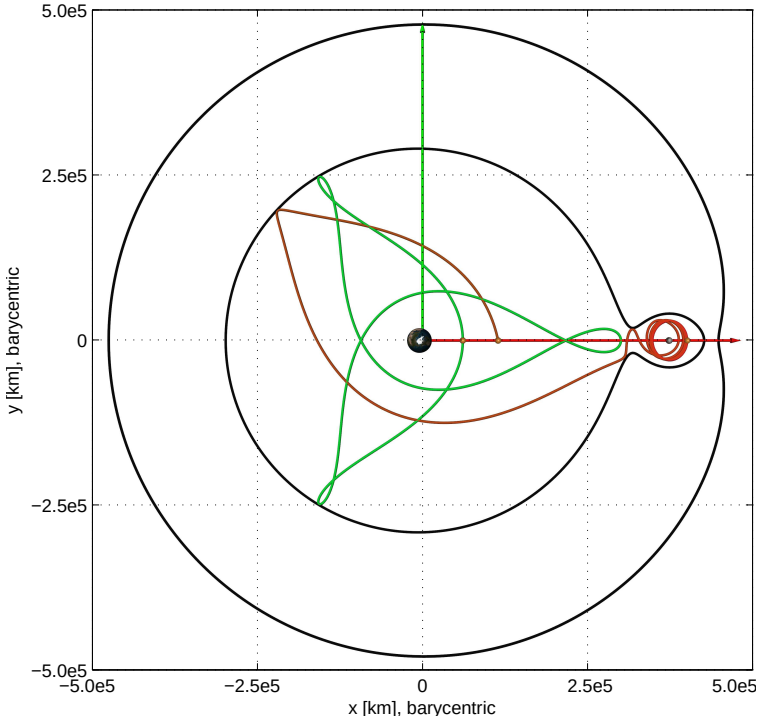

(a) Backward Trajectory Arc

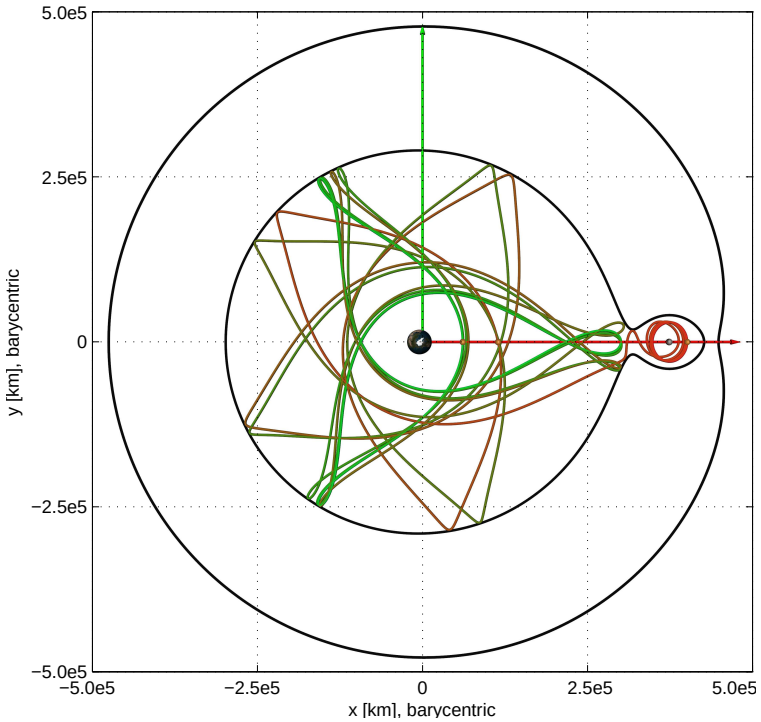

(b) Corrected CRP Solution

Figure 7.19.: Connected Forward and Backward Segments

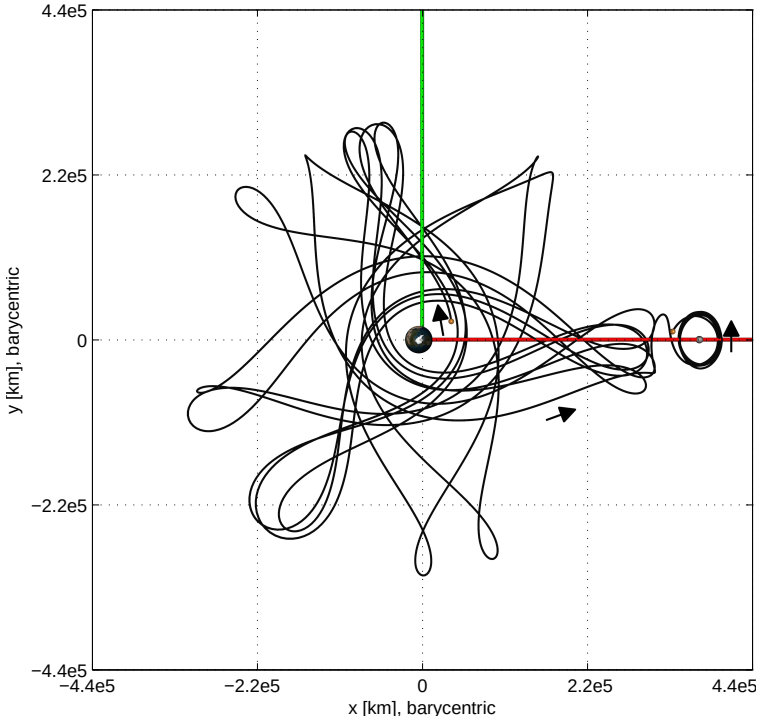

(a) Rotating View

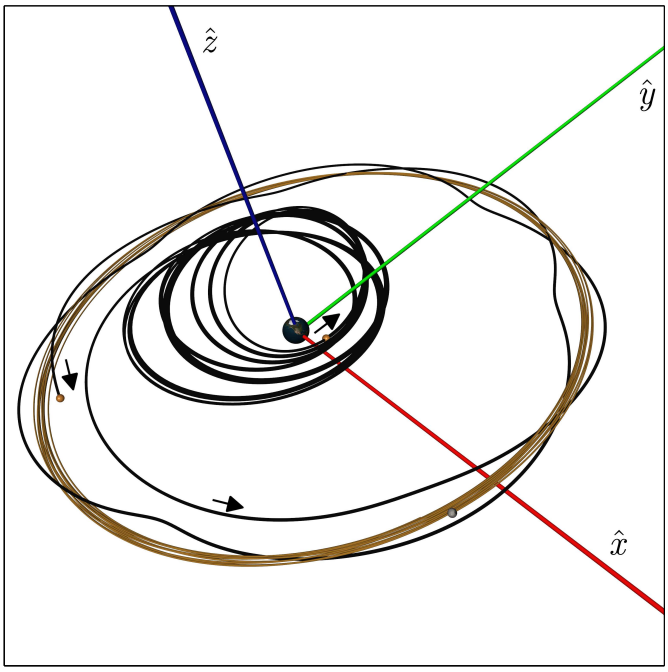

(b) Inertial View

Figure 7.20.: Corrected Ephemeris Solution

7.2.2 A More General Case

Before leaving the three-body problem as the primary model for analysis, another example serves to further reinforce the extensibility and flexibility of the flow control segment approach for identifying transfer trajectories. In this case, still in the Earth–Moon CRP, the system energy level is increased as reflected by a smaller Jacobi constant value of $C = 3.05$. Given this energy value, both the gateway allowing passage into the lunar region as well as the gateway offering exit from the system are open. That is, trajectories can transit through both the L_1 and L_2 regions. Consequently, the chaoticity of the resulting map space is increased.

To illustrate the continued applicability of the control segment approach, two map points are selected arbitrarily as control points for this example. These points are marked as "0" in Figure 7.21. In this case, there are no initial or terminal orbits, but rather the situation reflects the general notion of a spacecraft currently at some

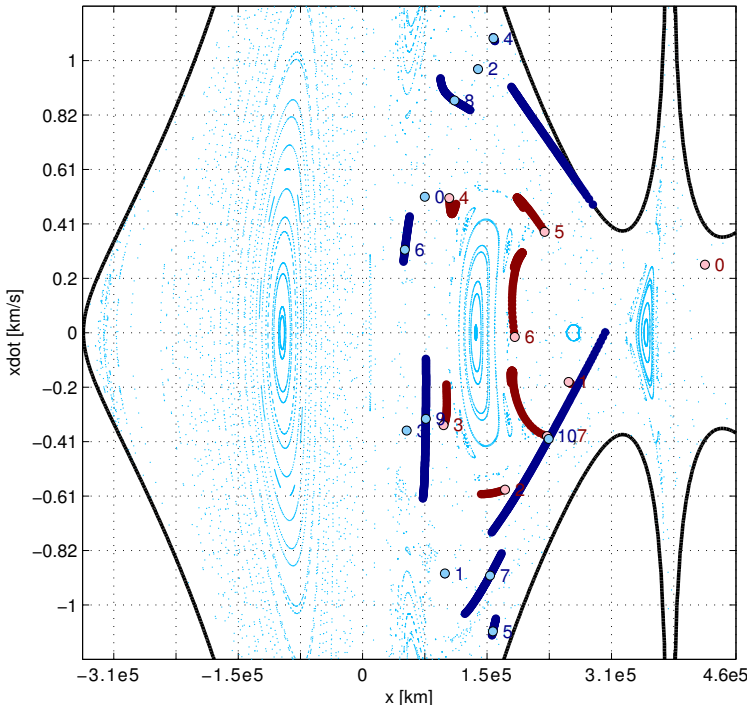

Figure 7.21.: Generic Control Points and Advected Curves

arbitrary state while it is desirable for it to be elsewhere in the state space. Subsequent iterations from the initial states of the associated $\boldsymbol{\xi}_2$ (1×10^{-4}) segments are also numbered in Figure 7.21. After 10 forward iterations (blue) and 7 backward iterations (red) a near intersection is observed. The discontinuity at the intersection point is significant, however, the end-to-end trajectory is otherwise well-behaved and the differential corrections process converges upon a solution quickly. As in Section 7.2.1, this trajectory is transitioned to the higher-fidelity model. In this example, since there are no revolutions about the Moon, the ephemeris solution more closely resembles the CRP solution. The corrected CRP and ephemeris trajectories appear (both in the rotating frame) in Figure 7.22. In the solution computed in the restricted problem, a maneuver of magnitude 0.70 $\frac{\text{m}}{\text{s}}$ is required at the departure point, while a 0.76 $\frac{\text{m}}{\text{s}}$ maneuver is required upon arrival at the final state (total: 1.46 $\frac{\text{m}}{\text{s}}$ with a time-of-flight just under 372 days). This example further establishes the stretchline/FCS targeting approach and demonstrates its application in more generic situations.

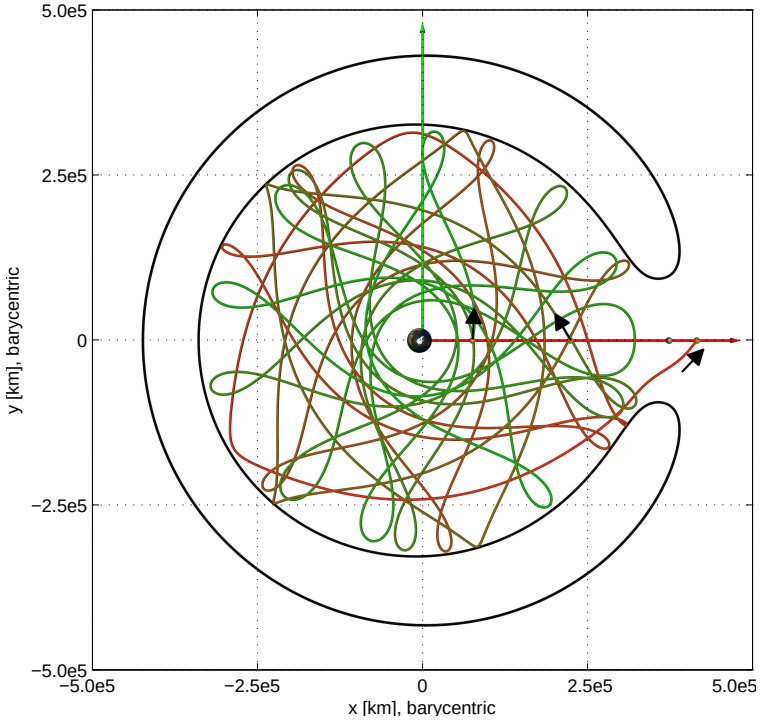

(a) Corrected CRP Solution

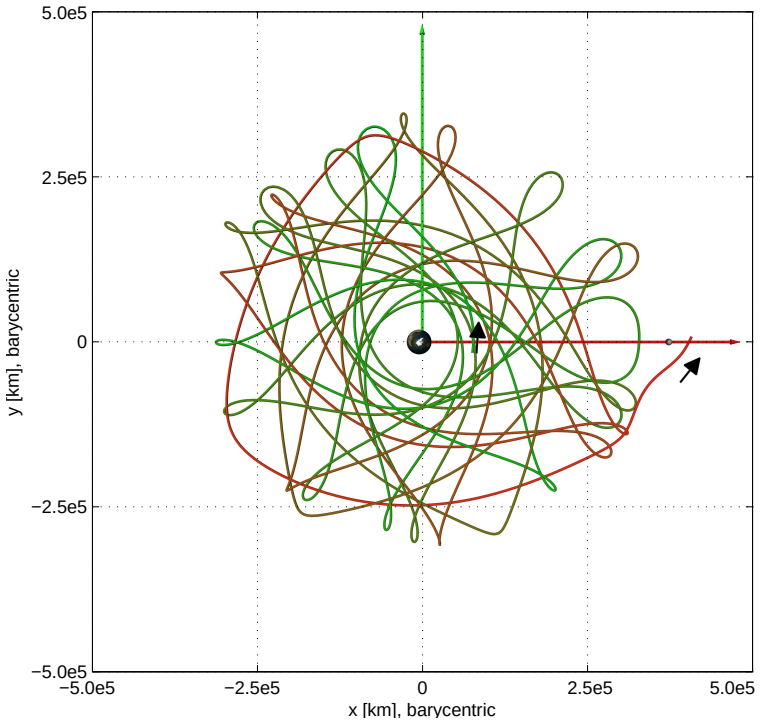

(b) Corrected Ephemeris Solution

Figure 7.22.: Connection of Arbitrarily Selected Map Points

7.3 Flow-guided System-to-system Transfers

A major focus in this investigation is illustrated by an example involving the flow control segment approach for targeting trajectories in the bicircular four-body problem. The motivating purpose behind this sample application is the possibility afforded of identifying solutions directly in a complex, nonautonomous model, a model that is not necessarily amenable to analysis methods that apply in simpler problems. The solutions that are constructed with this flow-based methodology represent trajectories that, inherently and simultaneously, accommodate, and thereby exploit, all gravitational forces available in the system. Leveraging all available natural forces frequently leads to various fuel-efficient solutions, but may result in longer times of flight. However, without flow-based tools, other, less-direct strategies must be utilized to determine solutions, and the associated solution space is generally more restricted and potentially less transparent.

7.3.1 Theoretical Establishment and Lower-fidelity Solutions

The bicircular four-body model is selected to provide a convenient context for a system-to-system transfer and to explore its increased complexity as a nonautonomous system. While the selected model is time-periodic and could be made autonomous with a stroboscopic mapping, the goal is to highlight the applicability of the present methodology to nonautonomous systems. This particular example focuses on transfers in the Uranian system—a potentially good candidate for future exploration as explored by Heaton and Longuski [95]. In [95] the authors indicate that the Uranian system is amenable to a Galileo-style tour of its moons. In the present investigation, the Uranus–Titania–Oberon system is selected for its mass and distance characteristics. Titania and Oberon are the same order of magnitude in mass, possessing two-body gravitational parameters of $Gm = 228.2\ \frac{\text{km}^3}{\text{s}^2}$ and $Gm = 192.4\ \frac{\text{km}^3}{\text{s}^2}$, respectively, while the mass parameter of Uranus is equal to 5,793,939 $\frac{\text{km}^3}{\text{s}^2}$ [96]. Moreover, the moons' orbits are relatively close to Uranus as well as each other with semimajor

axes of $\sim 4.36 \times 10^5$ and $\sim 5.83 \times 10^5$ kilometers with respect to Uranus. Finally, the orbits of both Titania and Oberon about Uranus are relatively circular (eccentricities: 0.0011 and 0.0014, respectively) and have low inclinations with respect to the Uranian equator (0.079° and 0.068°, respectively) [97]. Together, these considerations supply significant perturbing influences from the third primary, i.e., Oberon, to the behavior from the perspective of the Uranus–Titania (UT) system (as well as significant perturbations from Titania on motion as observed in the Uranus–Oberon (UO) system). Koon et al. [98] introduces a similar system-to-system analysis using manifolds in the patched circular restricted problems involving Jupiter–Europa and Jupiter–Ganymede. Kakoi [99] also invokes similar methodology in mixed three-body systems to achieve transfers between orbits in various systems.

For an illustration of the present concept, both Uranian satellites are depicted in Figure 7.23 in the Uranus–Titania rotating frame, along with artificial (in this model

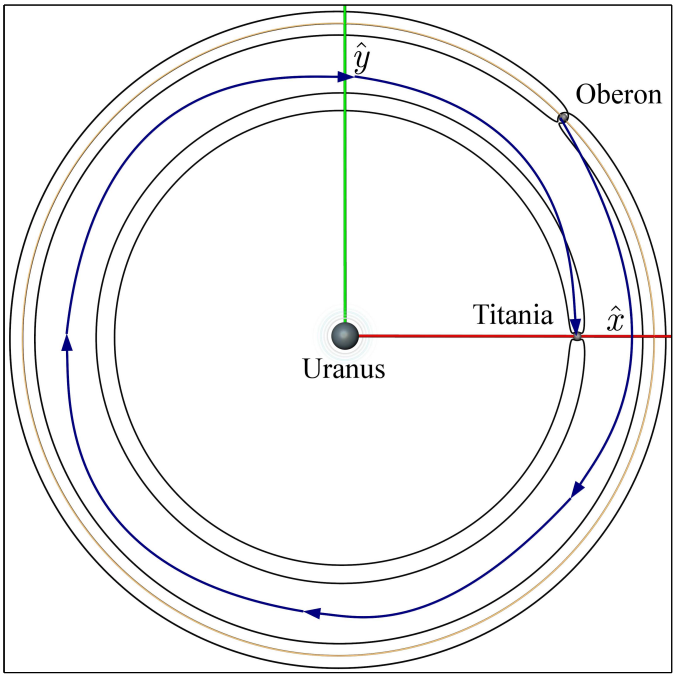

Figure 7.23.: System-to-system Transfer Illustration in Uranus–Titania (UT) Rotating Frame; Inspired by Figure 1.1 of [98]

and frame) zero velocity curves for energy levels that supply the necessary gateway dynamics *from the CRP*. Oberon's circular orbital path also appears in gold. The objective in the example is a trajectory that experiences a revolution about Oberon and then departs toward Titania, ultimately concluding with a revolution of Titania after following a transfer similar to the blue "path" sketched in Figure 7.23. Despite the inclusion of three-body zero velocity curves for illustration in Figure 7.23, there are no convenient bounds on energy like those available in the restricted problem. Taken in turn, both Titania and Oberon are incorporated as the "additional" body, thus, the third massive primary may circumscribe (or be circumscribed by) the second. In Figure 7.23, Oberon is placed at an initial angle of $\frac{\pi}{4}$ radians with respect to the x axis in the rotating Uranus–Titania frame (or, viewed alternately, Titania is depicted at $-\frac{\pi}{4}$ radians in the Uranus–Oberon rotating frame). For consistency, trajectory segments departing the Oberon region and moving inward toward Titania and Uranus are phased such that Oberon initiates in the geometry depicted in Figure 7.23. Trajectories that depart the Titania region outward toward Oberon (i.e., in reverse time) reflect the effects of Oberon originating at various locations in its orbit.

The process blends together several flow-based concepts to identify transfer solutions. Maps of FTLE values enhanced with reduced strainlines aid in the selection of candidate initial states while 4D stretchlines are employed as flow control segments to identify intersecting trajectories. The general mechanism for identifying transfers is described as follows:

1. Choose two-dimensional sections Σ_1 and Σ_2 near Oberon and Titania, and compute the respective backward and forward FTLE maps and strainlines.

2. Use the result from (1) to determine two orbits, one moving toward Titania in forward time and the other directed to Oberon in backward time.

3. From the initial conditions in the previous step, compute the $\boldsymbol{\xi}_4$ vectors for forward and backward integration times and iterate the $\boldsymbol{\xi}_4$ stretchlines (FCS) from positions consistent with their respective sections (Σ_1 and Σ_2) to an in-

termediate section Σ_3. In this step, the integration time for evaluating the Cauchy–Green tensor and obtaining $\boldsymbol{\xi}_4$ is selected consistent with the time required for the initial conditions to evolve to the intermediate section in the respective time directions.

A detailed description of the implementation of the above steps to obtain a transfer from Oberon to Titania follows. To isolate the desired behavior near Oberon and Titania, surfaces of section (generically, Σ) are constructed in the y–$\dot{y}$ phase space just beyond the gateways near L_1 and L_2, as illustrated in Figure 7.24. The sections are defined consistent with $-0.035 \leq y \leq 0.035$ nondimensional units (nd) and $-0.03 \leq \dot{y} \leq 0.03$ nd. These ranges translate to $-1.55 \times 10^4 \lesssim y \lesssim 1.55 \times 10^4$ km and $-0.1094 \lesssim \dot{y} \lesssim 0.1094$ $\frac{\text{km}}{\text{s}}$ with $\Sigma_2 : x \approx 4.49 \times 10^5$ km (1.03 nd) in the Uranus–Titania system. In the Uranus–Oberon system, the section definition dimensionalizes to $-2.05 \times 10^4 \lesssim y \lesssim 2.05 \times 10^4$ km and $-0.0945 \lesssim \dot{y} \lesssim 0.0945$ $\frac{\text{km}}{\text{s}}$ with $\Sigma_1 : x \approx 5.66 \times 10^5$ km (0.97 nd). In both cases, $\dot{x}$ is recovered from the CRP Jacobi constant value consistent with the ZVC depicted in Figures 7.23 and 7.24 (in fact, each value of C equals 3.004316 in its respective system). Specifically, the negative root is selected in the evaluation of $\dot{x}$ for both maps. Consequently, $\dot{x}$ is directed (for forward time evolution) "inward" toward Uranus as indicated by arrows in Figure 7.24. As demonstrated by [5], the associated initial conditions (IC) can be transitioned and evolved in another model—in this case, the IC are advected in the four-body model. Values of FTLE, resulting from forward integration for 10 nondimensional time steps (∼13.8 days) into the Titania region as well as backward evolution toward Oberon (10 nd; ∼21.4 days), appear colored consistently with the color scales in Figure 7.25. The two states investigated in this example are marked with black dots in Figures 7.25–7.26. When these states are evolved away from their respective sections in the opposite time direction, they are integrated for longer time durations, namely, the time required to cross the intermediate hyperplane. An area of particular numerical sensitivity is initially apparent in Figure 7.25(a) as a solid white curve of FTLE values interior to the main lobe. This white region, as well as

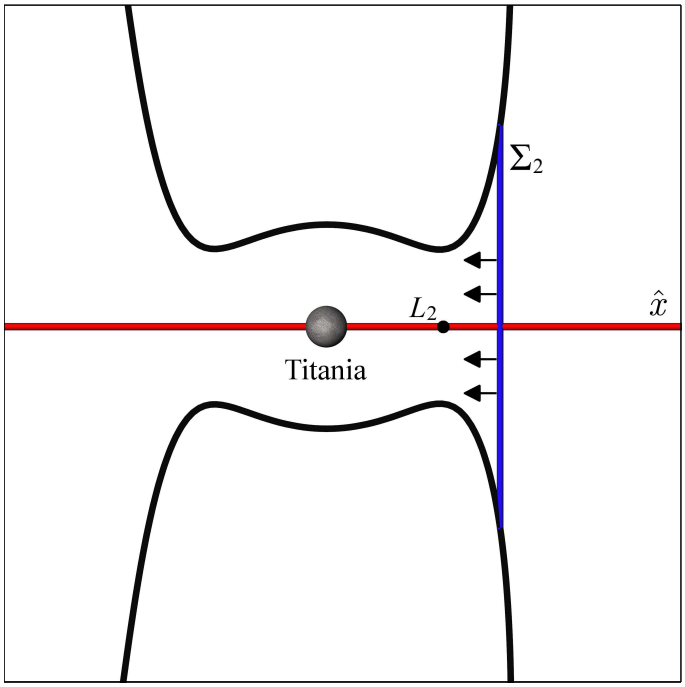

(a) Σ_2: x=1.03 nd; UT Rot. Frame

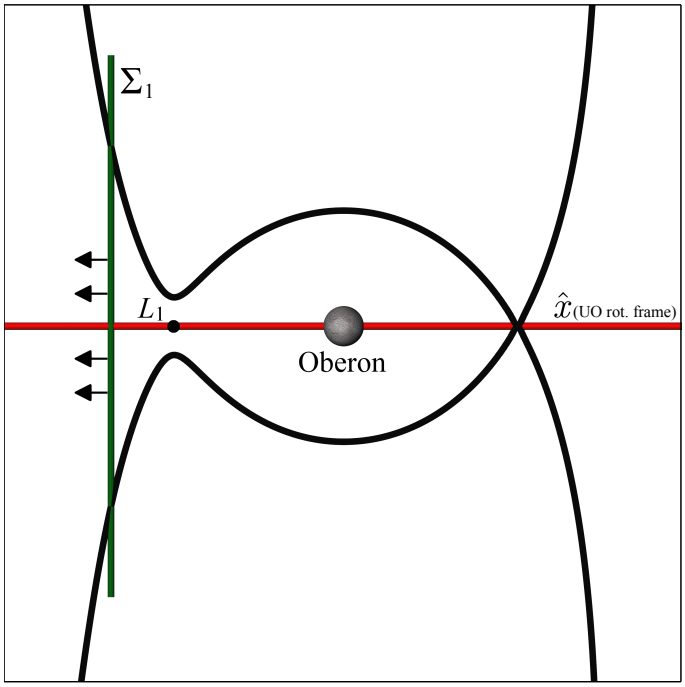

(b) Σ_1: x=0.97 nd; UO Rot. Frame

Figure 7.24.: Surfaces of Section for FTLE Grids

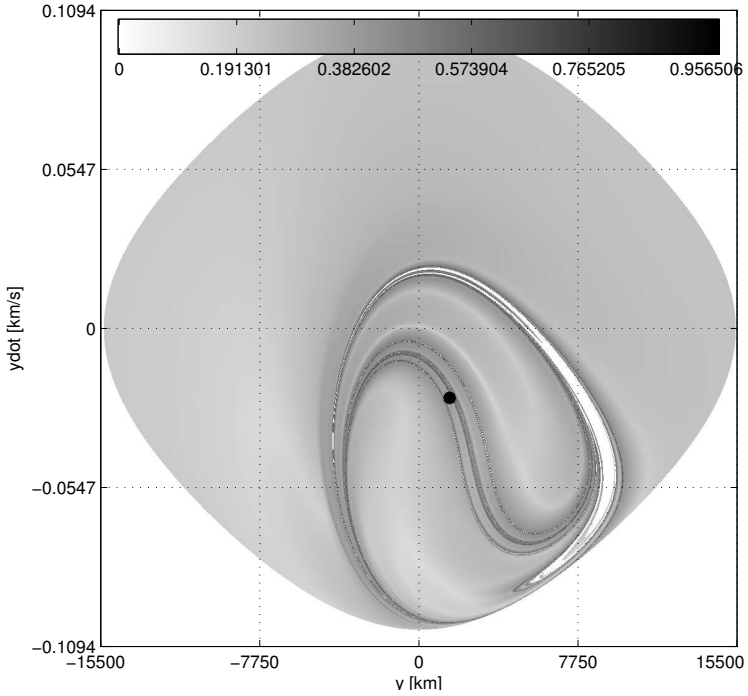

(a) Titania L_2 FTLE Gateway Map

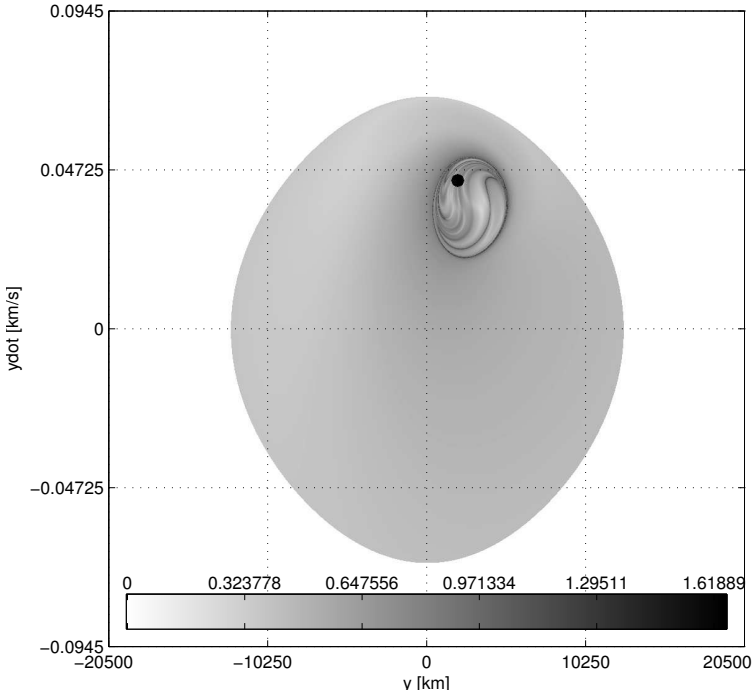

(b) Oberon L_1 FTLE Gateway Map

Figure 7.25.: Maps of FTLE Values Near Titania and Oberon

the areas beyond the larger gray shapes on both maps, reflect FTLE values set to zero based on integration issues or exclusion by the CRP zero velocity bounds.

Reduced strainlines are projected onto the FTLE maps in Figure 7.26. These strainlines help to characterize the flow originating from initial conditions and highlight various regions in the map. The reduced repelling strainlines on the y–$\dot{y}$ FTLE maps are computed. In general, the reduced strainlines represent potential structures that can signify a qualitative change in trajectory behavior. Particular regions are revealed where trajectories enter the nearby Uranian moon's neighborhood, and do not subsequently exit (for the duration of the simulation). These flow-distinguishing ideas are illustrated in Figure 7.27. The three-body ZVC (dark gray) are included in Figure 7.27 for context and the appropriate surface of section from Figures 7.23 and 7.24 is consistent with the green line. The outermost strainline in the central pane represents a flow boundary; states exterior to this boundary will not evolve into the Oberon region while states inside the contour will evolve toward Oberon. This outermost strainline is analogous to the boundaries reflected by the Jacobi limiting curves from the autonomous CRP where, in that case, the curve would correspond to the map image of a four-dimensional invariant manifold. In the nonautonomous four-body case the structures emerge solely as a reflection of the flow behavior. While trajectory behavior is generally consistent with the Jacobi limiting curves of the CRP, it does not, in fact, strictly conform to the underlying energy preservation of the restricted three-body problem (and the associated motion boundaries). In the left- and rightmost panes of Figure 7.27, the evolution of two states, one exterior (pane b.1) and one interior (pane b.2) to the outermost reduced strainline, is depicted. This illustrates the notion of the observed flow separation associated with this particular reduced strainline. Also depicted are two sets (panes a.1–3, and c.1–3) of three trajectories each taken from two distinct regions. Both sets display qualitatively similar behavior between their members and serve to illustrate the concept that states within specific regions, identifiable by the underlying FTLE features and the associated strainlines, display consistent characteristics while those belonging to other regions differ. Not all

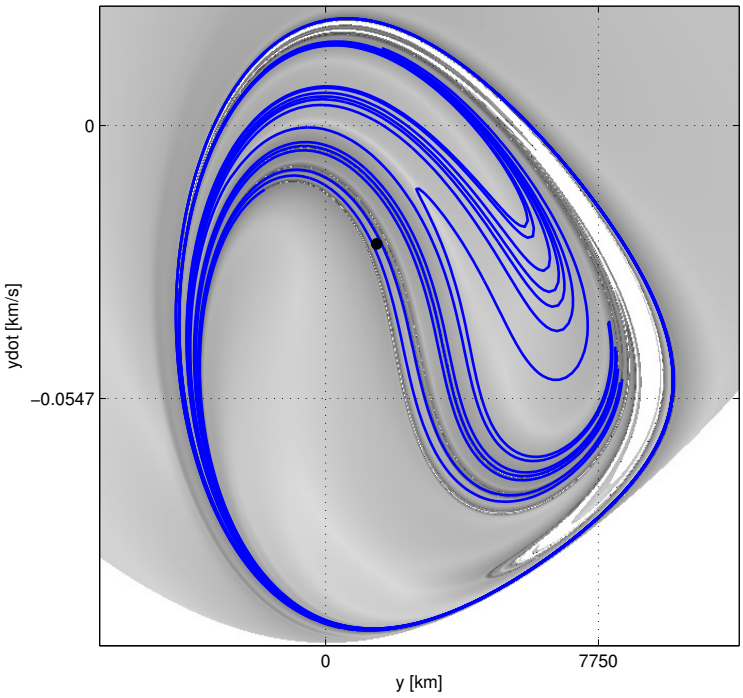

(a) Zoom of Figure 7.25(a) with Strainlines

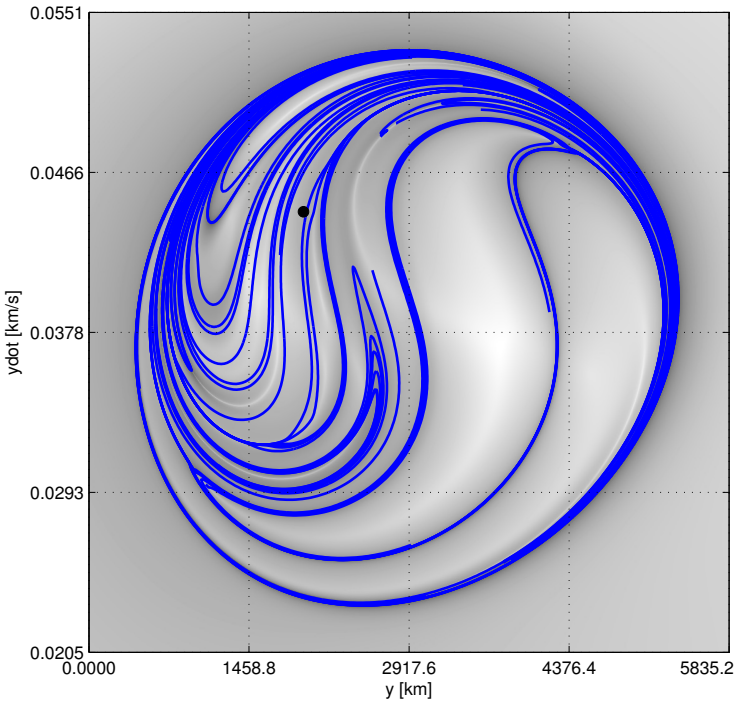

(b) Zoom of Figure 7.25(b) with Strainlines

Figure 7.26.: Strainlines for Figure 7.25

of the displayed reduced strainlines correspond to a flow distinguishing feature that is as dramatic as that associated with the outermost curve, however, they do represent more subtle changes in the state space. A particular strainline may signify a change in sign in a particular final state or a reversal in the evolution of trajectory behavior. For example, observing states on the map as they approach and cross strainlines may result in trajectories that display growth in terms of the final value of an orbital element, reach a stationary point, and then begin to reverse the previous growth. In general, the curves augment and enhance the map and supply a parametrized set of points to aid in additional analysis.

Given the guiding tools available from the maps, end-segment trajectory arcs can be identified. To help illustrate the FCS concept, segments are selected somewhat arbitrarily. That is, segments that evolve from the map and complete a few revolutions about the associated primary without impacting are desirable, but for the purposes of the ensuing example any, not necessarily the best, such arcs will suffice. Many possible choices are available and, from among these, the arcs consistent with the large black dots on the maps in Figures 7.25–7.26 are selected. In the case of the associated Oberon segment, the selection is consistent with the first $\sim$1.5 revolutions of the trajectory depicted in pane a.1 of Figure 7.27. Both end-segment trajectories appear in Figure 7.28 colored from green to red with increasing time. These initial segments and the corresponding FTLE maps are each calculated with the associated primary acting as P_2 in the four-body system. For example, the Oberon segment and map are calculated in the Uranus–Oberon rotating frame with Titania orbiting counter-clockwise "interior" to Oberon. In this case, Titania's motion initiates at an angle of $-\frac{\pi}{4}$ radians with respect to the Uranus–Oberon rotating x axis. Similarly, for the Titania segment, Oberon orbits the system "exterior" to Titania. However, Oberon orbits in a clockwise direction given a slower angular rate than Titania.

To simplify the analysis, the initial Oberon map state is transformed into the Uranus–Titania rotating frame using transformation matrices similar to those in [39] and, subsequently, evolved backward in time to verify its consistency under the al-

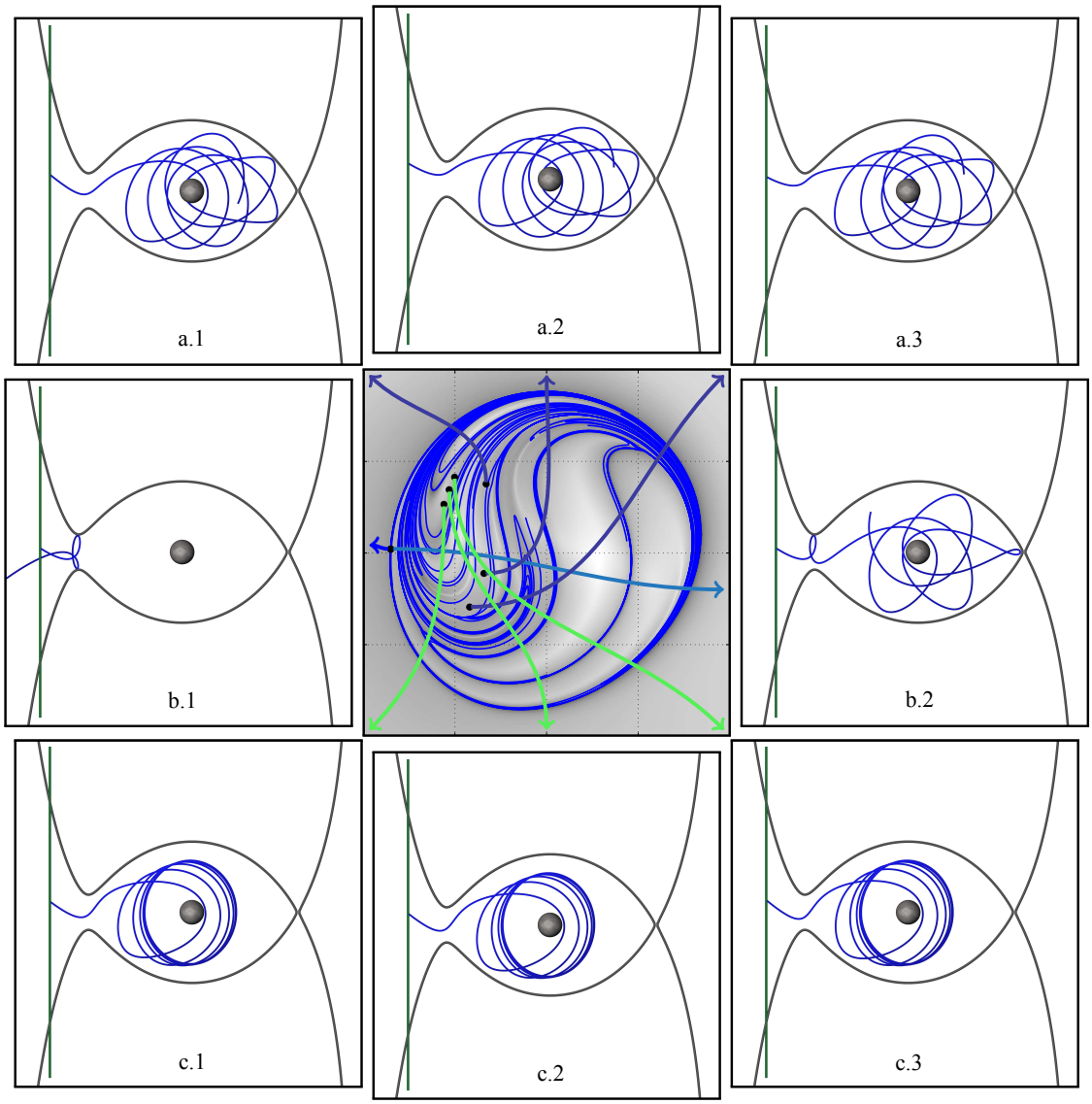

Figure 7.27.: Selected Trajectories (10 nd) from a Strainline Enhanced FTLE Map

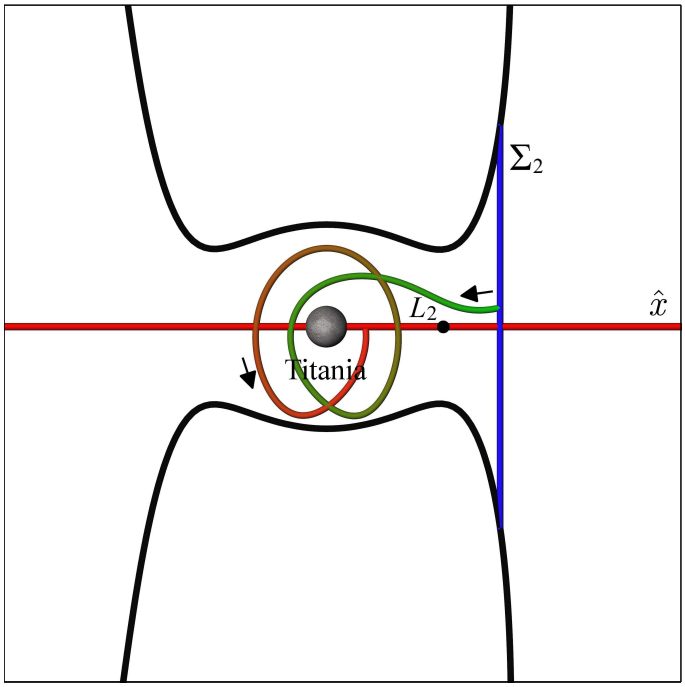

(a) Terminal Transfer Segment (UT Rot. Frame)

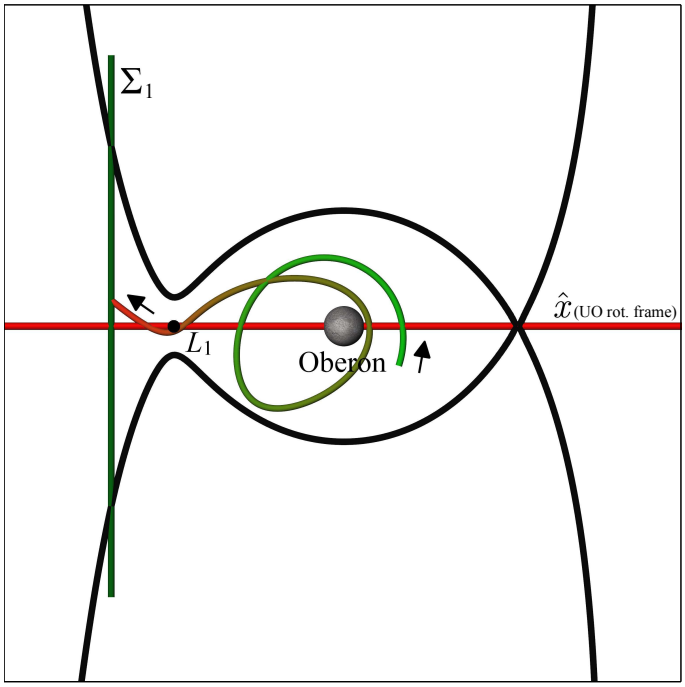

(b) Initial Transfer Segment (UO Rot. Frame)

Figure 7.28.: Transfer "Bookends": From Near Oberon, To Near Titania

ternate system. All additional analysis occurs in the Uranus–Titania rotating frame. Next, the states from the two map points are evolved, forward in time from the vicinity of Oberon and backward in time from the vicinity of Titania. These propagations are terminated after successive intersections with the negative x-axis segment colored magenta in Figure 7.29. This selection of the intersection region is inspired by [98]. The forward propagation from the vicinity of Oberon always originates with Oberon at $\frac{\pi}{4}$ rad in the Uranus–Titania rotating frame. The first crossings of the forward and backward propagations are displayed in Figure 7.29(a), and subsequent crossings in both forward and backward time are displayed, for illustration, in Figure 7.29(b). The backward propagation of the Oberon trajectory (from Figure 7.28(b)) in the Uranus–Titania–Oberon four-body system appears at the top in both Figures 7.29(a,b), initially colored black and evolving toward Oberon. Oberon's circular path is represented in gold, while the spacecraft trajectory segments are colored using a discrete, rotating color scheme that increments with each full nondimensional time unit ($\sim$1.38 days) as a means to aid in the time correlation. Forward and backward segments colored differently upon intersection immediately reveal a timing mismatch.

For the backward propagation from Titania to be valid, the initial angular position of Oberon must be adjusted. This adjustment is accomplished by summing the time required for the forward propagation from Oberon to the n^{th} crossing with the length of time required for the backward propagations to meet the x axis after m crossings. Given the total "inner" time duration (the forward time from the Oberon section plus the backward time from the Titania section), the angular position of Oberon is adjusted using its *constant* angular rate. However, the adjusted initial position impacts the time for the backward propagations to reach the x axis, so this adjustment procedure must be iterated until the timing and the initial Oberon position agree. In some cases, close primary passages cause this iterative process to diverge. Consequently, some combinations of forward and backward crossings are not attainable. Finally, it must be verified that the Titania end-segment (and, indirectly, the associated FTLE map) remains valid for the adjusted Oberon positions. The proximity

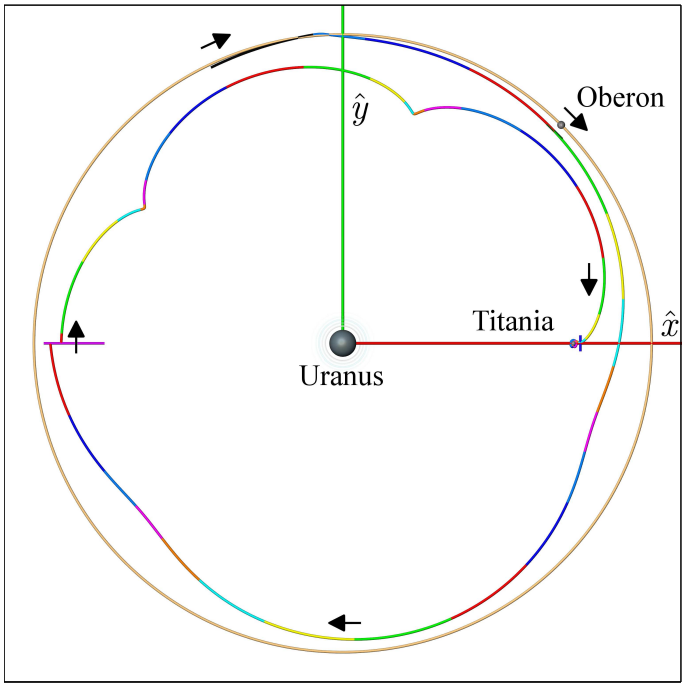

(a) First Crossings

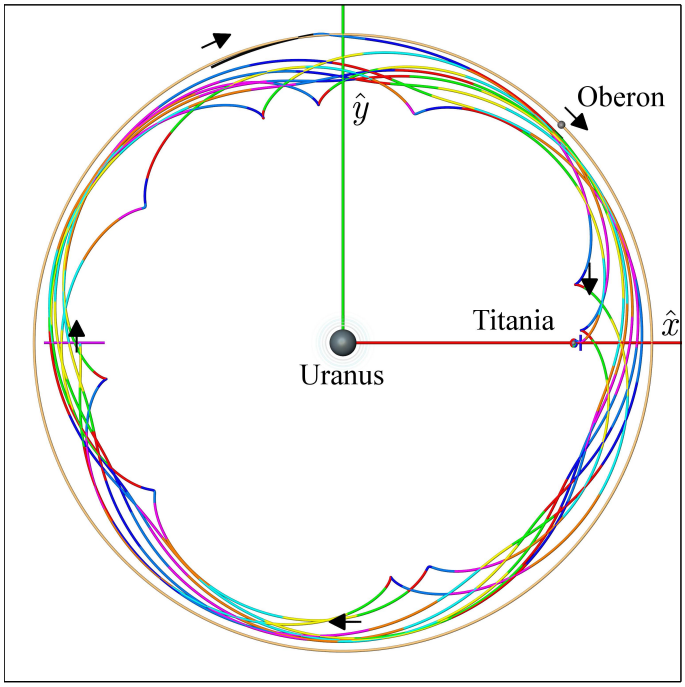

(b) Subsequent Crossings

Figure 7.29.: Negative x-axis Trajectory Crossings

to Titania generally overwhelms the perturbation from Oberon—its effects are still visible but, for each of the sampled cases, the selected trajectory near Titania remains qualitatively consistent. Given corrected timing and angular positions for Oberon, the Cauchy–Green tensor and its eigenvalue/eigenvector sets can be computed.

The present analysis is restricted to perturbations in velocity space along the associated eigenvector components and ultimately reveals solutions continuous in position that require three distinct velocity-changing maneuvers. The maximum perturbation associated with the segments is 1×10^{-2} or about 36 $\frac{\text{m}}{\text{s}}$ to induce sufficient stretching, i.e., the end points of the segments represent a 36 $\frac{\text{m}}{\text{s}}$ change in velocity. In Figure 7.30, the first forward crossing of the segment is depicted in red, while the first backward

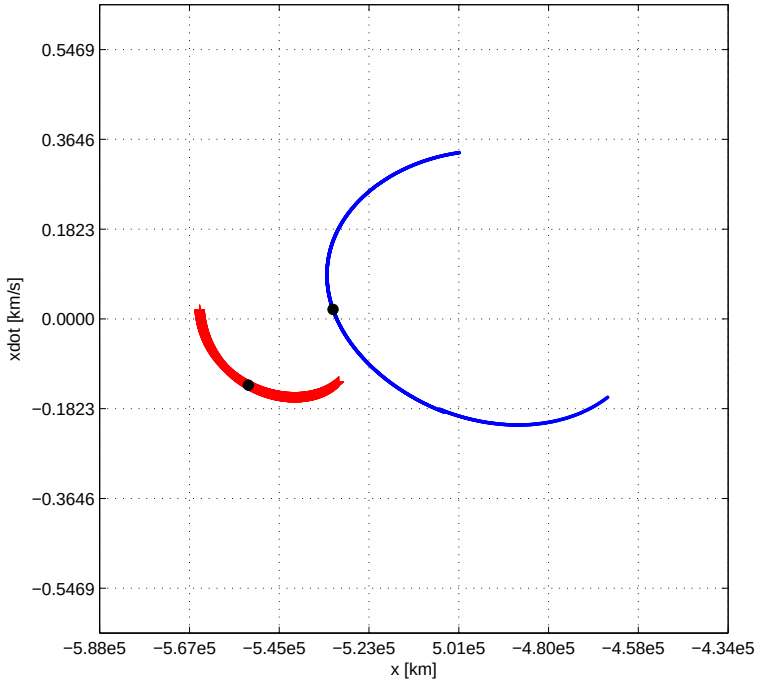

Figure 7.30.: Initial FCS Images on Σ_3 Hyperplane (on the Negative x Axis)

crossing is colored blue. The images of the "central" trajectories about which the FCS are taken are also depicted as black dots in Figure 7.30. No intersections exist between the initial 36 $\frac{\text{m}}{\text{s}}$ forward and backward FCS images as is apparent in the figure. Additional revolutions are observed to supply multiple potential connections,

however. A sampling of representative FCS images on the hyperplane appears as Figure 7.31. While the forward images will remain the same given their consistent initiating system geometry, the images of the backward FCS will vary significantly depending on the particular intersecting states and the associated time of flight to reach the intersection. In Figure 7.31, the 1^{st}–3^{rd} forward crossings of the $\boldsymbol{\xi}_4$-velocity aligned segments from the Oberon region are marked column wise in red, respectively from left to right. At the same time, the associated 1^{st}–3^{rd} backward crossings proceed by rows with the 1^{st} crossings depicted by blue points in the first row, the 2^{nd} crossings represented with green points on the second row, and the 3^{rd} crossings marked by black dots in the final row. It is apparent that the resulting backward FCS images are all different contingent upon the associated forward time of flight.

Inspection of the resulting intersections in Figure 7.31 reveals multiple connections. However, the new "time-to-crossing" associated with the perturbed states that should ultimately lead to an intersection must be incorporated. To do so, a potential intersection is selected from map images associated with the timing that is consistent with the "central" trajectories. Then, the times of flight associated with these candidate arcs are employed to adjust the initial placement of Oberon for the backward propagation from Titania (i.e., this state, in fact, represents the final position of Oberon once the trajectory arrives in the Titania region after transferring from Oberon in forward time). The candidate intersection now occurs elsewhere along the FCS, and, in cases of intersections near the edges of the control segments or intermediate close primary passages, may no longer exist. Frequently, the intersection is still apparent on the map and the new intersecting states are subsequently employed to repeat the process, which continues iteratively until agreement in timing and system geometry occurs. One example of the transfer initiating on the Oberon section and terminating at the Titania section is displayed in Figure 7.32. This particular case is selected for display simply to illustrate a result of the process.

Multiple solutions are tabulated in Table 7.1 where the total maneuver cost associated with the Oberon section departure (i.e., the perturbation along the FCS),

the adjustment in $\dot{y}$ required at the intermediate section, and the perturbation along the control segment at the Titania section is listed. The transfer time of flight is also included. Of particular note is the shortest time-duration transfer (81.56 days) characteristic of two forward and one backward iterations as well as the lowest (propellant) cost solution (123.43 $\frac{\text{m}}{\text{s}}$) from three forward and one backward crossings—these minimal cases belong to different solutions. While the main goal of this analysis is to highlight the ability of identifying solutions directly in systems incorporating higher-fidelity gravity models, some comparison with times of flight and maneuver costs associated with transfers in simpler models is useful. A Hohmann transfer between the two sections depicted in Figures 7.24 and 7.28, assuming the possibility of a 180$^{\text{o}}$ transfer angle, would require 5.46 days with a maneuver cost of 391.53 $\frac{\text{m}}{\text{s}}$. The orbital anomalies of Oberon and Titania at departure as well as that of Titania at arrival corresponding to the lowest propellant consumption listed in Table 1 reflects a transfer angle of 260.17$^{\text{o}}$. The solution in the table attends multiple revolutions of Titania and Oberon but the initial and final locations of the moons are consistent with a direct transfer experiencing less than one inertial revolution consistent with a 260.17$^{\text{o}}$ transfer angle. A Lambert-arc solution for the given geometry is accomplished in 6.29 days and requires 458.56 $\frac{\text{m}}{\text{s}}$ to match velocities at departure and arrival. Finally, comparisons of the Jacobi constant values at the two sections computed in a common Uranus–Titania three-body system indicate a minimum CRP change in velocity of 150.99 $\frac{\text{m}}{\text{s}}$ that is necessary to supply the requisite energy change. While the solutions identified from the FCS analysis involve significantly longer times of flight than simple comparisons from the two- and three-body models, they are obtained directly in the four-body model incorporating the gravities of all relevant bodies. As a consequence, they reflect lower costs as well as potential initial guess solutions for differential corrections which may further reduce propellant requirements.

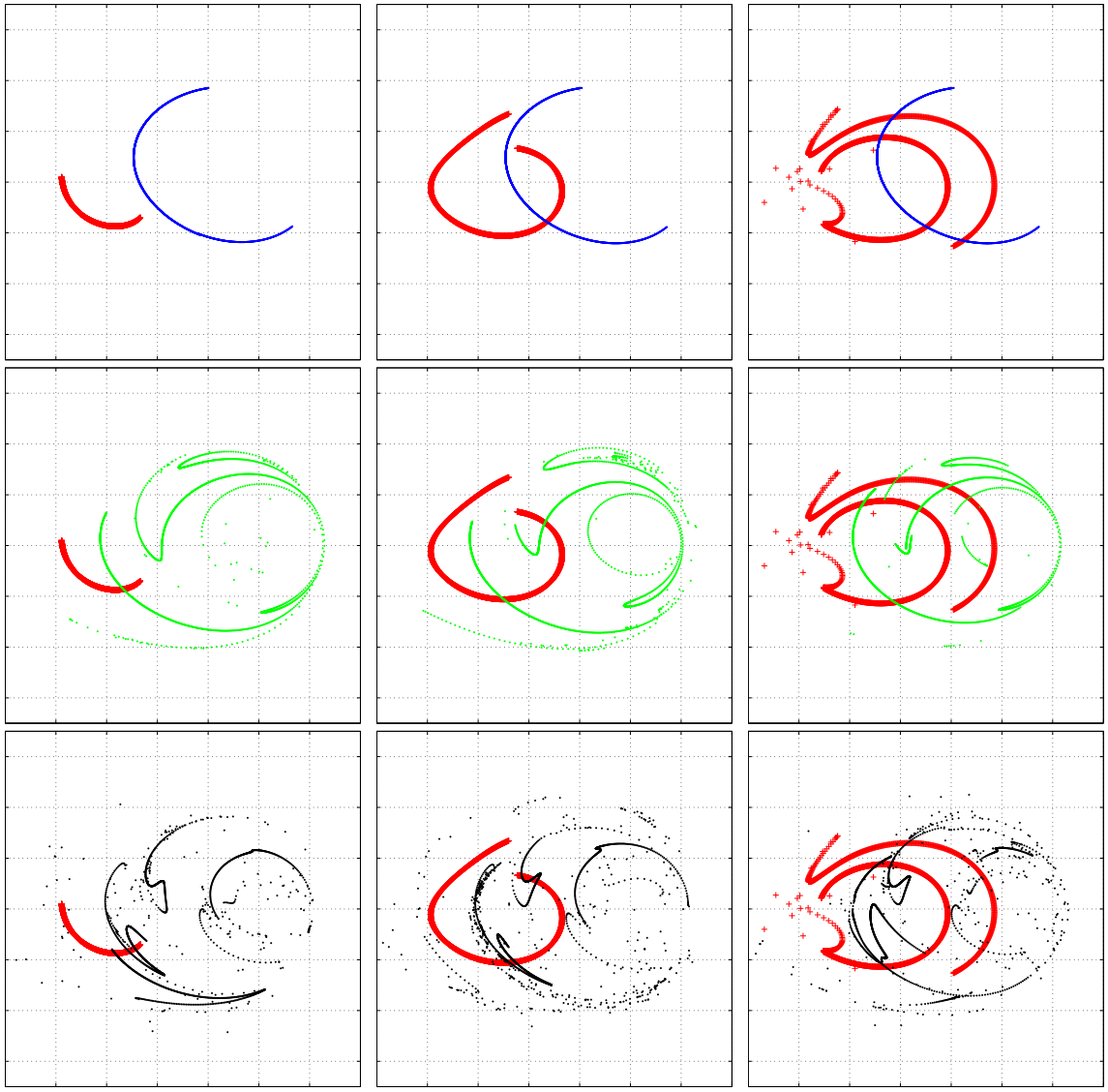

(a) Forward Crossings: 1
Backward (t–b): 1, 2, 3

(b) Forward Crossings: 2
Backward (t–b): 1, 2, 3

(c) Forward Crossings: 3
Backward (t–b): 1, 2, 3

Figure 7.31.: Crossing Combinations: The 1^{st}–3^{rd} forward crossings of the $\boldsymbol{\xi}_4$-velocity aligned segments from the Oberon region are marked in red from left to right. Representative 1^{st}–3^{rd} backward crossings are marked with blue, green and black points from top to bottom. Axes in each panel are consistent with Figure 7.30.

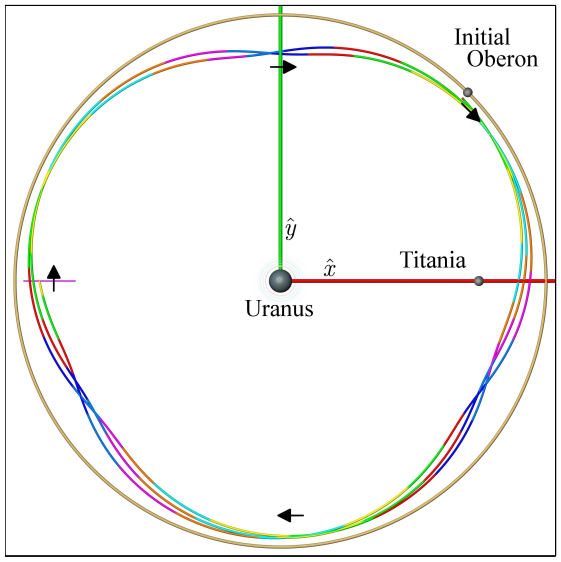

(a) Three Forward Crossings

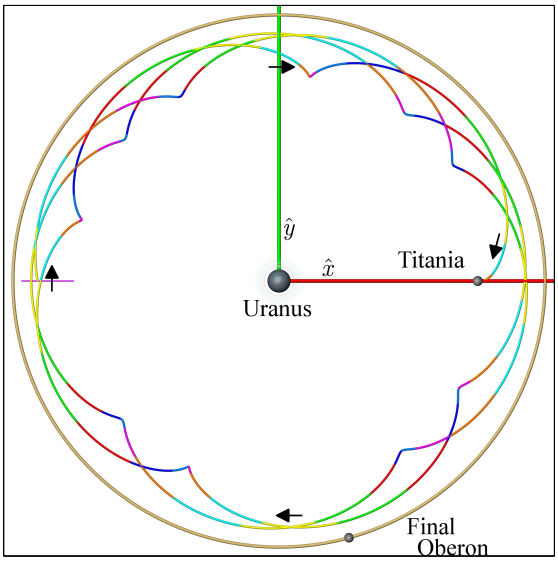

(b) Three Backward Crossings

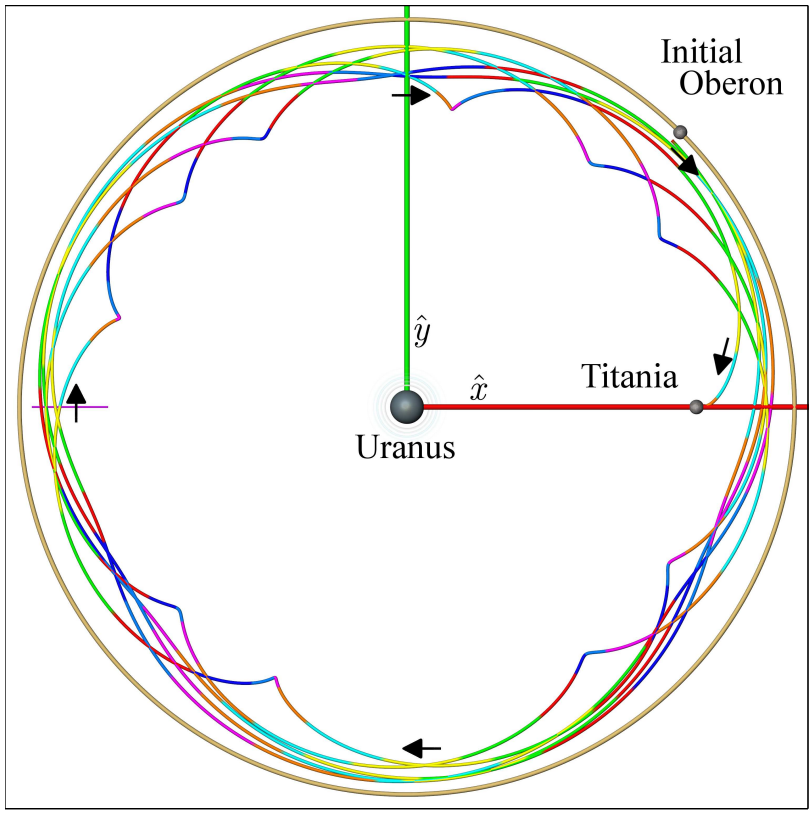

(c) Complete Transfer Trajectory

Figure 7.32.: FCS Identified System-to-system Transfer

Table 7.1: Transfer Data: Maneuver Costs and Times of Flight

	[m/s], [days]	[m/s], [days]	[m/s], [days]
BWD ↓ FWD →	1	2	3
			173.93, 116.41
1	No	182.97, 81.56	179.46, 125.81
	Intersections		123.43, 119.31
			163.93, 111.23
			133.74, 160.73
2	168.39, 91.23	142.71, 126.09	181.23, 186.53
		219.77, 138.94	167.90, 181.32
			164.77, 180.81
			195.42, 172.95
		126.82, 178.13	125.45, 204.55
	161.20, 134.90	144.94, 177.99	170.13, 212.14
3	153.86, 143.18	206.28, 190.69	160.14, 247.18
	180.54, 142.90	209.84, 190.51	182.08, 241.87
		208.14, 190.14	130.89, 232.53
			179.08, 224.29

7.3.2 Higher-fidelity Validation

To validate the process established in Section 7.3.1, a solution from Table 7.1 is selected for differential corrections in a higher-fidelity model. This validation exploits parallel-shooting differential corrections to converge the solution from the lower-fidelity four-body model under dynamics that incorporate the ephemeris time-histories for the gravitating bodies. Thus, the non-Keplerian and out-of-plane motions of the primaries are taken into account. This validation also serves to allow the *control surface* Σ_3 to float during differential corrections, taking advantage of the potential benefits offered by such flexibility.

The specific case that is selected for validation is consistent with 2 backward and 1 forward crossings—the entry in the table requiring 168.39 $\frac{\text{m}}{\text{s}}$ and 91.23 days. The solution is converged using the routines and interface of Adaptive Trajectory Design (ATD),[1] a many-faceted software package that utilizes dynamical systems theory and other concepts for trajectory design in multi-body environments. One view of a possible solution converged in the ephemeris system including the initial Oberon revolution (red), the transfer phase (green) and the terminal revolution about Titania (blue) is offered in Figure 7.33. In the figure, the three maneuver points are indicated by red asterisks. The out-of-plane excursion associated with the solution in Figure 7.33 is included in Figure 7.34. Such nonplanar motion is induced by the ephemeris system. Zoomed views for the maneuver locations comprise Figure 7.35 where the initial, uncorrected placement for each maneuver is indicated with an unlabeled asterisk. Dashed lines indicate the pre-converged, disconnected trajectory segments. After corrections, the labeled red asterisks indicate the final maneuver locations. A survey of ephemeris geometries supplies a variety of suitable epochs to converge solution options, and a few examples are tabulated in Table 7.2. In the table, maneuver costs are listed as velocity magnitude discontinuities at the designated maneuver nodes. When the lower-fidelity four-body solution is initially evolved in

[1]Principally developed by Amanda Haapala at Purdue University, see [100].

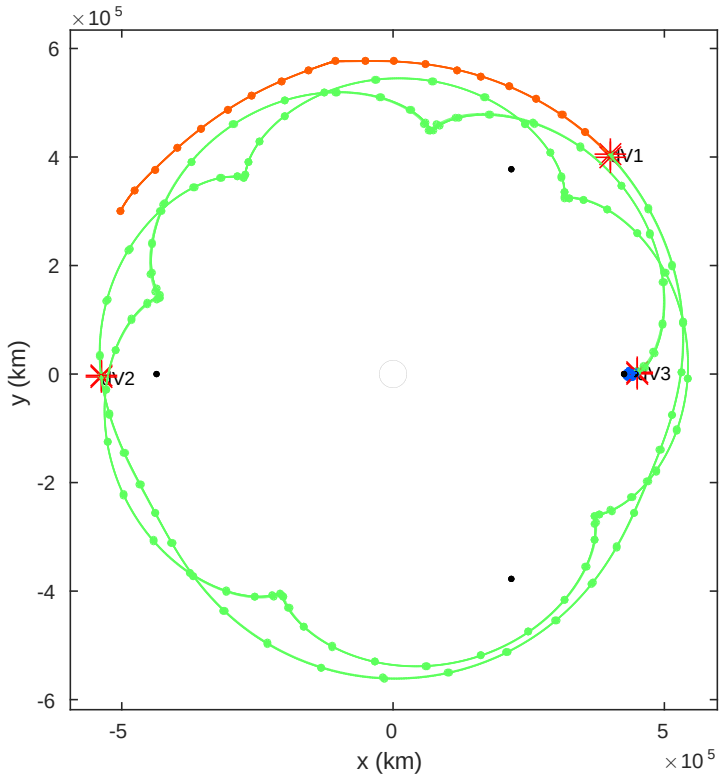

Figure 7.33.: Ephemeris UTO Transfer Solution

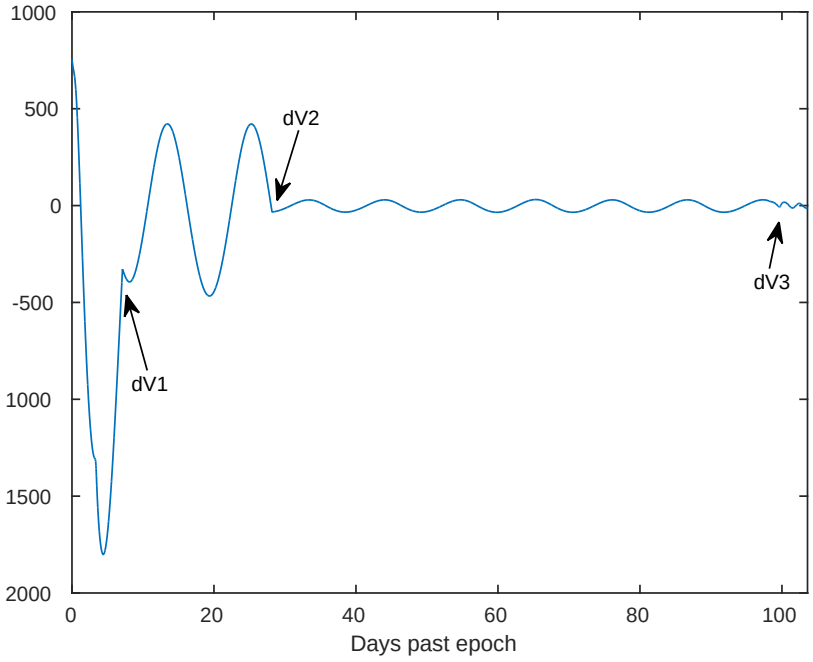

Figure 7.34.: Out-of-plane Excursions for Figure 7.33

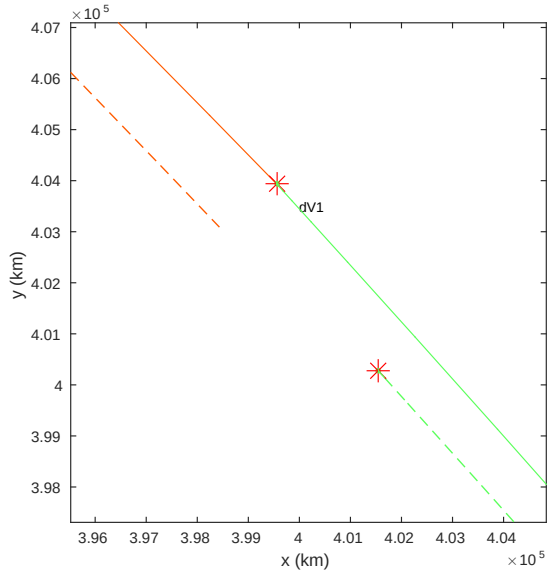

(a) Connection: Oberon and Transfer Legs

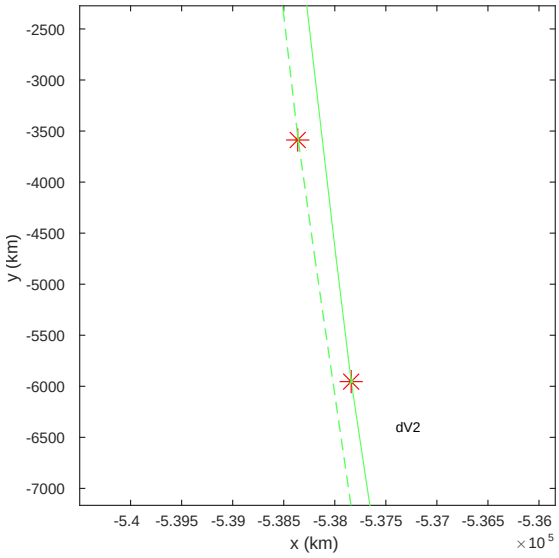

(b) Forward-backward Connection Point

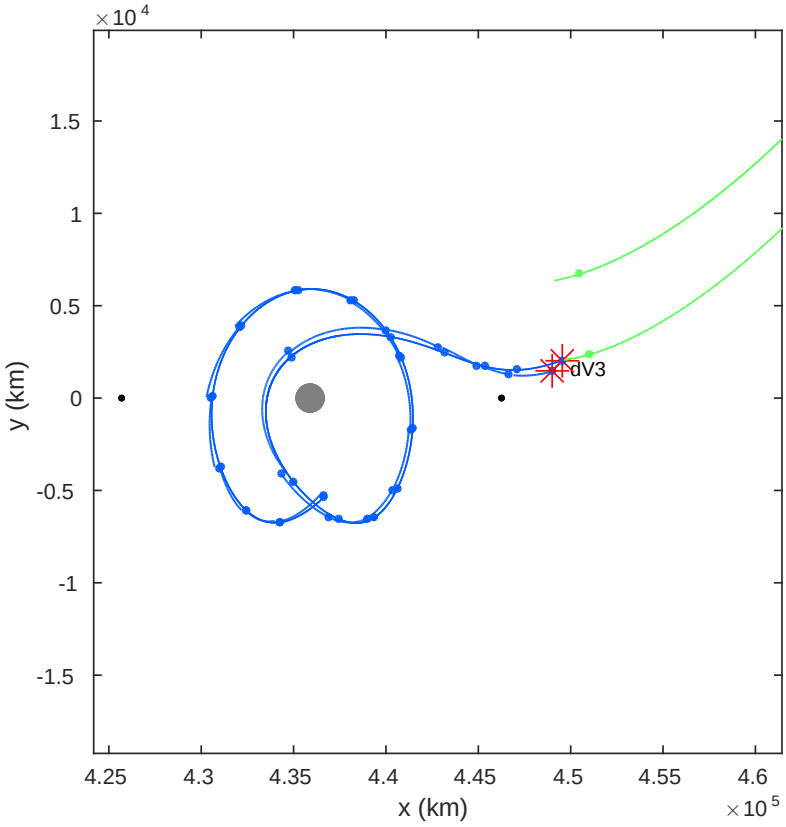

(c) Connection: Transfer and Titania Legs

Figure 7.35.: Zoomed Views of Maneuver Locations

the ephemeris model it becomes discontinuous, thus, the maneuver costs in the "pre" column are the velocity discontinuities before correction. The "post" column lists the maneuver costs after numerical correction. The result from the second converged epoch (2012 Nov 21) is used as input for subsequent corrections that gradually impose tighter constraints on the total maneuver cost, and the associated result is listed as the final data set in Table 7.2. For this final option, the epoch shifts by about 28 minutes, and the maneuver cost is reduced to 125.0 $\frac{\text{m}}{\text{s}}$. Further restrictions on the total maneuver cost ($\Delta v < 125.0$ $\frac{\text{m}}{\text{s}}$) cause the corrections process to diverge.

Finally, an option to capture at Titania is considered. By performing an additional maneuver at the first periapsis in the Titania leg, the spacecraft energy may be adjusted such that it becomes, at least temporarily, captured about Titania. A maneuver performed antiparallel to the spacecraft velocity direction results in an energy decrease. In Figure 7.36, a 5.2% decrease in velocity corresponding to a Δv of 15.60 $\frac{\text{m}}{\text{s}}$ reduces the instantaneous three-body energy from that consistent with the blue ZVC to a level associated with the black zero velocity curves (the energy level of L_1). However, as is apparent by the ZVC violation in the cyan trajectory evolution, the three-body energy is not conserved in the four-body ephemeris system, and the resulting trajectory will depart after subsequent evolution (slightly longer than the 8 days depicted by the cyan arc). In Figure 7.37, the velocity is decreased by 6.0% (17.95 $\frac{\text{m}}{\text{s}}$), and the resulting trajectory behavior is consistent with a longer duration capture. Again the instantaneous three-body ZVC are included for reference—blue for the energy level of the incoming Titania leg, black for the energy level of L_1 and cyan for the captured trajectory's instantaneous Jacobi constant value. The cyan orbit persists for at least the 98 days depicted in the figure.

The ability to converge lower-fidelity solutions serves a few purposes. This ability validates the models used for the simulation as well as the process for obtaining solutions. It also serves as a de facto optimization for shifting the control interface between intermediate arcs. Such a validation supports flow-based options for design.

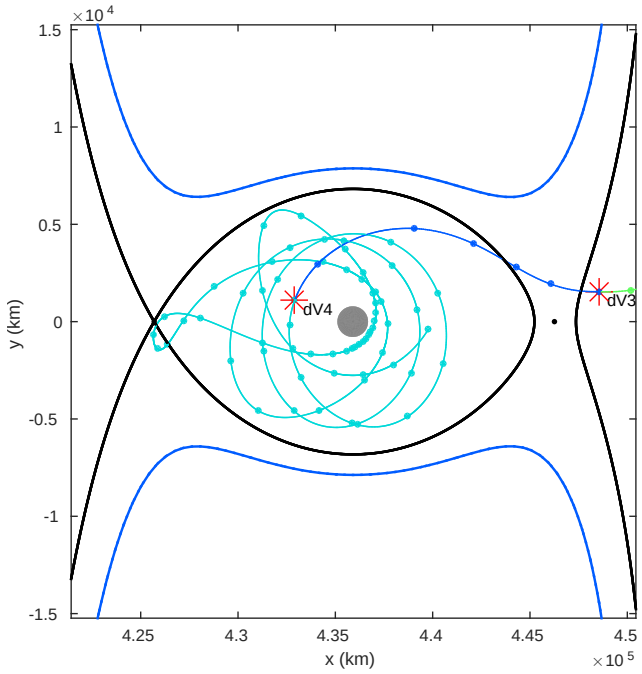

Figure 7.36.: Temporary Capture at Titania

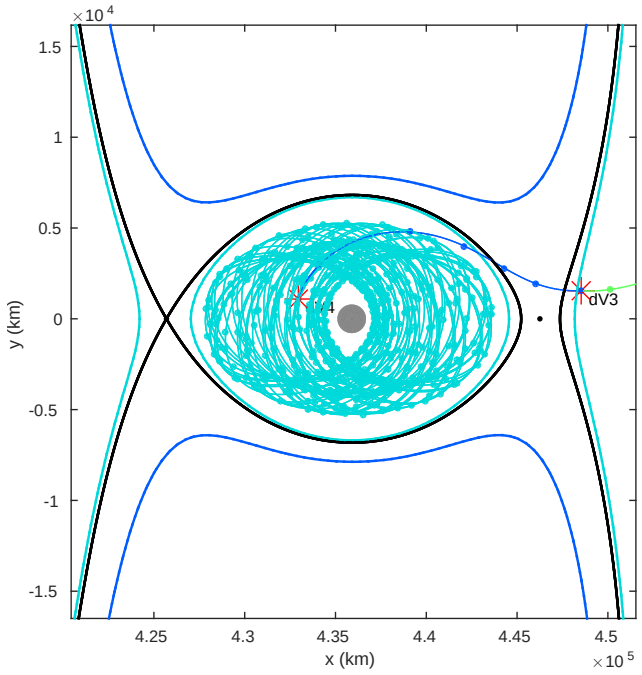

Figure 7.37.: Longer Duration Capture at Titania

Table 7.2: Corrected Ephemeris Solutions and Data

Epoch: 2010 Apr 22 15:33:29.399

Maneuver	[m/s] pre	[m/s] post	TOF [days]
Δv_1	18.3492	58.2259	
Δv_2	120.0539	120.2884	
Δv_3	40.4561	27.9302	
Total	178.8592	206.4444	103.60

Epoch: 2012 Nov 13 22:11:56.2078

Maneuver	[m/s] pre	[m/s] post	TOF [days]
Δv_1	44.247	40.7943	
Δv_2	120.2359	119.2965	
Δv_3	33.496	25.4108	
Total	197.9789	185.5015	103.61

Epoch: 2016 Jan 16 00:21:59.628

Maneuver	[m/s] pre	[m/s] post	TOF [days]
Δv_1	94.359	48.5728	
Δv_2	120.7792	116.7391	
Δv_3	29.8776	24.4999	
Total	245.0158	189.8119	103.61

Epoch: 2012 Nov 13 21:43:32.377

Maneuver	[m/s] pre	[m/s] post	TOF [days]
Δv_1	40.7943	2.6e-6	
Δv_2	119.2965	118.3039	
Δv_3	25.4108	6.6907	
Total	185.5015	125.0	103.63

7.4 Map Region Characterization and Trajectory Selection

The process of identifying particular points from their FTLE context and enhancing maps with strainlines as described in Section 5.2 enables additional applications. The resulting map effectively displays regions consistent with particular types of flow behavior. This map can be explored interactively to identify useful trajectories. The strainlines also represent a parametrization of features that can be invoked to propagate the boundaries of regions through the flow resulting in surfaces that describe natural flow pathways through a system. Additionally, the parametrized curves allow for bounded numerical analysis within a region. For example, a specific subset of initial conditions outlined by strainlines can be fed to an optimizer to isolate a particularly desirable result. The following example illustrates the possibilities afforded by accurately identifying flow-map features.

7.4.1 Isolating a Map Region

A particular example of the process of characterizing map regions is offered in Section 7.3.1, where maps of the flow approaching two Uranian moons are constructed. The strainline enhanced map introduced in Figure 7.26(b) is reproduced for convenience as Figure 7.38, and is the subject of the present discussion. Some discussion regarding flow behaviors associated with particular regions is also given in Section 7.3.1 and centers on Figure 7.27. Here, a particular region is isolated exploiting the previously computed strainlines.

The "sliver" encompassing the marked state in Figure 7.38 is selected for additional study. Recall that the marked state is associated with a particular trajectory option, taken somewhat arbitrarily from the map, that displays general characteristics desirable for orbiting Oberon. Further numerical analysis is possible within the given region. In Figure 7.39 precise boundaries have been utilized to isolate the associated region. Then, a constraint is initiated to maintain a minimum altitude of 240 km from Oberon, and initial states leading to immediate violations (colored red) are

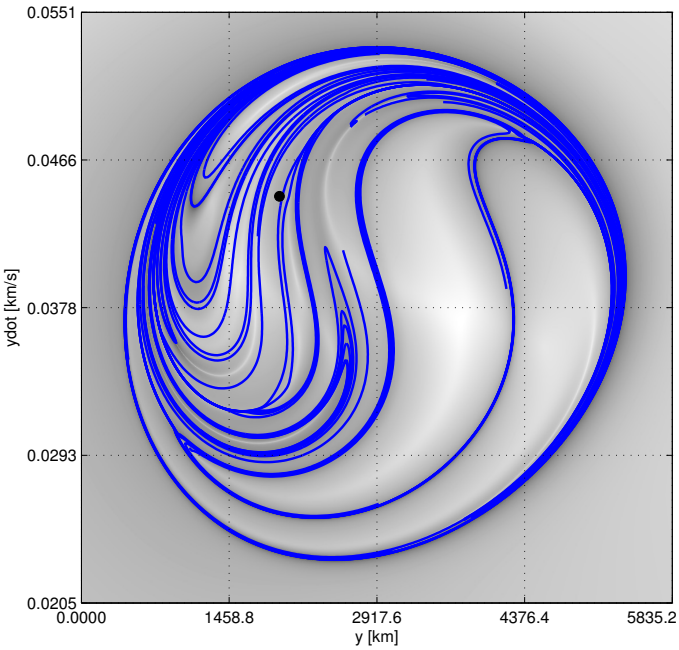

Figure 7.38.: Figure 7.26(b) Reproduced for Additional Analysis

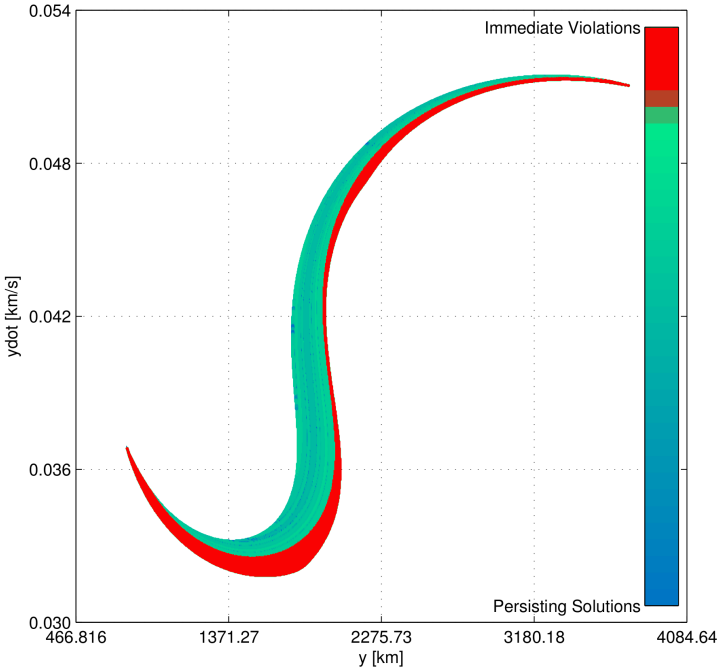

Figure 7.39.: Initial Filtering Within Isolated Region

removed. The remaining states mark the designated region for study. This resulting set of points is amenable to discrete analysis, and the boundaries may be further employed to ensure that a continuous numerical process remains in the domain.

7.4.2 Numerical Analysis Within the Example Region

To illustrate the utility of well-parametrized boundaries for numerical analysis, a simple example is offered. As noted, the particular state selected for the initial Oberon phase of the example from Section 7.3.1 is intentionally chosen somewhat indiscriminately to highlight the power of flow control segment approaches. That is to say, a state that displays some desired behavior in a particular region is selected, but no attempt is initially made to ensure that this state is the *best* state under some criterion. A closer inspection of the associated region allows for an optimal choice.

Within the region indicated in Figure 7.39, a relatively dense grid of 56,100 points is constructed prior to filtering. For the states that remain after initial filtering, FTLE values are plotted in Figure 7.40 consistent with an evolution for 20 nd time (∼43 days). These FTLE values mark the initial conditions (IC) for further analysis. From this set of IC, a discrete optimization problem is initiated. Accounting for Oberon's radius of ∼760 km, the objective is to maximize the time of flight, T, for a trajectory that maintains the lower altitude constraint (240 km) from Oberon as well as an upper altitude constraint (24240 km). The optimization problem is written,

$$\begin{aligned} \text{Minimize:} \quad & -T\left(\phi_{t_\text{o}}^{t}\left(\boldsymbol{x}_\text{o}\right)\right) \\ \text{Subject to:} \quad & g_1(\boldsymbol{x}) \geq 240 \text{ km} \\ & g_2(\boldsymbol{x}) \leq 24240 \text{ km}, \end{aligned} \tag{7.2}$$

where g_i are altitude constraints given as a function of the state, $\boldsymbol{x}$, at any time in the trajectory evolution and $\boldsymbol{x}_\text{o}$ is an initial condition. Also indicated in Figure 7.40 is the constrained discrete optimum marked with a black point, a trajectory that revolves about Oberon numerous times over the course of about 214 days before departing the region. The associated trajectory is illustrated in Figure 7.41 where two views

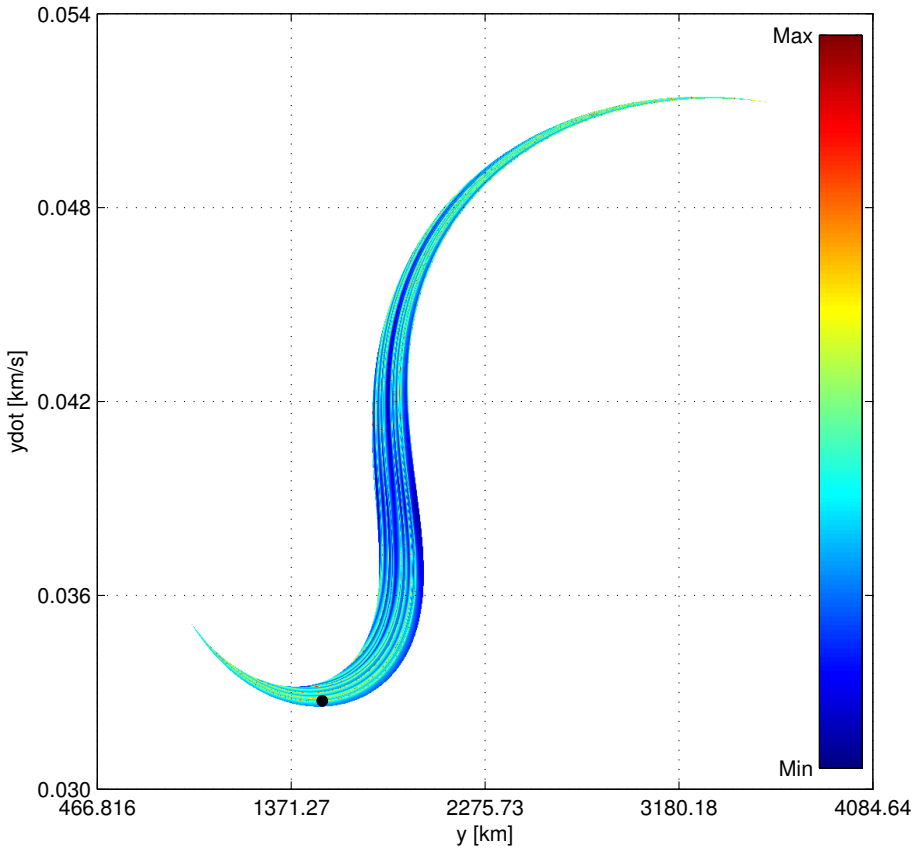

Figure 7.40.: FTLE Values and Discrete Constrained Optimum

are included. In Figure 7.41(a) the trajectory is colored by its distance from Oberon (smaller radii in violet, larger in red), while in 7.41(b) the trajectory's evolution is indicated from violet to red in time. Recall that the Oberon map and associated trajectories are computed in reverse time. Thus the trajectory is propagated from the left in the opposite direction of the upper arrow, evolves in reverse time into the Oberon vicinity and ultimately departs against the lower arrow continuing in reverse time out of the Oberon region. Of course, the arrows indicate the flow in forward time. While the included solution is taken as the best case from a discrete grid of solutions, the approach extends easily to a more continuous search strategy. In this particular case, only an illustration of the process is intended.

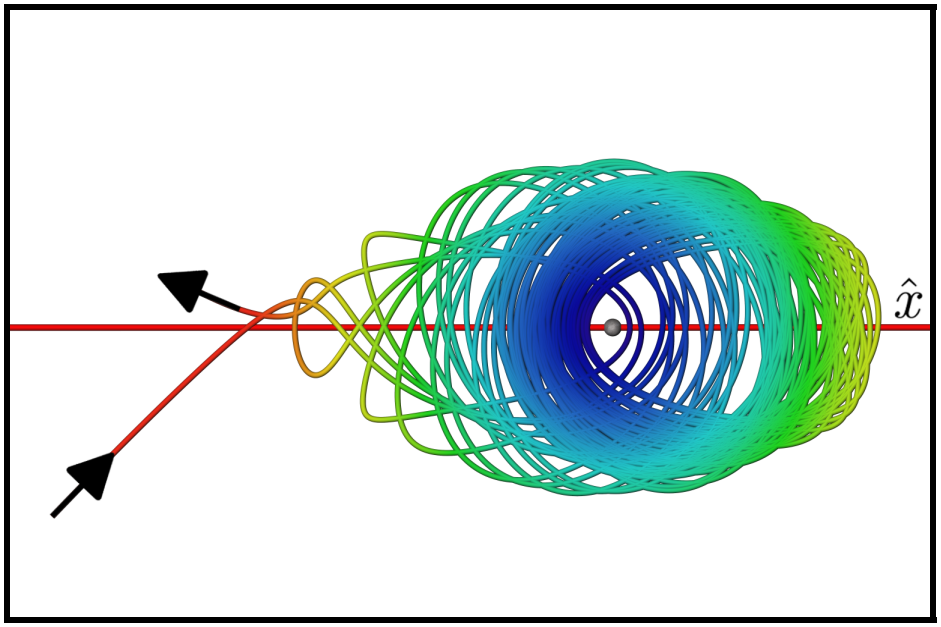

(a) Colored by Distance from Oberon

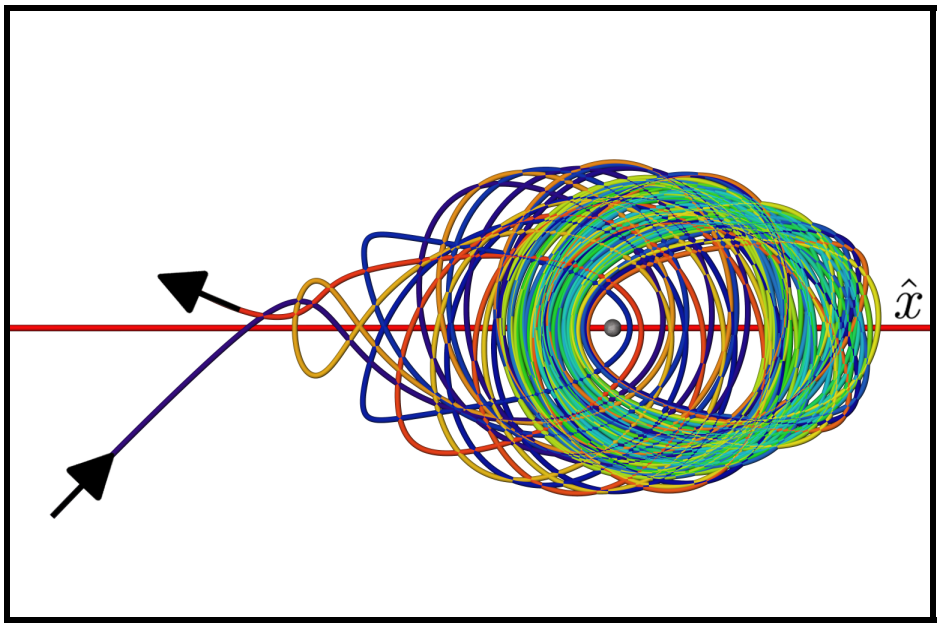

(b) Colored by Evolution in Time

Figure 7.41.: Views of a Discrete Constrained Optimal Solution

7.5 Maneuver Analysis and Insight

Flow-based concepts not only add insight for design, but also support analysis. Recent ARTEMIS[2] trajectory phases involved significant operations in the vicinity of the Earth–Moon L_1 and L_2 libration points. Effective stationkeeping during these phases was important for mission success. The computation of FTLE values adds some context for the ARTEMIS maneuver strategy. Investigations by Folta et al. [82, 83], as well as Pavlak and Howell [84], demonstrate that the optimal, plane-constrained stationkeeping maneuvers during the Lyapunov phases of the ARTEMIS trajectory correlate strongly with the stable direction recovered from an approximate monodromy matrix ($\mathbf{M}$) associated with revolutions of the trajectory. The optimal maneuver direction for a stationkeeping cycle aligns with the position projection of the stable eigenvector computed from an approximation to the monodromy matrix. The FTLE values in the vicinity of ARTEMIS maneuver points generally concur with the stable direction alignment of the constrained optimal maneuvers.

To explore one such stationkeeping maneuver, consider a reconstruction of one revolution along the path of the ARTEMIS $P1$ spacecraft. Specifically, the focus is one revolution about L_2 in the Earth–Moon system as depicted in Figure 7.42. The red horizontal line is the rotating x-axis, the red sphere, L_2, and the Moon is depicted to scale. The actual spacecraft implemented a maneuver near the x axis between the Moon and L_2, as marked with the black $\times$ in the figure, on November 17, 2010 08:45:00 UTC. The direction of motion along this arc is denoted with color; it begins in violet and terminates in red. Thus the trajectory is recovered by evolving forward in time (3.5 nd time steps, $\sim$15.198 days) from the maneuver point. To serve as a basis for comparison, the uncorrected ARTEMIS $P1$ state is evolved in an ephemeris system similar to the one described in Section 3.4. For this example, the central body is the Earth, and the system is denoted an Earth–Moon–Sun (EMS) system.

[2]NASA's Acceleration, Reconnection, Turbulence and Electrodynamics of the Moon's Interaction with the Sun (ARTEMIS) mission.

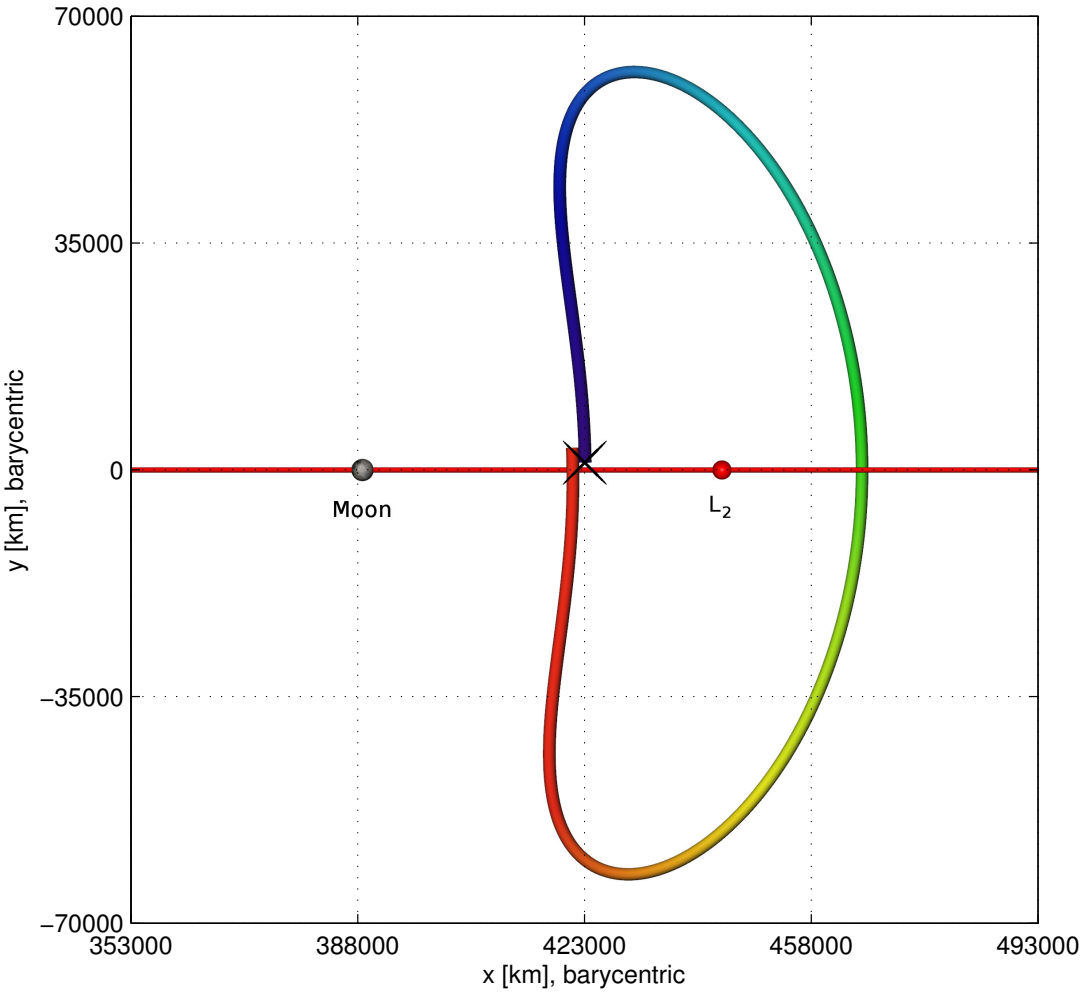

Figure 7.42.: Uncorrected ARTEMIS $P1$, L_2 Segment

Notwithstanding the planar representation of the trajectory in Figure 7.42, significant out-of-plane excursions occur during the plotted stationkeeping cycle.

To generate the stable and unstable directions for the arc shown in Figure 7.42, finite differences are used to generate the forward-time state transition matrix (STM, Φ), in this case, an approximate monodromy matrix ($\mathbf{M}$). The maneuver direction is then compared with (1) the stable direction as computed from $\mathbf{M}$, and (2) surrounding FTLE values. The directions of the relevant vectors and the FTLE values at various points in the surrounding field appear in Figs. 7.43–7.46. Three orthographic projections as well as a 3D view are included in the figures.

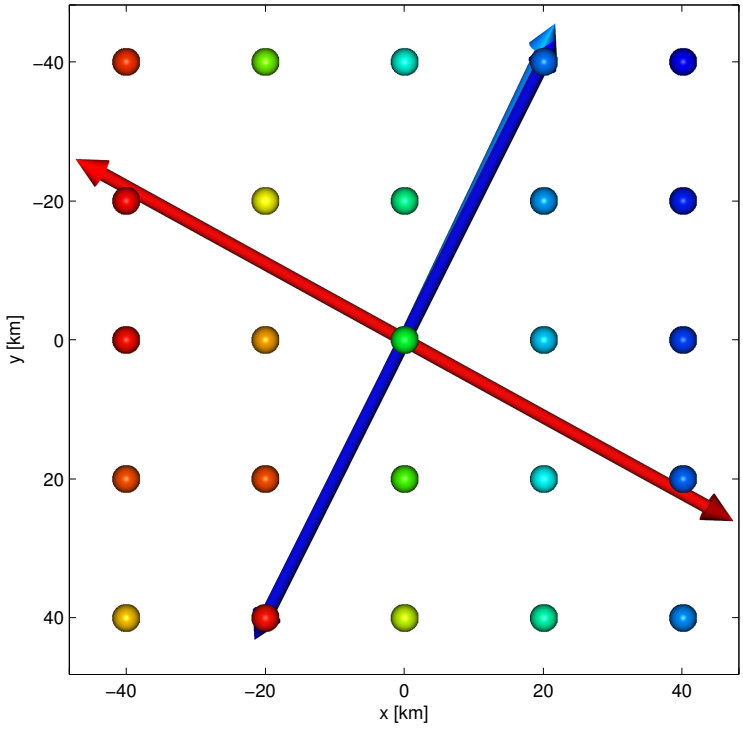

Figure 7.43.: Maneuver and Stability Directions (x–y)

In the figures, x–y–z Cartesian inertial axes appear; in the 3D view in Figure 7.46 the axes are colored in darker shades of red, green and blue, respectively. In each of the figures, the position projection of the stable eigendirections from the monodromy matrix are represented by double-headed blue arrows, while the corresponding unsta-

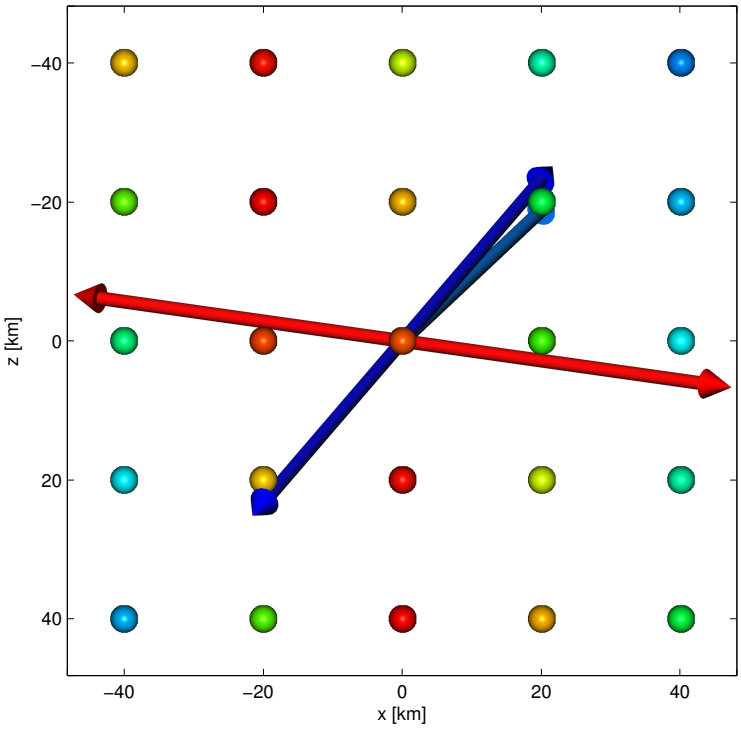

Figure 7.44.: Maneuver and Stability Directions (x–z)

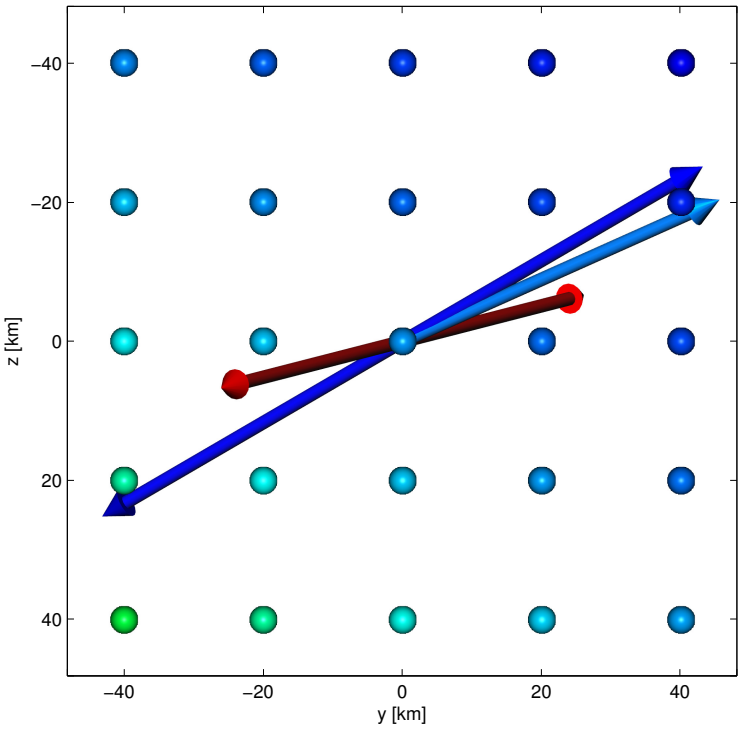

Figure 7.45.: Maneuver and Stability Directions (y–z)

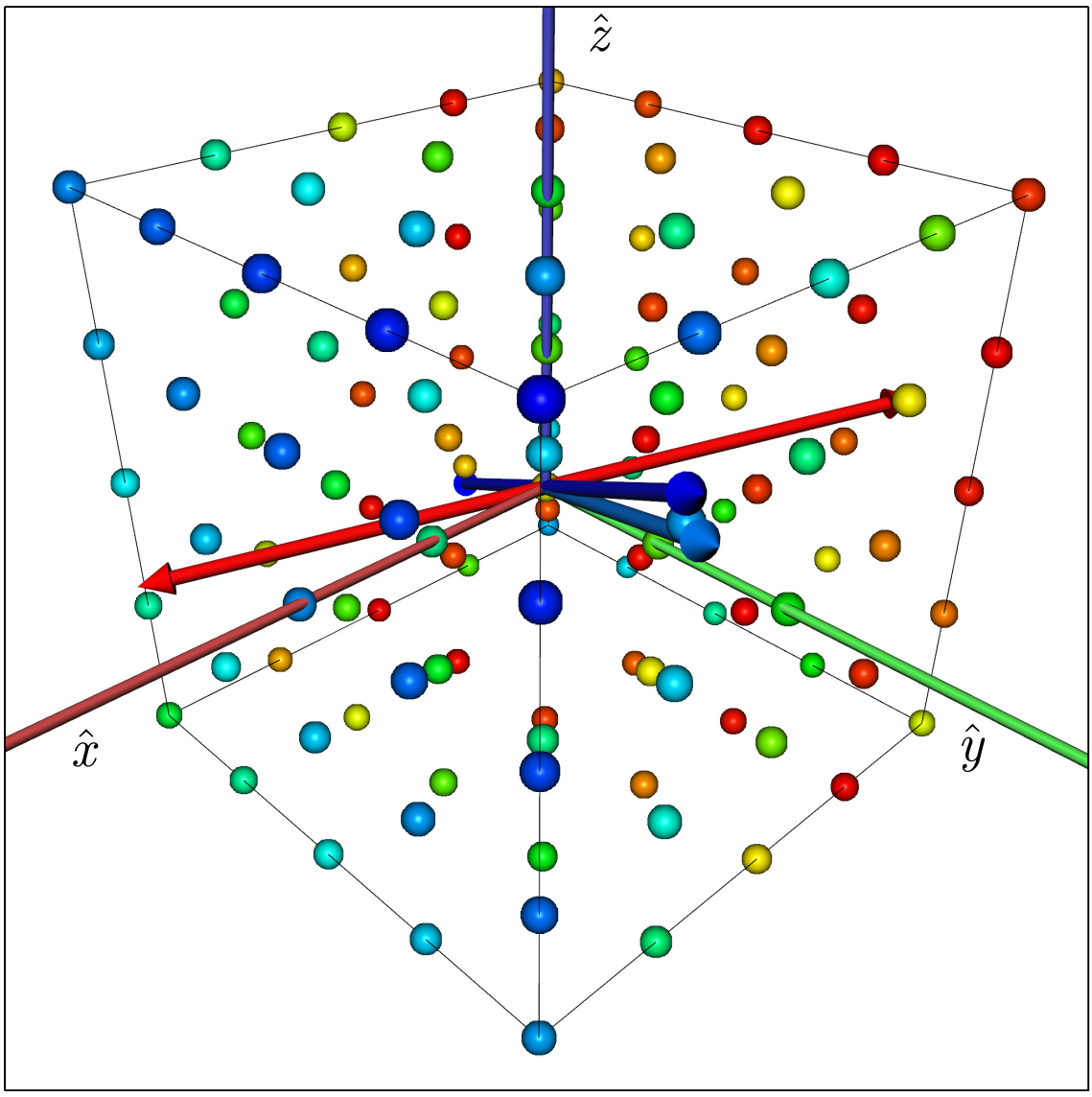

Figure 7.46.: Maneuver and Stability Directions (3D)

ble directions are depicted as double-headed red arrows. The direction of the actual ARTEMIS $P1$ maneuver is indicated in the figures with a cyan arrow. Each of the directions are scaled in length for visualization. Also plotted in the figures are points of forward time FTLE values colored using a "rainbow" color scale with red denoting the largest magnitude of the values of forward FTLE and blue coloring the lowest values. In the planar figures, the relative FTLE coloring is taken from the top-most slice, for a given projection, on the boundary of the cube (as seen in Figure 7.46). The FTLE values are generated by stepping away from the maneuver position in steps of 20 km to form a $5\times5\times5$ point grid of FTLE values spanning a cube of ±40 km. Each grid point is evolved forward for a time consistent with the forward propagation of the arc in Figure 7.42. Thus, a three-dimensional stroboscopic map of FTLE results. Observe that the actual maneuver direction aligns well with the stable direction as described by Folta et al. as well as Pavlak and Howell. Additionally, the optimal maneuver is directed generally in the least sensitive direction (the direction of the blue points) as illustrated by the 3D FTLE grid. That is, the maneuver direction, in this case, orients toward smaller FTLE values consistent with the stable direction.

Repeating the process of comparing the plane-constrained optimal ARTEMIS maneuver directions with surrounding FTLE values reveals a general correspondence similar to that illustrated above. Of 27 selected[3] maneuvers associated with the L_1/L_2 phase of the ARTEMIS $P1$ trajectory, all but 4 orient generally away from higher FTLE values. The directed nature of the analyzed maneuvers is summarized in Table 7.3. A few of the maneuvers (marked with an asterisk in the table) orient generally with *locally* lower values of FTLE rather than the minimum value in the FTLE cube. In these cases, where the maneuver points toward locally smaller values, the higher values of FTLE "slice" through the cube between two regions of lower values. In fact, this type of bifurcated FTLE field is observed in Figs. 7.43, 7.44 and 7.46. Finally, the gravitational influence of the Moon tends to promote stretching, and

[3]A few of the performed maneuvers during this phase are neglected as not solely stationkeeping maneuvers. For example, maneuvers 12–15 are associated with a transition from L_2 to L_1 regions.

Table 7.3: Maneuver and FTLE Alignment

Maneuver	L_1/L_2	Δt [nd]	Smaller FTLE Orientation
P1-03	L_2	3.50	Yes
P1-04	L_2	3.40	Yes
P1-05	L_2	3.70	Yes
P1-06	L_2	3.50	Yes
P1-07	L_2	3.40	Yes
P1-08	L_2	3.57	Yes*
P1-09	L_2	3.70	Yes
P1-10	L_2	3.50	Yes
P1-11	L_2	3.60	No
P1-16	L_1	2.92	Yes
P1-17	L_1	3.20	Yes*
P1-18	L_1	3.20	No
P1-19	L_1	3.00	Yes
P1-20	L_1	2.90	Yes
P1-21	L_1	3.05	Yes*
P1-22	L_1	3.30	Yes
P1-23	L_1	3.10	Yes
P1-25	L_1	2.97	Yes
P1-26	L_1	3.25	Yes
P1-27	L_1	3.20	Yes
P1-28	L_1	2.95	No
P1-29	L_1	2.95	No
P1-30	L_1	3.20	Yes
P1-31	L_1	3.20	Yes*
P1-32	L_1	2.95	Yes
P1-33	L_1	2.95	Yes
P1-34	L_1	3.20	Yes*

consequently higher FTLE, in the direction of the Moon. In the cases where the maneuver resolves along the stable direction toward the Moon to satisfy the constrained optimization problem, it necessarily points in the direction of larger FTLE. This is observed in the cases where the maneuver is not oriented toward smaller FTLE. That is, when the maneuver points toward larger FTLE it also points toward the Moon.

This analysis of ARTEMIS maneuvers from a flow perspective provides a compelling avenue for the application of FTLE as a predictive metric. A potential advantage exists for utilizing FTLE values to complement mode analysis to inform stationkeeping strategies. Moreover, the context supplied by the flow about maneuver points helps to correlate the inclination for the optimal maneuver to align in a stable direction in this particular case. Such an analysis supports understanding of trajectory behaviors and helps to inform future trajectory designs.

7.6 Perturbation Analysis: Investigating Long-term Behavior

Many interesting natural solar system behaviors can only be understood within the context of resonances that exist between the motions of the associated bodies. Recently, efforts to exploit resonance for spacecraft trajectory design have become a focus for practical applications. In particular, researchers have explored the possibility of harnessing resonant orbits for transfer trajectories [101–103], and for stable orbits with desirable repeating motions [70, 104, 105]. Such strategies support useful mission options, and reflect options afforded by carefully navigating a chaotic design space.

Of particular relevance for spacecraft trajectories are orbit-orbit resonances. Such resonances are those where the spacecraft's motion repeats in a near-integer ratio relationship with the motion of a massive system body. For example, in the Earth–Moon system, the Moon orbits the Earth once every sidereal period, q, of $\sim$27.3 days. A spacecraft moving in the Earth–Moon system with a characteristic period, p, that is some multiple of the Moon's period is said to be moving in a p:q resonance with the Moon. If the spacecraft completes two revolutions for each revolution of the Moon, this resonance is designated as a 2:1 resonance. Such exact integer ratio behaviors only appear in simple models of the dynamical system behavior. However, within higher-fidelity-model contexts, motion that oscillates about such resonances frequently persists and is often reflective of stable behavior.

The Transiting Exoplanet Survey Satellite (TESS) mission orbit is selected in a nearly 2:1 resonance with the Moon in the Earth–Moon system. Thus, the orbit is characteristic of a period roughly half that of the lunar sidereal period, or $\sim$13.67 days. While the orbit does not generally complete exactly two revolutions for each revolution of the Moon, it can be described as "in oscillation" about such a resonance [70]. The orbit is constructed such that its apogee approaches the lunar orbital distance, and remains at about $\pm 90^{\circ}$ from the Moon itself, alternately leading and lagging. It is convenient to observe such motion in a rotating frame fixed on the motion of the Moon about the Earth, and such a representation appears in the lower panel of Figure 7.47

along with an inertial view of the first 10 periods of a solution resembling the TESS science orbit. In both frames the trajectory evolution is indicated by color ranging from blue to red following a rainbow color mapping.

It is desirable for the spacecraft to be operationally stable, requiring no station-keeping, upon entering and for the 2–4 year duration of the science phase of the trajectory. Throughout the nominal mission and for, at least, 100 years beyond the end of the mission, the spacecraft trajectory is also required to avoid the geosynchronous orbital band at all times. The trajectory is designed to satisfy this requirement throughout all mission phases and employs a "dispose-in-place" strategy after the end of the mission. However, extended, long-term analysis of the trajectory reveals particular modes where the spacecraft behavior can settle into motion consistent with the avoidance of the geosynchronous band. These modes are trajectory phases that are induced by the natural dynamics but, without a more complete understanding of the dynamical environment, it is not certain that a perturbation or disturbance would not shift the modes into some undesirable behavior.

Initial explorations in the phase space nearby the TESS science orbit reveal particular solutions that eventually diverge from the nominal mission orbit but actually exhibit desirable end-of-life behavior. However, the existence of these alternate solutions also implies the potential for undesirable divergence, and a better understanding of the long-term behavior is necessary. Mission requirements constrain the perigee radius for the science phase of the trajectory to remain above 6.7 Earth radii (r_e) to avoid the geosynchronous satellite belt. To minimize communication times for data retrieval, perigee (r_p) should also remain below 22 r_e for the duration of the nominal science phase (2–4 years). The TESS mission calls for a dispose-in-place end-of-life strategy where the spacecraft will continue in the mission orbit. Avoidance of the GEO belt for at least 100 years is also required. However, after the science phase, the upper bound on r_p is no longer critical. Thus, behavior that settles into an orbit with higher perigee radii has the potential for greater stability while increasing the distance from the geosynchronous satellites.

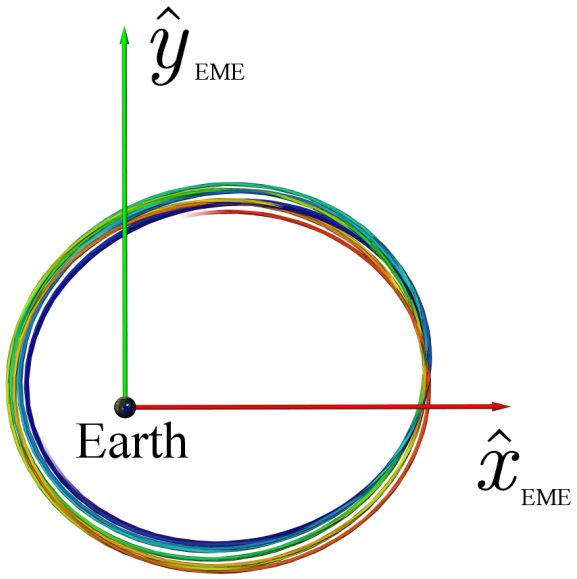

(a) Earth Mean Equatorial of J2000

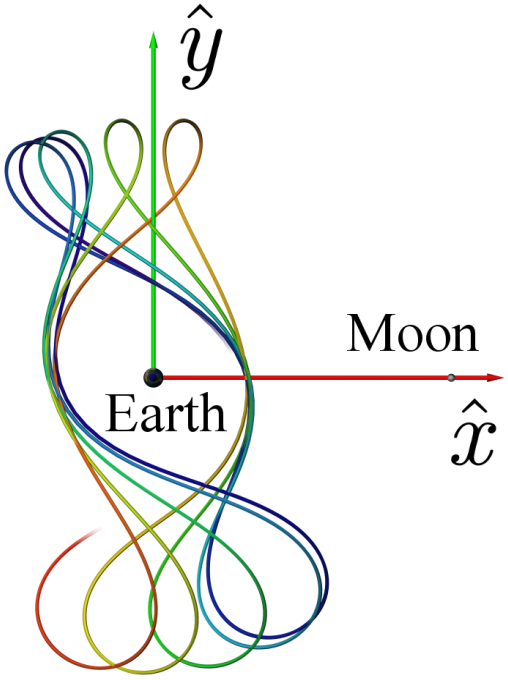

(b) Earth–Moon Rotating Frame

Figure 7.47.: 10 Periods of a TESS-like Science Orbit (Ephemeris Model)

To identify solutions that evolve into advantageous behavior modes, and to better understand the local neighborhood of perturbations near the reference solution, several strategies are invoked. Initially, a single-parameter exploration of small variations in the rotating-y component of the state at the Period Adjust Maneuver (PAM), that is, the maneuver to enter the TESS science orbit, reveals various solutions. Among these solutions are those displaying behavior consistent with the perturbed option investigated in this analysis. Inspection of the long-term behavior of the orbital elements and observation of individual frequency markers supports the characterization of certain behavioral transitions. From a particular solution, investigations in terms of small perturbations reveal additional insight into the long-term trajectory behavior. Toggling model-fidelity and examining the state components aids in illumination of the complexities of the cumulative effects of the various system influences on the spacecraft path over time. Invoking the flow context provides a clear picture of the truly chaotic nature of the system, and supports identification of potentially useful end-of-life solutions. A strategy for identifying specific conditions for entering these solutions is discussed. The chaotic nature of the spacecraft operating environment supplies many possibilities and all of these varied, but ultimately related, analysis options lead to a better understanding.

7.6.1 Perturbation Theory and the Kozai Parameter

Perturbation methods offer useful analysis options for understanding the contributing factors in orbital motion. Colombo [106] and Colombo et al. [107] examine the long-term perturbative effects on highly-elliptical and libration point orbits, and explore the possibility of engineering desired end-of-life options for various mission scenarios, including graveyard orbit and re-entry/impact options. The present analysis focuses on understanding the context associated with the effective graveyard orbit represented by the TESS dispose-in-place strategy. Rather than employing analytical or semi-analytical, general perturbation theory, the focus is on special perturbation

analysis through numerical simulation. As a stepping-off point from general perturbations, consider the evolution of the Kozai parameter plotted in Figure 7.48. This parameter reflects a constant of the motion under the Kozai formulation of the three-body problem where short-term oscillations due to the third-body perturbation are essentially averaged out [70, 108, 109]. The Kozai parameter is defined,

$$K = \cos i \cdot \sqrt{1 - e^2}, \tag{7.3}$$

and, similar to the Jacobi constant, is not expected to be conserved in higher-fidelity models. However, its evolution can be observed when calculated instantaneously at each time step along the trajectory using osculating elements. In Equation (7.3), i and e are the inclination and eccentricity of the spacecraft orbit with respect to the lunar orbital plane. As the Kozai mechanism features heavily in the design strategy for the TESS mission and supports some general trends consistent with the science orbit [69, 70], it seems reasonable and appropriate to initiate the present analysis with a discussion of the behavior of the Kozai parameter over time. The TESS orbit in the Design Reference Mission (DRM) has been selected for its transitioning behavior. Thus, the evolution of an initial state slightly perturbed from the TESS DRM trajectory reflects the potential differences in responses. Gangestad et al. [69] identify a suitable Kozai parameter to be 0.65 to maintain the upper and lower constraints on r_p. Apparent in Figure 7.48 is an initial value of K that oscillates about values lower than 0.65, and then shifts into two later phases oscillating above 0.65. These differences, aside from being expected as associated with a different solution, illustrate two relevant points. First, much of the previous analysis for the TESS DRM focuses on the first few decades of the mission, and is generally consistent with the results showcased in the orbit selected for this analysis. Second, these behavior-shifting trends, characteristic in many of the orbital measures associated with this solution, are reflective of the different modes through which the trajectory evolves. Various metrics reflect these modes and their associated transitions more or less clearly. This brief inspection of the Kozai parameter serves as an introduction to a series of observations that help establish the perturbed orbit that is investigated in this analysis.

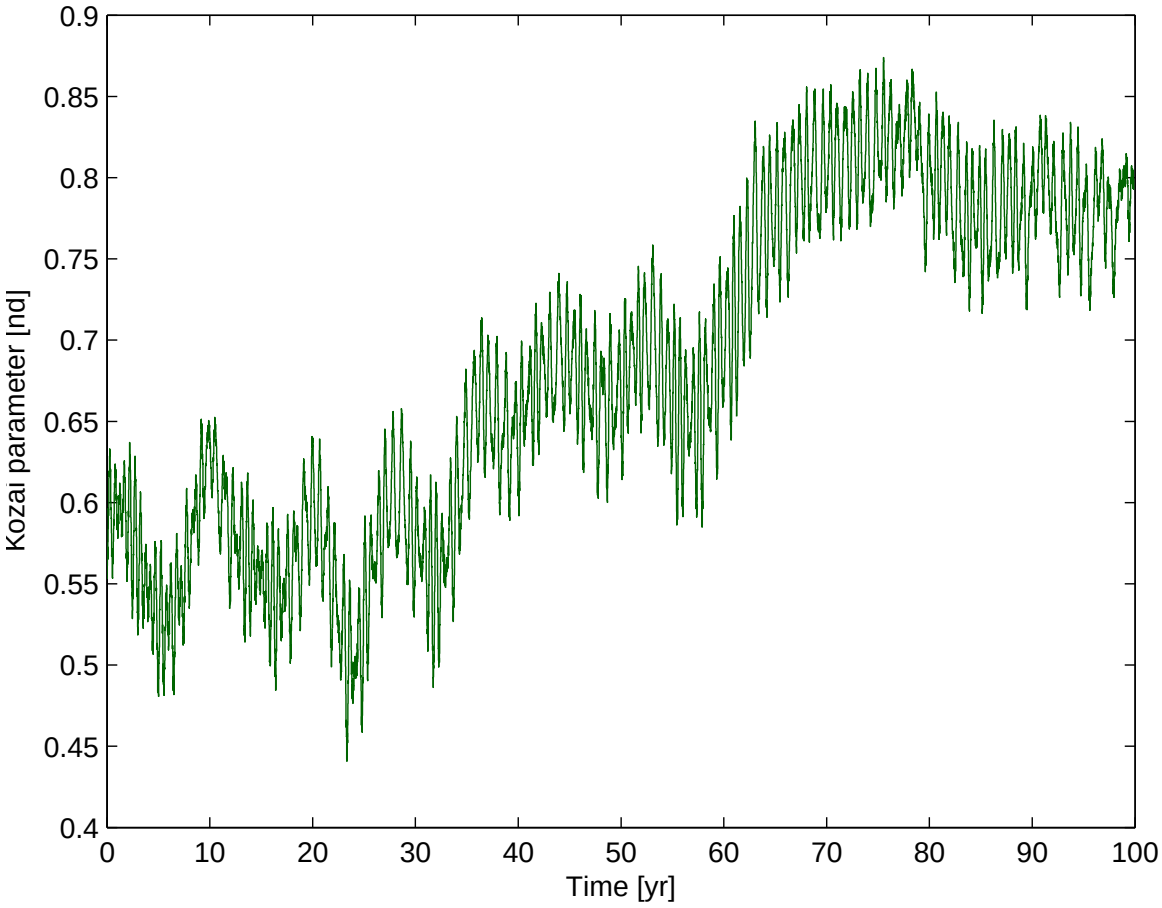

Figure 7.48.: Evolving Ephemeris Kozai Parameter for TESS-like Science Orbit

7.6.2 Orbital Elements

Inspection of the evolution of the osculating orbital elements serves to further establish the long-term behavior exhibited by a given particular solution. Given the TESS DRM orbit, perturbations that shift the initial state vector of the Period Adjust Maneuver (PAM) are explored. A significant percentage of perturbed trajectories display qualitatively distinct long-term behaviors and are discussed in later sections. As an example, a single "perturbed baseline" trajectory is inspected initially. Specifically, a modest perturbation to increase the rotating-y position coupled with a corresponding decrease in the rotating-z position and a velocity change results in a particular solution characteristic of interesting behavior modes. These modes are apparent in the various panels included in Figure 7.49 as well as in the evolution of the Kozai parameter depicted in Figure 7.48. These panels, all associated with the perturbed sample trajectory, depict the evolution of each of the osculating Keplerian orbital elements. Also included is an FTLE profile associated with the trajectory. There are several notable observations concerning the trajectory evolution. From panel (a) in Figure 7.49, it is apparent that this perturbed, particular solution leads to the spacecraft r_p initially evolving above 22 r_e after about 10 years. Each of the other panels reveal, to greater or lesser degree, two additional, major transitions in behavior as the evolution approaches 40 years and just after 60 years. As the radius of perigee increases above 22 r_e after 60 years, r_a decreases into the lower-to-mid 50 r_e range consistent with the drop in eccentricity observed in panel (b). This coupled increase in distance from the Earth and decrease in distance from the lunar orbit represents additional stabilization of the orbit. Each of these effects is reflected in the FTLE profile of panel (f). This FTLE profile, consistent with look-ahead times of $\sim$1.2 years for each point, clearly indicates and summarizes the mode shifts along the trajectory while supplying a measure for stability with respect to perturbations relative to the orbit. Larger values of FTLE indicate more sensitive trajectory regions.

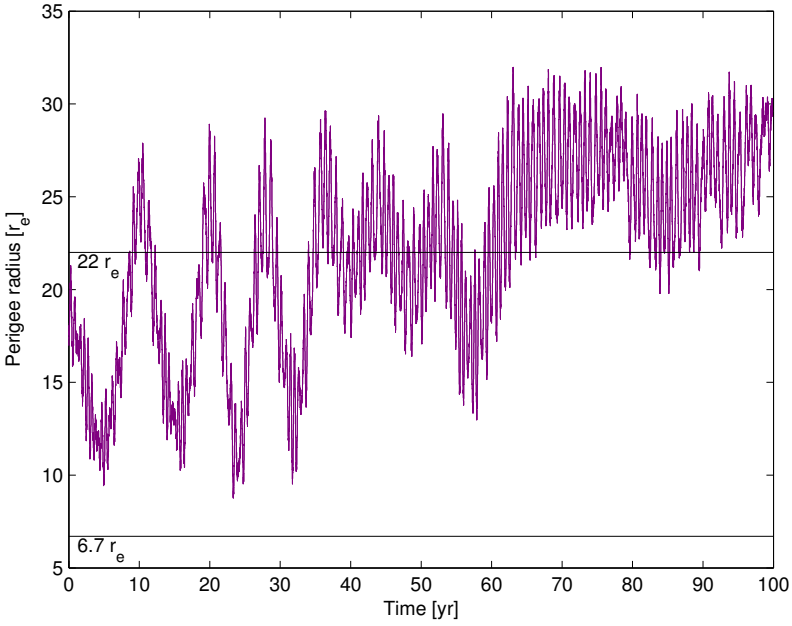
Perigee radius [r_e]
Time [yr]
22 r_e
6.7 r_e
35
30
25
20
15
10
5
0
10
20
30
40
50
60
70
80
90
100

(a)

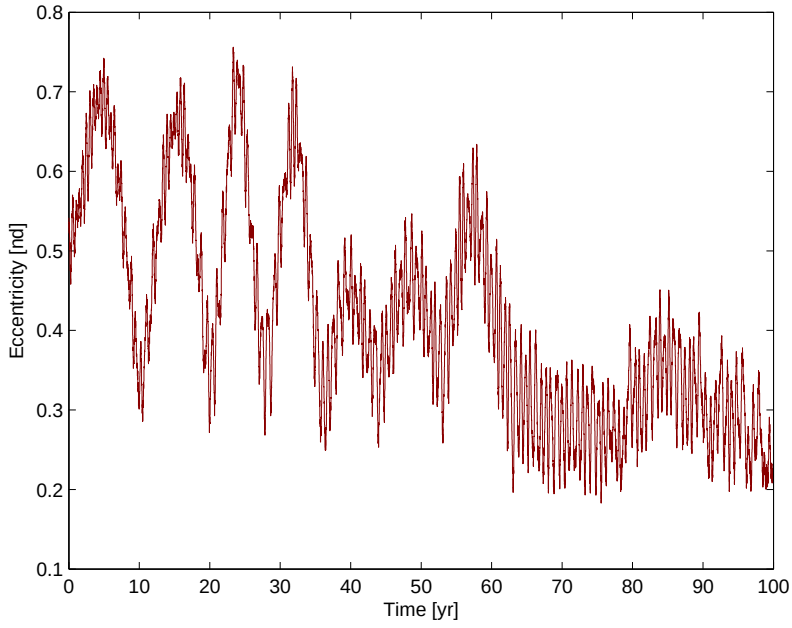
Eccentricity [nd]
Time [yr]
0.8
0.7
0.6
0.5
0.4
0.3
0.2
0.1
0
10
20
30
40
50
60
70
80
90
100

(b)

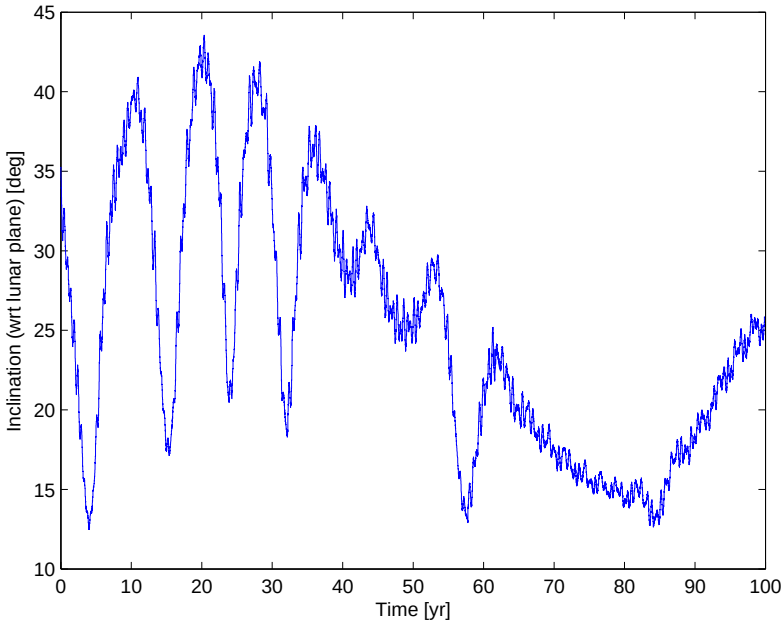
Inclination (wrt lunar plane) [deg]
Time [yr]
45
40
35
30
25
20
15
10
0
10
20
30
40
50
60
70
80
90
100

(c)

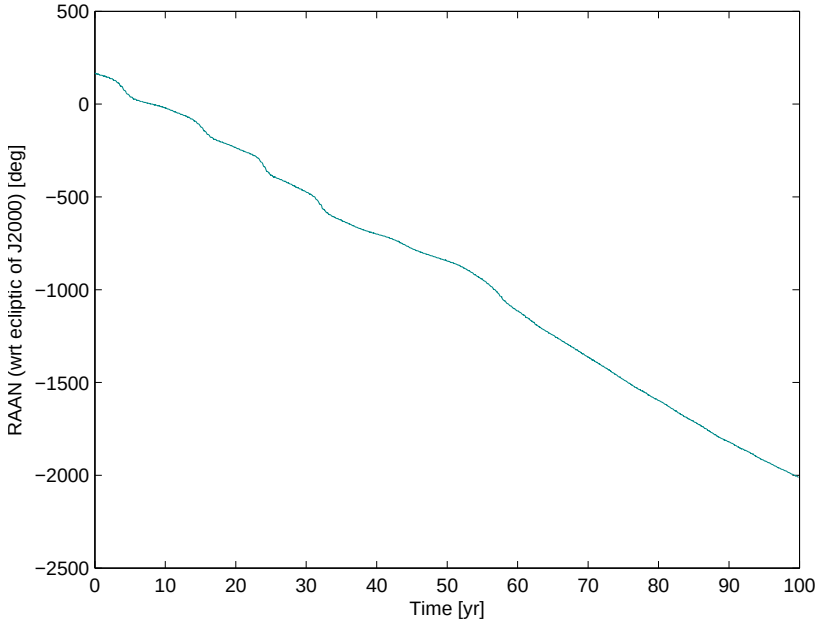
RAAN (wrt ecliptic of J2000) [deg]
Time [yr]
500
0
−500
−1000
−1500
−2000
−2500
0
10
20
30
40
50
60
70
80
90
100

(d)

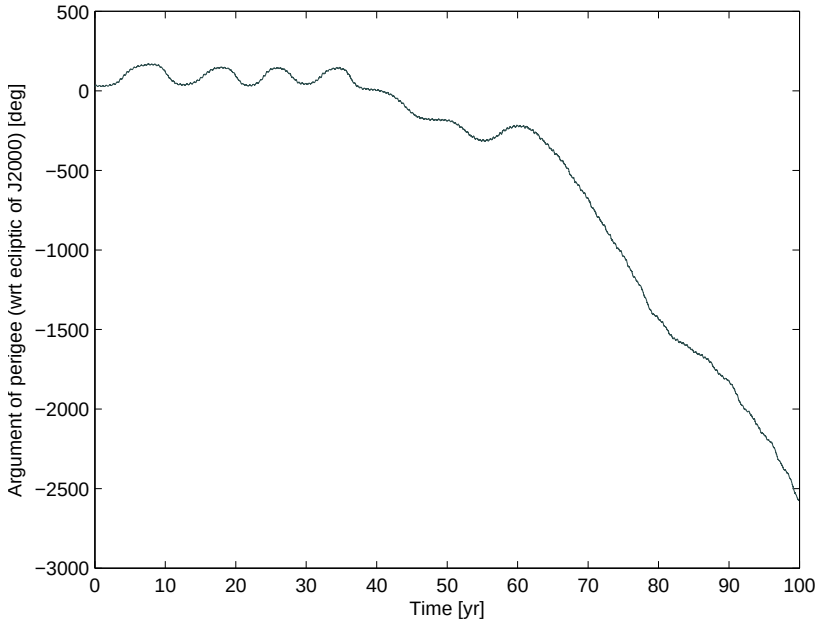

(e)

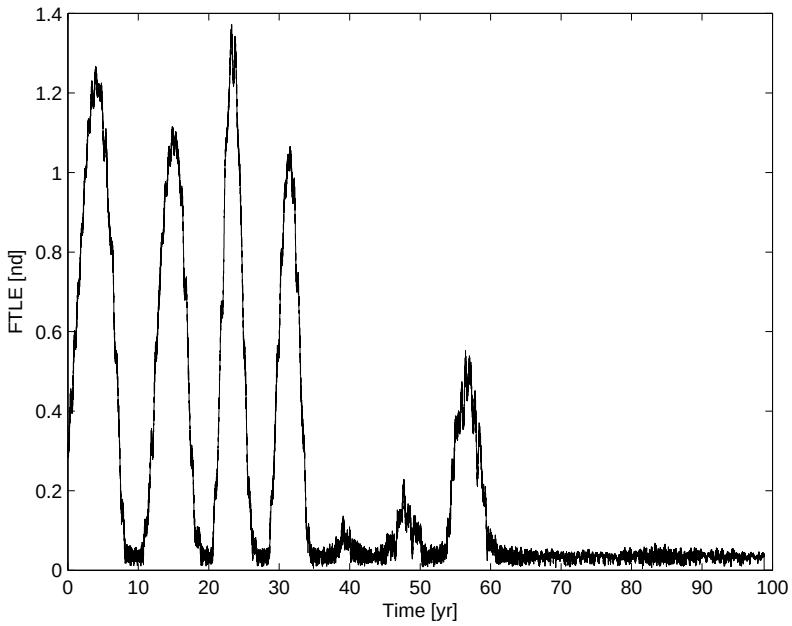

(f)

Figure 7.49.: Osculating Orbital Elements and FTLE Profile

7.6.3 Frequency Analysis

Inspection of the frequencies in the "signal" associated with a spacecraft trajectory can be a useful strategy to identify particular contributions to the motion of the spacecraft. For example, Bosanac, Howell and Fischbach [110] employ frequency analysis strategies to characterize the impact of including three-body interactions along with the inverse square pairwise contributions in a three-body system. In Figure 7.50, the amplitude density associated with the fundamental frequencies and some subharmonics embedded in the time-history of one acceleration component are plotted. These frequencies are associated with the y component of the spacecraft accelera-

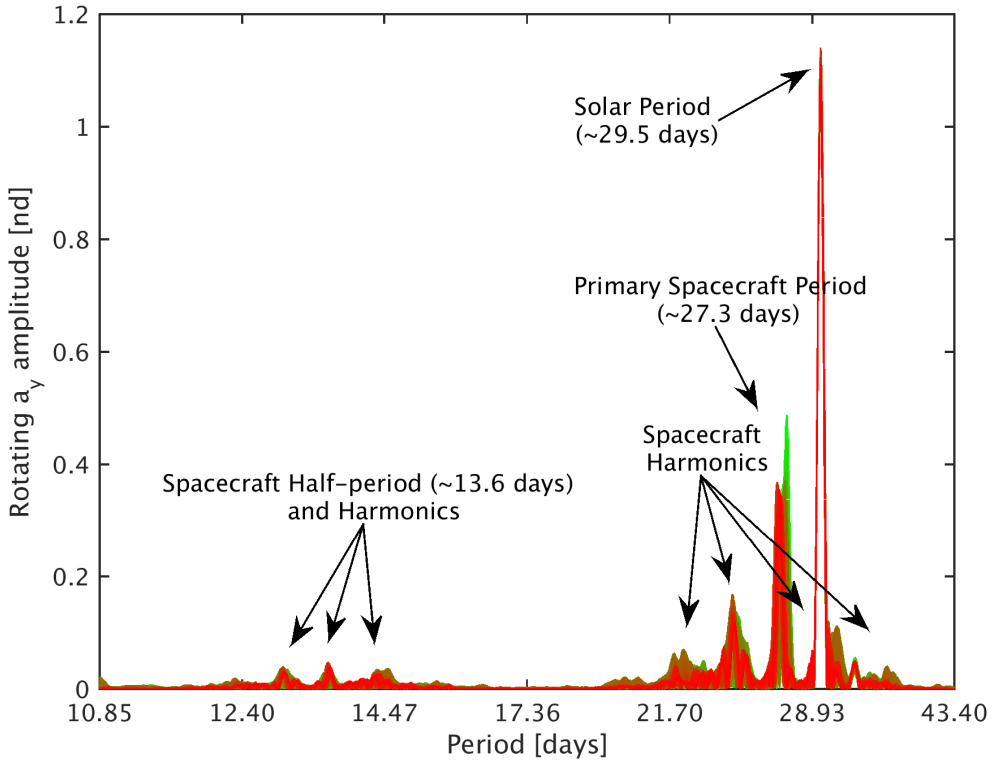

Figure 7.50.: Rotating Frame Frequencies in a_y from Perturbed Baseline

tion as viewed in the rotating-pulsating-librating frame that instantaneously fixes the Earth and Moon consistent with their ephemerides. Further, the frequency data are associated with the perturbed baseline trajectory that is evolved under the Sun–

Earth–Moon ephemeris dynamics—the trajectory that is characterized in Figures 7.48 and 7.49. These frequency responses result from discrete Fourier transforms, implemented numerically as a Fast Fourier Transform (FFT), of overlapping data intervals initiated every four months and spanning 10 years each. The curves are colored by the initial time of the associated FFT interval, and range from green to red. A closer inspection of how these curves evolve for a particular frequency is focused on Figure 7.51. Finally, the data intervals are pre-processed using a Hanning function that yields more distinct features in the frequency spectrum. Such a windowing reduces the observed amplitudes in the signal. A few of the major accelerations associated with/acting on the trajectory are labeled. For example, the peak labeled as the 'Primary Spacecraft Period' is associated with the y component of the accelerations from the Earth and Moon gravity terms in the equations of motion. Since both the Earth and Moon are instantaneously fixed in the rotating-pulsating-librating frame, the associated peaks may be considered to emerge as reflections of interactions between the spacecraft motion and the frame that is derived by the motion of the respective bodies. The solar effects on the spacecraft orbit are associated with the largest peak as a consequence of the Sun's very regular, sinusoidal motion in the rotating frame. However, the peaks associated with the accelerations from the Earth and Moon are distributed into multiple harmonics, including some higher-frequency harmonics that are not plotted. This dispersion is a consequence of the evolution in trajectory behavior over time. Allowing the FFT window to slide forward in time leads to an evolving frequency response. Generally, such an evolution would be rendered as a spectrogram. However, in this case, careful peak tracking is employed to inspect the evolving frequency and amplitude of particular signal components. In Figure 7.51, a trace of the signal contribution associated with the peak corresponding to the principal spacecraft period, as it is reflected in the trajectory's a_y signal, is depicted. The underlying frequency response (plotted in terms of period) is colored according to time with earlier peaks colored in green and later peaks colored in red. As this particular peak evolves, a distinctive difference is observable both in terms of contribution strength to the

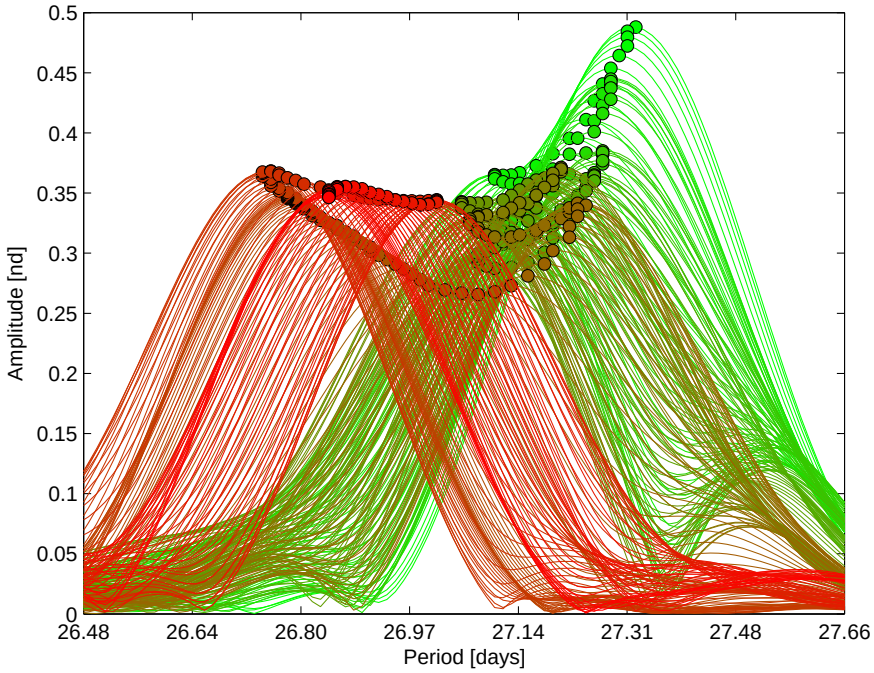

(a) Frequency Peaks Plotted as Periods

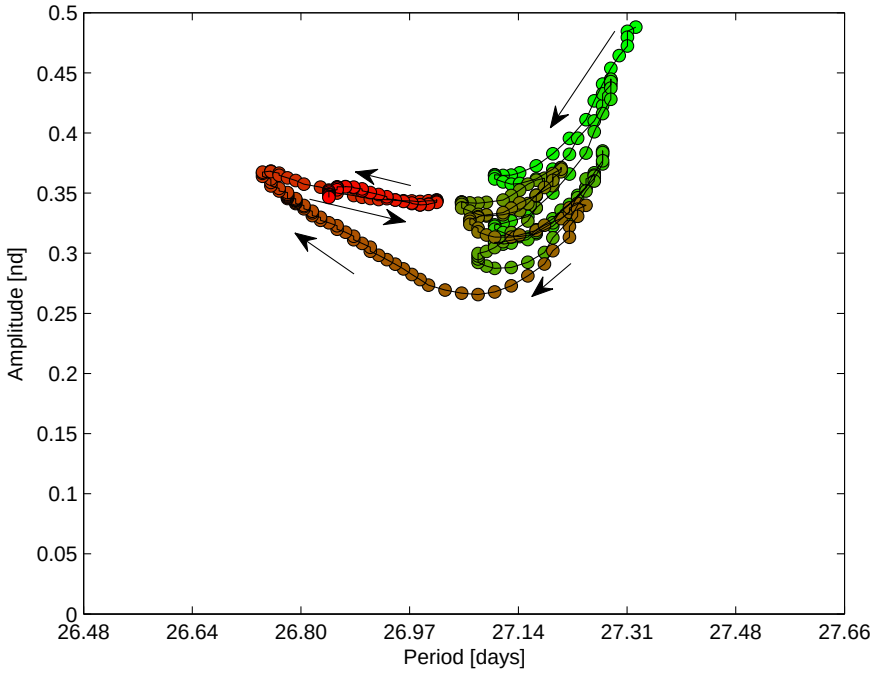

(b) Without Underlying Curves

Figure 7.51.: Trace of the Principal a_y Spacecraft Period (Over 90 Years; Points at 4 Month Intervals Represent FFT Results for the Subsequent 10 Years)

overall signal as well as in terms of the period of the signal component. As is apparent in the orbital elements, distinctive modes emerge in the frequency/period trace over time. Specifically, earlier peaks colored in green are dissociated from the later ones (consistent with the terminal trajectory behavior) colored red. In Figure 7.52, the signal component amplitudes are depicted in terms of their differences over time from their initial values. Rotating x, y, and z components are plotted and each of the three peaks with indicated periods from Figure 7.50 is tracked over time. At each point, the subsequent 10-year evolution is invoked to construct the discrete Fourier transform. Thus, the time ranges through the first ninety years of trajectory evolution. Since the frequency evolution can be interpreted not only as the evolution of spacecraft orbital characteristics but also as a consequence of the perturbations embedded in the system, it is challenging to establish any particular behavior as driven by any single factor. However, decomposing the frequency data and comparing the associated time-histories does reveal the change in the net impact in any particular component. It is notable that there are periods of time when both the Earth–Moon and solar impacts in the a_x signal trade off considerably. For example, from about 30–50 years, the Earth–Moon impact seems to decrease leading into the transitioning phases seen in Figures 7.48 and 7.49 around 50–60 years. There is some correlation between the a_x signal component associated with the "half-period peak" (green line in Figure 7.52(a)) and the primary a_y contribution (blue line in Figure 7.52(b)), which indicates a more apparent coupling of these components. While there is little change in the longer-period responses of the z signal, the associated "half-period" trace is largely reflective of the spacecraft's orbital inclination seen in Figure 7.49(c) or, more directly, its out-of-plane motion in the rotating frame. Further, in an a_z frequency spectrum, the $\sim$13.6-day period is dominant with comparable amplitudes to the $\sim$27.3-day peaks in Figure 7.50. Inspection of various frequency components lends some insight, and additional analysis of lunar and solar contributions further expands this insight.

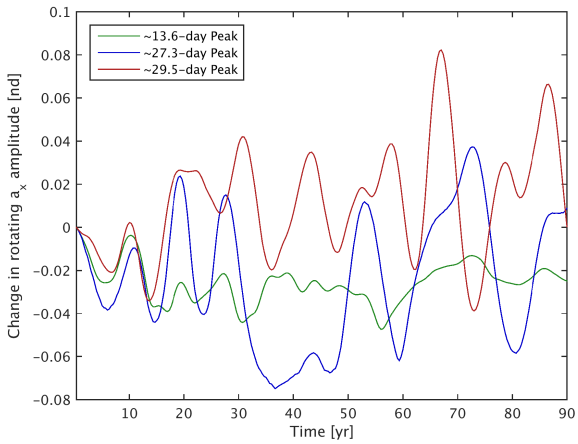

(a) From s/c a_x Signal

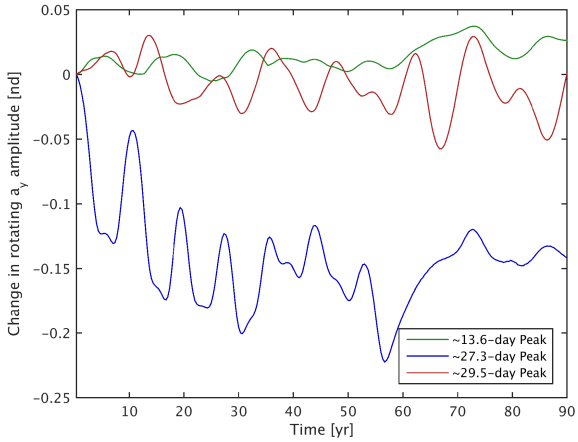

(b) From s/c a_y Signal

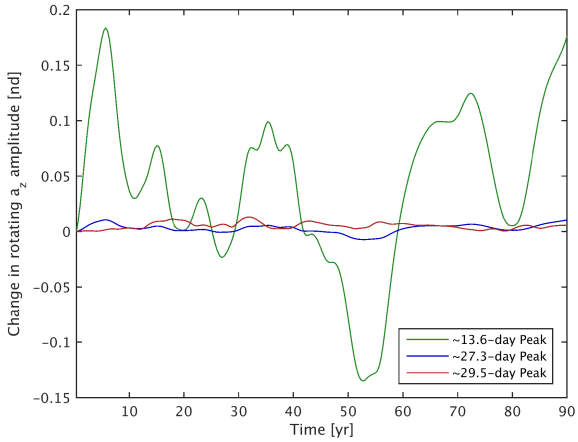

(c) From s/c a_z Signal

Figure 7.52.: Change in Amplitude for Three Tracked Peaks Over Time

7.6.4 Additional Analysis of Solar and Lunar Contributions

Recognizing that both the Sun and Moon impart significant accelerations to the spacecraft, it is useful to inspect the interplay between these bodies in terms of both relative configurations and gravity accelerations. Observation of the relative geometries of the system at important times lends some insight. Further, a quantitative analysis of the relative impacts of lunar and solar acceleration contributions supports the conclusion that the evolution of the spacecraft motion is a reflection of a coupling between the two perturbative influences.

While the general motion of the spacecraft is dominated by the influence of the Earth, neither the Moon nor the Sun can be neglected when attempting to understand the evolution of the associated orbit. Working backward from the particular epoch (September 20, 2017) associated with the particular PAM of the science orbit characterized in Figures 7.48–7.52, the early mission timeline and associated system geometry may be extrapolated. In Figure 7.53, the Sun's general direction is indicated graphically for particular events in the early phases of the DRM. The figure is depicted in the Earth–Moon rotating frame, and the central inset of the DRM is borrowed from Dichmann et al [70]. For each of the apoapses during the phasing loops, the Sun is located generally opposite the Earth from the spacecraft. This configuration is also maintained for the lunar swingby, but not for the period adjust maneuver where the Sun is on the same side of the Earth as the spacecraft. For all of the configurations in the figure, the spacecraft, Earth and Sun lie very roughly along the same line, and for the cases where this linear alignment is less accurate (e.g., apoapses 1 and 2) the spacecraft altitude is generally lower where the solar influence is decreased. The system geometry as depicted in the rotating frame is consistent with the time frame for the trajectory phasing segments when the Sun's motion is minimal as seen in an Earth-centered inertial frame. However, viewing the geometry in the rotating frame establishes the solar impact on the trajectory at these particular instances as described by Howell and Davis [111]. Linear orientations of the Sun,

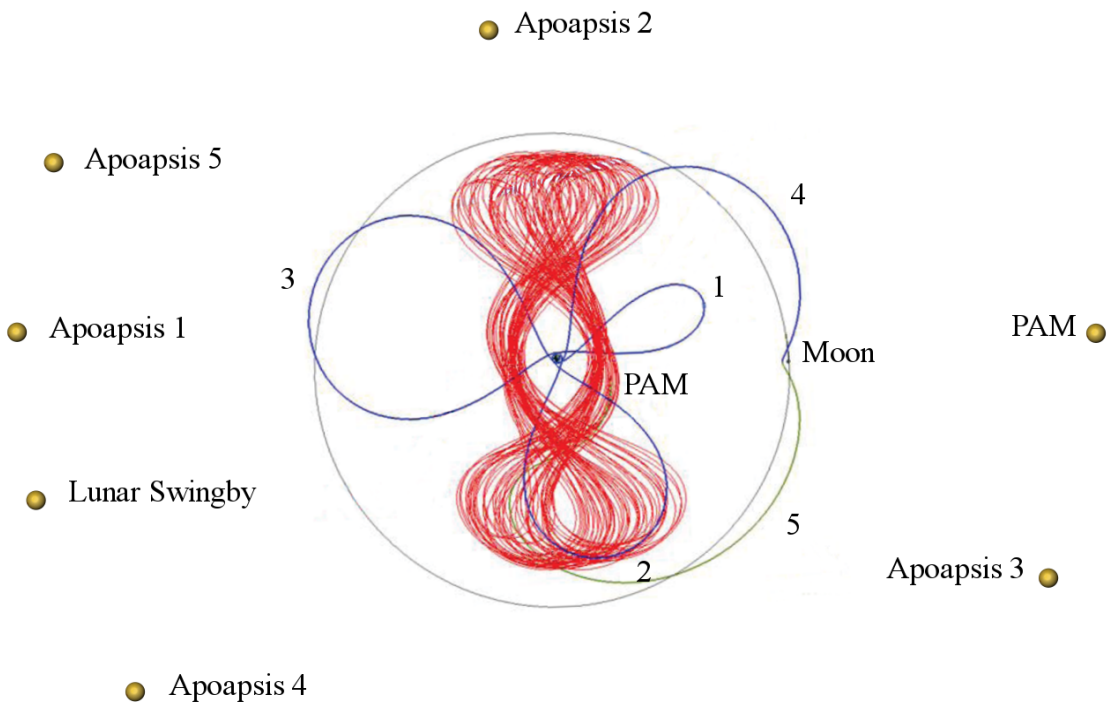

Figure 7.53.: Sun Directions in the Rotating Frame for Early DRM Events

Earth and spacecraft at apoapsis induce minimal change in the spacecraft's orbital elements from the solar influence. As the spacecraft moves into the science phase, the solar direction does not maintain a particular orientation in the rotating frame for trajectory apoapses. During the science phase the solar direction fills out a circular band at the solar distance from the barycenter of the rotating frame, extending above and below the x–y plane consistent with lunar orbital inclination.

A quantitative comparison of the accelerations imparted to the spacecraft from the Sun and the Moon aids in demonstrating that the trajectory behavior is a general reflection of all combined effects. Prado employs an approach to determine the total contribution of a particular perturbative effect over time by integrating the associated acceleration components [112, 113]. Sanchez et al. [114] further employs and expands this methodology. The cumulative effect of a particular perturbation over the time-interval, $I := [t_i, t_i + T]$, in a given direction may be calculated by integrating, $p_j =$

$\int_{t_i}^{t_i+T} a_j \, dt$, where a_j is the acceleration component corresponding to the perturbation along the specific direction coordinate j, t_i is some initial time and T is some later time (in this case, T is a time horizon similar to that employed for computing $\mathbf{C}$). Moreover, the total impact of the perturbation is then computed as $p = \int_{t_i}^{t_i+T} |\mathbf{a}| \, dt$, and the energy imparted to or removed from the spacecraft motion by the perturbation is evaluated as $\Delta E = \int_{t_i}^{t_i+T} \mathbf{a} \cdot \mathbf{v} \, dt$. All three scalar values are computed using J2000 ECI dimensional coordinates for this analysis. Invoking a sliding time-scale as used for computations in preceding sections, the traces in Figure 7.54 depict the integrated accelerations along the perturbed baseline solution corresponding to each component. At each time step, the subsequent ten years of acceleration data are integrated and plotted. The integrated acceleration components acting on the spacecraft due to lunar gravity, as seen in the ECI J2000 reference frame, appear in Figure 7.54(a) while the solar counterparts are plotted in Figure 7.54(b). Consistent with the more stable trajectory behavior observed from 30–50 years and again beginning around 60 years during the evolution, the particular component-wise acceleration contributions from both the Sun and the Moon are observed to experience periods of generally lower magnitude. During the transition in behavior that is apparently triggered at around 60 years, the solar perturbations are observed to pass through a phase of minimal contribution to the motion. This minimal phase, coupled with the lowered influence imparted from the Moon during the same time seems to mark the initiation of the subsequent increased stability phase of the trajectory behavior. Comparing the overall solar and lunar perturbation contributions in terms of both magnitude as well as alignment with the spacecraft velocity vector reveals additional insight. In Figure 7.55, the magnitude of the lunar and solar accelerations are integrated, again employing a ten-year sliding time interval. In general, the lunar influence is observed to be approximately double that of the solar influence over the 90-year interval and displays an increasing trend over time. In this case, the solar perturbations tend to decrease slightly over time. Periods of local minimal contribution appear consistently with the component-wise results observed in Figure 7.54. Finally, the transition at

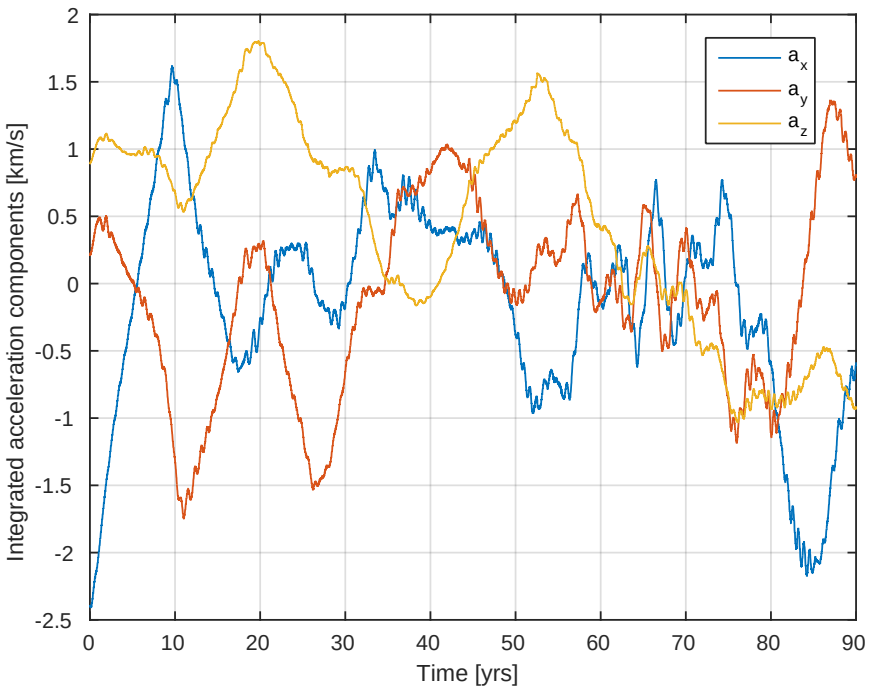

(a) Lunar Acceleration Components

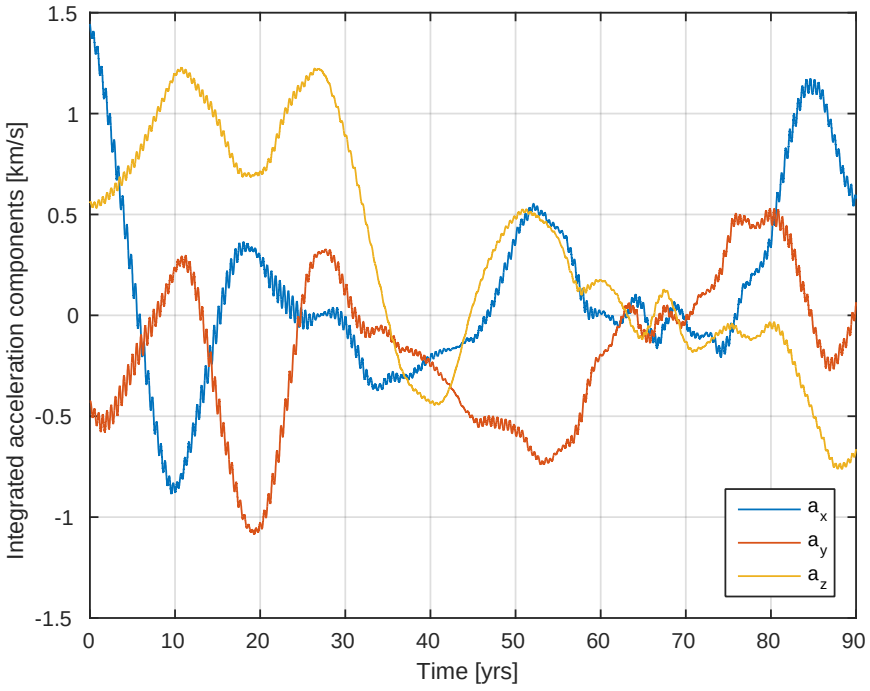

(b) Solar Acceleration Components

Figure 7.54.: Sliding Integrals of Gravity Perturbations on the Spacecraft (J2000)

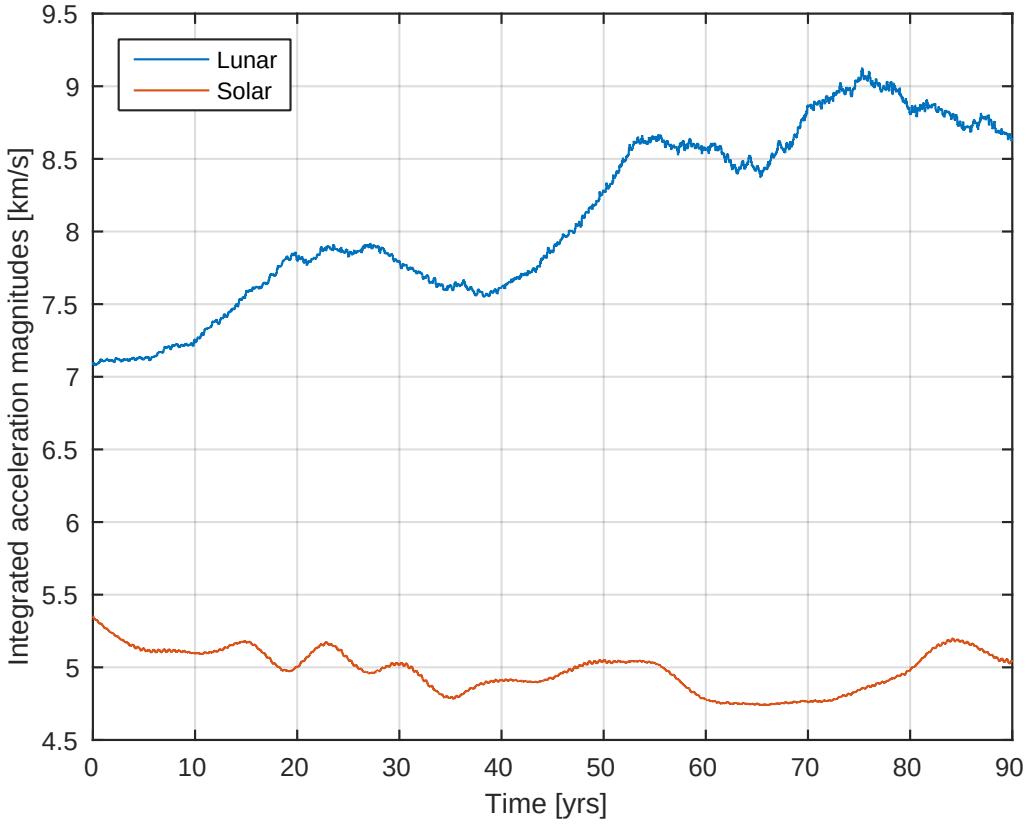

Figure 7.55.: Overall Solar and Lunar Perturbative Contributions to the Motion

around 60 years along the science orbit evolution is illustrated well by the ΔE integral, i.e., $\int \mathbf{a} \cdot \mathbf{v}\ dt$, again evaluated for the subsequent 10-year interval originating at each plotted point in Figure 7.56. Initially, the solar contribution over each subsequent ten-year interval imparts energy to the spacecraft motion. The lunar influence fluctuates more rapidly over this time frame, but it removes energy from the spacecraft motion on average. This lunar trend gradually decreases over time (i.e., the Moon's acceleration on the spacecraft and the spacecraft's velocity direction slowly begin to align). As the spacecraft evolution approaches 60 years, the average lunar influence shifts to impart energy to the spacecraft motion accompanied by an uptick in the solar contribution. At this point, the de facto equilibrium imparted by the lunar and solar perturbations inverts as the general system behavior changes and the trajectory enters a more

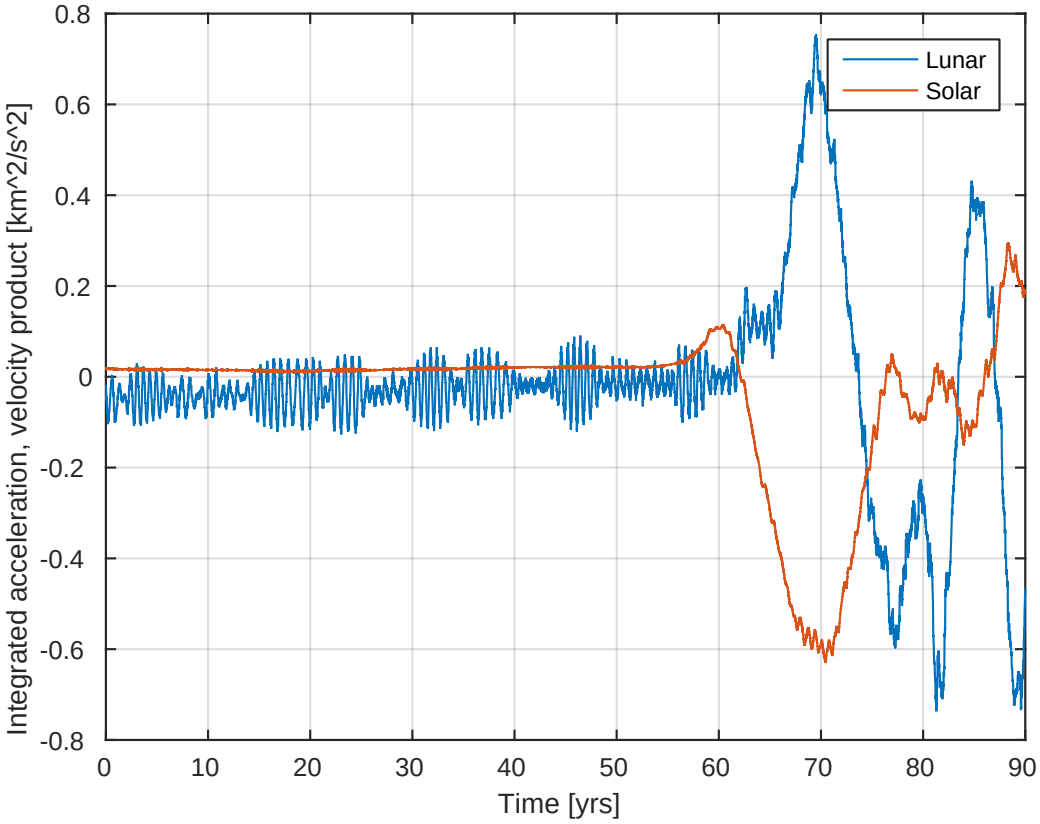

Figure 7.56.: Specific Energy Imparted to the Spacecraft Over Time

stable phase for a few decades. The spacecraft trajectory in this particular perturbed baseline case will eventually evolve out of this more stable phase. Comparisons of the individual lunar and solar perturbative contributions indicate that the general trends in behavior are a cumulative reflection of all the model components. Further exploration of these components and nearby solutions reveals that the trends are very sensitive to small initial variations.

7.6.5 Model Component Analysis

Comparison of the different components that influence the motion along the path yields some insight into the behavior. However, the goal is to identify particular aspects of the model that drive the trajectory into a given mode, thus, this analysis

must be performed relative to a solution displaying the behavior of interest. Since the CG tensor is model-agnostic, evolution of a particular initial state under the influence of different systems allows for the comparison of flow metrics that are derived from the Cauchy–Green tensor. In particular, the FTLE values computed along the trajectory may be compared to indicate a sense of the flow behavior. For these calculations, it is necessary to periodically reset the initial states for the lower-fidelity models to remain along the trajectory of interest. Consider the following strategy:

1. Calculate the baseline trajectory (generated from an initial condition of interest perturbed from the TESS DRM state) by evolving under the higher-fidelity ephemeris model, and retain intermediate states at specified intervals, regularly spaced in time.

2. For each of the intermediate points along the baseline path, calculate the CG tensor for the length of the given time interval.

3. In addition, transform the baseline state as appropriate to conform to lower-fidelity models.

4. Compute the STM under the lower-fidelity dynamics for each state.

5. Transform the STM as necessary to match the reference frame associated with the baseline, and compute the CGST and FTLE values.

By computing FTLE values for the baseline trajectory and then removing model components and computing comparative values, the impacts of some effects are captured. Selecting an appropriate time scale for discretizing the baseline path is a critical consideration so that the influence of the reduced models is allowed sufficient time to be observable without completely diverging. It is possible to impose smaller discretization steps and multiply the resulting state transition matrices to form a composite STM over a longer time interval; but, this method must also be approached with caution since a time slice that is too small may not allow the individual lower-fidelity effects to be discernible. Such a comparative FTLE analysis is generally sensitive

to the selection of both the integration and normalization times for the FTLE, and some intuition or experimentation is usually required. Traces of FTLE values associated with five separate model formulations are included in Figure 7.57. For these calculations, time slices are collected at each 0.025 nd time steps and composited to create an STM equivalent to one produced from ∼1.2 years (100 nd) of evolution. Experimentation with other time scales for slicing and compositing suggests that the present set of parameters represents an acceptable trade-off for meaningful comparisons. From Figure 7.57, it is immediately apparent that two general groupings of behavior emerge, that is, one group associated with lower-fidelity models and the other with the more realistic ephemeris options. Insets associated with the regions isolated with magenta and red boxes are included in Figure 7.57 to aid these comparisons. Embedded in the ephemeris options are many higher-order perturbative effects that are not captured by the circular restricted, elliptic restricted, and bicircular restricted problems. While general consistencies are apparent in the long-term behavior as the several large peaks and troughs appear correlated between lower- and higher-fidelity models, ultimately, over the prescribed time scales, the lower-fidelity models struggle to capture the combined cumulative effects of higher-order perturbations. It is also apparent that the addition of the fourth-body perturbation appears to produce a lesser effect than the introduction of other components of the lunar orbit. For example, compare the blue and red traces of inset (a) as well as the teal and black lines in inset (b) in Figure 7.57 (both sets generally overlap) to note the relatively small difference associated with introducing the fourth body (the Sun) into the model. Alternatively, compare the green and red data in inset (a) where the elliptic effects of the lunar orbit are apparent. Given the close association between the Earth–Moon ephemeris and the Earth–Moon–Sun ephemeris traces (teal and black), a reasonable conclusion is that the Earth–Moon dynamics are generally more significant, and the cumulative effect of higher-order lunar perturbations may play a larger role in this particular scenario. Further examination of the higher-order perturbations and model components suggests that the problem sensitivity over longer times is a critical com-

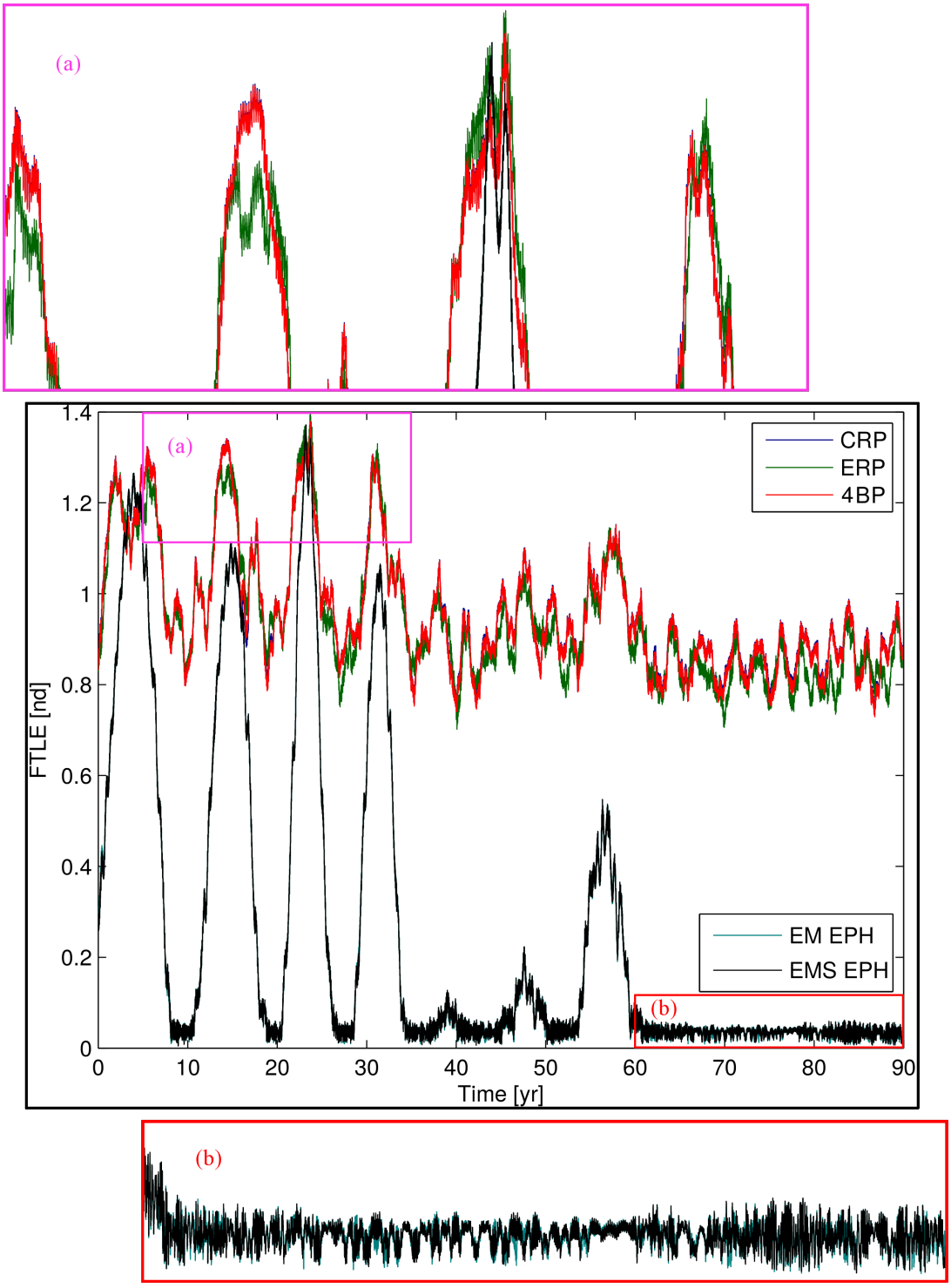

Figure 7.57.: FTLE Profiles for Ephemeris and Reduced-Fidelity Propagations

ponent in the trajectory behavior, potentially sufficient to overshadow any individual contributing factor, as illustrated by inspection of nearby solutions.

7.6.6 Nearby Solutions and FTLE Profiles

Further exploration in the phase space nearby the initial conditions associated with the perturbed baseline solution as characterized in Figures 7.48 and 7.49 adds compelling insight into the trajectory behavior. Various strategies for such an inspection are available. Rather than employing random nearby initial states or using a grid-based strategy, a flow-based approach is adopted. In general, the natural flow in the system will rapidly align with the largest stretching direction in the phase space. Thus, seeding initial states along the eigendirection associated with the largest eigenvalue from the Cauchy–Green tensor allows for a one-dimensional search direction that will most efficiently spread throughout the phase space. The CGST is evaluated from the initial state for increasing time horizons until the largest eigenvector, $\boldsymbol{\xi}_n$, stabilizes and before the computation numerically overflows. A time horizon of 100 nd time steps is sufficient to accomplish this numerical balance. The search, then, is *designed to maximize the divergence* from the initial state, and the subsequent evolution is associated with the long-term behavior of the set of seeded trajectories. Recall the FTLE profile depicted initially in Figure 7.49(f); such a profile may be viewed as a one-dimensional track colored by relative FTLE values and the profile from Figure 7.49(f) corresponds to the "row" marked as zero along the vertical axis in Figure 7.58 where lower-to-higher FTLE values are colored using a blue-to-red spectrum color mapping. Five hundred steps along both the $\pm$ directions in $\boldsymbol{\xi}_n$ are tagged as initial state vectors to form the search set. Each step is characteristic of a nondimensional step size of $1{\times}10^{-5}$. For reference, in position, $1{\times}10^{-5}$ nd ≈ 3.84 km while $1{\times}10^{-5}$ nd $\approx 1.02{\times}10^{-2}$ $\frac{\text{m}}{\text{s}}$ in terms of velocity, but a step along the eigendirection is distributed, likely unequally, in both position and velocity. The four initial peaks observed in the previous plots (e.g., Figure 7.49(f)) generally persist under

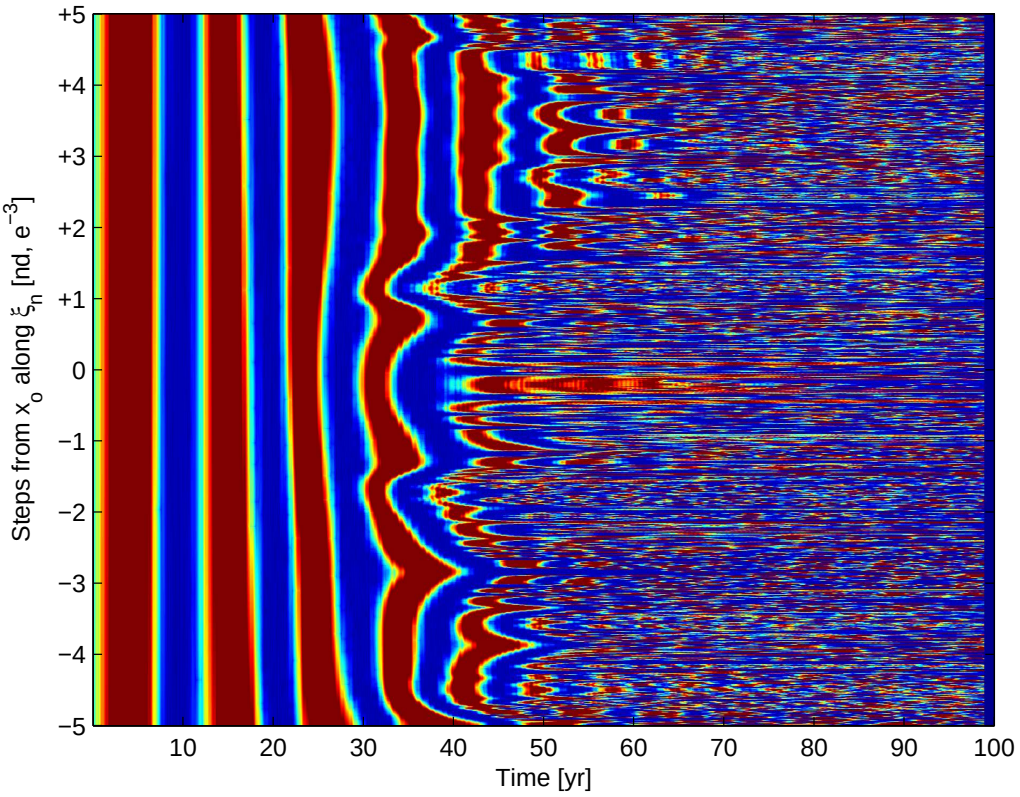

Figure 7.58.: FTLE Profiles from the Baseline (Vertical Axis: 0) and Along $\pm\boldsymbol{\xi}_n$

the specified perturbations and are observed as thick red bands in Figure 7.58. It is apparent that sometime between 40–60 years, the solution space becomes generally unpredictable, as the map bleeds into noise. This time frame correlates to notable shifts in behavior along the original baseline path. The transition into noisy behavior is a consequence of the chaotic regime, and is a reflection of the sensitive dependence on the initial conditions. This sensitivity must also be considered within the context of numerical integration error. For example, a variance in the last digit of only one state component from an initial condition (given to double precision) may be sufficient to shift a solution into behavior consistent with a neighboring perturbation after several decades of propagation. Further analysis, including additional propagations initiated near transitioning phases, is performed to ensure that the behaviors are, in fact, dynamical and not a reflection of numerics.

7.6.7 Conditions for Entering More Stable Modes

At the conclusion of the science phase of the TESS mission, it may be desirable to evolve the trajectory into a more constant "disposal mode" described by lower eccentricity and higher periapse altitude. Such a trajectory is consistent with the later phases of the perturbed baseline solution investigated in this analysis (Figures 7.48 and 7.49). With some insight into the dynamical context and the associated complexity, it is possible to isolate conditions for a solution that mimics the terminal phase of the perturbed baseline. Beginning near the peak at ∼57 years in Figure 7.49(f), the subsequent behavior in the nearby phase space is plotted as an FTLE profile map in Figure 7.59. In this case, larger (but fewer) steps along $\boldsymbol{\xi}_n$ are tagged (±100 steps of size 1×10^{-4} are traversed). The plot in Figure 7.59 illustrates a few key observa-

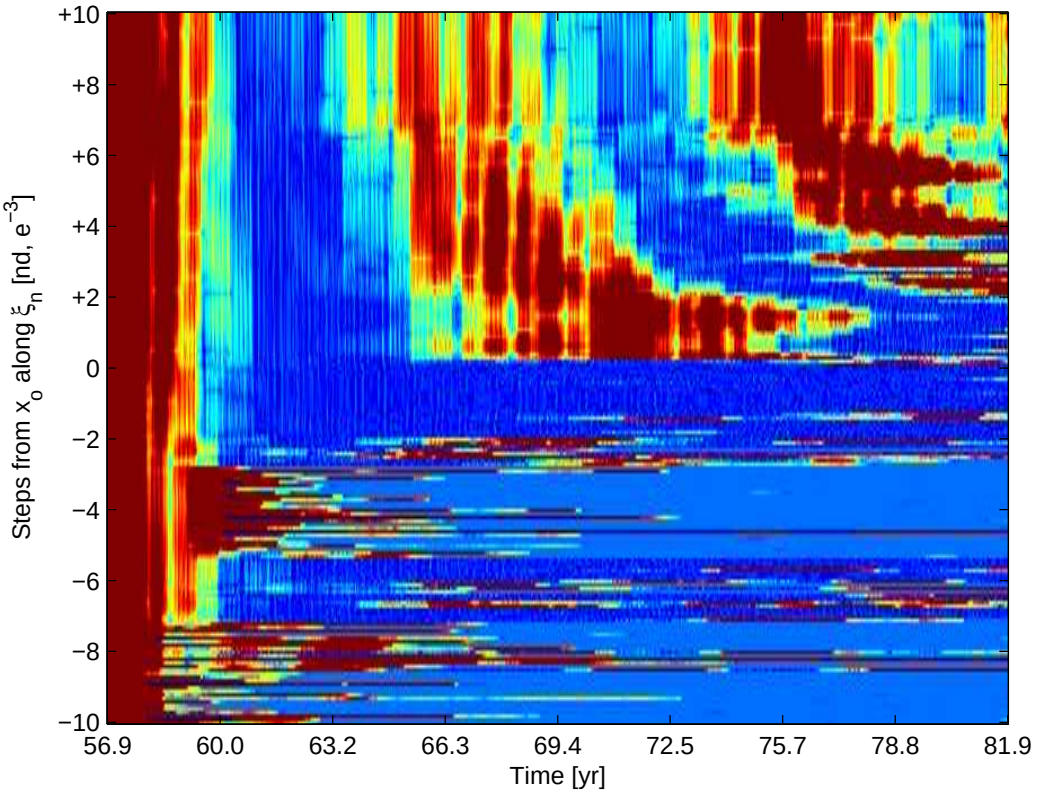

Figure 7.59.: FTLE Profiles Just Prior to Transition at ∼60 Years

tions. First, relatively small perturbations drastically shift the behavior—this fact is more pronounced since the perturbations are induced near the top of a modest FTLE peak (a more sensitive placement). A strip of relatively tame FTLE values (dark blue) is observed near the baseline (ordinate: 0) and persists for a few steps along the negative $\boldsymbol{\xi}_n$ extension. However, perturbing slightly further along the negative $\boldsymbol{\xi}_n$ direction produces profiles with "flat", cerulean FTLE values. These values, despite their calming coloring, are consistent with trajectories that have been ejected from the local neighborhood leading to FTLE stabilizations as the trajectory essentially orbits the Earth–Moon system (in a rotating perspective). This particular plot helps to characterize the nearby behavior after transition.

As a consequence of the observations from Figure 7.59, solutions reflecting transition into alternate modes are now sought earlier along the evolving trajectory path. To begin this process, an initial state is sought that minimizes the difference between the relative system orientation of the spacecraft, the Earth, the Moon and the Sun with respect to some later configuration that demonstrates desirable behavior. The inertial positions and velocities of the system components may not actually be equal to their respective values at the later time, but the overall relative system configuration should match as closely as possible. For example, conditions are sought such that the difference in the magnitude of the relative state vectors between the spacecraft and the Moon at two times is minimized, i.e.,

$$\Delta_{\mathrm{sM}} = \left| \left(\boldsymbol{x}_{t^*}^{\mathrm{s/c}} - \boldsymbol{x}_{t^*}^{\mathrm{Moon}} \right) - \left(\boldsymbol{x}_{t}^{\mathrm{s/c}} - \boldsymbol{x}_{t}^{\mathrm{Moon}} \right) \right|, \tag{7.4}$$

where values at time t^* are characteristic of desirable trajectory behavior. This process is repeated with respect to the Sun's relative configuration and, then, a weighted averaging that most closely satisfies all constraints is isolated at a specific time. In the process of seeking conditions consistent with Equation 7.4 and the analogous solar conditions, the spacecraft state is necessarily adjusted in position and velocity. Consequently, an upstream maneuver would be required to achieve the associated averaged spacecraft state. One such averaged state is identified at 7.77 years as the trajectory evolves into the first FTLE trough in Figure 7.49(f). The FTLE profile

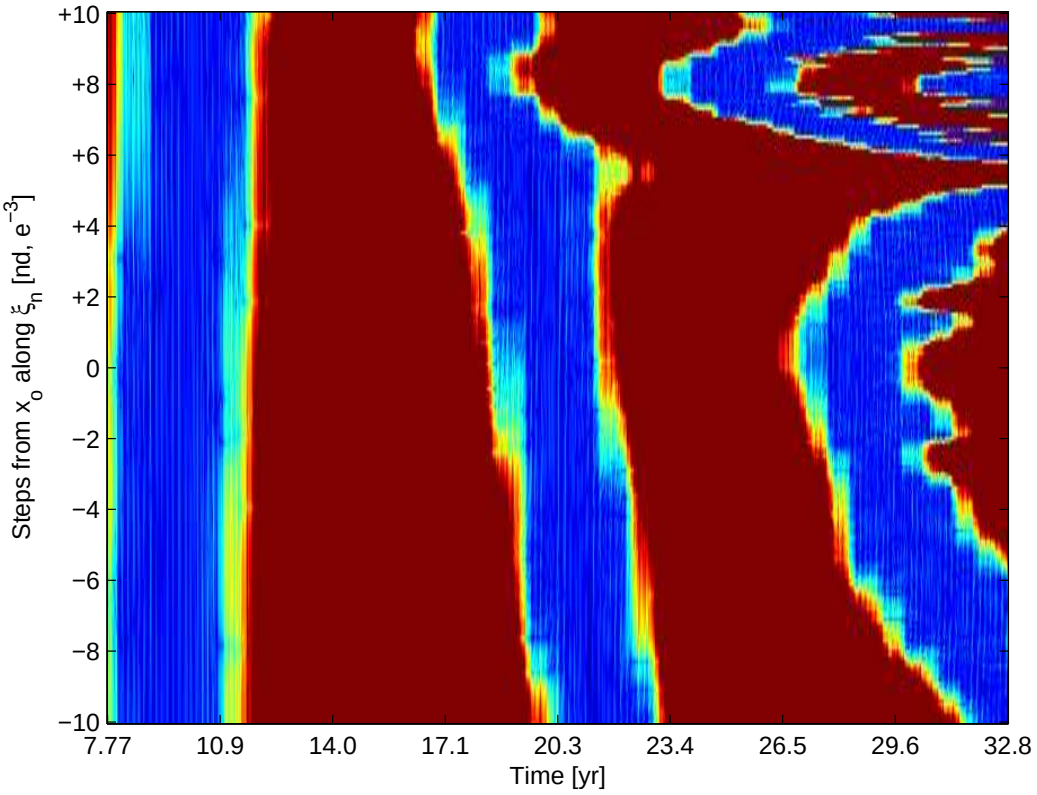

Figure 7.60.: Unaveraged, Baseline and Perturbation FTLE Traces

map associated with the *unaveraged*, baseline state and perturbations is included in Figure 7.60. Without adjusting the state to meet the necessary geometric constraints, the FTLE evolution is reflective of the peak-and-trough behavior along the baseline, however, some differences between Figures 7.58 and 7.60 are expected because $\boldsymbol{\xi}_n$ is computed at the later epoch. Alternatively, employing the *averaged* state, the landscape appears differently, as is apparent in Figure 7.61. Several features are notable in Figure 7.61. First, as also observed in Figure 7.58, transitioning into the later modes is characterized by an apparent increase in chaoticity of the system likely associated with an energy change at the transition. In the case associated with Figure 7.61, *the transitioning behavior is induced much earlier* and the resulting FTLE field is populated with several profiles that flatten out consistent with escapes (again, characteristic of cerulean coloring). In general, darker blue FTLE values are

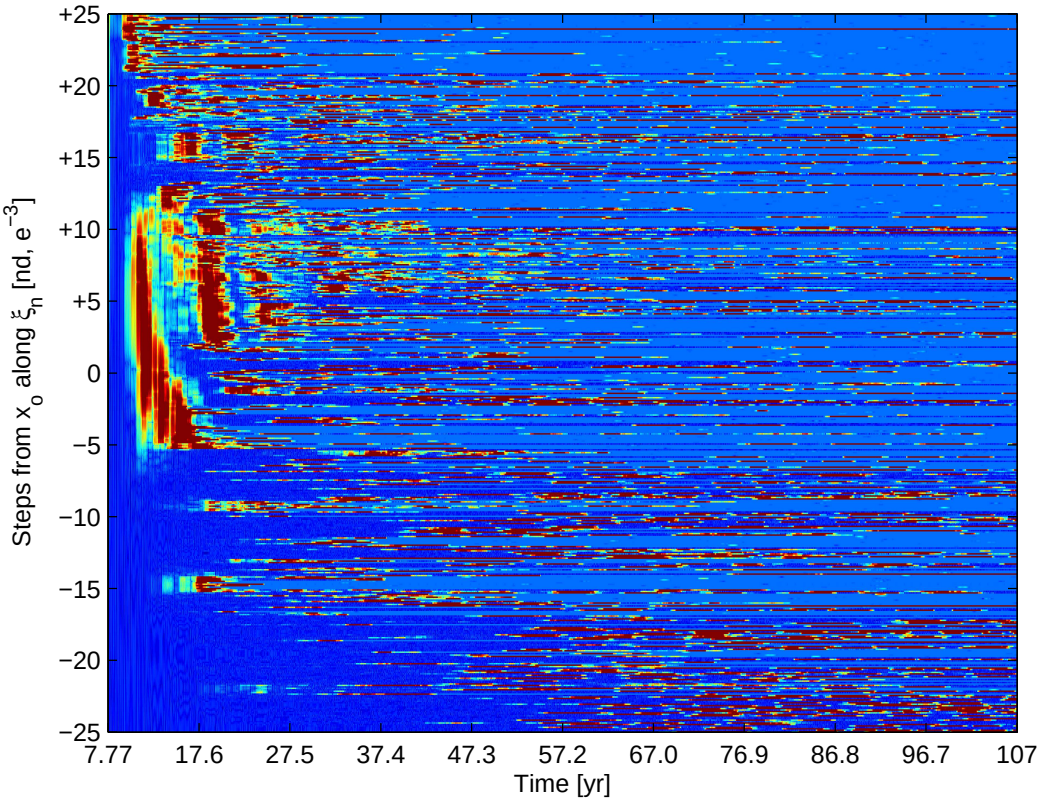

Figure 7.61.: Averaged State and Perturbation FTLE Traces

consistent with more stable behavior and several profiles reflect such values as well. A particular contiguous region of dark blue traces that run through the perturbations ranging $\boldsymbol{x}_{\mathrm{o}} + (-5 \times 10^{-3} > \Delta \cdot \boldsymbol{\xi}_n > -25 \times 10^{-3})$ is also noted. Traces characteristic of such FTLE profiles are reflective of the mode behavior observed in the terminal phase of the original perturbed baseline solution, and they persist for several decades in many cases. Moreover, interspersed throughout the entire map, roughly 4% of the trajectories maintain the ideal FTLE signatures with slight or no deviations. For example, consider the FTLE trace included as Figure 7.62(a) that results from a solution that has been propagated from initial conditions defined from a step equal to $-0.0121 \times \boldsymbol{\xi}_n$. The plot's vertical axis is held to scale with Figure 7.49(f) for comparison, and the FTLE data for the first 7.77 years from Figure 7.49(f) is also included prior to the red dashed line, where the perturbed state is invoked. The

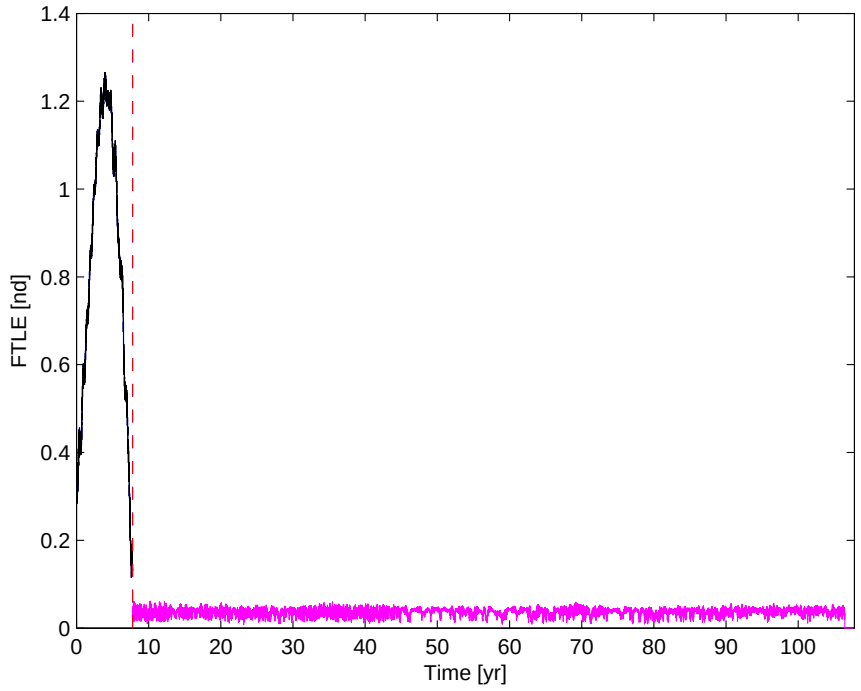

(a)

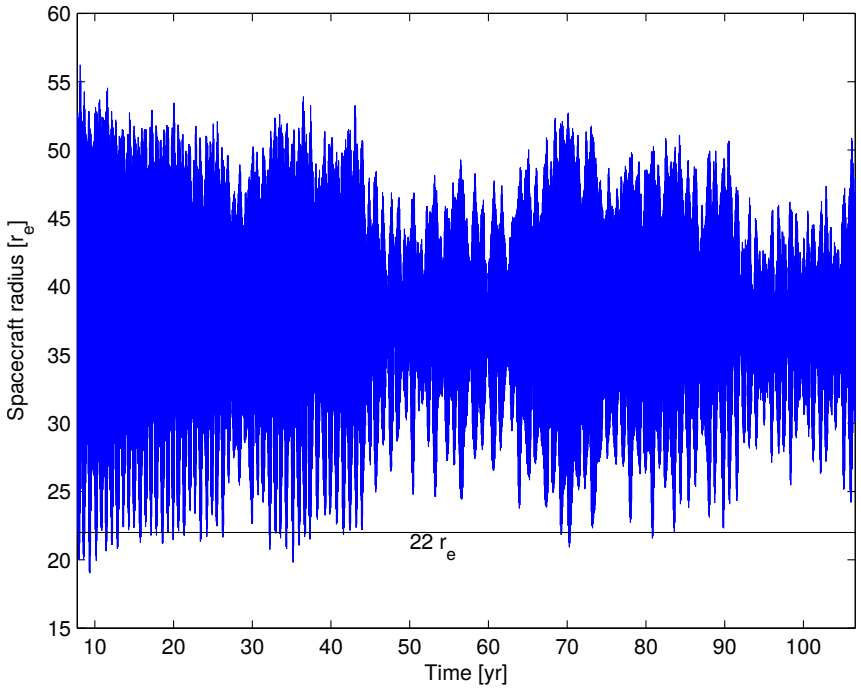

(b)

Figure 7.62.: FTLE Trace and Radius Profile from Perturbation to Averaged State

associated radius history is plotted in Figure 7.62(b). In general, the spacecraft perigee and apogee radii are further from the Earth and Moon, respectively, lessening the associated impact of perturbations from these bodies.

By inducing transitioning behavior earlier in the mission time-frame, potential long-term, increased stability options are available. A specific example associated with the FTLE trace from Figure 7.62(a) initiates 7.77 years after the beginning of the TESS mission, and the 100-year evolution of this solution is included in Figure 7.63. This orbit generally fills out a bounded shell in the rotating frame and serves as an example resulting from the process detailed here. The orbit is observed to evolve through various modes apparent through the coloring in Figure 7.63. As the orbit continues through its 100-year propagation, the coloring ranges from initial phases represented in blue through intermediate stages with mid-spectrum colors of yellow and green and ultimately concludes with red coloring interior to the shell traced out by earlier revolutions. The overall evolution is characterized by increased r_p with respect to the Earth while maintaining a modest upper bound on r_a as the orbit maintains an adequate distance from the Moon. Such a solution represents many possible options that may be isolated through numerical exploration of perturbations strategically placed in time. These options are isolated by (1) identifying specific modal behavior exhibited by perturbed solutions, (2) seeking similar system configurations at other times throughout the path evolution over time, and (3) searching the flow behavior of the nearby phase space to identify potential trajectory responses.

The selected science orbit for the TESS DRM supplies an effective end-of-life option with a dispose-in-place strategy. However, the sensitive operating regime allows for the possibility of transitions in the long-term spacecraft trajectory behavior that may or may not be acceptable. Greater knowledge of the complex environment in the vicinity of such a solution can lead to other, useful options. In the example highlighted in this analysis, particular solutions characterized by notable long-term behavior may be realized by identifying a particularly advantageous epoch for shifting into alternate modes and perturbing the spacecraft state to accomplish evolution

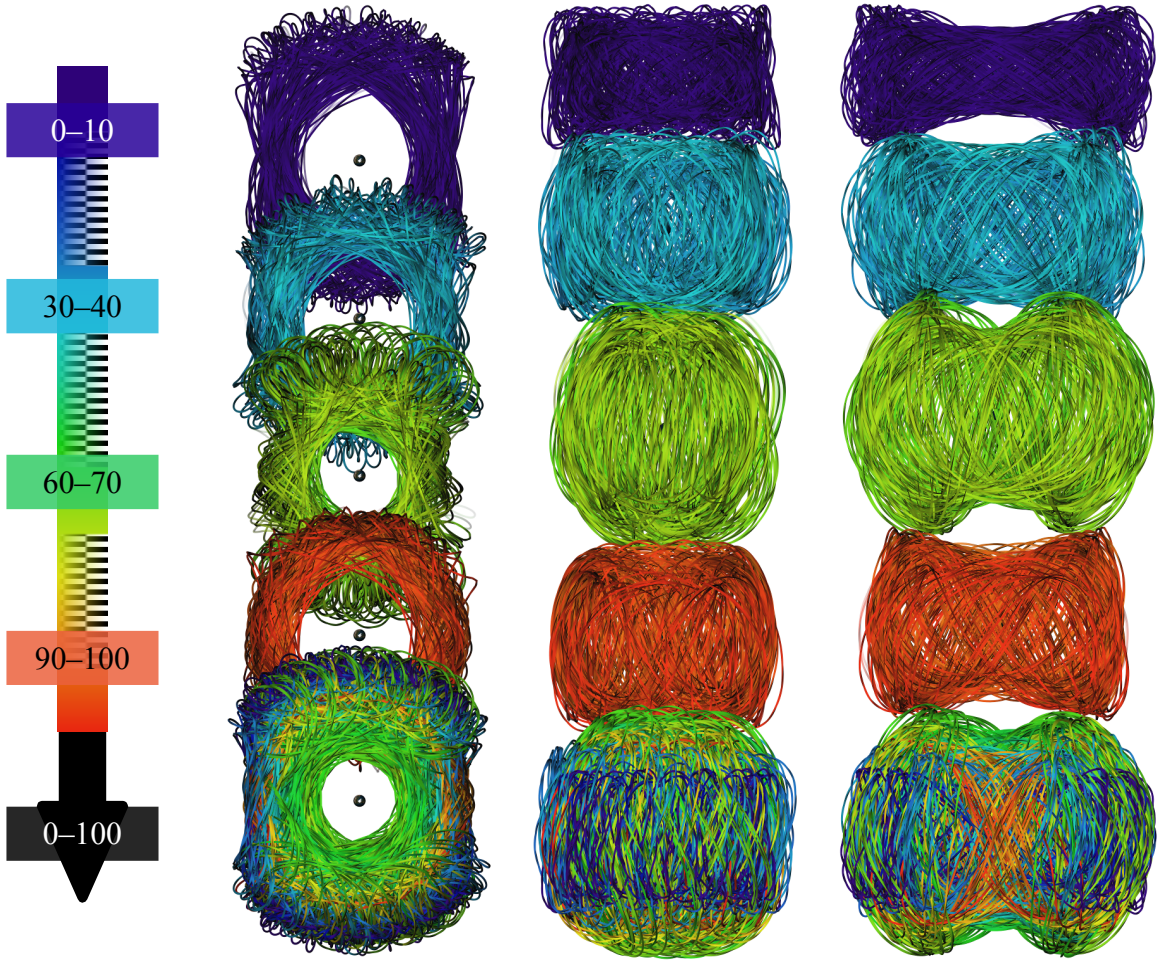

(a) Time [yr–7.8] (b) x–y View (c) x–z View (d) y–z View

Figure 7.63.: 100-year Ephemeris Orbit Evolution (Rotating Frame View)

into the new option. Such an engineered transition would likely require planning to execute one or more maneuvers at an earlier epoch along the trajectory evolution and, while likely feasible, would warrant additional analysis and assessment.

The dynamical regime associated with the Earth–Moon–Sun system is rich with complexity and includes intricate perturbations that lead to chaotic behavior. After characterizing an orbit, one that is slightly perturbed from and generally resembling the TESS DRM, this analysis further examines modes of evolving trajectory behavior in the nearby phase space. It is observed that contributing factors leading to transitioning behavior in associated long-term solutions are coupled and cumulative. Moreover, the sensitive nature of the design space generally overshadows any independent contribution. Transitions are likely associated with energy shifts over time that increase the chaoticity of the system. In the resulting, more complex environment, long-term increased stability options become available, but it is observed that increased system sensitivity may result in unfavorable behavior from perturbations. Care is warranted if the options discussed in this particular example are considered for use in mission applications.

Flow-based strategies are emerging as effective tools in support of trajectory design and analysis activities. The additional context and insight imparted directly from the flow supports such efforts in various ways. The preceding examples highlight some of the uses of flow-based methodologies in astrodynamics.

8. CONCLUDING REMARKS

This analysis is focused on augmenting and extending classical methods by introducing flow-based methodologies into astrodynamical design and analysis. Because these tools apply in extended phase spaces and through all levels of model fidelity, they apply where classical approaches begin to lose relevance and beyond. As they are applied to more intricate dynamical models, understanding of the space is expanded and new, feasible solutions are revealed. Some specialized computational approaches are necessary and useful to utilize such flow-based approaches, and several are discussed in Chapter 6. Given the appropriate tools, the example applications of Chapter 7 invoke the methods of Chapter 5 and build on the theory offered in Chapters 2–4. These applications represent a snapshot of the relevant effort to meaningfully adapt flow-based theory to astrodynamics, and a brief summary of the associated observations from those examples follows.

Parametrized strainlines provide a direct avenue for bounded numerical analysis. Since these curves help to isolate particular regions of interest in a flow, they can be used to guide such routines for finding the "best" solutions within a given region. For example, a region may be characteristic of particular flow behavior as witnessed by trajectory evolution. Each trajectory in this region displays qualitatively consistent behavior, however they will all also have slightly different performance. Thus, using strainlines to establish a domain for an optimization strategy or other numerical analysis is demonstrated as an effective strategy.

The strainlines depicted in this document represent powerful tools for increasing the understanding of the flow behaviors in many systems. These strainlines result from a fairly straightforward process and indicate varying levels of flow transitions. Methods exist in simpler models for further characterizing such strainlines in terms of some metric. The possibility for the extension of such ideas to higher-dimension,

higher-fidelity astrodynamical models exists and, while remaining useful for specific problems, ultimately reduces to the lower-dimensional problem as constraints are enforced. Further innovation into higher-dimensional strainlines remains a potential option for theoretical development.

Some of the results from lower-fidelity aspects of the overall effort summarized in this document have been further validated by identifying the geometrically consistent result in higher-fidelity models. In particular, solutions identified with flow-based analysis in the nonautonomous four-body problem, as well as three-body flow control segment isolated options are transitioned into ephemeris solutions. This process of validation represents a useful option for additional results from medium-fidelity investigations. Further, these validations serve to support the viability of flow-based approaches for astrodynamical analysis.

Aside from transitioning lower-fidelity solutions into higher-fidelity contexts, some analysis is performed directly in more complex models. Context for maneuver directions is offered by the surrounding flow, and helps to correlate optimal maneuver directions with the natural dynamics in an ephemeris model. Also, since flow-based tools apply regardless of model fidelity, they can highlight behaviors specifically associated with individual model components. In fact, these tools may be used to identify mechanisms that invoke transitional behavior in solutions (whether desired or not). Analysis of the TESS mission orbit is facilitated and informed by flow-based context. Such flow information helps to identify the chaotic nature of the design space in the TESS analysis, and highlights the potential for harnessing flow-based information to identify behavior-shifting mechanisms for desirable results.

The ability to identify flow behaviors that are generally advantageous to mission goals in complex astrodynamical systems expedites the search for viable options in a wide range of design scenarios. The principles of flow-based methodology imply potential application regardless of the complexity of the underlying system. The information supplied by these tools augments, generalizes and extends classical methods for trajectory design and analysis.

LIST OF REFERENCES

LIST OF REFERENCES

[1] G. Galilei, *Sidereus Nuncius (1610)*. Chicago: The University of Chicago Press, 1989. Translated, A. Van Helden.

[2] E. S. Gawlik, J. E. Marsden, P. C. du Toit, and S. Campagnola, "Lagrangian coherent structures in the planar elliptic restricted three-body problem," *Celestial Mechanics and Dynamical Astronomy*, vol. 103, no. 3, pp. 227–249, 2009.

[3] C. R. Short, K. C. Howell, and X. M. Tricoche, "Lagrangian Coherent Structures in the Restricted Three-Body Problem," in *AAS/AIAA Space Flight Mechanics Meeting*, (New Orleans, Louisiana), February 2011.

[4] D. Blazevski and C. Ocampo, "Periodic orbits in the concentric circular restricted four-body problem and their invariant manifolds," *Physica D*, vol. 241, pp. 1158–1167, 2012.

[5] C. R. Short and K. C. Howell, "Lagrangian Coherent Structures in Various Map Representations for Application to Multi-Body Gravitational Regimes," *Acta Astronautica*, vol. 94, no. 2, pp. 592–607, 2014.

[6] G. Haller, "A variational theory of hyperbolic Lagrangian Coherent Structures," *Physica D*, vol. 240, pp. 574–598, 2011.

[7] M. Farazmand and G. Haller, "Computing Lagrangian Coherent Structures from Variational LCS theory," *Chaos*, vol. 22, no. 013128, 2012.

[8] D. Blazevski and G. Haller, "Hyperbolic and elliptic transport barriers in three-dimensional unsteady flows," *Physica D*, vol. 273–274, pp. 46–64, 2014.

[9] C. R. Short, D. Blazevski, K. C. Howell, and G. Haller, "Stretching in Phase Space and Applications in General Nonautonomous Multi-body Problems," *Celestial Mechanics and Dynamical Astronomy*, vol. 122, no. 3, pp. 213–238, 2015.

[10] R. L. Anderson, M. W. Lo, and G. H. Born, "Application of Local Lyapunov Exponents to Maneuver Design and Navigation in the Three-Body Problem," in *AAS/AIAA Astrodynamics Specialist Conference*, (Big Sky, Montana), August 2003.

[11] G. K. Harden, "Automated Patch Point Placement for Autonomous Spacecraft Trajectory Targeting," M.S. Thesis, School of Aeronautics and Astronautics, Purdue University, West Lafayette, Indiana, 2013.

[12] G. Harden, A. Haapala, K. Howell, and B. Marchand, "Automated Patch Point Placement for Spacecraft Trajectory Targeting," in *AAS/AIAA Space Flight Mechanics Meeting*, (Santa Fe, New Mexico), January 2014.

[13] C. M. Spreen, K. C. Howell, and B. G. Marchand, "Node Placement Capability for Spacecraft Trajectory Targeting in an Ephemeris Model," in *AAS/AIAA Astrodynamics Specialist Conference*, (Vail, Colorado), August 2015.

[14] M. Lara, R. P. Russell, and B. Villac, "Classification of the Distant Stability Regions at Europa," *Journal of Guidance, Control, and Dynamics*, vol. 30, no. 2, pp. 409–418, 2007.

[15] B. F. Villac, "Using FLI maps for preliminary spacecraft trajectory design in multi-body environments," *Celestial Mechanics and Dynamical Astronomy*, vol. 102, no. 1–3, pp. 29–48, 2008.

[16] B. Villac and S. Broschart, "Applications of Chaoticity Indicators to Stability Analysis Around Small Bodies," in *AAS/AIAA Space Flight Mechanics Meeting*, (Savannah, Georgia), February 2009.

[17] S. D. Ross, W. S. Koon, M. W. Lo, and J. E. Marsden, "Design of a Multi-Moon Orbiter," in *AAS/AIAA Space Flight Mechanics Meeting*, (Ponce, Puerto Rico), February 2003.

[18] S. D. Ross, W. S. Koon, M. W. Lo, and J. E. Marsden, "Application of Dynamical Systems Theory to a Very Low Energy Transfer," in *AAS/AIAA Space Flight Mechanics Meeting*, (Maui, Hawaii), February 2004.

[19] P. Grover and S. Ross, "Designing Trajectories in a Planet–Moon Environment Using the Controlled Keplerian Map," *Journal of Guidance, Control, and Dynamics*, vol. 32, no. 2, pp. 436–443, 2009.

[20] S. D. Ross and P. Tallapragada, "Detecting and exploiting chaotic transport in mechanical systems," in *Applications of Chaos and Nonlinear Dynamics in Science and Engineering* (S. Banerjee, L. Rondoni, and M. Mitra, eds.), vol. 2, pp. 155–183, Springer, 2012.

[21] D. Pérez-Palau, "Determination of separating structures in low-dimension dynamical systems," M.S. Thesis, Facultat de Matemátiques, Universitat de Barcelona, Barcelona, Spain, 2011.

[22] D. Pérez-Palau, G. Gómez, and J. J. Masdemont, "Detecting Invariant Manifolds Using Hyperbolic Lagrangian Coherent Structures," in *1st IAA/AAS Conference on the Dynamics and Control of Space Systems*, (Porto, Portugal), March 2012.

[23] K. Oshima and T. Yanao, "Jumping mechanisms of Trojan asteroids in the planar restricted three- and four-body problems," *Celestial Mechanics and Dynamical Astronomy*, vol. 122, no. 1, pp. 53–74, 2015.

[24] D. Pérez-Palau, G. Gómez, and J. J. Masdemont, "Tools to detect structures in dynamical systems using Jet Transport," *Celestial Mechanics and Dynamical Astronomy*, vol. 123, no. 3, pp. 239–262, 2015.

[25] T. Peacock and J. Dabiri, "Introduction to focus issue: Lagrangian coherent structures," *Chaos*, vol. 20, pp. 017501–1–3, 2010.

[26] J. P. Richter, *The Literary Works of Leonardo da Vinci*. London: Phaidon Press Ltd., 1970.

[27] G. Haller, "Finding finite-time invariant manifolds in two-dimensional velocity fields," *Chaos*, vol. 10, no. 1, pp. 99–108, 2000.

[28] G. Haller, "Distinguished material surfaces and coherent structures in three-dimensional fluid flows," *Physica D*, vol. 149, pp. 248–277, 2001.

[29] G. Haller and G. Yuan, "Lagrangian coherent structures and mixing in two-dimensional turbulence," *Physica D*, vol. 147, pp. 352–370, 2000.

[30] G. Haller, "Lagrangian coherent structures from approximate velocity data," *Physics of Fluids*, vol. 14, no. 6, pp. 1851–1861, 2002.

[31] S. C. Shadden, F. Lekien, and J. E. Marsden, "Definition and properties of Lagrangian coherent structures from finite-time Lyapunov exponents in two-dimensional aperiodic flows," *Physica D*, vol. 212, pp. 271–304, 2005.

[32] M. Mathur, G. Haller, T. Peacock, J. Ruppert-Felsot, and H. Swinney, "Uncovering the Lagrangian Skeleton of Turbulence," *Physical Review Letters*, vol. 98, pp. 144502–1–4, 2007.

[33] F. Lekien, S. C. Shadden, and J. E. Marsden, "Lagrangian coherent structures in n-dimensional systems," *Journal of Mathematical Physics*, vol. 48, pp. 065404–1–19, 2007.

[34] G. Haller and F. J. Beron-Vera, "Geodesic theory of transport barriers in two-dimensional flows," *Physica D*, vol. 241, pp. 1680–1702, 2012.

[35] C. Garth, F. Gerhardt, X. Tricoche, and H. Hagen, "Efficient Computation and Visualization of Coherent Structures in Fluid Flow Applications," *IEEE Transactions on Visualization and Computer Graphics*, vol. 13, no. 2, pp. 1464–1471, 2007.

[36] D. R. Smith, *An Introduction to Continuum Mechanics — after Truesdell and Noll*. Dordrecht: Kluwer, 1993.

[37] A. M. Lyapunov, *The General Problem of the Stability of Motion (1892)*. Bristol, Pennsylvania: Taylor and Francis, 1992. Trans. Russian to French by Édouard Davaux; French to English by A. T. Fuller.

[38] V. I. Olseledec, "A Multiplicative Ergodic Theorem. Lyapunov Characteristic Numbers for Dynamical Systems," *Transactions of the Moscow Mathematical Society*, vol. 19, pp. 197–231, 1968.

[39] R. L. Anderson, *Low Thrust Trajectory Design for Resonance Flybys and Captures Using Invariant Manifolds*. Ph.D. Dissertation, University of Colorado at Boulder, Boulder, Colorado, 2005.

[40] T. S. Parker and L. O. Chua, *Practical Numerical Algorithms for Chaotic Systems*. New York: Springer–Verlag, 1989.

[41] T. Shinbrot, E. Ott, C. Grebogi, and J. A. Yorke, "Using chaos to direct trajectories to targets," *Physical Review Letters*, vol. 65, pp. 3215–3218, 1990.

[42] C. G. Schroer and E. Ott, "Targeting in Hamiltonian systems that have mixed regular/chaotic phase spaces," *Chaos*, vol. 7, no. 4, pp. 512–519, 1997.

[43] D. J. Grebow, *Trajectory Design in the Earth–Moon System and Lunar South Pole Coverage*. Ph.D. Dissertation, Purdue University, West Lafayette, Indiana, 2010.

[44] D. Eberly, R. Gardner, B. Morse, and S. Pizer, "Ridges for Image Analysis," *Journal of Mathematical Imaging and Vision*, vol. 4, pp. 355–371, 1994.

[45] F. Diacu, "The Solution of the n-body Problem," *The Mathematical Intelligencer*, vol. 18, no. 3, pp. 66–70, 1996.

[46] V. Szebehely, *Theory of Orbits: The Restricted Problem of Three Bodies*. New York: Academic Press, 1967.

[47] J. J. Guzman, *Spacecraft Trajectory Design in the Context of a Coherent Restricted Four-Body Problem*. Ph.D. Dissertation, Purdue University, West Lafayette, Indiana, 2001.

[48] T. Pavlak and K. Howell, "Evolution of the Out-of-Plane Amplitude for Quasi-Periodic Trajectories in the Earth–Moon System," *Acta Astronautica*, vol. 81, no. 2, pp. 456–465, 2012.

[49] J. Kepler, *New Astronomy (1609)*. Cambridge: Cambridge University Press, 1992. Translated, W. H. Donahue.

[50] S. Drake, *Discoveries and Opinions of Galileo*. New York: Anchor Books, 1957.

[51] I. Newton, *The Mathematical Principles of Natural Philosophy (1687)*. New York: Prometheus Books, 1995. Translated, A. Motte.

[52] J. Barrow-Green, *Poincaré and the Three Body Problem*. New York: Cambridge University Press, 1997.

[53] L. Euler, *Theoria Motuum Lunae*. Petropoli: Typis Academiae Imperialis Scientiarum, 1772. Reprinted in "Opera Omnia, Series 2" (L. Courvoisier, ed.), Vol. 22, Orell Füssli Turici, Lausanne, 1958.

[54] H. Poincaré, *New Methods of Celestial Mechanics (1893)*. New York: American Institute of Physics, 1993. Translated, D. Goroff.

[55] K. F. Sundman, "Mémoire Sur le Probléme des Trois Corps," *Acta Mathematica*, vol. 36, pp. 105–179, 1912.

[56] Q. Wang, "The global solution of the n-body problem," *Celestial Mechanics*, vol. 50, pp. 73–88, 1991.

[57] F. R. Moulton, *Periodic Orbits*. Washington: The Carnegie Institution, 1920. Publication No. 161.

[58] K. C. Howell, "Families of Orbits in the Vicinity of the Collinear Libration Points," *Journal of the Astronautical Sciences*, vol. 49, no. 1, pp. 107–125, 2001.

[59] M. Hénon, "Numerical Exploration of the Restricted Three-Body Problem," in *Proceedings of International Astronomical Union Symposium No. 25*, (London), pp. 157–169, Academic Press, 1966.

[60] J. F. Kennedy, "John F. Kennedy Moon Speech." [Online Publication, retrieved 24 Feb 2016], `http://er.jsc.nasa.gov/seh/ricetalk.htm`, 1962.

[61] W. E. Burrows, *This New Ocean: The Story of the First Space Age*. New York: Random House, Inc., 1998.

[62] J. V. Breakwell, A. A. Kamel, and M. J. Ratner, "Station-Keeping for a Translunar Communications Station," *Celestial Mechanics*, vol. 10, no. 3, pp. 357–373, 1974.

[63] R. Farquhar, "The Utilization of Halo Orbits in Advanced Lunar Operations," Tech. Rep. X-551-70-449, NASA Goddard, Greenbelt, MD, 1970.

[64] K. C. Howell and J. V. Breakwell, "Almost Rectilinear Halo Orbits," *Celestial Mechanics*, vol. 32, pp. 29–52, January 1984.

[65] K. C. Howell, "Three-Dimensional Periodic 'Halo' Orbits," *Celestial Mechanics*, vol. 32, pp. 53–72, January 1984.

[66] R. W. Farquhar, "The Flight of ISEE-3/ICE: Origins, Mission History, and a Legacy," *Journal of the Astronautical Sciences*, vol. 49, pp. 23–73, January–March 2001.

[67] M. Lo, B. G. Williams, W. E. Bollman, D. Han, Y. Hahn, J. L. Bell, E. A. Hirst, R. A. Corwin, P. E. Hong, K. C. Howell, B. Barden, and R. Wilson, "Genesis Mission Design," in *AIAA/AAS Astrodynamics Specialist Conference*, (Boston, Massachusetts), August 1998.

[68] D. C. Folta, M. Woodard, K. Howell, C. Patterson, and W. Schlei, "Applications of Multi-Body Dynamical Environments: The ARTEMIS Transfer Trajectory Design," in *IAF 61st International Astronautical Congress*, (Prague, Czech Republic), September 2010.

[69] J. W. Gangestad, G. A. Henning, R. Persinger, and G. R. Ricker, "A High Earth, Lunar Resonant Orbit for Lower Cost Space Science Missions," in *AAS/AIAA Astrodynamics Specialist Conference*, (Hilton Head, South Carolina), August 2013.

[70] D. J. Dichmann, J. J. K. Parker, T. Williams, and C. R. Mendelsohn, "Trajectory Design for the Transiting Exoplanet Survey Satellite," in *International Symposium on Space Flight Dynamics*, (Laurel, Maryland), May 2014.

[71] A. E. Roy and M. W. Ovenden, "On the Occurrence of Commensurable Mean Motions in the Solar System: II. The Mirror Theorem," *Monthly Notices of the Royal Astronomical Society*, vol. 115, pp. 296–309, 1955.

[72] D. J. Grebow, "Generating Periodic Orbits in the Circular Restricted Three-Body Problem with Applications to Lunar South Pole Coverage," M.S. Thesis, Purdue University, West Lafayette, Indiana, 2006.

[73] L. P. Chappaz, "The Dynamical Environment in the Vicinity of Small Irregularly-Shaped Bodies with Application to Asteroids," M.S. Thesis, Purdue University, West Lafayette, Indiana, 2011.

[74] Z. P. Olikara, "Computation of Quasi-Periodic Tori in the Circular Restricted Three-Body Problem," M.S. Thesis, Purdue University, West Lafayette, Indiana, 2010.

[75] A. F. Haapala, *Trajectory Design in the Spatial Circular Restricted Three-Body Problem Exploiting Higher-Dimensional Poincaré Maps*. Ph.D. Dissertation, Purdue University, West Lafayette, Indiana, 2014.

[76] G. Katsiaris and C. L. Goudas, "The Symplectic Property of Matrizants," *Astrophysics and Space Science*, vol. 8, pp. 243–250, 1970.

[77] B. G. Marchand, "Temporary Satellite Capture of Short Period Jupiter Family Comets from the Perspective of Dynamical Systems," M.S. Thesis, Purdue University, West Lafayette, Indiana, 2000.

[78] D. C. Davis and K. C. Howell, "Characterization of Trajectories Near the Smaller Primary in the Restricted Problem for Applications," *Journal of Guidance, Control, and Dynamics*, vol. 35, no. 1, pp. 116–128, 2012.

[79] M. Vaquero, *Spacecraft Transfer Trajectory Design Exploiting Resonant Orbits in Multi-Body Environments*. Ph.D. Dissertation, Purdue University, West Lafayette, Indiana, 2013.

[80] C. Geisel, *Spacecraft Orbit Design in the Circular Restricted Three-Body Problem Using Higher-Dimensional Poincaré Maps*. Ph.D. Dissertation, Purdue University, West Lafayette, Indiana, 2013.

[81] W. Squire and G. Trapp, "Using Complex Variables to Estimate Derivatives of Real Functions," *SIAM Review*, vol. 40, no. 1, pp. 110–112, 1998.

[82] D. Folta, M. Woodard, and D. Cosgrove, "Stationkeeping of Lissajous Trajectories in the Earth–Moon System with Applications to ARTEMIS," in *AAS/AIAA Astrodynamics Specialist Conference*, (Girdwood, Alaska), August 2011.

[83] D. Folta, M. Woodard, T. Pavlak, A. Haapala, and K. Howell, "Earth–Moon Libration Stationkeeping: Theory, Modeling, and Operations," in *1st IAA/AAS Conference on the Dynamics and Control of Space Systems*, (Porto, Portugal), March 2012.

[84] T. A. Pavlak and K. C. Howell, "Strategy for Optimal, Long-Term Stationkeeping of Libration Point Orbits in the Earth–Moon System," in *AIAA/AAS Astrodynamics Specialist Conference*, (Minneapolis, Minnesota), August 2012.

[85] "The GNU Scientific Library Manual." [Online Publication, retrieved 28 Feb 2016], `http://www.gnu.org/software/gsl/`, 2016.

[86] "Boost C++ Libraries." [Online Publication, retrieved 28 Feb 2016], `http://www.boost.org/`, 2016.

[87] X. Tricoche, *Vector and Tensor Topology Simplification, Tracking, and Visualization*. Ph.D. Dissertation, University of Kaiserslautern, Kaiserslautern, Germany, 2002.

[88] P. Breeuwsma, "Cubic Interpolation." [Online Publication, retrieved 28 Feb 2016], `http://www.paulinternet.nl/?page=bicubic`, 2016.

[89] F. Lekien and J. Marsden, "Tricubic Interpolation in Three Dimensions," *Journal of Numerical Methods and Engineering*, vol. 63, pp. 455–471, 2005.

[90] S. Barakat and X. Tricoche, "Adaptive Refinement of the Flow Map Using Sparse Samples," *IEEE Transactions on Visualization and Computer Graphics*, vol. 19, no. 12, pp. 2753–2672, 2013.

[91] J. R. R. A. Martins, P. Sturdza, and J. J. Alonso, "The Complex-Step Derivative Approximation," *ACM Transactions of Mathematical Software*, vol. 29, no. 3, pp. 245–262, 2003.

[92] "The OpenMP API Specification for Parallel Programming." [Online Publication, retrieved 28 Feb 2016], `http://openmp.org/wp/`, 2016.

[93] "Open MPI: Open Source High Performance Computing." [Online Publication, retrieved 28 Feb 2016], `http://www.open-mpi.org/`, 2016.

[94] T. Pavlak, *Trajectory Design and Orbit Maintenance Strategies in Multi-Body Dynamical Regimes*. Ph.D. Dissertation, Purdue University, West Lafayette, Indiana, 2013.

[95] A. F. Heaton and J. M. Longuski, "Feasibility of a Galileo-Style Tour of the Uranian Satellites," *Journal of Spacecraft and Rockets*, vol. 40, no. 4, pp. 591–596, 2003.

[96] R. A. Jacobson, "The Gravity Field of the Uranian System and the Orbits of the Uranian Satellites and Rings," *Bulletin of the American Astronomical Society*, vol. 39, p. 453, 1970.

[97] J. Laskar and R. A. Jacobson, "GUST86. An analytical ephemeris of the Uranian satellites," *Astronomy and Astrophysics*, vol. 188, p. 212, 1987.

[98] W. S. Koon, M. W. Lo, J. E. Marsden, and S. D. Ross, "Constructing a Low Energy Transfer Between Jovian Moons," *Contemporary Mathematics*, vol. 292, pp. 129–145, 2002.

[99] M. Kakoi, K. Howell, and D. Folta, "Access to Mars from Earth–Moon Libration Point Orbits: Manifold and Direct Options," *Acta Astronautica*, vol. 102, pp. 269–286, 2014.

[100] A. Haapala, M. Vaquero, T. Pavlak, K. Howell, and D. Folta, "Trajectory Selection Strategy for Tours in the Earth–Moon System," in *AAS/AIAA Astrodynamics Specialist Conference*, (Hilton Head, South Carolina), August 2013.

[101] J. S. Parker and M. W. Lo, "Unstable Resonant Orbits Near Earth and Their Applications in Planetary Missions," in *AIAA GNC Conference*, (Providence, Rhode Island), August 2004.

[102] R. L. Anderson and M. W. Lo, "Role of Invariant Manifolds in Low-thrust Trajectory Design," *Journal of Guidance, Control, and Dynamics*, vol. 32, no. 6, pp. 1921–1930, 2009.

[103] M. Vaquero and K. Howell, "Leveraging Resonant Orbit Manifolds to Design Transfers between Libration Point Orbits," *Journal of Guidance, Control, and Dynamics*, vol. 37, no. 4, pp. 1143–1157, 2014.

[104] J. Carrico Jr., D. Dichmann, L. Policastri, J. Carrico III, T. Craychee, J. Ferreira, M. Intelisano, R. Lebois, M. Loucks, T. Schrift, and R. Sherman, "Lunar-Resonant Trajectory Design for the Interstellar Boundary Explorer (IBEX) Extended Mission," in *AAS/AIAA Astrodynamics Specialist Conference*, (Girdwood, Alaska), August 2011.

[105] D. J. Dichmann, R. Lebois, and J. P. Carrico, "Dynamics of Orbits Near 3:1 Resonance in the Earth–Moon System," *Journal of the Astronautical Sciences*, vol. 60, no. 1, pp. 51–86, 2015.

[106] C. Colombo, "Long-term Evolution of Highly-Elliptical Orbits: Luni-solar Perturbation Effects for Stability and Re-entry," in *AAS/AIAA Space Flight Mechanics Meeting*, (Williamsburg, Virginia), January 2015.

[107] C. Colombo, E. M. Alessi, W. van der Weg, S. Soldini, F. Letizia, M. Vetrisano, M. Vasile, A. Rossi, and M. Landgraf, "End-of-life disposal concepts for Libration Point Orbit and Highly Elliptical Orbit missions," *Acta Astronautica*, vol. 110, pp. 208–312, 2015.

[108] Y. Kozai, "Secular perturbations of asteroids with high inclinations and high eccentricity," *Astronomical Journal*, vol. 67, pp. 591–598, 1962.

[109] M. Lidov, "The Evolution of Orbits of Artificial Satellites of Planets under the Action of Gravitational Perturbations of External Bodies," *Planetary and Space Science*, vol. 9, pp. 719–759, 1962.

[110] N. Bosanac, K. C. Howell, and E. Fischbach, "Exploring the Impact of a Three-Body Interaction Added to the Gravitational Potential Function in the Restricted Three-Body Problem," in *AAS/AIAA SFM Meeting*, (Kauai, Hawaii), February 2013.

[111] K. C. Howell and D. C. Davis, "Spacecraft Trajectory Design Strategies Based on Close Encounters with a Smaller Primary in a 4-body Model," in *AAS/AIAA Astrodynamics Specialist Conference*, (Honolulu, Hawaii), August 2008.

[112] A. F. B. A. Prado, "Searching for Orbits with Minimum Fuel Consumption for Station-Keeping Maneuvers: An Application to Lunisolar Perturbations," *Mathematical Problems in Engineering*, vol. 2013, no. Article ID 415015, 2013.

[113] A. F. B. A. Prado, "Mapping orbits around the asteroid $2001SN_{263}$," *Advances in Space Research*, vol. 53, pp. 877–889, 2014.

[114] D. M. Sanchez, A. F. B. A. Prado, and T. Yokoyama, "On the effects of each term of the geopotential perturbation along the time I: Quasi-circular orbits," *Advances in Space Research*, vol. 54, pp. 1008–1018, 2014.

VITA

VITA

In May 2001, Cody Short graduated from Council High School in Council, Idaho. It was through his studies in high school, and his experiences in the Boy Scouts of America, that he developed an interest in physics and astronomy. This interest, coupled with encouragement from family, led him to study at Brigham Young University. After a number of years, in April 2007, he left BYU with a B.S. in Physics and Astronomy. Along the way Cody met and married Lori (August 2006), and their first son, Jackson, joined them shortly after graduation in May 2007. Endeavoring to deflect his studies along a more hands-on trajectory, Cody joined the Multi-body Dynamics research group in the School of Aeronautics & Astronautics at Purdue University to study engineering. Despite his intentions, he was unable to quite shake off his earlier inclinations, and began investigating what turned out to be very theoretical and computational work (he has yet to build an actual spacecraft). While at Purdue, Grayson joined the family in June 2010, before Cody completed his M.S. in Astrodynamics in December 2010. After a few more years, Branson came along (August 2013) to help Cody complete his Ph.D., also in Astrodynamics, in May 2016. After graduation, Cody joined Analytical Graphics, Inc. as an Astrodynamics Software Engineer in Exton, Pennsylvania.